Abstract of "Spectral Methods and Absorbing Boundary Conditions for Maxwell's Equations," by Baolin Yang, Ph.D., Brown University, May 1998

In this dissertation, I present my research results in computational electromagnetics and pseudospectral methods. In 1-D, the comparisons of staggered and non-staggered finite difference and spectral methods have been done. I also give some new penalty methods for 1-D scalar hyperbolic equation and Maxwell's equations. It is shown that the advantage of staggering for low-order methods diminishes when we go to high-order and spectral methods, which is verified in numerical experiments.

In 2-D, I present a new polar PML method, a mapped ML method, and well-posed PML methods. Simulations of scattering by perfect electrically conducting (PEC) circular, elliptic, and rectangular cylinders using multidomain pseudospectral methods with the proposed absorbing layer methods have been done to validate the methods. For comparison, results of finite difference time domain (FD-TD) computations of the same problems are also presented, and spectral methods are shown to be superior to FD-TD methods.

Absorbing layers for more general 2-D structures are also discussed, where we give a multidomain implementation of the PML methods and an approximately matched layer method. Simulations of scattering by PEC parallelogram and triangular cylinders have been done to verify our claims. The proposed methods give better results than some other extensions of the PML method do.

In 3-D, we have developed split-field and well-posed PML methods in spherical and cylindrical coordinates. A general multidomain pseudospectral scheme is developed to simulate scattering by a PEC cube, a PEC sphere and a PEC finite cylinder. Efficacy of our proposed PML methods is demonstrated in numerical experiments.

For the simulation of scattering by bodies of revolution (axis symmetric), we develop a multidomain pseudospectral scheme with the mapped ML method as the absorbing boundary condition, where PML methods are not applicable. We solve modified BOR Maxwell's equations with proper boundary conditions at the axis that remove the singularity there. Simulations of scattering of both axially and obliquely incident waves by both smooth and non-smooth PEC scatterers have been done. The scheme has been extended to simulate scattering by dielectric spheres in the last chapter.

Spectral Methods and Absorbing Boundary Conditions for Maxwell's Equations

by

Baolin Yang

B.S., Nanjing University, 1990
M.S., Chinese Academy of Sciences, 1993

Thesis

Submitted in partial fulfillment of the requirements for
the Degree of Doctor of Science
in the Division of Applied Mathematics at Brown University

May 1998

Preface

In this dissertation I aim to include the research I have done in computational electromagnetics and spectral methods and show the efficiency in using high-order and spectral methods in computational electromagnetics. Computational electromagnetics is a fast-developing area and it is expected that high-order and spectral methods will play a more and more important role.

The dissertation grows out of some published and unpublished papers. Those papers are joint work with Dr. Lucia Dettori, Prof. David Gottlieb, and Dr. Jan S. Hesthaven. A list of those papers can be found in my vita. It has been my great pleasure to work with them. For convenience, some of them are included here more or less untouched.

During the unnecessary hard time or the necessary busy time of my graduate study, my wife has always been standing shoulder to shoulder with me. I take this opportunity to thank her for her support.

Acknowledgments

I would like to take this opportunity to express my great thanks to Prof. David Gottlieb for his years of insightful advice and encouragements. I owe my great thanks to Prof. Chi-Wang Shu and Prof. Paul Fischer. They arranged my coming to Brown and working in the numerical analysis and scientific computing group. Special thanks are given to Dr. Jan S. Hesthaven for numerous discussions and helps. Thanks are also given to Dr. Wai Sun Don for his help in getting me started. In the end I want to thank Dr. Lucia Dettori, Prof. David Gottlieb, and Dr. Jan S. Hesthaven for their great collaboration with me during the tenure of the joint work.

The author was supported by DARPA/AFOSR Grant F49620-95-1-0074 and F49620-96-1-0426.

Contents

Chapter 1

Introduction

Until 1990, the modeling of engineering systems involving electromagnetic wave interactions was dominated by frequency-domain techniques. The primary computational approach is the method of moments (MoM), which involves setting up and solving dense, full, complex-valued systems of thousands or even tens of thousands of linear equations using direct or iterative techniques. However, many important contemporary problems in electromagnetic wave engineering are not adequately treated by such models.

Prompted to a significant degree by perceived limitations of MoM for whole-aircraft radar cross section modeling, there has been an explosion of interest in direct solutions of the fundamental Maxwell's equations on space grids in either the time or frequency domain. These methods have been found to be remarkably robust, providing highly accurate modeling predictions for electromagnetic interaction problems. This approach is also efficient and has a systematic approach to deal with complex materials.

However, the primary time-domain method, the finite difference time domain (FD-TD) method, so extensively used for computing electromagnetic scattering by general objects, suffers from the requirement of having 10-20 grid points per wavelength to obtain sufficiently accurate solutions of the scattered fields, while spectral methods are known for requiring very few points per wavelength, 2 for the Fourier method and π for the Chebyshev method. Spectral methods are also efficient compared with FD-TD method, which will be shown in analysis and experiments.

The shortcoming of spectral methods is that they require a fixed distribution of grid points. However, with the introduction of multidomain decomposition method, spectral methods can be used in simulations involving complex geometries. We are going to present multidomain pseudospectral methods in 2-D, 3-D and 2.5-D (axis symmetric). Schemes capable of handling complex geometries are developed for solving Maxwell's equations.

An important issue in computational electromagnetics is the absorbing boundary condition, introduced to truncate the computational domain. The perfectly matched layer methods are very effective in reflectionless mesh truncation. We shall investigate PML methods in various coordinate systems, as well as the implementation of PML methods in more general domains. We also present two other absorbing boundary layer methods, the mapped matched layer method and the approximately matched layer method. The absorbing boundary conditions are validated and compared in extensive numerical experiments.

The remaining part of the dissertation is organized as follows. In chapter 2, we introduce Maxwell's equations, radar cross section, and some numerical ingredients of multidomain pseudospectral methods. In chapter 3, we investigate PML methods in various coordinate systems. Chapter 4 is devoted to the comparison of staggered and non-staggered schemes in 1-D. Penalty methods for 1-D Maxwell's equations are investigated in chapter 5. In chapter 6, we present the numerical results on the simulations in 2-D. In chapter 7, we discuss 2-D absorbing layer methods with more flexible vacuum-layer interface. Numerical results on 3-D simulations are presented in chapter 8. In chapter 9, we present methods for numerical computation of scattering by bodies of revolution, and we extend the scheme to simulate scattering by dielectric spheres in chapter 10.

Chapter 2

Preliminaries

2.1 Maxwell's Equations

2.1.1 Basic Equations

We consider a region of space that has no electric current sources, but may have materials that absorb electric or magnetic field energy. We assume that the materials are linear, isotropic nondispersive (i.e. , materials having field-independent, direction-independent, and frequency-independent electric and magnetic properties). In such materials we can relate the magnetic flux density vector $\vec{B}$ to the magnetic field vector $\vec{H}$ and the electric flux density vector $\vec{D}$ to the electric field vector $\vec{E}$ using:

$$\vec{B} = \mu \vec{H} \quad , \tag{2.1}$$

$$\vec{D} = \epsilon \vec{E} \quad , \tag{2.2}$$

where μ is the magnetic permeability in henrys per meter and ϵ is the electric permittivity in farads per meter. Permitting the possibility of electric and magnetic losses that can dissipate electromagnetic fields in materials via conversion to heat energy, we have the following time-dependent

Maxwell's curl equations for $\vec{E}$ and $\vec{H}$ fields:

$$\frac{\partial \vec{H}}{\partial t} = -\frac{1}{\mu}\nabla \times \vec{E} - \frac{\rho'}{\mu}\vec{H} \quad , \tag{2.3}$$

$$\frac{\partial \vec{E}}{\partial t} = \frac{1}{\epsilon}\nabla \times \vec{H} - \frac{\sigma}{\epsilon}\vec{E} \quad , \tag{2.4}$$

where ρ' is an equivalent magnetic resistivity in ohms per meter and σ is the electric conductivity in siemens per meter.

At an interface between two media, the properties of overall medium change discontinuously, and this may result in discontinuities in some components in the field. The transition conditions relating the fields on the two sides of the interface can be deduced from the integral form of Maxwell's equations using standard procedures [46]. The conditions, in terms of frequency domain fields, are:

$$[\vec{n} \times \vec{E}]_{-}^{+} = 0 \quad , \tag{2.5}$$

$$[\vec{n} \cdot \mu\vec{H}]_{-}^{+} = 0 \quad , \tag{2.6}$$

$$[\vec{n} \times \vec{H}]_{-}^{+} = \mathbf{J}_{e(s)} \quad , \tag{2.7}$$

$$[\vec{n} \cdot \epsilon\vec{E}]_{-}^{+} = -\rho_{e(s)} \quad , \tag{2.8}$$

where $[\,]_{-}^{+}$ denotes the discontinuity between the upper (+) and lower (-) sides of the interface, $\vec{n}$ is a unit vector normal to the interface directed into the upper medium, and $\mathbf{J}_{e(s)}$ and $\rho_{e(s)}$ are surface electric current and charge distributions respectively.

If the lower medium is a perfect electric conductor (PEC material), all fields there are zero by definition and $\mathbf{J}_{m(s)} = \rho_{m(s)} = 0$. Hence

$$\vec{n} \times \vec{E} = 0 \quad , \tag{2.9}$$

$$\vec{n} \cdot \mu\vec{H} = 0 \ . \tag{2.10}$$

For simulations of electromagnetic scattering by PEC scatterers, we apply this condition as the boundary condition at the scatterer surface. Note that the time domain formulation of the condition is the same.

2.1.2 Non-dimensionalized Maxwell's Equations

In the following we show how to non-dimensionalize the three-dimensional Maxwell's equations with respect to free space parameters. We apply the following transformation to non-dimensionalize Maxwell's equations (2.3)-(2.4) where we assume $\rho' = 0$ and $\sigma = 0$ for simplicity:

$$x = \tilde{x}/L \ , \ y = \tilde{y}/L \ , \ t = \tilde{c}\tilde{t}/L \ ,$$

where L represents a scale length and the fields are normalized as

$$H = \tilde{H} \ , \ E = \sqrt{\frac{\varepsilon_0}{\mu_0}}\tilde{E} = Z_0^{-1}\tilde{E} \ ,$$

where ϵ_0 is the free-space electric permittivity, μ_0 is the free-space permeability, and Z_0 represents the free-space impedance. We then obtain the non-dimensionalized and symmetric system that is more convenient for analysis:

$$\frac{\partial \vec{H}}{\partial t} = -\frac{1}{\mu_r}\nabla \times \vec{E} \ , \tag{2.11}$$

$$\frac{\partial \vec{E}}{\partial t} = \frac{1}{\epsilon_r}\nabla \times \vec{H} \ , \tag{2.12}$$

where $\epsilon_r = \frac{\epsilon}{\epsilon_0}$ is the relative permittivity and $\mu_r = \frac{\mu}{\mu_0}$ is the relative permeability. We can write out the vector components of the curl operator to yield the following system of six coupled scalar equations equivalent to Maxwell's curl equations:

$$\frac{\partial H_x}{\partial t} = \frac{1}{\mu_r}(-\frac{\partial E_z}{\partial y} + \frac{\partial E_y}{\partial z}) \ , \tag{2.13}$$

$$\frac{\partial H_y}{\partial t} = \frac{1}{\mu_r}(-\frac{\partial E_x}{\partial z} + \frac{\partial E_z}{\partial x}) \ , \tag{2.14}$$

$$\frac{\partial H_z}{\partial t} = \frac{1}{\mu_r}(-\frac{\partial E_y}{\partial x} + \frac{\partial E_x}{\partial y}) \ , \tag{2.15}$$

$$\frac{\partial E_x}{\partial t} = \frac{1}{\epsilon_r}(\frac{\partial H_z}{\partial y} - \frac{\partial H_y}{\partial z}) \ , \tag{2.16}$$

$$\frac{\partial E_y}{\partial t} = \frac{1}{\epsilon_r}(\frac{\partial H_x}{\partial z} - \frac{\partial H_z}{\partial x}) \ , \tag{2.17}$$

$$\frac{\partial E_z}{\partial t} = \frac{1}{\epsilon_r}(\frac{\partial H_y}{\partial x} - \frac{\partial H_x}{\partial y}) \ . \tag{2.18}$$

Note that in free space, $\epsilon_r = 1$ and $\mu_r = 1$.

2.1.3 Radar Cross Section

The radar cross section (RCS), closed related to the far field fields, is adopted as a primary criteria in assessing the accuracy of numerical schemes. In 3-D case, the differential scattering section or bistatic radar cross section $\sigma(\theta, \phi)$ is defined by

$$\sigma(\theta, \phi) = \lim_{r \to \infty} \frac{|\vec{E}^s|^2}{|\vec{E}^i|^2}$$

where $|\vec{E}|^2 = |E_x|^2 + |E_y|^2 + |E_z|^2$, $\vec{E}^s$ is the scattered field at the observation point (r, θ, ϕ), and $\vec{E}^i$ is the incident field.

2.2 Spectral Methods in Time-Domain Electromagnetics

To come to an understanding and appreciation of the need for high-order methods in time-domain electromagnetics, let us briefly recall the issue of phase-errors associated with finite-difference methods, as first presented in the pioneering work of Kreiss and Oliger [34].

We consider, for simplicity, the scalar wave equation

$$\frac{\partial u}{\partial t} = -c\frac{\partial u}{\partial x} \ , \ \ u(x, 0) = e^{ikx} \ ,$$

in the domain $x \in [0, 2\pi]$, subject to periodic boundary conditions and only the effect of the spatial approximation shall be discussed. After we introduce an equidistant grid

$$x_j = \frac{2\pi j}{N} = j\Delta x \quad , \quad j \in [0, N-1] \quad ,$$

such that $u(x_j, t) = u_j$, we obtain the $2m$'th central difference approximation to the 1'st derivative of $u(x,t)$ at x_j as

$$\left.\frac{\partial u}{\partial x}\right|_{x_j} = \sum_{n=1}^{m} \left(\frac{-2(-1)^n (m!)^2}{(m-n)!(m+n)!} \right) \frac{u_{j+n} - u_{j-n}}{2n\Delta x} \quad .$$

This approximation yields a discrete version of the wave equation with an exact solution on the form

$$u(x,t) = e^{ik(x - c_m(k)t)} \quad ,$$

where $c_m(k)$ is termed the numerical wave speed. Clearly we wish that $c \simeq c_m(k)$ over as large a range of the wavenumber, k, as possible. A measure, the phase error, of this property is thus given as

$$e_m(k) = |k(c - c_m(k))t| \quad .$$

The analysis of the phase error allows us to answer questions about the proper choice of schemes for a specified phase error and the important question of the overall efficiency of high-order methods.

To continue, let us introduce proper measures about the actual scheme. In particular, we introduce the non-dimensional numbers

$$p = \frac{N}{k} = \frac{2\pi}{k\Delta x} \quad , \quad \nu = \frac{ct}{\lambda} \quad ,$$

which are nothing else than the number of points per wavelength, p, and the number of wave-periods, ν, we wish to advance the wave. Utilizing this notation, the leading order phase-error takes the form

$$e_m(p,\nu) \simeq \frac{\pi\nu}{\alpha_m}\left(\frac{2\pi}{p}\right)^{2m} \quad ,$$

where α_m is specific to the truncation error of the different schemes, e.g. $\alpha_1 = 3$, $\alpha_2 = 15$, $\alpha_3 = 70$ etc. If we term the maximal acceptable phase-error, ε_p, we recover the bounds

$$p_m(\nu,\varepsilon_p) \geq 2\pi \sqrt[2m]{\frac{\nu\pi}{\alpha_m\varepsilon_p}} = \beta_m \sqrt[2m]{\frac{\nu}{\varepsilon_p}} \quad ,$$

telling an interesting story in that it gives a lower bound of the required number of points per wavelengths, $p_m(\nu,\varepsilon_p)$, in order to ensure a specified error, ε_p. Not only does the required number of points per wavelength depend on the acceptable accuracy, ε_p, but also on the number of periods, ν, required to complete the computation, i.e. the effect of the phase-error accumulates in time. However, this latter effect decreases rapidly as the order, $2m$, of the scheme increases. Utilizing staggering of the grids does not change this behavior qualitatively [25]. Consequently, this simple analysis shows that high-order methods are particularly well suited for dealing with electrically large problems, since only few points per wavelength is required to maintain acceptable accuracy, and for transient problems where long time integration is required. Indeed, computational electromagnetics of the future will required both, emphasizing the need for the development of high-order methods suitable for addressing such problems.

While it is accepted that high-order methods yield superior accuracy, one often encounters a misunderstanding regarding efficiency of such methods. To address this concern, let us define a measure of work, W_m, as

$$W_m = 2mp_m\frac{t}{\Delta t} = 2mp_m\frac{p_m\nu}{CFL_m} \quad ,$$

where CFL_m refers to the maximum CFL number for stability, i.e., we measure the amount of work per wavelength using a $2m$'th scheme during the required number of time-steps.

If we, for simplicity, assume that a 4th-order Runge-Kutta method is used for temporal integration, the estimated work for a 2nd, 4th and 6th order scheme are

$$W_1 \simeq 30\nu\frac{\nu}{\varepsilon_p} \;\;,\;\; W_2 \simeq 35\nu\sqrt{\frac{\nu}{\varepsilon_p}} \;\;,\;\; W_3 \simeq 48\nu\sqrt[3]{\frac{\nu}{\varepsilon_p}} \;\;,$$

confirming that high-order methods, also in terms of efficiency, is the proper choice when one requires accuracy and long-time integration.

If we take the above arguments to the limit of $m \rightarrow \infty$, it appears that $W_\infty \propto \nu$, i.e. the work depends only linearly on the number of periods or, in other words, the number of points per wavelength, p_∞, must be independent of ν. In this limit we recover the Fourier spectral methods for which only 2 points per wavelength is required to solve the problem *exactly* independent of the time of integration, ν. This dramatic reduction in the required number of grid points becomes even more important when multi-dimensional problems is considered, adding additional advantages to the use of high-order methods.

The Achilles Heel of high-order methods is the treatment of boundary conditions. Contrary to the situation discussed above, the majority of practical problems involves non-periodic phenomena and computational domains. The practice of embedding an object, e.g. a scatterer, inside the computational domain, so successfully employed in traditional FD-TD methods [51], becomes a source of significant problems when a high-order solution is attempted due to Gibbs-like oscillations close to the discontinuity and associated slow convergence. The solution to this problem is the use of body-conforming grids, introducing the need for additional grid points close to the boundary or, alternatively, the use of one-sided difference operators. While the first approach involves the introduction of additional/approximate information, the latter is notorious for causing stability problems and requires the construction of $(2m-1)$th order closures.

To circumvent these well known problems, we have chosen to use spectral methods based on Chebyshev polynomials for non-periodic problems. While these methods require a non-uniform grid distribution to ensure stability, they share all the properties of the Fourier spectral methods.

In particular, only π points per wavelength is required to accurately resolve the wave [22] in this case. However, as we shall experience later, the use of such polynomial spectral methods, when properly constructed, retains all the geometric flexibility of low-order methods while providing clear computational advantages associated with the use of high-order methods for the solution of time-dependent wave-dominated problems as they appear in time-domain electromagnetics.

Now we briefly introduce the formulations of the spectral methods we use and some other basic numerical ingredients.

2.2.1 Fourier Collocation Method

Given the values, $u(\theta_j)$, at the Fourier collocation points: $\theta_j = \frac{\pi j}{N}$, $j = 0, \ldots, 2N-1$, we seek an interpolating trigonometric polynomial of degree N:

$$I_N u(\theta) = \sum_{k=-N}^{N-1} \tilde{u}_k e^{ik\theta} \ , \tag{2.19}$$

where

$$\tilde{u}_k = \frac{1}{2N} \sum_{j=0}^{2N-1} u(\theta_j) e^{-ik\theta_j} \ , \tag{2.20}$$

and then compute the derivative of the trigonometric polynomial:

$$(I_N u)'(\theta) = \sum_{k=-N}^{N-1} ik\tilde{u}_k e^{ik\theta} \ , \tag{2.21}$$

at the Fourier collocation points θ_j.

This procedure involves two FFT's, requiring $O(N \log_2 N)$ operations, one for the interpolation and one for the evaluation of the derivatives. We can also compute the derivatives directly by a matrix-vector multiplication by noting that the interpolating Fourier series can be expressed in terms of a Lagrange interpolation polynomial $g_j(\theta)$.

The entries of the Fourier derivative matrix D are computed by taking the analytical derivative of $g_j(\theta)$ and evaluating it at the collocation points θ_k for $j, k = 0, \ldots, 2N-1$, i.e., $D_{kj} = g'_j(\theta_k)$.

Then the entries of the matrix are

$$\begin{aligned} D_{kj} &= \frac{1}{2}(-1)^{k+j}\cot\left(\frac{1}{2}(\theta_k-\theta_j)\right) , \quad j \neq k \ , \\ D_{jj} &= 0 \qquad\qquad\qquad\qquad\qquad\quad\; j = k \ . \end{aligned} \tag{2.22}$$

2.2.2 Chebyshev Collocation Method

Given the values, $u(r_j)$, at the Chebyshev Gauss-Lobatto collocation points given as $r_j = \cos\frac{\pi j}{N}$, $j = 0, \ldots, N$, we seek an interpolating polynomial of degree N:

$$I_N u(r) = \sum_{k=0}^{N} \tilde{u}_k T_k(r) \ , \tag{2.23}$$

and compute the derivative of the polynomial:

$$(I_N u)'(r) = \sum_{k=0}^{N} \tilde{u}'_k T_k(r) \ . \tag{2.24}$$

The coefficients, $\tilde{u}'_k$, are computed from the coefficients $\tilde{u}_k$ by using the backward recurrence relation

$$\begin{aligned} &\tilde{u}'_{N+1} = \tilde{u}'_N = 0 \\ &c_k \tilde{u}'_k = \tilde{u}'_{k+2} + 2(k+1)\tilde{u}_{k+1}, \ k = 0, 1, \ldots, N-1 \ , \end{aligned} \tag{2.25}$$

where

$$c_k = \begin{cases} 2 & \text{if } k = 0 \ , \\ 1 & \text{otherwise} \ . \end{cases} \tag{2.26}$$

This procedure involves two CFT's, requiring $O(N \log_2 N)$ operations, one for the interpolation and one for the evaluation of the derivatives. We can also compute the derivatives directly by a matrix-vector multiplication by noting that the interpolating polynomial can be expressed in terms of a Lagrange interpolation polynomial $g_j(x)$.

The entries of the Chebyshev derivative matrix D are computed by taking the analytical derivative of $g_j(x)$ and evaluating it at the collocation points x_k for $j,k = 0,\dots,N$, i.e., $D_{kj} = g'_j(x_k)$. Then the entries of the matrix are

$$\begin{aligned} D_{kj} &= \frac{c_k}{c_j}\frac{(-1)^{j+k}}{(x_k - x_j)} , & j \neq k \ , \\ D_{kk} &= -\frac{1}{2}\frac{x_k}{(1-x_k^2)} , & k \neq 0, N \ , \\ D_{00} &= -D_{NN} = \frac{2N^2+1}{6} \ . \end{aligned} \tag{2.27}$$

It is pointed out in [12] that calculating the matrix directly in this form results in unnecessarily large numerical error, and a formulation that yields more accuracy is given.

2.2.3 Filtering

Filtering is necessary when we simulate electromagnetic scattering by objects that have edges or corners, since the field values at edges or corners could become infinite.

Given the Fourier series interpolation for $u(\theta)$,

$$I_N u(\theta) = \sum_{k=-N}^{N-1} \tilde{u_k} e^{ik\theta} \ , \tag{2.28}$$

we modify the original sum (2.28) as

$$u_N^{\sigma}(\theta) = \sum_{k=-N}^{N-1} \tilde{u_k} \sigma(\frac{k}{N}) e^{ik\theta} \ . \tag{2.29}$$

using the exponential filter,

$$\sigma(\frac{k}{N}) = e^{-\alpha(\frac{k}{N})^m} \ , \tag{2.30}$$

where m is the order of the filter and $\alpha = -\log(\epsilon)$ with ϵ being the machine zero. By choosing m to be proportional to N, we maintain the exponential accuracy of the spectral methods.

The filtering formula for the Chebyshev case is similar. The only difference is that the Fourier interpolation, Eq. (2.28), is replaced by the Chebyshev interpolation, Eq. (2.23).

2.2.4 Cubic Grid Mapping

In our numerical computations of the pseudospectral methods, a cubic grid mapping is often adopted to map the Chebyshev Gauss-Lobatto collocation points r_j to a new set of points $R_j,\ j = 0, \ldots,\ N$ in an interval $[R_0, R_N]$ as desired, with the map being

$$R_j = C_1 \cdot (r_j + C_0)^3 + R_0 - C_1 \cdot (1 + C_0)^3 \ , \tag{2.31}$$

where

$$C_1 = \frac{R_N - R_0}{(C_0 - 1)^3 - (C_0 + 1)^3} \ , \ j = 0, \ldots,\ N \ . \tag{2.32}$$

The constant C_0 is chosen such that the transition of the grid is smooth.

2.2.5 Multidomain Method

Traditional spectral methods suffer from having a fixed distribution of grid points, thereby making it difficult to apply such methods for solving problems with strong internal layers or problems in complex geometries. Using a multi-domain approach, i.e. splitting the computational domain into several geometrically simple body conforming domains, has proven to be a powerful way of overcoming these restrictions on the applicability of spectral methods (see e.g. [28]). Moreover, such an approach allows for an efficient implementation on contemporary parallel computers [15] and relieves much of the computational burden of spectral methods even on serial computers, since one can increase the number of subdomains rather than the number of points in each subdomain.

In absorbing layers one often needs to solve a set of equations different from the original Maxwell's equations, and in different materials, the coefficients in Maxwell's equations may be different. In our work, multidomain method is also used to facilitate the application of absorbing boundary layer methods and to deal with problems in complex materials. We decompose the computational domain in such a way that we only need to consider one set of differential equations in each subdomain.

Patching solutions involving different materials and absorbing layers needs special consideration.

However, at the interface of any two subdomains having the same material property, the characteristic relations are used to patch the field values following a standard procedure. We enforce the characteristic variables along incoming characteristics in each subdomain to be the same as that along the outgoing characteristics in the neighboring subdomain. The zero speed characteristic variables are averaged across the interface and the outgoing characteristic variables are preserved. This procedure of interchanging information between neighboring subdomains is applied at each time step to ensure that a global solution is obtained.

In our 2-D and 3-D Chebyshev scheme, we apply a multi-step patching procedure, where the interface between different subdomains are separated into different groups. We will apply the patching conditions at one group of interfaces at one step. The separation is done in such a way that we can not find two neighboring interfaces, having an edge (3-D) or a vertex (2-D) in common, in the same group. As the outward normal vector of each interface is needed in patching the solutions at the interface, we avoid the problem of having two conflicting normal vector at an edge (3-D) or a vertex (2-D) that is shared by two non-smoothly connected interfaces. If the computational domain is not complex, the multi-step patching procedure usually can be implemented as patching direction by direction.

We note that this procedure is local in nature as each point at the interface only requires information from one point at the boundary of the neighboring subdomain. Hence, in a parallel setting, the communication grows only as the size of the surface of the subdomain rather than the subdomain itself, making the algorithm well suited for parallelization.

2.2.6 Transfinite Blending Functions and Curvilinear Coordinates

In obtaining approximate solutions to electromagnetic wave problems in the general three dimensional domain, $\Omega \subset \mathsf{R}^3$, enclosed by the boundary $\delta\Omega$, we employ polynomial approximations of the electromagnetic fields and their spatial derivatives. The most natural and computationally efficient extension to several dimensions appears through the use of tensor products.

The extension of polynomial approximations to several dimensions through the use of tensor products, however, requires that the computational domain is diffeomorphic to the unit cube, i.e. a one-domain solution is excluded for general multiply connected domains. To surround this obstruction, we construct Ω using K non-overlapping general hexahedrals, $\mathsf{D}^k \subset \mathsf{R}^3$, such that

$$\Omega = \bigcup_{k=1}^{K} \mathsf{D}^k \quad , \quad \delta\Omega = \bigcup_{k=1}^{K} \delta\mathsf{D}_{kk} \quad , \quad \delta\mathsf{D}^k = \bigcup_{i=1}^{K} \delta\mathsf{D}_{ki} \quad ,$$

where $\delta\mathsf{D}_{kk} = \mathsf{D}^k \cap \delta\Omega$ and $\delta\mathsf{D}_{ki} = \mathsf{D}^k \cap \mathsf{D}^i$ for $i \neq k$, and there exists a diffeomorphism, $\Psi : \mathsf{D}^k \to \mathsf{I}$, where $\mathsf{I} \subset \mathsf{R}^3$ is the unit cube, i.e. $\mathsf{I} \in [-1,1]^3$. For simplicity, we shall denote D^k by D with boundary $\delta\mathsf{D}$, refer to any curvilinear hexahedral domain, and we term the coordinates, $\boldsymbol{x} \in \mathsf{D}$, as (x,y,z) and (x_1,x_2,x_3), interchangeably. Likewise, we introduce the coordinates, $\boldsymbol{\xi} \in \mathsf{I}$, named (ξ,η,ζ). The terminology is illustrated in Fig. 2.1.

For the construction of the map, $\Psi : \mathsf{D} \to \mathsf{I}$, we define $\Xi_L = \Xi_L^\xi \times \Xi_L^\eta \times \Xi_L^\zeta$, through the subsets

$$\Xi_L^\xi = \{\bar{i} | \bar{i} \in [0,\ldots,L_\xi]\} \quad , \quad \Xi_L^\eta = \{\bar{j} | \bar{j} \in [0,\ldots,L_\eta]\} \quad , \quad \Xi_L^\zeta = \{\bar{k} | \bar{k} \in [0,\ldots,L_\zeta]\} \quad .$$

Associated with these sets are the nodal sets

$$\Lambda_L^\xi(\Xi_L^\xi) = \{\xi_{\bar{i}}\}_{\bar{i}=0}^{L_\xi} \quad , \quad \Lambda_L^\eta(\Xi_L^\eta) = \{\eta_{\bar{j}}\}_{\bar{j}=0}^{L_\eta} \quad , \quad \Lambda_L^\zeta(\Xi_L^\zeta) = \{\zeta_{\bar{k}}\}_{\bar{k}=0}^{L_\zeta} \quad ,$$

with the global nodal set, $\Lambda_L(\Xi_L) = \Lambda_L = \Lambda_L^\xi \times \Lambda_L^\eta \times \Lambda_L^\zeta$. The nodal sets are assumed to be ordered such that $\xi_0 = \eta_0 = \zeta_0 = -1$ and $\xi_{L_\xi} = \eta_{L_\eta} = \zeta_{L_\zeta} = 1$. Likewise, for the construction of the polynomial approximation inside the domain, I, we introduce the global set $\Xi_N = \Xi_N^\xi \times \Xi_N^\eta \times \Xi_N^\zeta$, where

$$\Xi_N^\xi = \{i | i \in [0,\ldots,N_\xi]\} \quad , \quad \Xi_N^\eta = \{j | j \in [0,\ldots,N_\eta]\} \quad , \quad \Xi_N^\zeta = \{k | k \in [0,\ldots,N_\zeta]\} \quad ,$$

with the corresponding nodal sets

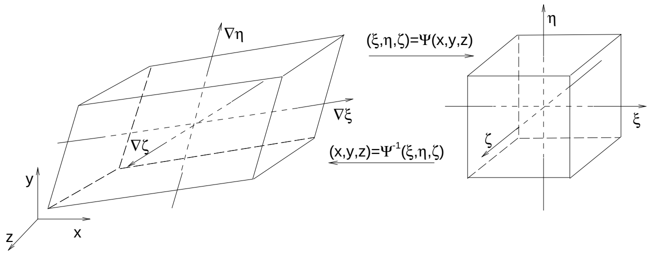

Figure 2.1: Three dimensional mapping between the general hexahedral, D, and the unit cube, I.

$$\Lambda_N^\xi(\Xi_N^\xi) = \{\xi_i\}_{i=0}^{N_\xi} \ , \ \ \Lambda_N^\eta(\Xi_N^\eta) = \{\eta_j\}_{j=0}^{N_\eta} \ , \ \ \Lambda_N^\zeta(\Xi_N^\zeta) = \{\zeta_k\}_{k=0}^{N_\zeta} \ ,$$

and the global nodal set inside the unit cube, $\Lambda_N(\Xi_N) = \Lambda_N = \Lambda_N^\xi \times \Lambda_N^\eta \times \Lambda_N^\zeta$. The nodes in Λ_N are assumed ordered as in Λ_L.

For simplicity, we shall use the notation $\Xi_N^{\xi\eta} = \Xi_N^\xi \times \Xi_N^\eta$ and likewise for various combinations of the sets. For ease of exposure, let us also introduce the global interior set, $\tilde{\Xi}_N = \tilde{\Xi}_N^\xi \times \tilde{\Xi}_N^\eta \times \tilde{\Xi}_N^\zeta \subset \Xi_N$, where

$$\tilde{\Xi}_N^\xi = \Xi_N^\xi \setminus \{0, N_\xi\} \ , \ \ \tilde{\Xi}_N^\eta = \Xi_N^\eta \setminus \{0, N_\eta\} \ , \tilde{\Xi}_N^\zeta = \Xi_N^\zeta \setminus \{0, N_\zeta\} \ ,$$

with the associated interior nodal set, $\tilde{\Lambda}_N$. The exact specification of the nodal sets, Λ_L and Λ_N, shall be addressed shortly.

To establish a one to one correspondence between the unit cube and the general hexahedral we will construct the global map, $\Psi : \mathsf{D} \rightarrow \mathsf{I}$, using transfinite blending functions [20, 21]. The correspondence between the two domains, expressed through the map $\boldsymbol{x} = \Psi^{-1}(\boldsymbol{\xi})$, is derived from the boolean sum

$$\begin{aligned} \boldsymbol{x} = & \quad (P_\xi \oplus P_\eta \oplus P_\zeta)\boldsymbol{x}(\boldsymbol{\xi}) \qquad (2.33) \\ = & \quad P_\xi(\boldsymbol{x}) + P_\eta(\boldsymbol{x}) + P_\zeta(\boldsymbol{x}) - P_\xi P_\eta(\boldsymbol{x}) - P_\xi P_\zeta(\boldsymbol{x}) - P_\eta P_\zeta(\boldsymbol{x}) + P_\xi P_\eta P_\zeta(\boldsymbol{x}) \ . \end{aligned}$$

where we have introduced the face projectors

$$P_\xi(\boldsymbol{x}) = \sum_{\Xi_L^\xi} N_{\bar{i}}^\xi(\xi)\boldsymbol{x}(\xi_{\bar{i}}, \eta, \zeta) \ \ ,$$

and likewise for $P_\eta(\boldsymbol{x})$ and $P_\zeta(\boldsymbol{x})$. The shape functions, $N_{\bar{i}}^\xi$, $N_{\bar{j}}^\eta$ and $N_{\bar{k}}^\zeta$, are nothing more than the interpolating Lagrange polynomials based on Λ_L^ξ, Λ_L^η and Λ_L^ζ, respectively. Using the properties of the projectors, the edge projectors become

$$P_\xi P_\eta(\boldsymbol{x}) = \sum_{\Xi_L^{\xi\eta}} N_{\bar{i}}^\xi(\xi) N_{\bar{j}}^\eta(\eta)\boldsymbol{x}(\xi_{\bar{i}}, \eta_{\bar{j}}, \zeta) \ \ ,$$

and likewise for $P_\xi P_\zeta(\boldsymbol{x})$ and $P_\eta P_\zeta(\boldsymbol{x})$, whereas the vertex projector becomes

$$P_\xi P_\eta P_\zeta(\boldsymbol{x}) = \sum_{\Xi_L} N_{\bar{i}}^\xi(\xi) N_{\bar{j}}^\eta(\eta) N_{\bar{k}}^\zeta(\zeta)\boldsymbol{x}(\xi_{\bar{i}}, \eta_{\bar{j}}, \zeta_{\bar{k}}) \ \ .$$

To simplify things further we may also apply the transfinite blending function to construct the face projectors as

$$\begin{aligned}
\boldsymbol{x}(\xi_{\bar{i}}, \eta, \zeta) = & \quad (P_\eta \oplus P_\zeta)(\boldsymbol{x}(\xi_{\bar{i}}, \eta, \zeta)) \\
= & \quad P_\eta(\boldsymbol{x}(\xi_{\bar{i}}, \eta, \zeta)) + P_\zeta(\boldsymbol{x}(\xi_{\bar{i}}, \eta, \zeta)) - P_\eta P_\zeta(\boldsymbol{x}(\xi_{\bar{i}}, \eta, \zeta)) \ \ ,
\end{aligned}$$

and similarly for the remaining faces.

Within this formulation, the construction of the global map, $\boldsymbol{\Psi}$, or rather its inverse, becomes feasible. In what remains we assume that the shape functions are linear, i.e. $L_\xi = L_\eta = L_\zeta = 1$ and $\Lambda_L^\xi = \Lambda_L^\eta = \Lambda_L^\zeta = \{-1, 1\}$, as $N_0^\xi = (1-\xi)/2$ and $N_1^\xi = (1+\xi)/2$ and is similar fashion for $N_{\bar{j}}^\eta$ and $N_{\bar{k}}^\zeta$. Thus, to construct the map we need to specify a parametric form for the edges enclosing D, e.g.

$$\boldsymbol{x}(\xi, -1, -1) = \sum_{\Xi_N^\xi} \boldsymbol{x}(\xi_i, -1, -1) L_i^\alpha(\xi) \ \ ,$$

where $L_i^\alpha(\xi)$ signifies the Lagrange polynomial based on the nodal set, Λ_N^ξ, employed in I. For a thorough discussion of the transfinite blending functions and their properties, we refer to [20, 21].

Once the global map is established, spatial derivatives in D of the function f is obtained through a general curvilinear coordinate transformation with the metric of the transformation being derived through the identity

$$\frac{\partial \boldsymbol{x}}{\partial \boldsymbol{\xi}}\frac{\partial \boldsymbol{\xi}}{\partial \boldsymbol{x}} = \begin{bmatrix} x_\xi & x_\eta & x_\zeta \\ y_\xi & y_\eta & y_\zeta \\ z_\xi & z_\eta & z_\zeta \end{bmatrix} \begin{bmatrix} \xi_x & \xi_y & \xi_z \\ \eta_x & \eta_y & \eta_z \\ \zeta_x & \zeta_y & \zeta_z \end{bmatrix} = \mathcal{I} \ ,$$

where $\mathcal{I}$ is the identity matrix, the first Jacobian is obtained from the map, Eq.(2.33) and the transformation Jacobian becomes

$$J = \left| \frac{\partial \boldsymbol{x}}{\partial \boldsymbol{\xi}} \right| = x_\xi y_\eta z_\zeta + x_\zeta y_\xi z_\eta + x_\eta y_\zeta z_\xi - x_\xi y_\zeta z_\eta - x_\eta y_\xi z_\zeta - x_\zeta y_\eta z_\xi \ .$$

Finally, we note that the local coordinate system in D is spanned by $(\nabla\xi, \nabla\eta, \nabla\zeta)$ (see Fig. 2.1), which, in the special case of an orthogonal curvilinear coordinate system, obeys the relation $\nabla\xi \cdot \nabla\eta = \nabla\xi \cdot \nabla\zeta = \nabla\eta \cdot \nabla\zeta = 0$.

Chapter 3

On PML Methods in Various Coordinate Systems

3.1 Introduction

In [3] Berenger proposed the perfectly matched layer (PML) method for truncating the computational domains in the numerical solution of Maxwell's equations. The method is developed for Maxwell's equations in Cartesian coordinates and the absorbing layer is shown to be nonreflecting at the vacuum-layer interface. It was extended into 3-D in [4]. The 2-D and 3-D PML's designed by Berenger have vacuum-layer interfaces that are planar by construction. The extension of the rectangular PML method into spherical or cylindrical coordinate system remained open.

In wave scattering problems involving objects such as spheres or finite cylinders, though it can be used, the rectangular PML method is awkward to use, especially when one uses body-conforming meshes. If we do not require the PML to be conforming to grid lines, we can even use the rectangular PML method to surround a circular scatterer. In [56], chapter 6, we did numerical experiments in 2-D, simulating infinitely long circular cylinders using the rectangular PML method with circular meshes. Though it turned out to be much better than applying characteristic relations to terminate the mesh, it is less accurate than the polar PML method in [56] by more than one order of magnitude.

From both a convenience (under most circumstances) and an accuracy point of view, we see from our experiences in 2-D that there is a need to develop and use "real" spherical and cylindrical PML methods in simulations involving spherical and cylindrical objects.

Some variations of Berenger's PML method have been reported, where the original fields rather than the split fields were adopted in the derivation of layers having the same perfect matching property. This turned out to be meaningful aside from just being more efficient. In [2] Abarbanel and Gottlieb proved that the split-field formulation of the PML method in [3] is only weakly well-posed and may suffer from instability problems. Unsplit-field PML methods only using ordinary differential equations and low-order terms to modify Maxwell's equations clearly keep the strong well-posedness property of the original symmetric hyperbolic system. In [2] Abarbanel and Gottlieb analyzed and compared different well-posed PML methods in 2-D. In [57] we presented some very accurate numerical results using well-posed PML methods in 2-D Cartesian and polar coordinates.

The extension of the 3-D rectangular PML method to other coordinate systems, however, has remained open. In [35], Kuzuoglu and Mittra presented nonplanar perfectly matched absorbers for finite-element mesh truncation. They designed PML's to absorb spherical and cylindrical waves. They also derived the reflection coefficients for the PML's and showed that the coefficients could no longer be made identically zero in general, unlike the rectangular PML method. They showed that the extension was effective when the radius of the vacuum-layer interface was electrically large. The existence of ideal nonreflecting PML methods in spherical or cylindrical coordinate system remained unclear. It is our purpose here to show that ideal nonreflecting PML methods can be obtained in spherical and cylindrical coordinate systems.

Note that in [56] we already obtained the polar perfectly matched layer method in polar coordinates (2-D) where the vacuum-layer interface is a circle. The numerical results of the method turned out to be superior to other methods. In this chapter, we continue to develop the cylindrical and spherical PML methods in 3-D by using the same techniques as we used in [56]. For 3-D spherical and cylindrical PML methods, the desired vacuum-layer interfaces are the surface of a sphere and the surface of a cylinder respectively. The methods we develop admit plane wave solutions that match perfectly at the vacuum-layer interface, i.e. , any plane waves can pass through the interface without causing any reflection. The property holds for plane waves of any frequency and any incident angle.

Our spherical PML method has the additional merit that plane waves of any incident angle decay in the propagation direction in the whole layer region, which is not true for the rectangular PML method. The rectangular PML method depends on the corner regions for the complete absorption of waves. Though for our cylindrical PML method, the complete absorption of plane waves also depends on corner regions, it has fewer regions and smaller range of incident angles where plane waves do not decay, as compared with the rectangular PML method.

There are two versions of PML methods proposed in this chapter, the split-field and the well-posed PML methods. The split-field spherical and cylindrical PML methods are obtained through splitting the original Maxwell's equations like what Berenger did in [3] and [4]. For the well-posed PML methods, we look for the modified Maxwell's equations that admit decaying plane wave solutions similar to those of the split-field PML methods with an additional scaling factor. With the additional degree of freedom of the scaling factor, we are able to design the solutions in such a way that they satisfy Maxwell's equations plus some low-order terms and it is possible for those low-order terms to be governed by ordinary differential equations only.

3.2 Maxwell's Equations and Its Solutions

We consider the non-dimensionalized Maxwell's equations in free space:

$$\frac{\partial H}{\partial t} = -\nabla \times E \ , \tag{3.1}$$

$$\frac{\partial E}{\partial t} = \nabla \times H \ . \tag{3.2}$$

The expression of the curl operator in the spherical coordinate system is

$$\begin{aligned}\nabla \times A = \quad & \hat{r}\tfrac{1}{r\sin\theta}[\tfrac{\partial}{\partial\theta}(\sin\theta A_\phi) - \tfrac{\partial A_\phi}{\partial\phi}]+ \\ & \hat{\theta}\tfrac{1}{r}[\tfrac{1}{\sin\theta}\tfrac{\partial A_r}{\partial\phi} - \tfrac{\partial}{\partial r}(rA_\phi)]+ \\ & \hat{\phi}\tfrac{1}{r}[\tfrac{\partial}{\partial r}(rA_\theta) - \tfrac{\partial A_r}{\partial\theta}] \ ,\end{aligned} \tag{3.3}$$

and the expression of the curl operator in the cylindrical coordinate system is

$$\nabla \times A = \hat{\rho}(\frac{1}{\rho}\frac{\partial A_z}{\partial\phi} - \frac{\partial A_\phi}{\partial z}) + \hat{\phi}(\frac{\partial A_\rho}{\partial z} - \frac{\partial A_z}{\partial\rho}) + \hat{z}(\frac{1}{\rho}\frac{\partial\rho A_\phi}{\partial\rho} - \frac{1}{\rho}\frac{\partial A_\rho}{\partial\phi}) \ . \tag{3.4}$$

Now we can write out the vector components of the curl operator to yield the following system of six coupled scalar equations equivalent to Maxwell's curl equations. In three-dimensional spherical coordinate system (r, θ, ϕ), we have:

$$\frac{\partial H_r}{\partial t} = -\frac{1}{r\sin\theta}\frac{\partial}{\partial\theta}(\sin\theta E_\phi) + \frac{1}{r\sin\theta}\frac{\partial E_\theta}{\partial\phi} \ ,$$

$$\frac{\partial H_\theta}{\partial t} = -\frac{1}{r\sin\theta}\frac{\partial E_r}{\partial\phi} + \frac{1}{r}\frac{\partial}{\partial r}(rE_\phi) \ ,$$

$$\frac{\partial H_\phi}{\partial t} = -\frac{1}{r}\frac{\partial}{\partial r}(rE_\theta) + \frac{1}{r}\frac{\partial E_r}{\partial\theta} \ ,$$

$$\frac{\partial E_r}{\partial t} = \frac{1}{r\sin\theta}\frac{\partial}{\partial\theta}(\sin\theta H_\phi) - \frac{1}{r\sin\theta}\frac{\partial H_\theta}{\partial\phi} \ ,$$

$$\frac{\partial E_\theta}{\partial t} = \frac{1}{r\sin\theta}\frac{\partial H_r}{\partial\phi} - \frac{1}{r}\frac{\partial}{\partial r}(rH_\phi) \ ,$$

$$\frac{\partial E_\phi}{\partial t} = \frac{1}{r}\frac{\partial}{\partial r}(rH_\theta) - \frac{1}{r}\frac{\partial H_r}{\partial\theta} \ .$$

In three-dimensional cylindrical coordinates (ρ, ϕ, z), we have:

$$\frac{\partial H_\rho}{\partial t} = \frac{\partial E_\phi}{\partial z} - \frac{1}{\rho}\frac{\partial E_z}{\partial\phi} \ ,$$

$$\frac{\partial H_\phi}{\partial t} = \frac{\partial E_z}{\partial\rho} - \frac{\partial E_\rho}{\partial z} \ ,$$

$$\frac{\partial H_z}{\partial t} = \frac{1}{\rho}\frac{\partial E_\rho}{\partial \phi} - \frac{1}{\rho}\frac{\partial \rho E_\phi}{\partial \rho} ,$$

$$\frac{\partial E_\rho}{\partial t} = \frac{1}{\rho}\frac{\partial H_z}{\partial \phi} - \frac{\partial H_\phi}{\partial z} ,$$

$$\frac{\partial E_\phi}{\partial t} = \frac{\partial H_\rho}{\partial z} - \frac{\partial H_z}{\partial \rho} ,$$

$$\frac{\partial E_z}{\partial t} = \frac{1}{\rho}\frac{\partial \rho H_\phi}{\partial \rho} - \frac{1}{\rho}\frac{\partial H_\rho}{\partial \phi} .$$

Maxwell's equations admit the following plane wave solutions:

$$H = (l_2\hat{x} + m_2\hat{y} + n_2\hat{z})e^{i\omega(t-lx-my-nz)} , \tag{3.5}$$

$$E = (l_1\hat{x} + m_1\hat{y} + n_1\hat{z})e^{i\omega(t-lx-my-nz)} , \tag{3.6}$$

where

$$l_1\hat{x} + m_1\hat{y} + n_1\hat{z} = (l_2\hat{x} + m_2\hat{y} + n_2\hat{z}) \times (l\hat{x} + m\hat{y} + n\hat{z}) , \tag{3.7}$$

$$l_2\hat{x} + m_2\hat{y} + n_2\hat{z} = (l\hat{x} + m\hat{y} + n\hat{z}) \times (l_1\hat{x} + m_1\hat{y} + n_1\hat{z}) . \tag{3.8}$$

For a plane wave incident in the direction (θ_0, ϕ_0), we have

$$e^{i\omega(t-lx-my-nz)} = e^{i\omega(t-r(\cos\theta_0\cos\theta+\sin\theta_0\sin\theta\cos(\phi-\phi_0)))} . \tag{3.9}$$

in the spherical coordinate system and

$$e^{i\omega(t-lx-my-nz)} = e^{i\omega(t-\sqrt{1-n^2}\rho\cos(\phi-\phi_0)-nz)} \tag{3.10}$$

in the cylindrical coordinate system.

Now we write out the plane-wave field components in spherical coordinate system as:

$$H_r = (\cos\phi\sin\theta l_2 + \sin\phi\sin\theta m_2 + \cos\theta n_2)e^{i\omega(t-r(\cos\theta_0\cos\theta+\sin\theta_0\sin\theta\cos(\phi-\phi_0)))} , \tag{3.11}$$

$$H_\theta = (\cos\phi\cos\theta l_2 + \sin\phi\cos\theta m_2 - \sin\theta n_2)e^{i\omega(t-r(\cos\theta_0\cos\theta+\sin\theta_0\sin\theta\cos(\phi-\phi_0)))}\ , \tag{3.12}$$

$$H_\phi = (-\sin\phi l_2 + \cos\phi m_2)e^{i\omega(t-r(\cos\theta_0\cos\theta+\sin\theta_0\sin\theta\cos(\phi-\phi_0)))}\ , \tag{3.13}$$

$$E_r = (\cos\phi\sin\theta l_1 + \sin\phi\sin\theta m_1 + \cos\theta n_1)e^{i\omega(t-r(\cos\theta_0\cos\theta+\sin\theta_0\sin\theta\cos(\phi-\phi_0)))}\ , \tag{3.14}$$

$$E_\theta = (\cos\phi\cos\theta l_1 + \sin\phi\cos\theta m_1 - \sin\theta n_1)e^{i\omega(t-r(\cos\theta_0\cos\theta+\sin\theta_0\sin\theta\cos(\phi-\phi_0)))}\ , \tag{3.15}$$

$$E_\phi = (-\sin\phi l_1 + \cos\phi m_1)e^{i\omega(t-r(\cos\theta_0\cos\theta+\sin\theta_0\sin\theta\cos(\phi-\phi_0)))}\ , \tag{3.16}$$

and the plane-wave field components in cylindrical coordinates as:

$$H_\rho = (\cos\phi l_2 + \sin\phi m_2)e^{i\omega(t-\sqrt{1-n^2}\rho\cos(\phi-\phi_0)-nz)}\ , \tag{3.17}$$

$$H_\phi = (-\sin\phi l_2 + \cos\phi m_2)e^{i\omega(t-\sqrt{1-n^2}\rho\cos(\phi-\phi_0)-nz)}\ , \tag{3.18}$$

$$H_z = n_2 e^{i\omega(t-\sqrt{1-n^2}\rho\cos(\phi-\phi_0)-nz)}\ , \tag{3.19}$$

$$E_\rho = (\cos\phi l_1 + \sin\phi m_1)e^{i\omega(t-\sqrt{1-n^2}\rho\cos(\phi-\phi_0)-nz)}\ , \tag{3.20}$$

$$E_\phi = (-\sin\phi l_1 + \cos\phi m_1)e^{i\omega(t-\sqrt{1-n^2}\rho\cos(\phi-\phi_0)-nz)}\ , \tag{3.21}$$

$$E_z = n_1 e^{i\omega(t-\sqrt{1-n^2}\rho\cos(\phi-\phi_0)-nz)}\ . \tag{3.22}$$

The plane wave solutions are to be matched by decaying plane wave solutions in the perfectly matched layers.

3.3 Perfectly Matched Layers in Various Coordinate Systems

We first explain Berenger's PML method with varying conductivity parameter, which is less complicated than Berenger's, and explain the ideas of various PML methods. Then we shall derive the spherical and cylindrical perfectly matched layer methods. For our spherical and cylindrical

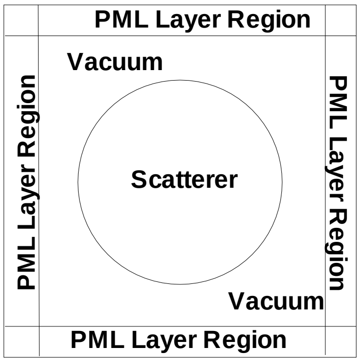

Figure 3.1: An illustration of the PML method for the truncation of a computational domain in electromagnetic scattering simulation.

PML methods, we will analyze their decaying property in the direction of wave propagation. This property is important for the success of PML methods, since in numerical computation, there are reflections at the outer boundaries of PML's due to the inexact boundary conditions applied there and one wants those reflected waves, though of very small magnitude, to be further absorbed rather than reversed in the PML's.

3.3.1 Berenger's Perfectly Matched Layer

In [3] Berenger gave the perfectly matched layer method suitable for rectangular grid truncation and wave absorption. The idea of the PML method is illustrated in 2-D, for simplicity, in Fig. 3.1, where the computational domain around the scatterer is terminated by 4 PML regions. The PML regions are designed such that waves can be absorbed in them without reflections. In the following we give the plane wave analysis of the method for which we consider a layer of continuously varying absorption strength.

Our objective is to obtain the equations that admit plane wave solutions with a decaying factor:

$$D(x,y,z) = e^{-l\sigma_x(x) - m\sigma_y(y) - n\sigma_z(z)} \ . \tag{3.23}$$

We want $D(x,y,z)$ to approach zero smoothly enough when (x,y,z) approaches the vacuum-layer interface.

The following is the Berenger-type split-field equations one needs to solve for the rectangular PML method.

$$\frac{\partial H_{xy}}{\partial t} = -\frac{\partial(E_{zx}+E_{zy})}{\partial y} - \sigma'_y(y)H_{xy} \ ,$$

$$\frac{\partial H_{xz}}{\partial t} = \frac{\partial(E_{yx}+E_{yz})}{\partial z} - \sigma'_z(z)H_{xz} \ ,$$

$$\frac{\partial H_{yz}}{\partial t} = -\frac{\partial(E_{xy}+E_{xz})}{\partial z} - \sigma'_z(z)H_{yz} \ ,$$

$$\frac{\partial H_{yx}}{\partial t} = \frac{\partial(E_{zx}+E_{zy})}{\partial x} - \sigma'_x(x)H_{yx} \ ,$$

$$\frac{\partial H_{zx}}{\partial t} = -\frac{\partial(E_{yx}+E_{yz})}{\partial x} - \sigma'_x(x)H_{zx} \ ,$$

$$\frac{\partial H_{zy}}{\partial t} = \frac{\partial(E_{xy}+E_{xz})}{\partial y} - \sigma'_y(y)H_{zy} \ ,$$

$$\frac{\partial E_{xy}}{\partial t} = \frac{\partial(H_{zx}+H_{zy})}{\partial y} - \sigma'_y(y)E_{xy} \ ,$$

$$\frac{\partial E_{xz}}{\partial t} = -\frac{\partial(H_{yx}+H_{yz})}{\partial z} - \sigma'_z(z)E_{xz} \ ,$$

$$\frac{\partial E_{yz}}{\partial t} = \frac{\partial(H_{xy}+H_{xz})}{\partial z} - \sigma'_z(z)E_{yz} \ ,$$

$$\frac{\partial E_{yx}}{\partial t} = -\frac{\partial(H_{zx}+H_{zy})}{\partial x} - \sigma'_x(x)E_{yx} \ ,$$

$$\frac{\partial E_{zx}}{\partial t} = \frac{\partial(H_{yx}+H_{yz})}{\partial x} - \sigma'_x(x)E_{zx} \ ,$$

$$\frac{\partial E_{zy}}{\partial t} = -\frac{\partial(H_{xy}+H_{xz})}{\partial y} - \sigma'_y(y)E_{zy} \ .$$

It is easily verified that we have the following decaying plane-wave solutions for the above equations:

$$H_{xz} = -m_2 n e^{i\omega(t-xl-ym-nz)}D(x,y,z) \ ,$$

$$H_{yz} = l_2 n e^{i\omega(t-xl-ym-nz)}D(x,y,z) \ ,$$

$$H_{yx} = -n_2 l e^{i\omega(t-xl-ym-nz)} D(x,y,z) \ ,$$

$$H_{zx} = m_2 l e^{i\omega(t-xl-ym-nz)} D(x,y,z) \ ,$$

$$H_{zy} = -l_2 m e^{i\omega(t-xl-ym-nz)} D(x,y,z) \ ,$$

$$E_{xy} = -n_2 m e^{i\omega(t-xl-ym-nz)} D(x,y,z) \ ,$$

$$E_{xz} = m_2 n e^{i\omega(t-xl-ym-nz)} D(x,y,z) \ ,$$

$$E_{yz} = -l_2 n e^{i\omega(t-xl-ym-nz)} D(x,y,z) \ ,$$

$$E_{yx} = n_2 l e^{i\omega(t-xl-ym-nz)} D(x,y,z) \ ,$$

$$E_{zx} = -m_2 l e^{i\omega(t-xl-ym-nz)} D(x,y,z) \ ,$$

$$E_{zy} = l_2 m e^{i\omega(t-xl-ym-nz)} D(x,y,z) \ .$$

According to the relations that couple (l,m,n), (l_1,m_1,n_1) and (l_2,m_2,n_2) in Eq. (3.7)-(3.8), we have $E_{xy}+E_{xz}=E_x D(x,y,z)$, $E_{yz}+E_{yx}=E_y D(x,y,z)$, $E_{zx}+E_{zy}=E_z D(x,y,z)$, $H_{xy}+H_{xz}=H_x D(x,y,z)$, $H_{yz}+H_{yx}=H_y D(x,y,z)$, and $H_{zx}+H_{zy}=H_z D(x,y,z)$, where E_x, E_y, E_z, H_x, H_y, and H_z are plane wave solutions in Eq. (3.5)-(3.6). So the decaying plane-wave solutions in the layer region match perfectly with the plane-wave solutions in vacuum as long as the functions $\sigma_x(x)$, $\sigma_y(y)$ and $\sigma_z(z)$ are properly chosen. Clearly it is better to choose a function that is zero at the interface and increases smoothly outwards.

3.3.2 Spherical Perfectly Matched Layer

In this section we want to develop a spherical perfectly matched layer method for terminating the computational domain and the vacuum-layer interface we desire is a sphere surface. Our objective is that plane waves of any incident direction and any frequency can pass the vacuum-layer interface without causing any reflection, and decay in all directions of propagation in the layer region. We also want strength of the layer to vary only with the radius r and approach zero smoothly towards the interface.

In designing such a perfectly matched layer, we need to do some manipulations of the original Maxwell's equations to obtain equations that admit a particular set of solutions having the properties of a PML. For this purpose, one basically has two approaches. One approach is to split the original equations and add low-order absorbing terms, and the other approach is to modify the original equations by adding low-order terms and additional ordinary differential equations. The first approach, which is presented in the following, results in plane wave solutions that are simpler than those of the second approach, which will be presented later.

To derive the spherical PML method, our objective is to obtain differential equations that admit plane wave solutions with a decaying factor of the following form:

$$D(r,\theta,\phi) = e^{-\sigma_r(r)(\cos\theta_0\cos\theta+\sin\theta_0\sin\theta\cos(\phi-\phi_0))} . \tag{3.24}$$

The equations we get is the following split-field formulation of Maxwell's equations:

$$\frac{\partial H_r}{\partial t} = -\frac{1}{r\sin\theta}\frac{\partial}{\partial\theta}(\sin\theta(E_{\phi r}+E_{\phi\theta})) + \frac{1}{r\sin\theta}\frac{\partial(E_{\theta\phi}+E_{\theta r})}{\partial\phi} - \frac{\sigma_r(r)}{r}H_r , \tag{3.25}$$

$$\frac{\partial H_{\theta\phi}}{\partial t} = -\frac{1}{r\sin\theta}\frac{\partial E_r}{\partial\phi} + \frac{1}{r}(E_{\phi r}+E_{\phi\theta}) - \frac{\sigma_r(r)}{r}H_{\theta\phi} , \tag{3.26}$$

$$\frac{\partial H_{\theta r}}{\partial t} = \frac{\partial(E_{\phi r}+E_{\phi\theta})}{\partial r} - \sigma_r'(r)H_{\theta r} , \tag{3.27}$$

$$\frac{\partial H_{\phi r}}{\partial t} = -\frac{\partial(E_{\theta\phi}+E_{\theta r})}{\partial r} - \sigma_r'(r)H_{\phi r} , \tag{3.28}$$

$$\frac{\partial H_{\phi\theta}}{\partial t} = \frac{1}{r}\frac{\partial E_r}{\partial\theta} - \frac{1}{r}(E_{\theta\phi}+E_{\theta r}) - \frac{\sigma_r(r)}{r}H_{\phi\theta} . \tag{3.29}$$

$$\frac{\partial E_r}{\partial t} = \frac{1}{r\sin\theta}\frac{\partial}{\partial\theta}(\sin\theta(H_{\phi r}+H_{\phi\theta})) - \frac{1}{r\sin\theta}\frac{\partial(H_{\theta\phi}+H_{\theta r})}{\partial\phi} - \frac{\sigma_r(r)}{r}E_r , \tag{3.30}$$

$$\frac{\partial E_{\theta\phi}}{\partial t} = \frac{1}{r\sin\theta}\frac{\partial H_r}{\partial\phi} - \frac{1}{r}(H_{\phi r}+H_{\phi\theta}) - \frac{\sigma_r(r)}{r}E_{\theta\phi} , \tag{3.31}$$

$$\frac{\partial E_{\theta r}}{\partial t} = -\frac{\partial(H_{\phi r}+H_{\phi\theta})}{\partial r} - \sigma_r'(r)E_{\theta r} , \tag{3.32}$$

$$\frac{\partial E_{\phi r}}{\partial t} = \frac{\partial(H_{\theta\phi} + H_{\theta r})}{\partial r} - \sigma'_r(r) E_{\phi r} \ , \tag{3.33}$$

$$\frac{\partial E_{\phi\theta}}{\partial t} = -\frac{1}{r}\frac{\partial H_r}{\partial \theta} + \frac{1}{r}(H_{\theta\phi} + H_{\theta r}) - \frac{\sigma_r(r)}{r} E_{\phi\theta} \ . \tag{3.34}$$

We note that we only need to solve ten equations, compared with twelve equations that one needs to solve for the split-field rectangular PML method.

In order for the PML to effectively match and absorb incident plane waves, the function $\sigma_r(r)$ has to be properly chosen. Let the vacuum-layer interface be at $r = r_0$. Hence, we should have $\sigma_r(r) = 0$ for $rleqr_0$. Following the considerations of the absorbing and reflectionless properties of the polar PML method, $\sigma_r(r)$ must satisfy the requirements:

$$\sigma_r(r) = 0, \text{ and } \sigma_r(r) > 0 \quad \text{for } r > r_0 \ , \tag{3.35}$$

so that the plane wave solutions decays for $r > r_0$. We also require that

$$\sigma'_r(r) > 0 \quad \text{for } r > r_0 \ . \tag{3.36}$$

An example of a valid choice of $\sigma_r(r)$ is

$$\sigma_r(r) = C(r - r_0)^n, \ n = 1, 2, \ldots \ , \ r \geq r_0 \ , \tag{3.37}$$

where C is a positive constant. This family of functions satisfies the requirements in (3.35) - (3.36).

We have a set of plane wave solutions with the desired decaying factor for the above equations. The solutions are given in the following:

$$H_r = (\cos\phi \sin\theta l_2 + \sin\phi \sin\theta m_2 + \cos\theta n_2) e^{i\omega(t - r(\cos\theta_0 \cos\theta + \sin\theta_0 \sin\theta \cos(\phi - \phi_0)))} D(r, \theta, \phi) \ , \tag{3.38}$$

$$\begin{aligned} H_{\theta\phi} = -(\cos\phi \sin\theta l_1 + \sin\phi \sin\theta m_1 + \cos\theta n_1) \sin\theta_0 \sin(\phi - \phi_0) \\ \cdot e^{i\omega(t - r(\cos\theta_0 \cos\theta + \sin\theta_0 \sin\theta \cos(\phi - \phi_0)))} D(r, \theta, \phi) \ , \end{aligned} \tag{3.39}$$

$$H_{\theta r} = -(-\sin\phi l_1 + \cos\phi m_1)(\cos\theta_0\cos\theta + \sin\theta_0\sin\theta\cos(\phi-\phi_0))$$
$$\cdot e^{i\omega(t-r(\cos\theta_0\cos\theta+\sin\theta_0\sin\theta\cos(\phi-\phi_0)))}D(r,\theta,\phi)\ , \tag{3.40}$$

$$H_{\phi r} = (\cos\phi\cos\theta l_1 + \sin\phi\cos\theta m_1 - \sin\theta n_1)(\cos\theta_0\cos\theta + \sin\theta_0\sin\theta\cos(\phi-\phi_0))$$
$$\cdot e^{i\omega(t-r(\cos\theta_0\cos\theta+\sin\theta_0\sin\theta\cos(\phi-\phi_0)))}D(r,\theta,\phi)\ , \tag{3.41}$$

$$H_{\phi\theta} = (\cos\phi\sin\theta l_1 + \sin\phi\sin\theta m_1 + \cos\theta n_1)(\cos\theta_0\sin\theta - \sin\theta_0\cos\theta\cos(\phi-\phi_0))$$
$$\cdot e^{i\omega(t-r(\cos\theta_0\cos\theta+\sin\theta_0\sin\theta\cos(\phi-\phi_0)))}D(r,\theta,\phi)\ , \tag{3.42}$$

$$E_r = (\cos\phi\sin\theta l_1 + \sin\phi\sin\theta m_1 + \cos\theta n_1)e^{i\omega(t-r(\cos\theta_0\cos\theta+\sin\theta_0\sin\theta\cos(\phi-\phi_0)))}D(r,\theta,\phi)\ , \tag{3.43}$$

$$E_{\theta\phi} = (\cos\phi\sin\theta l_2 + \sin\phi\sin\theta m_2 + \cos\theta n_2)\sin\theta_0\sin(\phi-\phi_0)$$
$$\cdot e^{i\omega(t-r(\cos\theta_0\cos\theta+\sin\theta_0\sin\theta\cos(\phi-\phi_0)))}D(r,\theta,\phi)\ , \tag{3.44}$$

$$E_{\theta r} = (-\sin\phi l_2 + \cos\phi m_2)(\cos\theta_0\cos\theta + \sin\theta_0\sin\theta\cos(\phi-\phi_0))$$
$$\cdot e^{i\omega(t-r(\cos\theta_0\cos\theta+\sin\theta_0\sin\theta\cos(\phi-\phi_0)))}D(r,\theta,\phi)\ , \tag{3.45}$$

$$E_{\phi r} = -(\cos\phi\cos\theta l_2 + \sin\phi\cos\theta m_2 - \sin\theta n_2)(\cos\theta_0\cos\theta + \sin\theta_0\sin\theta\cos(\phi-\phi_0))$$
$$\cdot e^{i\omega(t-r(\cos\theta_0\cos\theta+\sin\theta_0\sin\theta\cos(\phi-\phi_0)))}D(r,\theta,\phi)\ , \tag{3.46}$$

$$E_{\phi\theta} = -(\cos\phi\sin\theta l_2 + \sin\phi\sin\theta m_2 + \cos\theta n_2)(\cos\theta_0\sin\theta - \sin\theta_0\cos\theta\cos(\phi-\phi_0))$$
$$\cdot e^{i\omega(t-r(\cos\theta_0\cos\theta+\sin\theta_0\sin\theta\cos(\phi-\phi_0)))}D(r,\theta,\phi)\ , \tag{3.47}$$

where (l_2, m_2, n_2), (l_1, m_1, n_1) and (l, m, n) satisfy the relations in Eq. (3.7)-(3.8). Note that now we have $l = \cos\phi_0\sin\theta_0$, $m = \sin\phi_0\sin\theta_0$, and $n = \cos\theta_0$. One can verify that

$$\begin{aligned}
E_{\theta\phi} + E_{\theta r} &= [(\cos\phi\sin\theta l_2 + \sin\phi\sin\theta m_2 + \cos\theta n_2)\sin\theta_0\sin(\phi-\phi_0)+\\
&(-\sin\phi l_2 + \cos\phi m_2)(\cos\theta_0\cos\theta + \sin\theta_0\sin\theta\cos(\phi-\phi_0))\\
&\cdot e^{i\omega(t-r(\cos\theta_0\cos\theta+\sin\theta_0\sin\theta\cos(\phi-\phi_0)))}D(r,\theta,\phi)\\
&= (\cos\phi\cos\theta l_1 + \sin\phi\cos\theta m_1 - \sin\theta n_1)]\\
&\cdot e^{i\omega(t-r(\cos\theta_0\cos\theta+\sin\theta_0\sin\theta\cos(\phi-\phi_0)))}D(r,\theta,\phi)\\
&= E_\theta D(r,\theta,\phi)
\end{aligned}$$

by applying the relations in Eq. (3.8), and, similarly, one can verify that

$$E_{\phi r} + E_{\phi\theta} = E_\phi D(r,\theta,\phi) \ ,$$

$$H_{\theta\phi} + H_{\theta r} = H_\theta D(r,\theta,\phi) \ ,$$

$$H_{\phi r} + H_{\phi\theta} = H_\phi D(r,\theta,\phi) \ ,$$

by applying the relations that couple (l,m,n), (l_1,m_1,n_1), and (l_2,m_2,n_2) in Eq. (3.7)-(3.8), where E_ϕ, E_θ, H_ϕ, and H_θ are plane wave solutions in Eq. (3.11)-(3.16). Hence, at the vacuum-layer interface where $\sigma_r(r) = 0$, the decaying plane waves corresponding to E_r, $E_{\theta\phi} + E_{\theta r}$, $E_{\phi r} + E_{\phi\theta}$, H_r, $H_{\theta\phi} + H_{\theta r}$, and $H_{\phi r} + H_{\phi\theta}$ match the plane wave solutions E_r, E_θ, E_ϕ, H_r, H_θ, and H_ϕ in free-space perfectly. Note that this is true for plane waves of any frequency and any incident angle.

It is not straightforward to understand the decaying property of the decaying plane wave solutions by looking at the decaying factor $e^{-\sigma_r(r)(\cos\theta_0\cos\theta+\sin\theta_0\sin\theta\cos\phi-\phi_0))}$. In order to get a clear idea of the rate of change of the magnitude of the wave, one can then look at the directional derivative of the decaying factor.

Lemma 3.3.1 *Let* $\mathbf{l} = (\cos\phi_0\sin\theta_0, \sin\phi_0\sin\theta_0, \cos\theta_0)$ *be the normalized wave vector and assume that* $\sigma_r(r)$ *satisfies the conditions (3.35)-(3.36). Then all plane waves decay in the direction of propagation as*

$$\frac{\partial D(r,\theta,\phi)}{\partial \mathbf{l}} = \frac{\partial e^{-\sigma_r(r)(\cos\theta_0\cos\theta+\sin\theta_0\sin\theta\cos(\phi-\phi_0))}}{\partial \mathbf{l}} < 0 \ , \tag{3.48}$$

when $r > r_0$ *for any* ϕ_0 *and* θ_0.

Proof:

$$
\begin{aligned}
&\frac{\partial D(r,\theta,\phi)}{\partial \mathbf{l}} \\
&= \cos\phi_0 \sin\theta_0 \frac{\partial D(r,\theta,\phi)}{\partial x} + \sin\phi_0 \sin\theta_0 \frac{\partial D(r,\theta,\phi)}{\partial y} + \cos\theta_0 \frac{\partial D(r,\theta,\phi)}{\partial z} \\
&= \cos\phi_0 \sin\theta_0 \cos\phi \sin\theta \frac{\partial D(r,\theta,\phi)}{\partial r} - \cos\phi_0 \sin\theta_0 \frac{\sin\phi}{r\sin\theta} \frac{\partial D(r,\theta,\phi)}{\partial \phi} \\
&\quad + \cos\phi_0 \sin\theta_0 \frac{\cos\phi\cos\theta}{r} \frac{\partial D(r,\theta,\phi)}{\partial \theta} \\
&\quad + \sin\phi_0 \sin\theta_0 \sin\phi \sin\theta \frac{\partial D(r,\theta,\phi)}{\partial r} + \sin\phi_0 \sin\theta_0 \frac{\cos\phi}{r\sin\theta} \frac{\partial D(r,\theta,\phi)}{\partial \phi} \\
&\quad + \sin\phi_0 \sin\theta_0 \frac{\sin\phi\cos\theta}{r} \frac{\partial D(r,\theta,\phi)}{\partial \theta} \\
&\quad + \cos\theta_0 \cos\theta \frac{\partial D(r,\theta,\phi)}{\partial r} - \cos\theta_0 \frac{\sin\theta}{r} \frac{\partial D(r,\theta,\phi)}{\partial \theta} \\
&= (\sin\theta_0 \sin\theta \cos(\phi-\phi_0) + \cos\theta_0\cos\theta) \frac{\partial D(r,\theta,\phi)}{\partial r} - \sin\theta_0 \sin(\phi-\phi_0) \frac{1}{r\sin\theta} \frac{\partial D(r,\theta,\phi)}{\partial \phi} \\
&\quad + (\sin\theta_0 \cos\theta \cos(\phi-\phi_0) - \cos\theta_0 \sin\theta) \frac{1}{r} \frac{\partial D(r,\theta,\phi)}{\partial \theta} \\
&= -[(\sin\theta_0 \sin\theta \cos(\phi-\phi_0) + \cos\theta_0\cos\theta)^2 \sigma_r'(r) + (\sin\theta_0 \sin(\phi-\phi_0))^2 \frac{\sigma_r(r)}{r} \\
&\quad + (\sin\theta_0 \cos\theta \cos(\phi-\phi_0) - \cos\theta_0 \sin\theta)^2 \frac{\sigma_r(r)}{r}] D(r,\theta,\phi)
\end{aligned}
$$

Hence we have

$$
\frac{\partial D(r,\theta,\phi)}{\partial \mathbf{l}} = \frac{\partial e^{-\sigma_r(r)(\cos\theta_0\cos\theta + \sin\theta_0\sin\theta\cos(\phi-\phi_0))}}{\partial \mathbf{l}} < 0
$$

for any ϕ_0 and θ_0.

□

The lemma shows that all plane waves entering the PML decay exponentially along any direction of propagation inside the layer. The PML does not extend to infinity and there will be reflections from the outer boundary of the truncated domain. In this case, the decaying relation (3.48) still holds for the reflected waves. Thus, the reflected waves get further decayed along its way back to the computational domain. This is the reason for the success of PML methods. Moreover, since

$$
\begin{aligned}
&(\sin\theta_0 \sin\theta \cos(\phi-\phi_0) + \cos\theta_0\cos\theta)^2 \sigma_r'(r) + (\sin\theta_0 \sin(\phi-\phi_0))^2 \tfrac{\sigma_r(r)}{r} \\
&\quad + (\sin\theta_0 \cos\theta \cos(\phi-\phi_0) - \cos\theta_0 \sin\theta)^2 \frac{\sigma_r(r)}{r} \geq min(\sigma_r'(r), \frac{\sigma_r(r)}{r}) > 0 \ ,
\end{aligned}
\tag{3.49}
$$

for $r > r_0$, we have a lower bound for the rate of decay regardless of the direction of wave propagation ϕ_0 and θ_0, in the layer region away from the interface. We note that we can not find such a lower bound for PML in Cartesian coordinates.

3.3.3 Cylindrical Perfectly Matched Layer

It is also desirable to have a perfectly matched layer method in the cylindrical coordinates. Here the vacuum-layer interface is required to be $\rho = \rho_0$ and $|z| = z_0$, where ρ_0 and z_0 are constants. For this purpose, we can apply the polar perfectly matched layer [56] in the $\rho - \phi$ plane and apply rectangular perfectly matched layer method in the z-direction.

Our objective is to obtain the equations that admit plane wave solutions with a decaying factor such as:

$$D(\rho, \phi, z) = e^{-\sigma_\rho(\rho)\sqrt{1-n^2}\cos(\phi-\phi_0)-\sigma_z(z)nz} \ . \tag{3.50}$$

With the split-field approach, we need to solve the following equations:

$$\frac{\partial H_{\rho z}}{\partial t} = \frac{\partial(E_{\phi z} + E_{\phi\rho})}{\partial z} - \sigma_z'(z)H_{\rho z} \ , \tag{3.51}$$

$$\frac{\partial H_{\rho\phi}}{\partial t} = -\frac{1}{\rho}\frac{\partial(E_{z\rho} + E_{z\phi})}{\partial \phi} - \frac{\sigma_\rho(\rho)}{\rho}H_{\rho\phi} \ , \tag{3.52}$$

$$\frac{\partial H_{\phi z}}{\partial t} = -\frac{\partial(E_{\rho z} + E_{\rho\phi})}{\partial z} - \sigma_z'(z)H_{\phi z} \ , \tag{3.53}$$

$$\frac{\partial H_{\phi\rho}}{\partial t} = \frac{\partial(E_{z\rho} + E_{z\phi})}{\partial \rho} - \sigma_\rho'(\rho)H_{\phi\rho} \ , \tag{3.54}$$

$$\frac{\partial H_{z\rho}}{\partial t} = -\frac{\partial(E_{\phi z} + E_{\phi\rho})}{\partial \rho} - \sigma_\rho'(\rho)H_{z\rho} \ , \tag{3.55}$$

$$\frac{\partial H_{z\phi}}{\partial t} = \frac{1}{\rho}\frac{\partial(E_{\rho z} + E_{\rho\phi})}{\partial \phi} - \frac{E_{\phi z} + E_{\phi\rho}}{\rho} - \frac{\sigma_\rho(\rho)}{\rho}H_{z\phi} \ , \tag{3.56}$$

$$\frac{\partial E_{\rho z}}{\partial t} = -\frac{\partial(H_{\phi z} + H_{\phi\rho})}{\partial z} - \sigma_z'(z)E_{\rho z} \ , \tag{3.57}$$

$$\frac{\partial E_{\rho\phi}}{\partial t} = \frac{1}{\rho}\frac{\partial(H_{z\rho} + H_{z\phi})}{\partial \phi} - \frac{\sigma_\rho(\rho)}{\rho}E_{\rho\phi} \ , \tag{3.58}$$

$$\frac{\partial E_{\phi z}}{\partial t} = \frac{\partial (H_{\rho z} + H_{\rho\phi})}{\partial z} - \sigma_z'(z) E_{\phi z} \ , \tag{3.59}$$

$$\frac{\partial E_{\phi\rho}}{\partial t} = -\frac{\partial (H_{z\rho} + H_{z\phi})}{\partial \rho} - \sigma_\rho'(\rho) E_{\phi\rho} \ , \tag{3.60}$$

$$\frac{\partial E_{z\rho}}{\partial t} = \frac{\partial (H_{\phi z} + H_{\phi\rho})}{\partial \rho} - \sigma_\rho'(\rho) E_{z\rho} \ , \tag{3.61}$$

$$\frac{\partial E_{z\phi}}{\partial t} = -\frac{1}{\rho}\frac{\partial (H_{\rho z} + H_{\rho\phi})}{\partial \phi} + \frac{H_{\phi z} + H_{\phi\rho}}{\rho} - \frac{\sigma_\rho(\rho)}{\rho} E_{z\phi} \ . \tag{3.62}$$

Let the vacuum-layer interface be at $\rho = \rho_0$ and $|z| = z_0$. In order for the PML to effectively match and absorb incident plane waves, the function $\sigma_\rho(\rho)$ and $\sigma_z(z)$ have to be properly chosen. Hence, we should have $\sigma_\rho(\rho) = 0$ for $\rho < \rho_0$ and $\sigma_z(z) = 0$ for $|z| < z_0$. Following the considerations of the absorbing and reflectionless properties of the polar PML method, $\sigma_\rho(\rho)$ and $\sigma_z(z)$ must satisfy the requirements:

$$\sigma_\rho(\rho_0) = 0, \ \ \sigma_z(z)|_{|z|=z_0} = 0 \ , \tag{3.63}$$

and

$$\sigma_\rho(\rho) > 0 \quad \text{for } \rho > \rho_0, \ \ \sigma_z(z) > 0 \quad \text{for } |z| > z_0 \ , \tag{3.64}$$

so that the plane wave solutions decays for $\rho > \rho_0$ or $|z| > z_0$. We also require that

$$\sigma_\rho'(\rho) > 0 \quad \text{for } \rho > \rho_0, \ \ \sigma_z'(z) > 0 \quad \text{for } |z| > z_0 \ . \tag{3.65}$$

An example of a valid choice of $\sigma_\rho(r)$ is

$$\sigma_\rho(\rho) = C(\rho - \rho_0)^n, \ \ n = 1, 2, \dots \ , \ \ \rho \geq \rho_0 \ , \tag{3.66}$$

$$\sigma_z(z) = C(|z| - z_0)^n, \ \ n = 1, 2, \dots \ , \ \ |z| \geq z_0 \ , \tag{3.67}$$

where C is a positive constant. This family of functions satisfies the requirements in (3.63) - (3.65).

For the cylindrical perfectly matched layer method, it can be verified that we have the following decaying plane wave solutions:

$$H_{\rho z} = -(-\sin\phi l_1 + \cos\phi m_1) n e^{i\omega(t-\rho\cos(\phi-\phi_0)-nz)} D(\rho,\phi,z) \ , \tag{3.68}$$

$$H_{\rho\phi} = -n_1 \sin(\phi-\phi_0) e^{i\omega(t-\rho\cos(\phi-\phi_0)-nz)} D(\rho,\phi,z) \ , \tag{3.69}$$

$$H_{\phi z} = (\cos\phi l_1 + \sin\phi m_1) n e^{i\omega(t-\rho\cos(\phi-\phi_0)-nz)} D(\rho,\phi,z) \ , \tag{3.70}$$

$$H_{\phi\rho} = -n_1 \cos(\phi-\phi_0) e^{i\omega(t-\rho\cos(\phi-\phi_0)-nz)} D(\rho,\phi,z) \ , \tag{3.71}$$

$$H_{z\rho} = (-\sin\phi l_1 + \cos\phi m_1)\cos(\phi-\phi_0) e^{i\omega(t-\rho\cos(\phi-\phi_0)-nz)} D(\rho,\phi,z) \ , \tag{3.72}$$

$$H_{z\phi} = (\cos\phi l_1 + \sin\phi m_1)\sin(\phi-\phi_0) e^{i\omega(t-\rho\cos(\phi-\phi_0)-nz)} D(\rho,\phi,z) \ , \tag{3.73}$$

$$E_{\rho z} = (-\sin\phi l_2 + \cos\phi m_2) n e^{i\omega(t-\rho\cos(\phi-\phi_0)-nz)} D(\rho,\phi,z) \ , \tag{3.74}$$

$$E_{\rho\phi} = n_2 \sin(\phi-\phi_0) e^{i\omega(t-\rho\cos(\phi-\phi_0)-nz)} D(\rho,\phi,z) \ , \tag{3.75}$$

$$E_{\phi z} = -(\cos\phi l_2 + \sin\phi m_2) n e^{i\omega(t-\rho\cos(\phi-\phi_0)-nz)} D(\rho,\phi,z) \ , \tag{3.76}$$

$$E_{\phi\rho} = n_2 \cos(\phi-\phi_0) e^{i\omega(t-\rho\cos(\phi-\phi_0)-nz)} D(\rho,\phi,z) \ , \tag{3.77}$$

$$E_{z\rho} = -(-\sin\phi l_2 + \cos\phi m_2)\cos(\phi-\phi_0) e^{i\omega(t-\rho\cos(\phi-\phi_0)-nz)} D(\rho,\phi,z) \ , \tag{3.78}$$

$$E_{z\phi} = -(\cos\phi l_1 + \sin\phi m_1)\sin(\phi-\phi_0) e^{i\omega(t-\rho\cos(\phi-\phi_0)-nz)} D(\rho,\phi,z) \ , \tag{3.79}$$

where (l_2, m_2, n_2), (l_1, m_1, n_1) and (l, m, n) satisfy the relations in Eq. (3.7)-(3.8). Note that now we have $l = \sqrt{1-n^2}\cos\phi_0$, $m = \sqrt{1-n^2}\sin\phi_0$, and $n = n$. One can verify that

$$\begin{aligned} H_{z\rho} + H_{z\phi} &= ((-\sin\phi l_1 + \cos\phi m_1)\cos(\phi-\phi_0) + (\cos\phi l_1 + \sin\phi m_1)\sin(\phi-\phi_0)) \\ &\quad \cdot e^{i\omega(t-\rho\cos(\phi-\phi_0)-nz)} D(\rho,\phi,z) \\ &= (-\sin\phi_0 l_1 + \cos\phi_0 m_1) e^{i\omega(t-\rho\cos(\phi-\phi_0)-nz)} D(\rho,\phi,z) \\ &= n e^{i\omega(t-\rho\cos(\phi-\phi_0)-nz)} D(\rho,\phi,z) \\ &= H_z D(\rho,\phi,z) \end{aligned}$$

by applying the relations in Eq. (3.8), and similarly, one can also verify that

$$E_{\rho z} + E_{\rho\phi} = E_\rho D(\rho,\phi,z) \ ,$$

$$E_{\phi z} + E_{\phi\rho} = E_\phi D(\rho,\phi,z) \ ,$$

$$H_{\rho z} + H_{\rho\phi} = H_\rho D(\rho,\phi,z) \ ,$$

$$H_{\phi z} + H_{\phi\rho} = H_\phi D(\rho,\phi,z) \ ,$$

$$H_{z\rho} + H_{z\phi} = H_z D(\rho,\phi,z) \ ,$$

by applying the relations that couple (l, m, n), (l_1, m_1, n_1), and (l_2, m_2, n_2) in Eq. (3.7)-(3.8), where E_ρ, E_ϕ, E_z, H_ρ, H_ϕ, and H_z are plane wave solutions in Eq. (3.17)-(3.22). Hence, at the vacuum-layer interface where $\sigma_\rho(\rho) = \sigma_z(z) = 0$, the decaying plane waves corresponding to $E_{\rho z} + E_{\rho\phi}$, $E_{\phi z} + E_{\phi\rho}$, $E_{z\rho} + E_{z\phi}$, $H_{\rho z} + H_{\rho\phi}$, $H_{\phi z} + H_{\phi\rho}$, and $H_{z\rho} + H_{z\phi}$ match the plane wave solutions E_ρ, E_ϕ, E_z, H_ρ, H_ϕ, and H_z in free-space perfectly. Note that this is true for plane waves of any frequency and any incident angle.

Like in the spherical case, one can look at the directional derivative of the decaying factor to get a clear idea of the rate of change of the magnitude of the plane waves.

Lemma 3.3.2 *Let* $\mathbf{l} = (\sqrt{1-n^2}\cos\phi_0, \sqrt{1-n^2}\sin\phi_0, n)$ *be the normalized wave vector and assume that* $\sigma_\rho(\rho)$ *and* $\sigma_z(z)$ *satisfies the conditions (3.63)-(3.65). Then plane waves do not increase in all* *directions of propagation as*

$$\frac{\partial D(\rho,\phi,z)}{\partial \mathbf{l}} = \frac{\partial e^{-\sigma_\rho(\rho)\cos(\phi-\phi_0)-\sigma_z(z)z}}{\partial \mathbf{l}} \leq 0 \ , \tag{3.80}$$

when $\rho > \rho_0$ or $|z| > z_0$ for any ϕ_0 and n.

Proof:

$$\begin{aligned}
&\frac{\partial D(\rho,\phi,z)}{\partial \mathbf{l}} = \frac{\partial e^{-\sigma_\rho(\rho)\cos(\phi-\phi_0)-\sigma_z(z)z}}{\partial \mathbf{l}} \\
&= \sqrt{1-n^2}\cos\phi_0\frac{\partial D(\rho,\phi,z)}{\partial x} + \sqrt{1-n^2}\sin\phi_0\frac{\partial D(\rho,\phi,z)}{\partial y} \\
&\quad + n\frac{\partial D(\rho,\phi,z)}{\partial z} \\
&= \sqrt{1-n^2}\cos\phi_0\cos\phi\frac{\partial D(\rho,\phi,z)}{\partial \rho} - \sqrt{1-n^2}\cos\phi_0\frac{\sin\phi}{\rho}\frac{\partial D(\rho,\phi,z)}{\partial \theta} \\
&\quad + \sqrt{1-n^2}\sin\phi_0\sin\phi\frac{\partial D(\rho,\phi,z)}{\partial \rho} + \sqrt{1-n^2}\sin\phi_0\frac{\cos\phi}{\rho}\frac{\partial D(\rho,\phi,z)}{\partial \theta} \\
&\quad + n\frac{\partial D(\rho,\phi,z)}{\partial z} \\
&= \sqrt{1-n^2}\cos(\phi_0-\phi)\frac{\partial D(\rho,\phi,z)}{\partial \rho} - \sqrt{1-n^2}\frac{\sin(\phi-\phi_0)}{\rho}\frac{\partial D(\rho,\phi,z)}{\partial \theta} \\
&\quad + n\frac{\partial D(\rho,\phi,z)}{\partial z} \\
&= -[\sqrt{1-n^2}(\cos^2(\phi_0-\phi)\sigma'_\rho(\rho) + \sin^2(\phi-\phi_0)\frac{\sigma_\rho(\rho)}{\rho}) + n\sigma'_z(z)]D(\rho,\phi,z)
\end{aligned}$$

Hence we have

$$\frac{\partial D(\rho,\phi,z)}{\partial \mathbf{l}} = \frac{\partial e^{-\sigma_\rho(\rho)\cos(\phi-\phi_0)-\sigma_z(z)z}}{\partial \mathbf{l}} \leq 0 \tag{3.81}$$

for any ϕ_0 and any n.

□

The decaying property of the cylindrical PML share that of both rectangular PML method and polar PML method [56]. In two special cases plane wave solutions do not decay in the PML, i.e. when plane waves propagate in the z-direction and in the region $\rho > \rho_0$ and $|z| \leq z_0$, or plane waves propagate in the direction orthogonal to z and in the region $\rho \leq \rho_0$ and $|z| > z_0$. The corner regions, $\rho > r_0$ and $|z| > z_0$ are important for all plane waves to be absorbed. However, the situation here is much less severe than that for the rectangular PML method.

3.4 Well-Posed Perfectly Matched Layer Methods

Since Berenger presented the split-field PML method, efforts have been seen to modify the method to unsplit-field formulation PML methods. Besides from the latter methods' being computationally more efficient, the efforts are worthwhile since the split-field PML equations are only weakly well-posed and may suffer from instability problems.

The unsplit-field PML methods we present in this section modify Maxwell's equations by adding low-order source terms and ordinary differential equations. Hence the governing equations are symmetric hyperbolic and strongly well-posed just like the original Maxwell's equations. We also show that the well-posedness is achieved while keeping almost all the merits of the split-field PML methods. Computationally, it has been observed by us in [57] and some other researchers that the split-field PML methods are a little more accurate, which seems to be due to the simplicity in their decaying plane wave solutions in the layer.

3.4.1 The Discrete Perfectly Matched Uniaxial Medium

In [45] a PML method using an anisotropic lossy uniaxial medium was presented by Sacks et al., and was applied to frequency-domain-based finite-element methods. In [19] Gedney implemented the uniaxial medium as a PML for the FD-TD algorithm. The constitutive parameters of this anisotropic medium are given in terms of the complex permittivity and permeability tensors, $\bar{\bar{\epsilon}} = \epsilon_0[\Lambda]$ and $\bar{\bar{\mu}} = \mu_0[\Lambda]$, where $[\Lambda]$ is a diagonal matrix defined as

$$[\Lambda] = \begin{bmatrix} 1 + \frac{\sigma_z'(z)}{i\omega} & 0 & 0 \\ 0 & 1 + \frac{\sigma_z'(z)}{i\omega} & 0 \\ 0 & 0 & \frac{1}{1+\frac{\sigma_z'(z)}{i\omega}} \end{bmatrix} \tag{3.82}$$

for a uniaxial medium in the z-direction in the context of this chapter. In the uniaxial medium, the non-dimensionalized Ampere's law can be expressed in matrix form as

$$\begin{bmatrix} \frac{\partial H_z}{\partial y} - \frac{\partial H_y}{\partial z} \\ \frac{\partial H_x}{\partial z} - \frac{\partial H_z}{\partial x} \\ \frac{\partial H_y}{\partial x} - \frac{\partial H_x}{\partial y} \end{bmatrix} = i\omega \begin{bmatrix} 1+\frac{\sigma_z'(z)}{i\omega} & 0 & 0 \\ 0 & 1+\frac{\sigma_z'(z)}{i\omega} & 0 \\ 0 & 0 & \frac{1}{1+\frac{\sigma_z'(z)}{i\omega}} \end{bmatrix} \begin{bmatrix} E_x \\ E_y \\ E_z \end{bmatrix} . \tag{3.83}$$

It was assumed that this method was advantageous over Berenger's PML and could be extended to nonorthogonal and unstructured grid techniques. However, there might be a problem with this method.

One can verify that the above equations admit the following plane wave solutions:

$$H = (l_2\hat{x} + m_2\hat{y} + n_2(1+\frac{\sigma_z'(z)}{i\omega})\hat{z})e^{i\omega(t-lx-my-nz)}e^{-\sigma_z(z)n} , \tag{3.84}$$

$$E = (l_1\hat{x} + m_1\hat{y} + n_1(1+\frac{\sigma_z'(z)}{i\omega})\hat{z})e^{i\omega(t-lx-my-nz)}e^{-\sigma_z(z)n} , \tag{3.85}$$

where (l,m,n), (l_1,m_1,n_1), and (l_2,m_2,n_2) are coupled by the relations in Eq. (3.7)-(3.8). One can see from the analytical solution that if $\frac{\sigma_z'(z)}{\omega}$ is very large and $\sigma_z(z)n$ is not large, which is possible if ω and n are very small, the magnitude of the solutions could become too large for numerical computation. An analysis of a 2-D case of this problem can be found in [1] where the directional derivative of the magnitude of the plane wave solutions are calculated and analyzed. It was observed that if in a coming pulse there is significant component of moderate frequencies there might be a problem.

Hence we propose to design a biaxial layer that has the following plane wave solutions:

$$H = (l_2\frac{i\omega}{\sigma_z'(z)+i\omega}\hat{x} + m_2\frac{i\omega}{\sigma_z'(z)+i\omega}\hat{y} + n_2\hat{z})e^{i\omega(t-lx-my-nz)}e^{-\sigma_z(z)n} , \tag{3.86}$$

$$E = (l_1\frac{i\omega}{\sigma_z'(z)+i\omega}\hat{x} + m_1\frac{i\omega}{\sigma_z'(z)+i\omega}\hat{y} + n_1\hat{z})e^{i\omega(t-lx-my-nz)}e^{-\sigma_z(z)n} , \tag{3.87}$$

where (l,m,n), (l_1,m_1,n_1), and (l_2,m_2,n_2) are coupled by the relations in Eq. (3.7)-(3.8). The magnitude of this set of plane wave solutions are uniformly bounded. It can be verified that they are the solutions of the following equations:

$$\begin{bmatrix} \frac{\partial H_z}{\partial y} - \frac{\partial H_y}{\partial z} \\ \frac{\partial H_x}{\partial z} - \frac{\partial H_z}{\partial x} \\ \frac{\partial H_y}{\partial x} - \frac{\partial H_x}{\partial y} \end{bmatrix} + \begin{bmatrix} \frac{\sigma_z''(z)}{\sigma_z'(z)+i\omega} H_y \\ -\frac{\sigma_z''(z)}{\sigma_z'(z)+i\omega} H_x \\ 0 \end{bmatrix} = i\omega \begin{bmatrix} 1+\frac{\sigma_z'(z)}{i\omega} & 0 & 0 \\ 0 & 1+\frac{\sigma_z'(z)}{i\omega} & 0 \\ 0 & 0 & \frac{1}{1+\frac{\sigma_z'(z)}{i\omega}} \end{bmatrix} \begin{bmatrix} E_x \\ E_y \\ E_z \end{bmatrix}. \quad (3.88)$$

An application of Sacks' anisotropic medium idea in spherical and cylindrical coordinate systems was presented in [35] by Kuzuoglu and Mittra. They gave a fully analysis of the reflection and absorption of cylindrical or spherical waves in the medium. Some restrictions and problems with this direct application of Sacks' anisotropic medium idea in those coordinate systems were observed by them. Kuzuoglu and Mittra obtained the spherical and cylindrical wave solutions in the medium and their reflection coefficients at vacuum-layer interface. It was observed that the medium was not ideally nonreflecting anymore. They showed that the medium could effectively absorb waves without reflection only under the condition that the radius of the vacuum-layer interface is electrically large.

In our previous work in [56]-[57] and the current work, we found that direct extensions of 2-D and 3-D rectangular PML's to polar (2-D), spherical and cylindrical (3-D) coordinates result in equations for which plane wave solutions could not be easily found. In fact, the equations we propose, which admit plane wave solutions having the same or even better properties than those of the rectangular PML's, are somewhat different in formulation compared with other extensions. In our work, we always choose to work on analyzing the analytical plane wave solutions in the layer. In other words, we want to make sure that a PML indeed admit analytical plane wave solutions that have the same merits as those of the rectangular PML's.

We have obtained the split-field formulations of the PML methods in spherical and cylindrical coordinate systems which is ideal and as advantageous as the rectangular PML's. For those PML methods, we obtained plane wave solutions that match at spherical and cylindrical vacuum-layer interfaces. However, since the unsplit-field PML methods may suffer from their drawback of being only weakly well-posed, in the following we want to show that unsplit-field spherical and cylindrical

PML methods could also be derived. We want the layer to admit solutions that are bounded like the solutions in (3.86)-(3.87) rather than those solutions in (3.84)-(3.85).

3.4.2 Well-posed Spherical Perfectly Matched Layer Method

In this section we give the equations and solutions of an unsplit-field spherical PML method. This method, by construction, is symmetric hyperbolic and strongly well-posed. For this well-posed spherical PML method, the following plane wave solution is what we desired in the layer:

$$\tilde{H}_r = H_r D(r,\theta,\phi) \ , \tag{3.89}$$

$$\tilde{H}_\theta = \frac{\frac{\sigma_r(r)}{r} + i\omega}{\sigma_r'(r) + i\omega} H_\theta D(r,\theta,\phi) \ , \tag{3.90}$$

$$\tilde{H}_\phi = \frac{\frac{\sigma_r(r)}{r} + i\omega}{\sigma_r'(r) + i\omega} H_\phi D(r,\theta,\phi) \ , \tag{3.91}$$

$$\tilde{E}_r = E_r D(r,\theta,\phi) \ , \tag{3.92}$$

$$\tilde{E}_\theta = \frac{\frac{\sigma_r(r)}{r} + i\omega}{\sigma_r'(r) + i\omega} E_\theta D(r,\theta,\phi) \ , \tag{3.93}$$

$$\tilde{E}_\phi = \frac{\frac{\sigma_r(r)}{r} + i\omega}{\sigma_r'(r) + i\omega} E_\phi D(r,\theta,\phi) \ , \tag{3.94}$$

where E_ϕ, E_θ, H_ϕ, and H_θ are plane wave solutions in Eq. (3.11)-(3.16) and

$$D(r,\theta,\phi) = e^{-\sigma_r(r)(\cos\theta_0\cos\theta + \sin\theta_0\sin\theta\cos(\phi-\phi_0))} \tag{3.95}$$

is the decaying factor. Let the vacuum-layer interface be at $r = r_0$. We should require that $\sigma_r(r) = 0$ for $r \leq r_0$ for the decaying plane waves in the PML to match incident plane waves perfectly. Following the considerations of the absorbing and reflectionless properties of the polar PML method, $\sigma_r(r)$ must satisfy the requirements in Eqs. (3.35)-(3.36). In practice, we choose $\sigma_r(r)$ as

$$\sigma_r(r) = C(r - r_0)^n, \ n = 1, 2, \ldots \ , \ r \geq r_0 \ , \tag{3.96}$$

where C is a positive constant. This family of functions satisfies the requirements in (3.35) - (3.36). Hence the decaying plane wave solutions are perfectly matched with the free-space plane wave solutions. For the type of function $\sigma_r(r)$ we use, one notes that

$$\frac{\sigma_r(r)}{r} < \sigma_r'(r) \tag{3.97}$$

holds for all $r > r_0$. Hence the above plane wave solutions are uniformly bounded.

Lemma 3.4.1

$$\frac{1}{r\sin\theta}\frac{\partial\tilde{H}_r}{\partial\phi} - \frac{\partial\tilde{H}_\phi}{\partial r} - \frac{\tilde{H}_\phi}{r} - \sigma_r''(r)\frac{\tilde{H}_\phi}{\sigma_r'(r)+i\omega} = \frac{\frac{\sigma_r(r)}{r}+i\omega}{i\omega}D(r,\theta,\phi)\frac{\partial E_\phi}{\partial t} \tag{3.98}$$

Proof: We have

$$\begin{gathered}
\tfrac{1}{r\sin\theta}\tfrac{\partial\tilde{H}_r}{\partial\phi} - \tfrac{\partial\tilde{H}_\phi}{\partial r} - \tfrac{\tilde{H}_\phi}{r} - \sigma_r''(r)\tfrac{\tilde{H}_\phi}{\sigma_r'(r)+i\omega} = \\
\tfrac{\frac{\sigma_r(r)}{r}+i\omega}{i\omega}\left(\tfrac{1}{r\sin\theta}D\tfrac{\partial H_r}{\partial\phi} - \tfrac{1}{r}DH_\phi\right) - \tfrac{\frac{\sigma_r(r)}{r}+i\omega}{i\omega}\left(D\tfrac{\partial H_\phi}{\partial r}\right) \\
+\tfrac{1}{r}DH_\phi - \tfrac{\frac{\sigma_r(r)}{r}+i\omega}{\sigma_r'(r)+i\omega}\tfrac{1}{r}DH_\phi - \sigma_r''(r)\tfrac{\tilde{H}_\phi}{\sigma_r'(r)+i\omega} - \left(\tfrac{\frac{\sigma_r(r)}{r}+i\omega}{\sigma_r'(r)+i\omega}\right)'DH_\phi = \\
\tfrac{\frac{\sigma_r(r)}{r}+i\omega}{i\omega}\left(\tfrac{1}{r\sin\theta}D\tfrac{\partial H_r}{\partial\phi} - \tfrac{1}{r}DH_\phi - D\tfrac{\partial H_\phi}{\partial\phi}\right)+ \\
\tfrac{\sigma_r'-\frac{\sigma_r}{r}}{\sigma_r'+i\omega}\tfrac{1}{r}DH_\phi - \tfrac{(\frac{\sigma_r}{r})'}{\sigma_r'+i\omega}DH_\phi + \tfrac{\sigma_r''}{\sigma_r'+i\omega}\tilde{H}_\phi - \sigma_r''(r)\tfrac{\tilde{H}_\phi}{\sigma_r'(r)+i\omega} = \\
\tfrac{\frac{\sigma_r(r)}{r}+i\omega}{i\omega}D(r,\theta,\phi)\left(\tfrac{1}{r\sin\theta}\tfrac{\partial H_r}{\partial\phi} - \tfrac{\partial H_\phi}{\partial r} - \tfrac{\tilde{H}_\phi}{r}\right)\ .
\end{gathered}$$

Hence Eq. (3.98) holds. □

Remark 3.4.1 *Similarly, we can prove other relations that are needed to obtain the equations that admits the desired set of equations. The principle of the construction is to keep the principal part of Maxwell's equations unchanged.*

$$\frac{\partial\tilde{H}_\theta}{\partial r} - \frac{1}{r}\frac{\partial\tilde{H}_r}{\partial\theta} + \frac{\tilde{H}_\theta}{r} + \sigma_r''(r)\frac{\tilde{H}_\phi}{\sigma_r'(r)+i\omega} = \frac{\frac{\sigma_r(r)}{r}+i\omega}{i\omega}D(r,\theta,\phi)\frac{\partial E_\theta}{\partial t} \tag{3.99}$$

In obtaining a set of equations that admit the desired solutions, we only want to add complementary source terms to the original Maxwell's equations. The evolution of the source terms can be governed by ordinary differential equations if necessary. Now we first give the equations in the frequency domain that admit the desired plane wave solutions.

$$\begin{aligned} &\frac{(\frac{\sigma_r(r)}{r}+i\omega)^2}{\sigma_r'(r)+i\omega}\tilde{H}_r \\ &= -\frac{1}{r\sin\theta}\frac{\partial}{\partial\theta}(\sin\theta(\tilde{E}_\phi)) + \frac{1}{r\sin\theta}\frac{\partial\tilde{E}_\theta}{\partial\phi} \ , \end{aligned} \tag{3.100}$$

$$\begin{aligned} &(i\omega+\sigma_r'(r))\tilde{H}_\theta \\ &= -\frac{1}{r\sin\theta}\frac{\partial\tilde{E}_r}{\partial\phi} + \frac{\partial\tilde{E}_\phi}{\partial r} + \frac{\tilde{E}_\phi}{r} + \sigma_r''(r)Q_E \ , \end{aligned} \tag{3.101}$$

$$\begin{aligned} &(i\omega+\sigma_r'(r))\tilde{H}_\phi \\ &= -\frac{\partial\tilde{E}_\theta}{\partial r} + \frac{1}{r}\frac{\partial\tilde{E}_r}{\partial\theta} - \frac{\tilde{E}_\theta}{r} - \sigma_r''(r)R_E \ , \end{aligned} \tag{3.102}$$

$$\begin{aligned} &\frac{(\frac{\sigma_r(r)}{r}+i\omega)^2}{\sigma_r'(r)+i\omega}\tilde{E}_r \\ &= \frac{1}{r\sin\theta}\frac{\partial}{\partial\theta}(\sin\theta(\tilde{H}_\phi)) - \frac{1}{r\sin\theta}\frac{\partial\tilde{H}_\theta}{\partial\phi} \ , \end{aligned} \tag{3.103}$$

$$\begin{aligned} &(i\omega+\sigma_r'(r))\tilde{E}_\theta \\ &= \frac{1}{r\sin\theta}\frac{\partial\tilde{H}_r}{\partial\phi} - \frac{\partial\tilde{H}_\phi}{\partial r} - \frac{\tilde{H}_\phi}{r} - \sigma_r''(r)Q_H \ , \end{aligned} \tag{3.104}$$

$$\begin{aligned} &(i\omega+\sigma_r'(r))\tilde{E}_\phi \\ &= \frac{\partial\tilde{H}_\theta}{\partial r} - \frac{1}{r}\frac{\partial\tilde{H}_r}{\partial\theta} + \frac{\tilde{H}_\theta}{r} + \sigma_r''(r)R_H \ . \end{aligned} \tag{3.105}$$

To verify Eq. (3.103), one needs to notice that

$$\frac{1}{r\sin\theta}\frac{\partial}{\partial\theta}(\sin\theta(\tilde{H}_\phi)) - \frac{1}{r\sin\theta}\frac{\partial\tilde{H}_\theta}{\partial\phi} = \frac{\frac{\sigma_r(r)}{r}+i\omega}{\sigma_r'(r)+i\omega}(i\omega\tilde{E}_r + \frac{\sigma_r(r)}{r}) \ . \tag{3.106}$$

To verify Eq. (3.105) and Eq. (3.103), one needs to apply Eq. (3.98) and Eq. (3.99) respectively. Evolution equations for H_r, H_θ, and H_ϕ can be proven by the same token.

For the above set of plane wave solutions, we can not recover E_x, E_y, and E_z from H_r, H_θ, and H_ϕ since the magnitudes of H_r, H_θ, and H_ϕ are different and dependent on the frequency. In a multidomain computational scheme in spherical coordinates, we apply a rotated coordinate system in subdomains near north and south poles to avoid the $\frac{1}{\sin\theta}$ singularity. Hence we want to transform forward and backward between (E_x, E_y, E_z) and (H_r, H_θ, H_ϕ) so that we can patch E_x, E_y, and E_z at the subdomain interface. For more detail on this issue, one needs to refer to section 8.4.2. We introduce

$$\bar{H}_r = \frac{\frac{\sigma_r(r)}{r} + i\omega}{\sigma_r'(r) + i\omega}\tilde{H}_r \ , \tag{3.107}$$

$$\bar{E}_r = \frac{\frac{\sigma_r(r)}{r} + i\omega}{\sigma_r'(r) + i\omega}\tilde{E}_r \ , \tag{3.108}$$

and denote $D_E = \tilde{E}_r - \bar{E}_r$, $D_H = \tilde{H}_r - \bar{H}_r$. We propose the following set of equations in the time domain:

$$\begin{aligned} &\tfrac{\partial \tilde{H}_r}{\partial t} + (\tfrac{2\sigma_r(r)}{r} - \sigma_r'(r))\tilde{H}_r \\ &= -\tfrac{1}{r\sin\theta}\tfrac{\partial}{\partial\theta}(\sin\theta(\tilde{E}_\phi)) + \tfrac{1}{r\sin\theta}\tfrac{\partial \tilde{E}_\theta}{\partial\phi} + (\tfrac{\sigma_r(r)}{r} - \sigma_r'(r))D_H \ , \end{aligned} \tag{3.109}$$

$$\begin{aligned} &\tfrac{\partial \tilde{H}_\theta}{\partial t} + \sigma_r'(r)\tilde{H}_\theta \\ &= -\tfrac{1}{r\sin\theta}\tfrac{\partial \tilde{E}_r}{\partial\phi} + \tfrac{\partial \tilde{E}_\phi}{\partial r} + \tfrac{\tilde{E}_\phi}{r} + \sigma_r''(r)Q_E \ , \end{aligned} \tag{3.110}$$

$$\begin{aligned} &\tfrac{\partial \tilde{H}_\phi}{\partial t} + \sigma_r'(r)\tilde{H}_\phi \\ &= -\tfrac{\partial \tilde{E}_\theta}{\partial r} + \tfrac{1}{r}\tfrac{\partial \tilde{E}_r}{\partial\theta} - \tfrac{\tilde{E}_\theta}{r} - \sigma_r''(r)R_E \ , \end{aligned} \tag{3.111}$$

$$\begin{aligned} &\tfrac{\partial \tilde{E}_r}{\partial t} + (\tfrac{2\sigma_r(r)}{r} - \sigma_r'(r))\tilde{E}_r \\ &= \tfrac{1}{r\sin\theta}\tfrac{\partial}{\partial\theta}(\sin\theta(\tilde{H}_\phi)) - \tfrac{1}{r\sin\theta}\tfrac{\partial \tilde{H}_\theta}{\partial\phi} + (\tfrac{\sigma_r(r)}{r} - \sigma_r'(r))D_E \ , \end{aligned} \tag{3.112}$$

$$\begin{aligned} &\tfrac{\partial \tilde{E}_\theta}{\partial t} + \sigma_r'(r)\tilde{E}_\theta \\ &= \tfrac{1}{r\sin\theta}\tfrac{\partial \tilde{H}_r}{\partial\phi} - \tfrac{\partial \tilde{H}_\phi}{\partial r} - \tfrac{\tilde{H}_\phi}{r} - \sigma_r''(r)Q_H \ , \end{aligned} \tag{3.113}$$

$$\begin{aligned} &\tfrac{\partial \tilde{E}_\phi}{\partial t} + \sigma_r'(r)\tilde{E}_\phi \\ &= \tfrac{\partial \tilde{H}_\theta}{\partial r} - \tfrac{1}{r}\tfrac{\partial \tilde{H}_r}{\partial\theta} + \tfrac{\tilde{H}_\theta}{r} + \sigma_r''(r)R_H \ , \end{aligned} \tag{3.114}$$

and the supplementary ordinary differential equations are given in the following:

$$\frac{\partial D_H}{\partial t} = (\sigma_r'(r) - \frac{\sigma_r}{r})\tilde{H}_r - \sigma_r'(r)D_H, \ \frac{\partial D_E}{\partial t} = (\sigma_r'(r) - \frac{\sigma_r}{r})\tilde{E}_r - \sigma_r'(r)D_E \ , \tag{3.115}$$

$$\frac{\partial Q_E}{\partial t} = \tilde{E}_\phi - \sigma_r'(r)Q_E, \ \frac{\partial Q_H}{\partial t} = \tilde{H}_\phi - \sigma_r'(r)Q_H \ , \tag{3.116}$$

$$\frac{\partial R_E}{\partial t} = \tilde{E}_\theta - \sigma_r'(r) R_E, \; \frac{\partial R_H}{\partial t} = \tilde{H}_\theta - \sigma_r'(r) R_H \; . \tag{3.117}$$

Note that $\tilde{E}_r - D_E = \bar{E}_r$, $\tilde{H}_r - D_E = \bar{H}_r$, and the magnitudes of $\bar{E}_r$, $\tilde{E}_\theta$, and $\tilde{E}_\phi$ are the same, as well as the magnitudes of $\bar{H}_r$, $\tilde{H}_\theta$, and $\tilde{H}_\phi$. This is the property one desires for the multidomain numerical computation purpose, for which the detail will be given elsewhere. Note that the above set of equations are just Maxwell's equations with low order terms that are governed by ordinary differential equations in Eqs. (3.115)-(3.117). The set of equations are still symmetric hyperbolic and well-posed. If the second-derivative terms are set to be zero, then we need only 2 supplementary fields instead of 6. This corresponds to the case of $\sigma_r(r)$ being a linear function. Otherwise the above equations admit solutions of the uniaxial medium type, the detail of which is not discussed here.

3.4.3 Well-posed Cylindrical Perfectly Matched Layer Method

Like in spherical coordinate system, we also have a well-posed PML method in cylindrical coordinate system. For the well-posed cylindrical PML method, the following plane wave solution is what we desire in the layer:

$$\tilde{H}_\rho = \frac{i\omega}{\sigma_z'(z) + i\omega} H_\rho D(\rho, \phi, z) \; , \tag{3.118}$$

$$\tilde{H}_\phi = \frac{i\omega}{\sigma_z'(z) + i\omega} \frac{\frac{\sigma_\rho(\rho)}{\rho} + i\omega}{\sigma_\rho'(\rho) + i\omega} H_\phi D(\rho, \phi, z) \; , \tag{3.119}$$

$$\tilde{H}_z = \frac{i\omega}{\sigma_\rho'(\rho) + i\omega} H_z D(\rho, \phi, z) \; , \tag{3.120}$$

$$\tilde{E}_\rho = \frac{i\omega}{\sigma_z'(z) + i\omega} E_\rho D(\rho, \phi, z) \; , \tag{3.121}$$

$$\tilde{E}_\phi = \frac{i\omega}{\sigma_z'(z) + i\omega} \frac{\frac{\sigma_\rho(\rho)}{\rho} + i\omega}{\sigma_\rho'(\rho) + i\omega} E_\phi D(\rho, \phi, z) \; , \tag{3.122}$$

$$\tilde{E}_z = \frac{i\omega}{\sigma_\rho'(\rho) + i\omega} E_z D(\rho, \phi, z) \; , \tag{3.123}$$

where E_ϕ, E_θ, H_ϕ, and H_θ are plane wave solutions in Eq. (3.11)-(3.16) and

$$D(\rho, \phi, z) = e^{-\sigma_\rho(\rho)\sqrt{1-n^2}\cos(\phi-\phi_0) - \sigma_z(z) n z} \tag{3.124}$$

is the decaying factor. Let the vacuum-layer interface be at $\rho = \rho_0$ and $|z| = z_0$. We should require that $\sigma_\rho(\rho) = 0$ for $\rho \le \rho_0$ and $\sigma_z(z) = 0$ for $|z| \le z_0$ in order for the decaying plane waves in the PML to match incident plane waves perfectly. Following the considerations of the absorbing and reflectionless properties of the polar PML method, $\sigma_\rho(\rho)$ and $\sigma_z(z)$ must satisfy the requirements in Eqs. (3.63)-(3.65). In practice, we choose $\sigma_\rho(r)$ and $\sigma_z(z)$ as

$$\sigma_\rho(\rho) = C(\rho - \rho_0)^n, \ n = 1, 2, \dots \ , \ \rho \ge \rho_0 \ , \tag{3.125}$$

$$\sigma_z(z) = C(|z| - z_0)^n, \ n = 1, 2, \dots \ , \ |z| \ge z_0 \ , \tag{3.126}$$

where C is a positive constant. This family of functions satisfies the requirements in (3.63) - (3.65). Hence the solutions are perfectly matched with the free-space plane wave solutions. One can easily see that the above plane wave solutions are uniformly bounded like those in Cartesian and spherical coordinate systems.

To get a set of equations that admit the above solutions, we add complementary source terms to the original Maxwell's equations. The evolution of the source terms are only governed by ordinary differential equations. To reach this objective, we obtain the following system of equations:

$$\begin{aligned} \frac{\partial \tilde{H}_\rho}{\partial t} + (\sigma_z'(z) + \frac{\sigma_\rho(\rho)}{\rho} - \sigma_\rho'(\rho))\tilde{H}_\rho + (\frac{\sigma_\rho(\rho)}{\rho} - \sigma_\rho'(\rho))(\sigma_z'(z) - \sigma_\rho'(\rho))P_H \\ = \frac{\partial \tilde{E}_\phi}{\partial z} - \frac{1}{\rho}\frac{\partial \tilde{E}_z}{\partial \phi} + \sigma_z''(z)T_E \ , \end{aligned} \tag{3.127}$$

$$\begin{aligned} \frac{\partial \tilde{H}_\phi}{\partial t} + (\sigma_z'(z) + \sigma_\rho'(\rho) - \frac{\sigma_\rho(\rho)}{\rho})\tilde{H}_\phi + (\sigma_\rho'(\rho) - \frac{\sigma_\rho(\rho)}{\rho})(\sigma_z'(z) - \frac{\sigma_\rho(\rho)}{\rho})Q_H \\ = \frac{\partial \tilde{E}_z}{\partial \rho} - \frac{\partial \tilde{E}_\rho}{\partial z} + \sigma_\rho''(\rho)V_E - \sigma_z''(z)U_E \ , \end{aligned} \tag{3.128}$$

$$\begin{aligned} \frac{\partial \tilde{H}_z}{\partial t} + (\frac{\sigma_\rho(\rho)}{\rho} + \sigma_\rho'(\rho) - \sigma_z'(z))\tilde{H}_z + (\sigma_\rho'(\rho) - \sigma_z'(z))(\frac{\sigma_\rho(\rho)}{\rho} - \sigma_z'(z))R_H \\ = \frac{1}{\rho}\frac{\partial \tilde{E}_\rho}{\partial \phi} - \frac{\partial \tilde{E}_\phi}{\partial \rho} - \frac{\tilde{E}_\phi}{\rho} - \sigma_\rho''(\rho)W_E \ , \end{aligned} \tag{3.129}$$

$$\begin{aligned} \frac{\partial \tilde{E}_\rho}{\partial t} + (\sigma_z'(z) + \frac{\sigma_\rho(\rho)}{\rho} - \sigma_\rho'(\rho))\tilde{E}_\rho + (\frac{\sigma_\rho(\rho)}{\rho} - \sigma_\rho'(\rho))(\sigma_z'(z) - \sigma_\rho'(\rho))P_E \\ = \frac{1}{\rho}\frac{\partial \tilde{H}_z}{\partial \phi} - \frac{\partial \tilde{H}_\phi}{\partial z} - \sigma_z''(z)T_H \ , \end{aligned} \tag{3.130}$$

$$
\begin{aligned}
\frac{\partial \tilde{E}_\phi}{\partial t} + (\sigma_z'(z) + \sigma_\rho'(\rho) - \frac{\sigma_\rho(\rho)}{\rho})\tilde{E}_\phi + (\sigma_\rho'(\rho) - \frac{\sigma_\rho(\rho)}{\rho})(\sigma_z'(z) - \frac{\sigma_\rho(\rho)}{\rho})Q_E \\
= \frac{\partial \tilde{H}_\rho}{\partial z} - \frac{\partial \tilde{H}_z}{\partial \rho} + \sigma_z''(z)U_H - \sigma_\rho''(\rho)V_H \ ,
\end{aligned}
\tag{3.131}
$$

$$
\begin{aligned}
\frac{\partial \tilde{E}_z}{\partial t} + (\frac{\sigma_\rho(\rho)}{\rho} + \sigma_\rho'(\rho) - \sigma_z'(z))\tilde{E}_z + (\sigma_\rho'(\rho) - \sigma_z'(z))(\frac{\sigma_\rho(\rho)}{\rho} - \sigma_z'(z))R_E \\
= \frac{\partial \tilde{H}_\phi}{\partial \rho} - \frac{1}{\rho}\frac{\partial \tilde{H}_\rho}{\partial \phi} + \frac{\tilde{H}_\phi}{\rho} + \sigma_\rho''(\rho)W_H \ ,
\end{aligned}
\tag{3.132}
$$

and the supplementary ordinary differential equations are given in the following:

$$
\frac{\partial P_H}{\partial t} = \tilde{H}_\rho - \sigma_\rho'(\rho)P_H, \ \frac{\partial P_E}{\partial t} = \tilde{E}_\rho - \sigma_\rho'(\rho)P_E \ , \tag{3.133}
$$

$$
\frac{\partial Q_H}{\partial t} = \tilde{H}_\phi - \frac{\sigma_\rho(\rho)}{\rho}Q_H, \ \frac{\partial Q_E}{\partial t} = \tilde{E}_\phi - \frac{\sigma_\rho(\rho)}{\rho}Q_E \ , \tag{3.134}
$$

$$
\frac{\partial R_H}{\partial t} = \tilde{H}_z - \sigma_z(z)R_H, \ \frac{\partial R_E}{\partial t} = \tilde{E}_z - \sigma_z(z)R_E \ , \tag{3.135}
$$

$$
\frac{\partial T_E}{\partial t} = \tilde{E}_\phi - \sigma_z'(z)E_H, \ \frac{\partial T_H}{\partial t} = \tilde{H}_\phi - \sigma_z'(z)H_E \ , \tag{3.136}
$$

$$
\frac{\partial U_E}{\partial t} = \tilde{E}_\rho - \sigma_z'(z)U_E, \ \frac{\partial U_H}{\partial t} = \tilde{H}_\rho - \sigma_z'(z)U_H \ , \tag{3.137}
$$

$$
\frac{\partial V_E}{\partial t} = \tilde{E}_z - \sigma_\rho'(\rho)V_E, \ \frac{\partial V_H}{\partial t} = \tilde{H}_z - \sigma_\rho'(\rho)V_H \ , \tag{3.138}
$$

$$
\frac{\partial W_E}{\partial t} = \tilde{E}_\phi - \sigma_\rho'(\rho)W_E, \ \frac{\partial W_H}{\partial t} = \tilde{H}_\phi - \sigma_\rho'(\rho)W_H \ . \tag{3.139}
$$

Note that the system of equations are symmetric hyperbolic and hence strongly well-posed. If the second-derivative terms are set to be zero, then we need only 6 supplementary fields instead of 14. This corresponds to the case of $\sigma_\rho(\rho)$ and $\sigma_z(z)$ being linear functions. Otherwise the above equations admit solutions of the uniaxial medium type, the detail of which is not discussed here. One also notes that there is not much computational work involved with the computation of the supplementary ordinary differential equations, especially for higher order methods where the computation of spatial differentiation needs much more computational work. For the purpose of completeness, we give the plane wave solutions for the supplementary fields in the following:

$$P_H = \frac{\tilde{H}_\rho}{\sigma'_\rho(\rho) + i\omega}, \; P_E = \frac{\tilde{E}_\rho}{\sigma'_\rho(\rho) + i\omega} \; ,$$

$$Q_H = \frac{\tilde{H}_\phi}{\frac{\sigma_\rho(\rho)}{\rho} + i\omega}, \; Q_E = \frac{\tilde{E}_\phi}{\frac{\sigma_\rho(\rho)}{\rho} + i\omega} \; ,$$

$$R_H = \frac{\tilde{H}_z}{\sigma'_z(z) + i\omega}, \; R_E = \frac{\tilde{E}_z}{\sigma'_z(z) + i\omega} \; ,$$

$$T_E = \frac{\tilde{E}_\phi}{\sigma'_z(z) + i\omega}, \; T_H = \frac{\tilde{H}_\phi}{\sigma'_z(z) + i\omega} \; ,$$

$$U_E = \frac{\tilde{E}_\rho}{\sigma'_z(z) + i\omega}, \; U_H = \frac{\tilde{H}_\rho}{\sigma'_z(z) + i\omega} \; ,$$

$$V_E = \frac{\tilde{E}_z}{\sigma'_\rho(\rho) + i\omega}, \; V_H = \frac{\tilde{H}_z}{\sigma'_\rho(\rho) + i\omega} \; ,$$

$$W_E = \frac{\tilde{E}_\phi}{\sigma'_\rho(\rho) + i\omega}, \; W_H = \frac{\tilde{H}_\phi}{\sigma'_\rho(\rho) + i\omega} \; .$$

3.5 Concluding Remarks

Our emphasis in this chapter is to present the perfectly matched layer (PML) methods in spherical and cylindrical coordinate systems. Both the split-field formulation and the unsplit-field formulation are given. The PML methods have all the merits of the rectangular PML method. The reflectionless property at the vacuum-layer interface is demonstrated by matching the plane wave solutions of Maxwell's equations and the decaying plane wave solutions of the equations for the PML methods. We also analyze the decaying property of the waves in the layer in the direction of propagation. We see that the spherical PML method has an exceptional merit that its plane wave solutions decay in all directions of propagation, while the plane wave solutions of rectangular and cylindrical PML's decay in all directions of propagation except the grazing direction.

Chapter 4

Comparisons of Numerical Schemes in 1-D

4.1 Introduction

We consider, in this chapter, the numerical solution of the fundamental time dependent Maxwell's curl equations in 1-D. The standard scheme in finite difference time domain (FD-TD) methods is the Yee scheme [51]. This scheme is second order accurate scheme both in space and time and the unknowns E and H are given in a staggered set of grid points. It had been argued that the staggering is one of the most important features of this scheme. Recently, Petropoulos [42] gave a convincing evidence for the superiority of fourth order schemes over second order schemes. It has been also suggested (see [51]) that it may be necessary to convert second-order accurate FD-TD algorithms to those having fourth-order accuracy. The same type of analysis indicates that spectral methods might be of value as a possible alternative to finite differences for the solution of Maxwell's equations. In fact, since polynomial spectral methods require only π points to resolve a wave, one can minimize the amount of total work needed for computations.

This chapter is addressing the question whether staggering is also necessary for high accuracy schemes as fourth order methods and spectral methods. In particular we consider second order schemes (staggered and non-staggered), fourth order explicit schemes (staggered and non-staggered), fourth order compact schemes (S and NS) as well as spectral polynomial methods (S and NS). All of those schemes were applied to the one dimensional Maxwell's equations.

To answer the above question we define the concept of the total work $W(e)$ needed to achieve a given accuracy e for the phase of a wave solution for the Maxwell's equation. Basically we look at the number of points N required to achieve a certain accuracy in the phase and the time step Δt, allowable by the scheme. The work W then is defined as

$$W = \frac{N}{\Delta t} . \tag{4.1}$$

We then compute the work required for the various schemes.

The results can be summarized as follows

- For second order schemes the staggered scheme requires *half* of the work of the non-staggered scheme. This explains the success of the Yee scheme.
- The fourth order staggered explicit schemes is more efficient than the non-staggered. However the improvement is not that dramatic. In fact we can only expect an improvement of about 36%.
- The staggered and non-staggered compact schemes are equivalent.
- The compact fourth order schemes are preferable to the explicit schemes.
- Within spectral polynomial schemes there is no difference between staggered and non staggered schemes.

It seems that the attractiveness of the staggered grid method diminishes as the order of accuracy increases.

The main advantage of non-staggered grids, in our opinion, is the imposition of boundary conditions. In the staggered grid approximation one can impose the boundary conditions only on the variables that are defined on the boundary points. Thus boundary conditions in terms of *character-*

istic variables are not easily implemented. It is our opinion that characteristic boundary conditions are important in the numerical solutions of the Maxwell's equations, especially for increased order of accuracy.

4.2 The Equations and Schemes

Consider the free space 1-D Maxwell's equations:

$$\begin{cases} \dfrac{\partial E}{\partial t} = -\dfrac{1}{\epsilon}\dfrac{\partial H}{\partial x} \\ \dfrac{\partial H}{\partial t} = -\dfrac{1}{\mu}\dfrac{\partial E}{\partial x} \end{cases} \tag{4.2}$$

where E is the electric field vector and H is the magnetic field vector. Also ϵ is the permittivity, and μ is the permeability.

Denote the speed of the wave by

$$c = \frac{1}{\sqrt{\epsilon\mu}} \tag{4.3}$$

and assume the initial condition

$$\begin{cases} E(x,0) = e^{2\pi i\omega x} \\ H(x,0) = \sqrt{\frac{\epsilon}{\mu}}e^{2\pi i\omega x} \quad , \end{cases} \tag{4.4}$$

The solution of the system is then given by

$$\begin{cases} E(x,t) = e^{2\pi i\omega(x-ct)} \\ H(x,t) = \sqrt{\frac{\epsilon}{\mu}}e^{2\pi i\omega(x-ct)} \end{cases} \tag{4.5}$$

We now discretize (4.5) in space by several different finite difference approximations:

Consider the differencing and averaging operators, respectively,

$$\delta_x q_i = q_{i+\frac{1}{2}} - q_{i-\frac{1}{2}}, \ \mu_x q_i = \frac{1}{2}(q_{i+\frac{1}{2}} + q_{i-\frac{1}{2}}) \tag{4.6}$$

Then the second order difference operators for the staggered and non-staggered second order schemes are given by:

I. *Second-order Staggered:*

$$\frac{du}{dx}|_i = \frac{1}{\Delta x}\delta_x u|_i + O(\Delta x^2) \tag{4.7}$$

II. *Second-order Non-staggered:*

$$\frac{du}{dx}|_i = \frac{1}{\Delta x}\delta_x \mu_x u|_i + O(\Delta x^2) \tag{4.8}$$

The fourth order explicit schemes are given by;

III. *Fourth-order Explicit Staggered:*

$$\frac{du}{dx}|_i = \frac{1}{\Delta x}\delta_x (I - \frac{1}{24}\delta_x^2) u|_i + O(\Delta x^4) \tag{4.9}$$

IV . *Fourth-order Explicit Non-staggered:*

$$\frac{du}{dx}|_i = \frac{1}{\Delta x}\delta_x \mu_x (I - \frac{1}{6}\delta_x^2) u|_i + O(\Delta x^4) \tag{4.10}$$

And finally the fourth order compact schemes are given by

V . *Fourth-order Compact Staggered:*

$$(I + \frac{1}{24}\delta_x^2)\frac{du}{dx}|_i = \frac{1}{\Delta x}\delta_x u|_i + O(\Delta x^4) \tag{4.11}$$

VI . *Fourth-order Compact Non-staggered:*

$$(I + \frac{1}{6}\delta_x^2)\frac{du}{dx}|_i = \frac{1}{\Delta x}\delta_x \mu_x u|_i + O(\Delta x^4) \tag{4.12}$$

Our analysis is based on the following considerations: 1. The total amount of work is proportional to the number of grid points N and the number of time steps $n \sim (\Delta t)^{-1}$. 2. The number of operations needed per time step is the same for staggered and non-staggered schemes. We therefore define

Definition 1: The total Work to achieve an accuracy e for the phase is defined as

$$W(e) = \frac{N(e)}{\Delta t} \tag{4.13}$$

Thus the work depends on two factors. First the time step Δt is restricted by the stability condition of the scheme. Secondly the number of grid points should be enough to resolve the different wave lengths of the problem.

We first consider the CFL condition for the schemes **I** - **VI**. We assume that the discretization in time is the same for the various schemes, i.e., second order for second order schemes, and fourth order for the fourth order schemes. Clearly the time step is inversely proportional to the maximum of the magnitude of the *symbol* $F(z)$ where $z = \sin(k\frac{\Delta x}{2})$ can range between -1 and 1. We list the symbols and there maximum in the following:

$$F_{\mathbf{I}} = 2zi \tag{4.14}$$

$$F_{\mathbf{II}} = 2z\sqrt{1-z^2}\,i \tag{4.15}$$

$$F_{\mathbf{III}} = 2z(1+\frac{1}{6}z^2)i \tag{4.16}$$

$$F_{\mathbf{IV}} = 2z\sqrt{1-z^2}(1+\frac{2}{3}z^2)i \tag{4.17}$$

$$F_{\mathbf{V}} = \frac{2z}{(1-\frac{1}{6}z^2)}i \tag{4.18}$$

$$F_{\mathbf{VI}} = \frac{2z\sqrt{1-z^2}}{1-\frac{2}{3}z^2}i \tag{4.19}$$

If we denote now the number of points by $N \sim (\Delta x)^{-1}$ we get the following estimation for the allowable time steps:

$$
\begin{aligned}
c\Delta t_{\mathbf{I}} N_I &\sim .5 && (4.20)\\
c\Delta t_{\mathbf{II}} N_{II} &\sim 1. && (4.21)\\
c\Delta t_{\mathbf{III}} N_{III} &\sim .4286 && (4.22)\\
c\Delta t_{\mathbf{IV}} N_{IV} &\sim .7287 && (4.23)\\
c\Delta t_{\mathbf{V}} N_{V} &\sim .4167 && (4.24)\\
c\Delta t_{\mathbf{VI}} N_{VI} &\sim .5774 && (4.25)
\end{aligned}
$$

It is clear that non-staggered methods allow larger time steps than the staggered methods, however this will be compensated by the better accuracy of the staggered scheme. This allows coarser grids and therefore smaller number of grid points to achieve the same accuracy.

We consider now the number of points required for a certain limit on the *phase error*. Assume the following solutions for the finite difference equations

$$
\begin{cases} E(x,t) = e^{2\pi i\omega(x-\tilde{c}(\omega)t)} \\ H(x,t) = \sqrt{\frac{\epsilon}{\mu}} e^{2\pi i\omega(x-\tilde{c}(\omega)t)} \end{cases} \tag{4.26}
$$

The Phase Error is defined by [33] and [34] as

$$
e(\omega, t) = |2\pi i\omega t(c - \tilde{c}(\omega))| \ . \tag{4.27}
$$

We also define $j = \omega c t$ to be the number of periods in time and $p = \frac{1}{\omega \Delta x}$ to be the number of grid points per wave length. We get the following formulae for the phase errors

$$
\begin{aligned}
e_{\mathbf{I}}(p,j) &= 2\pi j[1 - \frac{\sin(\frac{\pi}{p})}{\frac{\pi}{p}}] && (4.28)\\
e_{\mathbf{II}} &= 2\pi j[1 - \frac{\sin(\frac{2\pi}{p})}{\frac{2\pi}{p}}] && (4.29)
\end{aligned}
$$

$$
\begin{aligned}
e_{\mathbf{III}} &= 2\pi j[1-\frac{27\sin(\frac{\pi}{p})-\sin(\frac{3\pi}{p})}{\frac{24\pi}{p}}] && (4.30)\\
e_{\mathbf{IV}} &= 2\pi j[1-\frac{8\sin(\frac{2\pi}{p})-\sin(\frac{4\pi}{p})}{\frac{12\pi}{p}}] && (4.31)\\
e_{\mathbf{V}} &= 2\pi j[1-\frac{\sin(\frac{\pi}{p})}{\frac{\pi}{p}(1-\frac{1}{6}\sin^2(\frac{\pi}{p}))}] && (4.32)\\
e_{\mathbf{VI}} &= 2\pi j[1-\frac{\sin(\frac{2\pi}{p})}{\frac{2\pi}{p}(1-\frac{2}{3}\sin^2(\frac{\pi}{p}))}] && (4.33)
\end{aligned}
$$

If we replace the $\sin(\cdot)$ by its power series and retain only the terms of the lowest order, we get the leading order estimates for the phase error. Now to attain the same level of error, we know approximately how many grid points we need per wave length (N_{ppw}).

$$
\begin{aligned}
N_{\mathbf{I}} &= 2\pi(\frac{2}{6})^{\frac{1}{2}}(\frac{\pi j}{e})^{\frac{1}{2}} && (4.34)\\
N_{\mathbf{II}} &= 2\pi(\frac{8}{6})^{\frac{1}{2}}(\frac{\pi j}{e})^{\frac{1}{2}} && (4.35)\\
N_{\mathbf{III}} &= 2\pi(\frac{3}{320})^{\frac{1}{4}}(\frac{\pi j}{e})^{\frac{1}{4}} && (4.36)\\
N_{\mathbf{IV}} &= 2\pi(\frac{1}{15})^{\frac{1}{4}}(\frac{\pi j}{e})^{\frac{1}{4}} && (4.37)\\
N_{\mathbf{V}} &= 2\pi(\frac{17}{2880})^{\frac{1}{4}}(\frac{\pi j}{e})^{\frac{1}{4}} && (4.38)\\
N_{\mathbf{VI}} &= 2\pi(\frac{1}{90})^{\frac{1}{4}}(\frac{\pi j}{e})^{\frac{1}{4}} && (4.39)
\end{aligned}
$$

Non-staggered schemes have a larger time step limit. But staggered schemes need less number of grid points per wave length. In order to determine which method is better, the most appropriate way is to look at the total Work.

4.3 Comparisons

To this end, we are able to give the total Work ($W(e)$ see (4.13)) for different schemes to attain the same level of **phase error**:

$$W_{\mathbf{I}} \sim 82.68(\frac{j}{e}) \tag{4.40}$$

$$W_{\mathbf{II}} \sim 165.37(\frac{j}{e}) \tag{4.41}$$

$$W_{\mathbf{III}} \sim 15.81(\frac{j}{e})^{\frac{1}{2}} \tag{4.42}$$

$$W_{\mathbf{IV}} \sim 24.79(\frac{j}{e})^{\frac{1}{2}} \tag{4.43}$$

$$W_{\mathbf{V}} \sim 12.90(\frac{j}{e})^{\frac{1}{2}} \tag{4.44}$$

$$W_{\mathbf{VI}} \sim 12.77(\frac{j}{e})^{\frac{1}{2}} \tag{4.45}$$

An immediate observation is that if $\frac{j}{e}$ is large then the fourth order schemes are always superior. Thus, if long time integration is needed or high accuracy is required then fourth order are better. The aim of this chapter though is to compare staggered and non-staggered schemes. To see this, we give the factors between the total Work in the following:

$$\frac{W_{\mathbf{II}}}{W_{\mathbf{I}}} = 2 \tag{4.46}$$

$$\frac{W_{\mathbf{IV}}}{W_{\mathbf{III}}} = 1.5682 \tag{4.47}$$

$$\frac{W_{\mathbf{VI}}}{W_{\mathbf{V}}} = 0.9901 \; . \tag{4.48}$$

Note that in the case of second order schemes the improvement is dramatic. For fourth order explicit schemes the staggered scheme is still better, but the improvement is less than that in the second order case. It is interesting to notice that the non-staggered compact fourth order scheme is even faster than the staggered one. In the next section we will show that the there is no improvement for spectral methods. Thus staggered mesh methods lose the superiority when the order of accuracy increases.

Remark 4.3.1 *We haven't considered discretization error in time in our analysis. However, numerical experiments of fourth order schemes with fourth order Runge-Kutta scheme in time show that the factors in (46)-(48) still hold approximately when we consider the computation work needed* *for non-staggered and staggered schemes to attain* **the same level of accuracy**.

4.4 Staggered Chebyshev Collocation Method

In this section, we will consider the Chebyshev collocation methods on the staggered mesh:

$$\text{Gauss-Lobatto points: } x_i = \cos(i\pi/N), \quad i = 0, \ldots, N\ ,$$

for the discretization of H(x,t) and

$$\text{Gauss points: } y_j = \cos((j + \frac{1}{2})\pi/N), \quad j = 0, \ldots, N-1\ ,$$

for the discretization of E(x,t).

Chebyshev collocation methods are based on the interpolating polynomials on the grid points. The Chebyshev-Lagarange polynomials on the Gauss-Lobatto points are given by:

$$g_j(x) = \frac{(-1)^{j+1}(1-x^2)\,T'_N(x)}{c_j N^2 (x - x_j)}, \qquad j = 0, \ldots, N\,, \tag{4.49}$$

where

$$c_j = \begin{cases} 2 & j = 0, N \\ 1 & j = 1, \ldots, N-1 \end{cases} .$$

At present, we compute the derivative with the Matrix-Vector Multiplication Method. The Chebyshev derivative matrix D, the entries of which have been given in chapter 2, is needed for the computation of non-staggered Chebyshev method. For staggered Chebyshev method, however, we need two different derivative matrices, since the derivatives are desired on a different set of points than the set of points the field values are defined.

The Chebyshev-Lagarange polynomial at the Gauss points are given by:

$$h_j(x) = \begin{cases} \frac{T_N(x)}{T'_N(y_j)(x-y_j)} & , \quad x \neq y_j \\ 1 & , \quad x = y_j \end{cases} , \qquad j = 0, \ldots, N \ . \tag{4.50}$$

We denote the differentiation matrix for E by D^E and that for H by D^H. D^E is $h'_j(x)$ evaluated at the Gauss-Lobatto points, and D^H is $g'_j(x)$ evaluated at the Gauss points. Now we give the entries of the differentiation matrices:

$$\begin{aligned} D^E_{0j} &= \frac{(N^2(1-y_j)-1)\sin\frac{\pi(j+\frac{1}{2})}{N}}{(-1)^j(1-y_j)^2} , \\ D^E_{Nj} &= \frac{(N^2(-1-y_j)-(-1)^{N+1})\sin\frac{\pi(j+\frac{1}{2})}{N}}{(-1)^j(1+y_j)^2} , \\ D^E_{ij} &= \frac{-(-1)^i\sin\frac{\pi(j+\frac{1}{2})}{N}}{(-1)^j(x_i-y_j)^2} , \qquad 0 < j < N-1; 0 < i < N \ . \end{aligned} \tag{4.51}$$

and that for H(x,t)

$$D^H_{ij} = \frac{(x_j y_i - 1)(-1)^{i+j+1}}{c_j N \sin\frac{\pi(j+\frac{1}{2})}{N}(y_i - x_j)^2} , \qquad 0 < i < N-1; 0 < j < N \ . \tag{4.52}$$

Through the type error analysis as that in [12], one can show that the above formulation of D^E and D^H are ill-conditioned. Fortunately, the same type of remedy as that in [12] is also applicable for reducing the roundoff error of the entries in D^E and D^H. The idea is to apply the following trigonometric identities:

$$\begin{aligned} x_i - y_j &= \cos\frac{\pi i}{N} - \cos\frac{\pi(j+\frac{1}{2})}{N} \\ &= -2\sin\frac{\pi(i+j+\frac{1}{2})}{2N}\sin\frac{\pi(i-j-\frac{1}{2})}{2N} , \\ x_j y_i - 1 &= \cos\frac{\pi j}{N}\cos\frac{\pi(i+\frac{1}{2})}{N} - 1 \\ &= \frac{1}{2}(\cos\frac{\pi(j+i+\frac{1}{2})}{N} + \cos\frac{\pi(j-i-\frac{1}{2})}{N}) - 1 \\ &= -\sin^2\frac{\pi(j+i+\frac{1}{2})}{2N} - \sin^2\frac{\pi(j-i-\frac{1}{2})}{2N} \ . \end{aligned} \tag{4.53}$$

Thus we get a better conditioned for the differentiation matrices:

$$
\begin{aligned}
D^E_{0j} &= \frac{(-1)^j N + \frac{(-1)^j}{2N}\sin^2(\frac{\pi(j+\frac{1}{2})}{2N})}{\tan\frac{\pi(j+\frac{1}{2})}{2N}} \ , \\
D^E_{Nj} &= ((-1)^{j+N} N + \frac{(-1)^j}{2N}\cos^2(\frac{\pi(j+\frac{1}{2})}{2N}))\tan\frac{\pi(j+\frac{1}{2})}{2N} \ , \\
D^E_{ij} &= \frac{(-1)^{i+j-1}\sin(\frac{\pi(j+\frac{1}{2})}{N})}{4N\sin^2(\frac{\pi(i+j+\frac{1}{2})}{2N})\sin^2(\frac{\pi(i-j-\frac{1}{2})}{2N})} \ , \quad 0<j<N-1;\ 0<i<N \ .
\end{aligned}
\tag{4.54}
$$

and

$$
\begin{aligned}
D^H_{i0} &= \frac{(-1)^i}{4N\sin\frac{\pi(i+\frac{1}{2})}{N}\sin^2(\frac{\pi(i+\frac{1}{2})}{2N})} \ , \\
D^H_{iN} &= \frac{(-1)^{i+N}}{4N\sin\frac{\pi(i+\frac{1}{2})}{N}\cos^2(\frac{\pi(i+\frac{1}{2})}{2N})} \ , \\
D^H_{ij} &= \frac{(-1)^{i+j}}{4N\sin\frac{\pi(i+\frac{1}{2})}{N}\sin^2(\frac{\pi(i+j+\frac{1}{2})}{2N})} \ , \\
&\quad + \frac{(-1)^{i+j}}{4N\sin\frac{\pi(i-\frac{1}{2})}{N}\sin^2(\frac{\pi(j-i-\frac{1}{2})}{2N})} \ , \quad 0<i<N-1; \quad 0<j<N \ .
\end{aligned}
\tag{4.55}
$$

It is also pointed in [12] that $\sin(x)$ can be calculated with relative error comparable to machine precision ϵ while $\sin(\pi - x)$ can only be computed with absolute error comparable to ϵ. Hence by considering the structure of the matrix properly in calculating the entries one can increase the accuracy of the differentiation matrix being computed.

For the staggered Chebyshev collocation method, we impose boundary condition on H:

$$
\begin{cases}
H(1,t) = h_1(t) \\
H(-1,t) = h_{-1}(t)
\end{cases} \ .
\tag{4.56}
$$

Then the semidiscrete formulation of the method is given by:

$$
\begin{aligned}
&\frac{\partial E_{N-1}(y_j,t)}{\partial t} = -\frac{1}{\epsilon}\frac{\partial H_N(x,t)}{\partial x}|_{x=y_j} \ , \qquad j=0,\ldots,N-1 \ , \\
&\frac{\partial H_N(x_i,t)}{\partial t} = -\frac{1}{\mu}\frac{\partial E_{N-1}(x,t)}{\partial x}|_{x=x_i} \ , \qquad i=1,\ldots,N-1 \ , \\
&H_N(1,t) = h_1(t) \ , \\
&H_N(-1,t) = h_{-1}(t) \ .
\end{aligned}
\tag{4.57}
$$

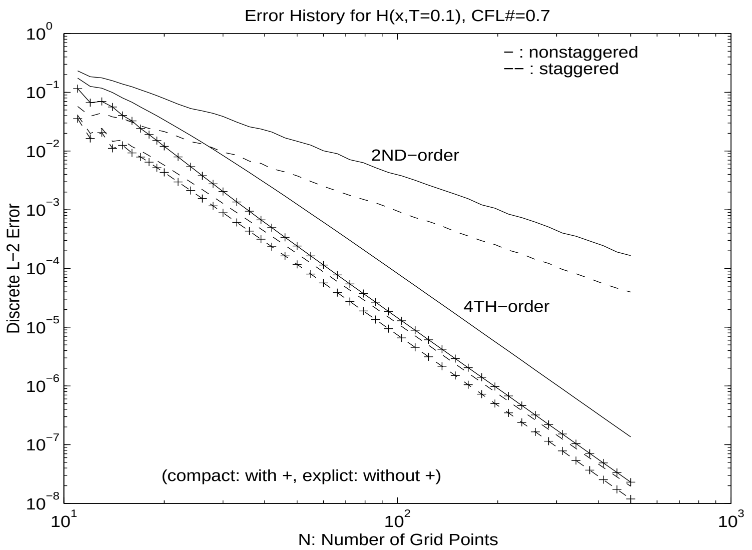

Figure 4.1: The error history of staggered, solid line, and non-staggered, dashed line, 2nd-order and 4th-order finite difference schemes. For 4th-order schemes, both the explicit, without +, and compact, with +, schemes are considered.

where $E_{N-1}(x,t)$ is the approximating Chebyshev polynomial of degree $N-1$ and $H_N(x,t)$ is the approximating Chebyshev polynomial of degree N. Numerical computations of staggered and non-staggered Chebyshev collocation method don't show any advantage of staggered method over non-staggered method.

4.5 Examples

Example 4.5.1 *In this experiment, we use leap-frog scheme in time for second order schemes and fourth order Runge-Kutta method in time for the fourth order schemes. The time step is chosen according to the conditions in section 2 with the same scaling. We plot their error history for different number of grid points, see figure 4.1.*

Table 4.1: Number of grid points needed for second order Schemes to attain the same level of error.

error	8e-5	4e-5	2e-5	1e-5
Non-staggered($N \cdot Work$)	$394 \cdot 77618$	$592 \cdot 175232$	$793 \cdot 314425$	$996 \cdot 496008$
Staggered ($N \cdot Work$)	$197 \cdot 38809$	$296 \cdot 87616$	$397 \cdot 157609$	$498 \cdot 248004$
ratio	$2. \cdot 2.$	$2. \cdot 2.$	$2. \cdot 2.$	$2. \cdot 2.$

Table 4.2: Number of grid points needed for fourth order non-compact schemes to attain the same level of error ($CFL \approx 0.9$).

error	8e-6	4e-6	2e-6	1e-6
Non-staggered($N \cdot Work$)	$183 \cdot 45957$	$217 \cdot 64621$	$259 \cdot 92056$	$308 \cdot 130183$
Staggered($N \cdot Work$)	$112 \cdot 29267$	$133 \cdot 41272$	$158 \cdot 58245$	$188 \cdot 82464$
ratio	$1.634 \cdot 1.570$	$1.632 \cdot 1.566$	$1.639 \cdot 1.581$	$1.638 \cdot 1.579$

Example 4.5.2 *In this experiment, we verify the ratios of the $N'_{ppw}s$ needed for staggered and non-staggered schemes. Leap-frog scheme is used in time for second order schemes and fourth order Runge-Kutta scheme is used in time for fourth order schemes. We choose the* **time steps** *according to the conditions in section 2 and we got the N needed for staggered and non-staggered schemes to attain the same level of accuracy.*

The factors between $N'_{ppw}s$ and the factors between work of staggered and non-staggered schemes in section 2 and 3 are verified here. See table (4.1)-(4.3). Note that the scale we took for estimated Work is the same in the same table. So the ratios of Work reflect the relative efficiency of staggered and non-staggered schemes.

Table 4.3: Number of grid points needed for fourth order compact schemes to attain the same level of error ($CFL \approx 0.7$).

error	8e-6	4e-6	2e-6	1e-6
Non-staggered ($N \cdot Work$)	$116 \cdot 23304$	$138 \cdot 32982$	$164 \cdot 46581$	$195 \cdot 65856$
Staggered ($N \cdot Work$)	$99 \cdot 23521$	$117 \cdot 32851$	$139 \cdot 46367$	$166 \cdot 66129$
ratio	$1.172 \cdot 0.991$	$1.180 \cdot 1.004$	$1.180 \cdot 1.005$	$1.175 \cdot 0.996$

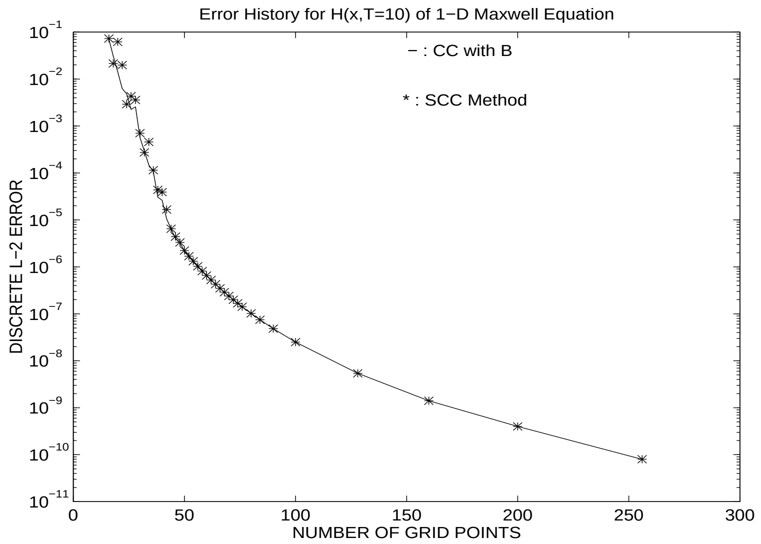

Figure 4.2: The error history of the staggered and the non-staggered Chebyshev method. CC with B: fixing H for the boundary treatment of the Chebyshev Collocation method, to be close to the boundary treatment of staggered methods.

Example 4.5.3 *The error history of staggered and non-staggered Chebyshev methods is compared. For the comparison to be meaningful, we impose H strictly in the boundary treatments of both methods. See figure (4.2). There is no gain in accuracy for non-staggered method. We also experimented with the largest time step we can choose for the two methods and no difference was observed.*

4.6 Concluding Remarks

The total work needed to achieve a certain accuracy for different schemes is estimated by considering the stability condition and phase error of staggered and non-staggered schemes. Through a comparison of the efficiency of staggered vs. non-staggered methods for the numerical solution of the one dimensional Maxwell's equations, our conclusion is that staggered grid methods are much better than non-staggered schemes for low order accuracy schemes, but their advantage decreases as the order of accuracy increases. In particular, fourth order compact schemes are almost equivalent.

We also introduce a spectral staggered grid method and demonstrate that there is no advantage in using staggered grid spectral methods. Numerical results verifying our claims are presented.

Chapter 5

Penalty Methods for 1-D Maxwell's Equations

5.1 Introduction

How to impose boundary conditions plays a crucial role in spectral and pseudospectral methods. One way of applying a collocation method to a partial differential equation is to satisfy the equation at the interior points and impose boundary conditions strictly at the boundary points. An alternative way is to collocate the differential equation at all the grid points and introduce the boundary conditions weakly as a penalty term.

The main difference between the two methods is that, in the latter, the boundary conditions are not satisfied exactly but only at the limit. The penalty method, in the context of a Legendre collocation approximation of a linear hyperbolic systems, has been first introduced by Funaro and Gottlieb in [17]. In [16] the case of a Chebyshev penalty method for a scalar hyperbolic equation has been studied.

In this chapter we first present a Chebyshev penalty method for a linear hyperbolic equation. The method differs from the one considered in [16] in the functional form of the penalty term. In our method the penalty term is non zero also at the interior points; which introduces a correction at all the interpolation points. We prove stability of the semidiscrete scheme in the appropriate norm and we give an optimal estimate of the penalty parameter.

In [13] Don and Gottlieb presented a penalty method, called the Chebyshev-Legendre (CL) method, that has the advantages of both the Chebyshev and Legendre methods. Here we also consider the application of these type of penalty methods for Maxwell's equations. We shall give two stable staggered Chebyshev-Legendre methods. The stable CL methods for non-staggered mesh can be obtained similarly, and for the non-staggered methods one has the extra flexibility in considering the characteristic relations at the boundary.

We have applied all the penalty methods to compute 1-D Maxwell's equations. Numerical results verify the stability condition of the penalty methods. It is also possible to apply the penalty methods to 2-D and 3-D Maxwell's equations and obtain stable pseudospectral schemes.

5.2 Preliminaries

In this section we summarize the notation and some general results regarding the Chebyshev polynomials. For an overview of those results the reader is referred to [24, 10] and [9]. In this chapter we will work in the following space:

$$\mathbf{P}_N = \{polynomials \quad of \quad degree \leq N\}. \tag{5.1}$$

We denote by T_N the Chebyshev polynomial of degree N,

$$T_N(x) = \cos(N \cos^{-1} x). \tag{5.2}$$

Throughout the chapter we will make use of the following formulas:

$$2T_k = \frac{T'_{k+1}}{k+1} - \frac{T'_{k-1}}{k-1}, \tag{5.3}$$

$$xT_k = \frac{1}{2}\left(T_{k+1} + T_{k-1}\right); \tag{5.4}$$

and the orthogonality property:

$$\int_{-1}^{1} T_N T_M \frac{dx}{\sqrt{1-x^2}} = \frac{\pi}{2}\delta_{NM}. \tag{5.5}$$

We will use the Gauss-Lobatto set of collocation points:

$$x_j^N = \cos\left(\frac{\pi j}{N}\right), \qquad 0 \le j \le N. \tag{5.6}$$

These points are the zeros of $(1-x^2)T_N'(x)$. Associated with this set of collocation points is the Gauss quadrature formula through which we define the discrete scalar product $(\cdot,\cdot)_N$:

$$(f,g)_N = \sum_{j=0}^{N} f(x_j^N) g(x_j^N)\omega_j, \tag{5.7}$$

where

$$\begin{cases} \omega_j = \frac{\pi}{N}, & 1 \le j \le N, \\ \omega_0 = \omega_N = \frac{\pi}{2N}. \end{cases} \tag{5.8}$$

If $fg \in \mathbf{P}_{2N-1}$ we have:

$$\int_{-1}^{1} f(x)g(x)\omega(x)\,dx = \sum_{j=0}^{N} f(x_j^N)g(x_j^N)\omega_j, \tag{5.9}$$

where $\omega(x) = (1-x^2)^{-1/2}$.

5.3 Hyperbolic equations

In this section we present a Chebyshev penalty method for the linear hyperbolic equation.

$$\begin{cases} v_t = v_x, & x \in (-1,1), \quad t > 0, \\ v(1,t) = g^+(x), & t > 0, \\ v(x,0) = v_0, & x \in (-1,1). \end{cases} \tag{5.10}$$

We seek an approximate solution u in the space $\mathbf{P}_{N-1}$ that satisfies:

$$u_t(x) = u_x - \tau(u(1,t) - g^+)\frac{T_N'(x)}{N^2}, \tag{5.11}$$

at the points x_j^N, $0 \le j \le N$. Note that the penalty term $T_N'(x)$ is zero at the interior points but it is non zero at *both* boundary points. A different Chebyshev penalty method for equation (5.10) has been studied in [17], where the penalty term was $\frac{(1+x)T_N'(x)}{2N^2}$.

Remark 5.3.1 *In a similar way we can define a penalty method for the equation*

$$\begin{cases} v_t = -v_x, & x \in (-1,1), \quad t > 0, \\ v(-1,t) = g^-(x), & t > 0. \end{cases} \tag{5.12}$$

In this case the penalty term would be:

$$-\tau(u(-1,t) - g^-)\frac{T_N'(x)}{N^2}. \tag{5.13}$$

The extension to this case of all the results is straightforward.

As shown in [24], problem (5.10) is not well posed in the usual Chebyshev norm, corresponding to the weight function $\omega(x) = (1-x^2)^{-1/2}$. Instead we prove stability in the norm corresponding to the weight function

$$\tilde{\omega}(x) = (1+x)\omega(x) = (1+x)^{1/2}(1-x)^{-1/2}. \tag{5.14}$$

Theorem 5.3.1 *(Coercivity) Let $u \in \mathbf{P}_{N-1}$ and $\omega_0 = \pi/2N$ be the Chebyshev weight defined in (5.8). Then*

$$\int_{-1}^{1} u_x(x)u(x)\,\tilde{\omega}(x)\,dx \le \tau\omega_0 u^2(1), \tag{5.15}$$

provided τ satisfies

$$\tau \ge \frac{N^2}{2}. \tag{5.16}$$

Remark 5.3.2 *Note that in the penalty method (5.11) the approximate solution u does not satisfy the boundary condition exactly but only as N tends to ∞.*

Remark 5.3.3 *Let $f(x)$ be a function such that*

$$\lim_{x \to 1} \widetilde{\omega}(x) f(x) = 0, \tag{5.17}$$

then we can prove the following coercivity property

$$\int_{-1}^{1} f(x) f_x(x) \widetilde{\omega}(x)\, dx \le 0. \tag{5.18}$$

In our case the function $u(x)$ does not satisfy zero boundary conditions and (5.18) does not hold. However, as shown in Theorem (5.3.1), coercivity can be proved, if we restrict the set of function to polynomial and we impose a condition on the penalty term. This is sufficient for our purpose since we will use Theorem (5.3.1) for the solution of (5.11), $u(x)$, which is a polynomial.

Proof: (*of the Coercivity Theorem*) Let us define

$$U(x) = u(x) - u(1) T_N(x). \tag{5.19}$$

It is clear that $U(1) = 0$. We write:

$$\begin{aligned} \int_{-1}^{1} u(x) u_x(x)(1+x)\omega(x) dx = \int_{-1}^{1} U(x) U_x(x) \widetilde{\omega}(x) dx \\ + u(1) \int_{-1}^{1} u(x) T_N'(x)(1+x)\omega(x) dx \\ + u(1) \int_{-1}^{1} u_x(x) T_N(x)(1+x)\omega(x) dx \\ - u^2(1) \int_{-1}^{1} T_N(x) T_N'(x)(1+x)\omega(x) dx. \end{aligned} \tag{5.20}$$

Due to the orthogonality property (5.5) and the fact that $u_x(x) \in \mathbf{P}_{N-2}$ we have:

$$\int_{-1}^{1} u(x) T_N'(x)(1+x)\omega(x) dx = 0 = \int_{-1}^{1} T_N(x) T_N'(x) \omega dx. \tag{5.21}$$

Combining Remark 5.3.3, 5.4 and 5.9, we obtain:

$$\begin{aligned}\int_{-1}^{1} u(x)u_x(x)\widetilde{\omega}(x)dx &\leq \pi N u^2(1) - \frac{u^2(1)}{2}\int_{-1}^{1} T_{N-1}T_N\omega(x)dx \\ &\leq \pi N u^2(1) - \frac{\pi}{2}N u^2(1) \leq \frac{\pi}{2}N u^2(1). \end{aligned} \tag{5.22}$$

Therefore we obtain:

$$\int_{-1}^{1} u(x)u_x(x)\,\widetilde{\omega}(x)\,dx - \tau\omega_0 u^2(1) \leq \left(\frac{N}{2} - \frac{\tau}{N}\right)\pi u^2(1). \tag{5.23}$$

We conclude that if (5.16) is satisfied (5.15) holds. □

Using the previous Lemma we can prove the following stability result for the scheme (5.11).

Theorem 5.3.2 *Let u be the solution of (5.10) with $g^+ = 0$. If τ satisfies (5.16) then the Chebyshev penalty method is stable in the $L^2_{\widetilde{\omega}}$. More precisely,*

$$\frac{d}{dt}\sum_{j=0}^{N} u^2(x_j^N)(1+x_j^N)\omega_j \leq 0. \tag{5.24}$$

Remark 5.3.4 *The condition on the penalty parameter is optimal in this case. This can easily be seen by taking, for example, $u(x) = T_{N-1}(x)$.*

5.4 Two Stable Staggered Chebyshev-Legendre Methods

The Chebyshev-Legendre method in [13] is stable in the discrete L_2 norm. But it can not be directly extended to the staggered mesh to yield a stable penalty method. In the following we will give two Chebyshev-Legendre methods for the staggered mesh which are stable in the L_2 norm rather than discrete L_2 norm. The two methods are applicable to non-staggered mesh too. All the analysis for the staggered grid can be easily modified to the non-staggered case.

Unlike the Chebyshev points that are known explicitly, there is no explicit formula for the Legendre points. They must be computed numerically. But there is a simple formula, easily and robustly computed, for the values of the Legendre polynomials and their derivative at Chebyshev points. In fact we have the following explicit formula for $P'_N(x_j)$ (taken from [7]),

$$P'_N(\cos\theta) = \sum_{m=0}^{N-1} \frac{(\frac{3}{2})_m(\frac{3}{2})_{N-1-m}}{m!(N-1-m)!}\cos(N-1-2m)\theta \tag{5.25}$$

This is the basis for the computational advantage of Chebyshev-Legendre method.

5.4.1 L_2 Stable Staggered Chebyshev-Legendre Method

As the staggered method we consider is designed for Maxwell's equations, we also present our staggered Chebyshev-Legendre methods in that regime. Let $P_{N+1}(x)$, $P_N(x)$ and $P_{N-1}(x)$ be Legendre polynomial of degree $N+1$, N and $N-1$ respectively. In the Chebyshev-Legendre method for the staggered mesh we seek a polynomial $E_{N-1}(x,t)$ of degree $N-1$ and a polynomial $H_N(x,t)$ of degree N in x that satisfy

$$\begin{aligned}
\frac{\partial E_{N-1}(y_j,t)}{\partial t} = \; & -\frac{1}{\epsilon}\frac{\partial H_N(x,t)}{\partial x}|_{x=y_j} \\
& +\frac{1}{2}\frac{1}{\epsilon}(P_N(x)+P_{N-1}(x))'|_{x=y_j}(H_N(1,t)-h_1(t)) \\
& +\frac{1}{2}\frac{1}{\epsilon}\frac{(P_N(x)-P_{N-1}(x))'}{P_N(-1)}|_{x=y_j}(H_N(-1,t)-h_{-1}(t)) \;\;, \\
& \quad j=0,\ldots,N-1 \;,
\end{aligned}$$

and

$$\begin{aligned}
\frac{\partial H_N(x_i,t)}{\partial t} = \; & -\frac{1}{\mu}\frac{\partial E_{N-1}(x,t)}{\partial x}|_{x=x_i} \\
& -\tau\frac{1}{\mu}(P_{N+1}(x)+P_N(x))'|_{x=x_i}(H_N(1,t)-h_1(t)) \\
& -\tau\frac{1}{\mu}\frac{(P_{N+1}(x)-P_N(x))'}{P_{N+1}(-1)}(H_N(-1,t)-h_{-1}(t)) \;, \\
& \quad i=0,\ldots,N \;.
\end{aligned} \tag{5.26}$$

The Chebyshev-Legendre method (5.26) is stable in the usual L_2 norm, as shown in the following theorem.

Theorem 5.4.1 *(The L_2 Stability of the CL method). Let $E_{N-1}(x,t)$ and $H_N(x,t)$ be the solution of (5.26). Then the staggered Chebyshev-Legendre method is stable in the L_2 norm, that is*

$$\begin{aligned} &\epsilon \int_{-1}^{1} E_N^2(x,t)dx + \mu \int_{-1}^{1} H_N^2(x,t)dx \\ &\leq \epsilon \int_{-1}^{1} E_N^2(x,0)dx + \mu \int_{-1}^{1} H_N^2(x,0)dx \ . \end{aligned} \tag{5.27}$$

as long as $\tau \geq 0$

Proof: First note that from (5.26) we have

$$\left\{ \begin{aligned} \frac{\partial E_{N-1}(x,t)}{\partial t} = & -\frac{1}{\epsilon}\frac{\partial H_N(x,t)}{\partial x} + \frac{1}{2}\frac{1}{\epsilon}(P_N(x)+P_{N-1}(x))'(H_N(1,t)-h_1(t)) \\ & +\frac{1}{2}\frac{1}{\epsilon}\frac{(P_N(x)-P_{N-1}(x))'}{P_N(-1)}(H_N(-1,t)-h_{-1}(t)) \ , \\ \frac{\partial H_N(x,t)}{\partial t} = & -\frac{1}{\mu}\frac{\partial E_{N-1}(x,t)}{\partial x} \\ & -\tau\frac{1}{\mu}(P_{N+1}(x)+P_N(x))'(H_N(1,t)-h_1(t)) \\ & -\tau\frac{1}{\mu}\frac{(P_{N+1}(x)-P_N(x))'}{P_{N+1}(-1)}(H_N(-1,t)-h_{-1}(t)) \end{aligned} \right. \tag{5.28}$$

This is because both sides of the equations in (5.26) are polynomials of degree $\leq N-1$ and $\leq N$ that agree at N Gauss points and $N+1$ Gauss-Lobatto points respectively.

For simplicity, we only need to prove for $h_1(t) = h_{-1}(t) = 0$. Now multiply both sides of the two equations in (5.28) by $\epsilon E_{N-1}(x,t)$ and $\mu H_N(x,t)$ respectively and integrate from -1 to 1. After we add the left and right hand sides respectively, we get the following equality:

$$\begin{aligned} &\frac{1}{2}(\epsilon\frac{d}{dt}\int_{-1}^{1} E_{N-1}^2(x,t)dx + \mu\frac{d}{dt}\int_{-1}^{1} H_N^2(x,t)dx = \\ &-\int_{-1}^{1} E_{N-1}(x,t)\frac{\partial H_N(x,t)}{\partial x}dx - \int_{-1}^{1} H_N(x,t)\frac{\partial E_{N-1}(x,t)}{\partial x}dx \\ &+\frac{1}{2}H_N(1,t)\int_{-1}^{1}(P_N(x)+P_{N-1}(x))'E_{N-1}(x,t)dx \\ &-\frac{1}{2}H_N(-1,t)\int_{-1}^{1}\frac{(P_N(x)-P_{N-1}(x))'}{P_N(-1)}E_{N-1}(x,t)dx \\ &-\frac{1}{2}H_N(1,t)\int_{-1}^{1}(P_{N+1}(x)+P_N(x))'H_N(x,t)dx \\ &-\frac{1}{2}H_N(-1,t)\int_{-1}^{1}\frac{(P_{N+1}(x)-P_N(x))'}{P_{N+1}(-1)}H_N(x,t)dx \end{aligned} \quad . \tag{5.29}$$

Now we integrate by part:

$$
\begin{aligned}
\frac{1}{2}\int_{-1}^{1}(P_N(x)+P_{N-1}(x))'E_N(x,t)dx &= \frac{1}{2}(P_N(x)+P_{N-1}(x))E_N(x,t)|_{-1}^{1} \\
&-\frac{1}{2}\int_{-1}^{1}(P_N(x)+P_{N-1}(x))\frac{\partial E_N(x,t)}{\partial x}dx \\
&= E_N(1,t)\ .
\end{aligned}
\tag{5.30}
$$

The last step holds because $\frac{\partial E_{N-1}(x,t)}{\partial x}$ is a polynomial of degree $N-1$ and hence orthogonal to $P_{N+1}(x)$ and $P_N(x)$.

Similarly we have

$$
\frac{1}{2}\int_{-1}^{1}\frac{(P_N(x)-P_{N-1}(x))'}{P_N(-1)}E_{N-1}(x,t)dx = E_{N-1}(-1,t)\ , \tag{5.31}
$$

$$
\int_{-1}^{1}(P_{N+1}(x)+P_{N-1}(x))'H_N(x,t)dx = 2H_N(1,t)\ , \tag{5.32}
$$

$$
\int_{-1}^{1}\frac{(P_{N+1}(x)-P_N(x))'}{P_{N+1}(-1)}H_N(x,t)dx = 2H_N(-1,t)\ . \tag{5.33}
$$

So (5.29) becomes

$$
\begin{aligned}
&\frac{1}{2}(\epsilon\frac{d}{dt}\int_{-1}^{1}E_N^2(x,t)dx+\mu\frac{d}{dt}\int_{-1}^{1}H_N^2(x,t)dx) \\
&= -\int_{-1}^{1}E_{N-1}(x,t)\frac{\partial H_N(x,t)}{\partial x}dx - \int_{-1}^{1}H_N(x,t)\frac{\partial E_{N-1}(x,t)}{\partial x}dx \\
&+E_{N-1}(1,t)H_N(1,t)-E_{N-1}(-1,t)H_N(-1,t) \\
&\quad -2\tau H_N^2(1,t)-2\tau H_N^2(1,t) \\
&= -2\tau H_N^2(1,t)-2\tau H_N^2(-1,t) \\
&\leq 0
\end{aligned}
\tag{5.34}
$$

as long as

$$
\tau \leq 0\ . \tag{5.35}
$$

□

Remark 5.4.1 *Note that we only use the boundary values of $H(x,t)$ to enforce the penalty term according to the situation of the staggered mesh we use.*

5.4.2 Impose Boundary Condition with Penalty Method

We know that the previous penalty method does not satisfy the boundary condition exactly, but does in the limit as $N \to \infty$. In this section we will give a Chebyshev-Legendre method that does satisfy the boundary condition.

In the Chebyshev-Legendre boundary condition imposed method for the staggered mesh we seek a polynomial $E_{N-1}(x,t)$ of degree $N-1$ and a polynomial $H_N(x,t)$ of degree N in x that satisfy

$$\begin{cases} \dfrac{\partial E_{N-1}(y_j,t)}{\partial t} = & -\dfrac{1}{\epsilon}\dfrac{\partial H_N(x,t)}{\partial x}|_{x=y_j} \ , \qquad j=0,\ldots,N-1 \ , \\ \dfrac{\partial H_N(x_i,t)}{\partial t} = & -\dfrac{1}{\mu}\dfrac{\partial E_{N-1}(x,t)}{\partial x}|_{x=x_i} \\ & +\dfrac{(P_{N+1}(x)+P_N(x)\frac{P'_{N+1}(1)}{P'_N(1)})'|_{x=x_i}}{2P'_{N+1}(1)}(\dfrac{1}{\mu}\dfrac{\partial E_{N-1}(1,t)}{\partial x}+h'_1(t)) \\ & +\dfrac{(P_{N+1}(x)+P_N(x)\frac{P'_{N+1}(-1)}{P'_N(-1)})'|_{x=x_i}}{2P'_{N+1}(-1)}(\dfrac{1}{\mu}\dfrac{\partial E_{N-1}(-1,t)}{\partial x}+h'_{-1}(t)) \ , \\ & \quad i=0,\ldots,N \ . \end{cases} \tag{5.36}$$

The Chebyshev-Legendre method (5.36) is stable in the usual L_2 norm, as can be shown in the following theorem.

Lemma 5.4.1 *Suppose $h_1(t)=h_{-1}(t)=0$, we have*

$$H_N(1,t) = H_N(-1,t) = 0 \ . \tag{5.37}$$

Proof: Note that

$$\frac{(P_{N+1}(x)+P_N(x)\frac{P'_{N+1}(1)}{P'_N(1)})'}{2P'_{N+1}(1)} = \begin{cases} 1 \ , & x=1 \\ 0 \ , & x=-1 \end{cases} \tag{5.38}$$

and

$$\frac{(P_{N+1}(x)+P_N(x)\frac{P'_{N+1}(-1)}{P'_N(-1)})'}{2P'_{N+1}(-1)} = \begin{cases} 0\ , & x=1 \\ 1\ , & x=-1 \end{cases} \quad . \tag{5.39}$$

From (5.36) it is clear that (5.37) holds. □

Theorem 5.4.2 *(The L_2 Stability of the CL method). Let $E_{N-1}(x,t)$ and $H_N(x,t)$ be the solution of (5.36).Then the staggered Chebyshev-Legendre method is stable in the L_2 norm, that is*

$$\begin{aligned} &\epsilon\int_{-1}^{1} E_{N-1}^2(x,t)dx+\mu\int_{-1}^{1} H_N^2(x,t)dx \\ &=\epsilon\int_{-1}^{1} E_{N-1}^2(x,0)dx+\mu\int_{-1}^{1} H_N^2(x,0)dx\ . \end{aligned} \tag{5.40}$$

Proof: It follows from (5.36) that:

$$\begin{cases} \dfrac{\partial E_{N-1}(x,t)}{\partial t} = & -\dfrac{1}{\epsilon}\dfrac{\partial H_N(x,t)}{\partial x}\ , \\ \dfrac{\partial H_N(x,t)}{\partial t} = & -\dfrac{1}{\mu}\dfrac{\partial E_{N-1}(x,t)}{\partial x} \\ & +\dfrac{(P_{N+1}(x)+P_N(x)\frac{P'_{N+1}(1)}{P'_N(1)})'}{2P'_{N+1}(1)}(\dfrac{1}{\mu}\dfrac{\partial E_{N-1}(1,t)}{\partial x}+h'_1(t)) \\ & +\dfrac{(P_{N+1}(x)+P_N(x)\frac{P'_{N+1}(-1)}{P'_N(-1)})'}{2P'_{N+1}(-1)}(\dfrac{1}{\mu}\dfrac{\partial E_{N-1}(-1,t)}{\partial x}+h'_{-1}(t)) \end{cases} \quad . \tag{5.41}$$

This is because both sides of the equations in (5.36) are polynomials of degree $\leq N-1$ and $\leq N$ that agree at the N Gauss points and N+1 Gauss-Lobatto points respectively.

For simplicity, we prove for $h_1(t)=h_{-1}(t)=0$. Multiply both sides of the two equations in (5.41) by $\epsilon E_{N-1}(x,t)$ and $\mu H_N(x,t)$ respectively and integrate from -1 to 1. After we add the left and right hand sides respectively, we get the following equality:

$$
\begin{aligned}
&\frac{1}{2}(\epsilon\frac{d}{dt}\int_{-1}^{1}E_{N-1}^2(x,t)dx+\mu\frac{d}{dt}\sum_{-1}^{1}H_N^2(x,t)dx)= \\
&-\int_{-1}^{1}E_{N-1}(x,t)\frac{\partial H_N(x,t)}{\partial x}dx-\int_{-1}^{1}H_N(x,t)\frac{\partial E_{N-1}(x,t)}{\partial x}dx \\
&+\int_{-1}^{1}\frac{(P_{N+1}(x)+P_N(x)\frac{P'_{N+1}(1)}{P'_N(1)})'}{2P'_{N+1}(1)}H_N(x)dx\times(\ldots) \\
&+\int_{-1}^{1}\frac{(P_{N+1}(x)+P_N(x)\frac{P'_{N+1}(-1)}{P'_N(1)})'}{2P'_{N+1}(-1)}H_N(x)dx\times(\ldots) \\
&=0\ .
\end{aligned}
\tag{5.42}
$$

if we integrate by parts, use (5.37) and note that $\frac{\partial H_N(x)}{\partial x}$ is orthogonal to $P_{N+1}(x)$ and $P_N(x)$. □

Remark 5.4.2 *If $h_1(t)=h_{-1}(t)=0$, we know that the boundary condition is indeed satisfied for this method. And for $h_1(t)=h_{-1}(t)\neq 0$, we know from (5.36) that on the boundary points, the values of $H(x,t)$ in numerical computation will be the numerical solution of*

$$
\frac{dh_{1,-1}(t)}{dt}=h'_{1,-1}(t) \tag{5.43}
$$

which depends only on the time integration method used.

5.5 Numerical Experiments

Consider 1-D Maxwell's equation

$$
\begin{cases}
\dfrac{\partial E}{\partial t}=-\epsilon c\dfrac{\partial H}{\partial x} \\
\dfrac{\partial H}{\partial t}=-\mu c\dfrac{\partial E}{\partial x}
\end{cases}
\tag{5.44}
$$

with the initial condition

$$
\begin{aligned}
E(x,0)&=-e^{\sin(2\pi x)}\ , \\
H(x,0)&=\sqrt{\frac{\epsilon}{\mu}}e^{\sin(2\pi x)}\ .
\end{aligned}
\tag{5.45}
$$

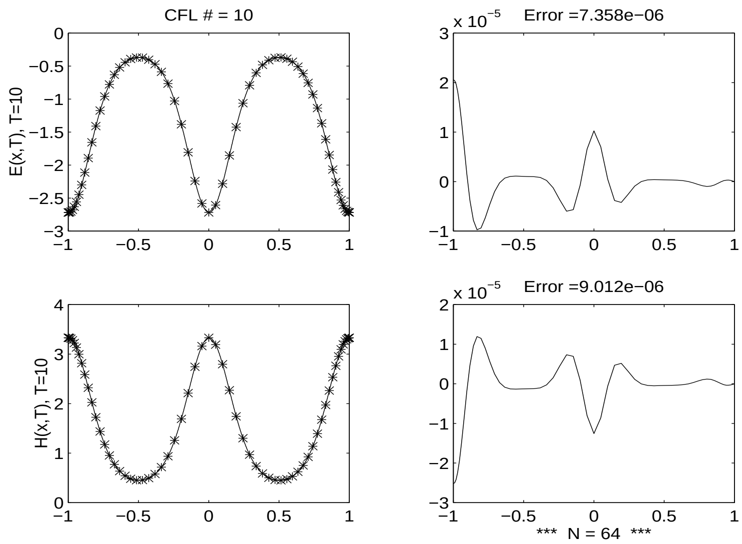

Figure 5.1: The numerical solution and error at $T = 10$ of 1-D Maxwell's equations using the new Chebyshev penalty method ($\tau = 1/2$).

We have the following exact solution:

$$
\begin{aligned}
E(x,t) &= -e^{\sin(2\pi(\sqrt{\epsilon\mu}ct+x))} \quad , \\
H(x,t) &= \sqrt{\frac{\epsilon}{\mu}}e^{\sin(2\pi(\sqrt{\epsilon\mu}ct+x))} \quad .
\end{aligned}
\tag{5.46}
$$

We will use the exact solution to impose the boundary condition along incoming characteristic. Thus we are indeed solving two scalar hyperbolic equations. One has positive eigenvalue $\sqrt{\epsilon\mu}$ and the other has negative eigenvalue $-\sqrt{\epsilon\mu}$. We will use third order R-K scheme for time integration. In computation, take $\epsilon = 2,\ \mu = 1,\ c = 1$. We take the time step as $\Delta t = \frac{CFL\ Number}{N^2}$ where N is the number of modes.

In numerical computation it is verified that the method (5.11) is stable as long as $\tau \geq \frac{1}{2}$. Accurate numerical results are given in Fig. (5.1) and Fig. (5.2).

Numerical experiments that validate the staggered Chebyshev-Legendre methods are also presented. Numerical stability of the methods is verified in the experiments.

The results of the staggered Chebyshev-Legendre method (SCL) is given in Fig. 5.3. And the results of the staggered boundary-condition-imposed Chebyshev-Legendre method (BSCL) is given in Fig. 5.4. Though the accuracy of the results of the staggered methods is satisfying, it is not any

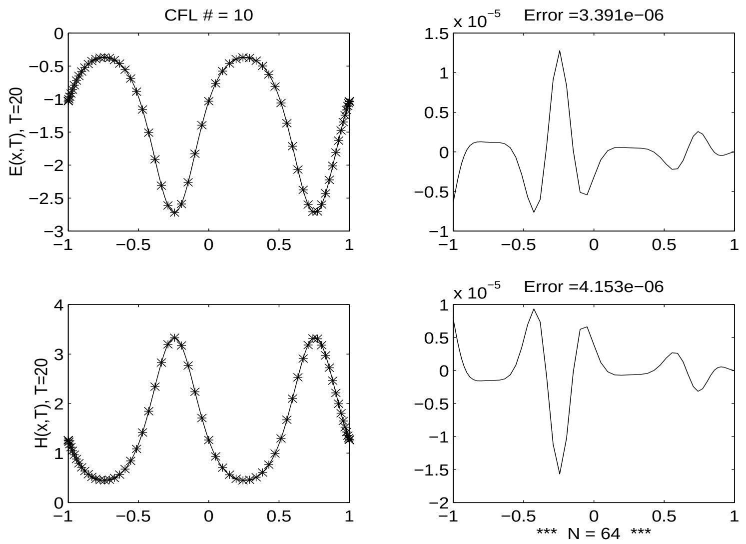

Figure 5.2: The numerical solution and error at $T = 20$ of 1-D Maxwell's equations using the new Chebyshev penalty method ($\tau = 1/2$).

better than those of the non-staggered methods. For the staggered methods, the time step we can use is a little smaller than that for the non-staggered methods. These observations are in line with our analysis in chapter 4. In our numerical experiments, the penalty methods pose no restriction on the time step compared with those methods that impose (characteristic) boundary condition strictly.

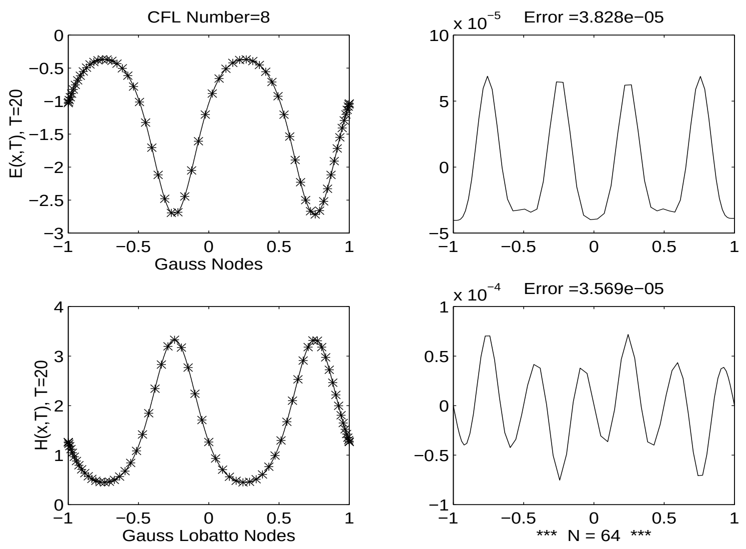

Figure 5.3: The numerical solution and error at $T = 20$ of 1-D Maxwell's equations using the new staggered Chebyshev-Legendre penalty method.

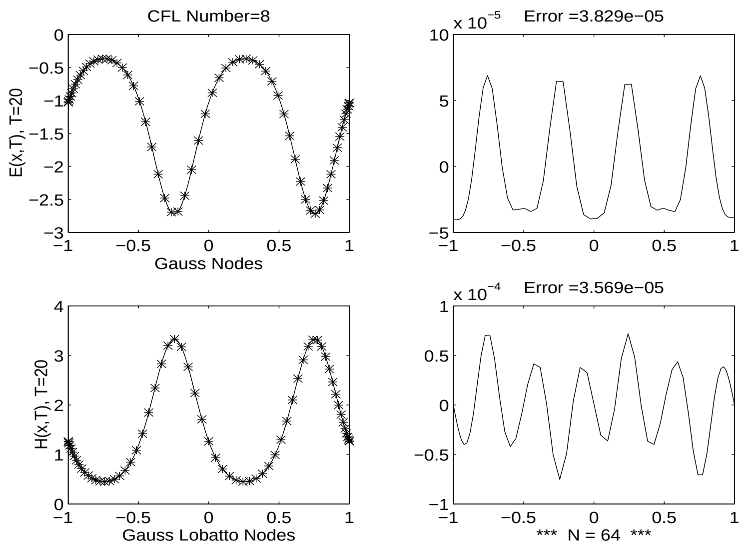

Figure 5.4: The numerical solution and error at $T = 20$ of 1-D Maxwell's equations using the staggered Chebyshev penalty method where the boundary condition is imposed strictly.

Chapter 6

Simulations of 2-D Electromagnetic Scattering

6.1 Introduction

The FD-TD method suffers from the requirement of having 10-20 grid points per wavelength to obtain sufficiently accurate solutions of the scattered fields. Indeed, in cases of transient excitation of the scatterer one must often use a significantly denser grid. These requirements inhibit the use of FD-TD methods for accurately computing electromagnetic scattering by electrically large objects and transient phenomena.

Using spectral methods for the solution of scattering problems promises a very significant decrease in the required number of grid points compared to FD-TD methods while maintaining the accuracy in time and space. Indeed, our analysis in chapter 2 suggests that spectral methods are very well suited for the simulation of electrically large or transient problems in electromagnetics ([42], [25]).

One of the most important problems in computational electromagnetics is the issue of obtaining solutions of infinite domain problems from finite domain numerical computations. The truncation of the computational domain introduces an artificial boundary and the crucial issue is how to design absorbing boundary conditions (ABC) such that outgoing waves are absorbed without reflections which may otherwise re-enter the domain and falsify the computational results. In this chapter, we test and compare several different ABC's.

The characteristic type ABC, requiring the incoming characteristic variable to vanish at the boundary, has often been used with high order methods. In [30], Kabakian proposed a single-domain spectral algorithm for electromagnetic wave scattering, using characteristic type boundary condition and satisfying results at earlier stages of the time integration (5-6 wave periods) were presented. However, we shall show that applying a characteristic type boundary condition causes significant reflections at the outer boundary, unless the outer boundary is put very far away from the scatter, i.e. at a distance of 12-20 wavelengths from the scatter.

As a very attractive alternative to the characteristic ABC, Berenger [3] proposed a perfectly matched layer (PML) method for reflectionless truncation of FD-TD wave simulations, as introduced in chapter 3 with many extensions. The PML methods are given in 3-D. However, one can reduce the methods to 2-D Cartesian and polar coordinates. In this chapter, we will give the formulations of the 2-D PML methods and present extensive numerical results that validate these methods. In particular, we present a generalization of the rectangular PML method to polar coordinates which differs from those proposed in previous works ([44], [41] and [51]). This new polar PML is shown to admit plane wave solutions that match at the circular vacuum-layer interface, while decaying in any angle of propagation inside the layer [56].

An alternative way of applying the matched layer (ML) method, involving a grid mapping and the use of high order filtering, is considered in this chapter too. The mapped ML method have the advantage that, unlike the PML methods, one only needs to solve Maxwell's equations with additional absorbing terms.

The presentation of our 2-D simulations of electromagnetic scattering from infinite cylinders are composed of two parts. In the first part, we use the Fourier-Chebyshev method to simulate scattering from circular and elliptic cylinders. In the second part, we use the Chebyshev-Chebyshev method to simulate scattering from circular and rectangular cylinders with the numerical scheme being designed for simulating cylinders of more general shapes. The purpose of our numerical experiments is to show the importance of using spectral methods in computational electromagnetics and using modern absorbing layer methods as ABC's. For this purpose, in addition to presenting the numerical results of the proposed methods, we shall also show computational results of the Finite-Difference-Time-Domain (FD-TD) method with the rectangular PML method and the pseudospectral method with the characteristic boundary condition for comparison with our proposed methods.

In the first part of our numerical experiments, we use a multi-domain Fourier-Chebyshev method. The scheme is primarily developed for accurate computation of scattering by simple two-dimensional objects and utilizes a Fourier collocation method in the azimuthal direction and a multi-domain Chebyshev collocation method in the radial direction. We emphasize on showing the advantage of spectral method over the FD-TD method and the advantage of the proposed absorbing layer methods, including the split-field PML and the mapped ML method, over characteristic type absorbing boundary condition.

In simulations of wave scattering by PEC circular cylinders, we give a direct implementation of the original rectangular PML method in the circular computational domain. It is compared with the mapped ML method and the polar PML method. Although the direct implementation of the rectangular PML method in the circular computational domain gives much better results than the characteristic type ABC method does, which suggests that the PML layer that is not conformal to the computational mesh is still effective, yet it is inferior to the new polar PML method, which yields the most accurate result, by more than an order of magnitude. In simulations of wave scattering by PEC elliptic cylinders, the polar PML method is not yet applicable and the ML method is shown to yield satisfying results.

The main purpose of the second part of our numerical experiments is to compare different PML methods. The numerical scheme we use for these experiments is a multidomain Chebyshev-Chebyshev method, where a general 2-D multi-domain decomposition method is applied in the outer domain of a scatterer of a general shape.

Here the requirement for complex absorbing boundary conditions highlights yet another advantage of this multi-domain approach as we may simply dedicate the outer subdomains to deal with such boundary conditions. Whether we need to solve equations different from Maxwell's equations, as in the PML methods, or we need to modify the equations with absorbing terms, as in the ML methods, everything is done locally in the out-most subdomain. In the FD-TD implementation of the rectangular PML method [3], a small amount of numerical reflection at the vacuum-layer interface was observed. However, in a multi-domain approach, derivatives are not computed across the vacuum-layer interface, thereby reducing the numerical reflections significantly.

6.2 The Equations

In this chapter we consider the two-dimensional transverse magnetic (TM) mode. The free-space non-dimensionalized Maxwell's equations in 2-D for the TM case is:

$$\frac{\partial W}{\partial t} = A\frac{\partial W}{\partial x} + B\frac{\partial W}{\partial y} \ , \tag{6.1}$$

where $W = (H_x,\ H_y,\ E_z)^T$ and

$$A = \begin{pmatrix} 0 & 0 & 0 \\ 0 & 0 & 1 \\ 0 & 1 & 0 \end{pmatrix} , \quad B = \begin{pmatrix} 0 & 0 & -1 \\ 0 & 0 & 0 \\ -1 & 0 & 0 \end{pmatrix} . \tag{6.2}$$

In general curvilinear coordinates the system (6.1) becomes

$$\frac{\partial \hat{W}}{\partial t} = \frac{\partial \hat{F}}{\partial \xi} + \frac{\partial \hat{G}}{\partial \eta} = \hat{A}\frac{\partial \hat{W}}{\partial \xi} + \hat{B}\frac{\partial \hat{W}}{\partial \eta} \ , \tag{6.3}$$

where $\hat{W} = JW$ with J being the transformation Jacobian

$$J = x_\xi y_\eta - x_\eta y_\xi \ ,$$

while

$$\hat{F} = J \begin{pmatrix} -\xi_y E_z \\ \xi_x E_z \\ \xi_x H_y - \xi_y H_x \end{pmatrix}, \quad \hat{G} = J \begin{pmatrix} -\eta_y E_z \\ \eta_x E_z \\ \eta_x H_y - \eta_y H_x \end{pmatrix}, \tag{6.4}$$

leading to

$$\hat{A} = \frac{\partial \hat{F}}{\partial \hat{W}} = \begin{pmatrix} 0 & 0 & -\xi_y \\ 0 & 0 & \xi_x \\ -\xi_y & \xi_x & 0 \end{pmatrix}, \quad \hat{B} = \frac{\partial \hat{G}}{\partial \hat{W}} = \begin{pmatrix} 0 & 0 & -\eta_y \\ 0 & 0 & \eta_x \\ -\eta_y & \eta_x & 0 \end{pmatrix}. \tag{6.5}$$

We show how to diagonalize $\hat{A}$ in the η-direction. It is similar in the ξ-direction. We assume that $\eta_x^2 + \eta_y^2 = 1$ such that the eigenvalues of matrix $\hat{A}$ are:

$$\lambda_1 = 0, \ \lambda_2 = -1, \ \text{and} \ \lambda_3 = 1 \ , \tag{6.6}$$

and we observe that $\hat{A}$ can be diagonalized as

$$S^T \hat{A} S = \Lambda = \begin{pmatrix} 0 & 0 & 0 \\ 0 & -1 & 0 \\ 0 & 0 & 1 \end{pmatrix}, \quad S = \begin{pmatrix} \eta_x & \frac{\eta_y}{\sqrt{2}} & -\frac{\eta_y}{\sqrt{2}} \\ \eta_y & -\frac{\eta_x}{\sqrt{2}} & \frac{\eta_x}{\sqrt{2}} \\ 0 & \frac{1}{\sqrt{2}} & \frac{1}{\sqrt{2}} \end{pmatrix}.$$

The characteristic variables, $S^T W$, are needed for applying characteristic boundary condition.

6.3 The Computational Schemes

6.3.1 Fourier-Chebyshev Scheme

Our first set of experiments involves the simulations of electromagnetic wave scattering by circular and elliptic cylinders. For this geometry it is natural to use a multi-domain Fourier-Chebyshev collocation method. The solution is periodic in the azimuthal direction, denoted by ξ and the Fourier collocation method is suitable in this direction. The Chebyshev collocation method is used in the radial direction, denoted by η. Take circular cylinders as an example, we can easily map the computational domain into $[0, 2\pi] \times [-1, 1]$. Approximation in $[0, 2\pi] \times [-1, 1]$ is done using tensor products of interpolating Lagrange trigonometric polynomials based on the Fourier collocation points and interpolating Lagrange polynomials based on the Chebyshev Gauss-Lobatto collocation points. Hence, we seek solutions to Eq.(6.3) of the form

$$\mathcal{I}_{M,N}\boldsymbol{q}(x,y) = \sum_{i=0}^{M}\sum_{j=0}^{N} \boldsymbol{q}(x(\xi_i,\eta_j), y(\xi_i,\eta_j))L_i^F(\xi(x,y))L_j^T(\eta(x,y)) \ ,$$

where $L_i^F(\xi)$ corresponds to the interpolating Lagrange trigonometric polynomials based on the Fourier collocation points in ξ and $L_j(\eta)$ corresponds to the interpolating Lagrange polynomials based on the Chebyshev Gauss-Lobatto collocation points in η.

For the temporal discretization, a third or fourth order Runge-Kutta method is used. High order filtering, multi-domain decomposition technique and a cubic grid mapping technique are also employed. For a review of these numerical ingredients, one can go back to see chapter 2. Here the multi-domain decomposition method is applied in the radial direction to allow for the implementation of various types of absorbing boundary conditions in the out-most subdomain and to decrease the computational workload. At the interface of any two subdomains, which is a circle, the characteristic relations are used to patch the field values as introduced in chapter 2. The detail of the procedure will be explained shortly.

At the scatter surface, a characteristic type boundary condition is applied. Due to the fact that E_z field is known at the surface, we impose the exact boundary condition for E_z and apply the type of boundary treatments outlined for linear hyperbolic systems by Gottlieb et al. [23], i.e. , use the characteristic relations to recover the other field values.

6.3.2 Chebyshev-Chebyshev Scheme

If we consider a more general structure, the Fourier-Chebyshev method may not be applicable. In the second set of numerical computations we develop a general 2-D multi-domain scheme applying the Chebyshev-Chebyshev method.

Here we want to seek solutions to Eq.(6.3) in the general domain $\Omega \subset \mathsf{R}^2$, enclosed by the boundary, $\delta\Omega$. To obtain such solutions we employ polynomial expansions to approximate the unknown functions and their spatial derivatives through the use of tensor products. Like in the procedure in 3-D (chapter 2), we construct Ω using K non-overlapping general quadrilaterals, $\mathsf{D}^k \subset \mathsf{R}^2$, such that $\Omega = \bigcup_{k=1}^{K} \mathsf{D}^k$.

To apply the tensor product formulation we require that there exists a diffeomorphism, $\Psi : \mathsf{D} \to \mathsf{I}$, where $\mathsf{I} \subset \mathsf{R}^2$ is the unit square, i.e., $\mathsf{I} \in [-1,1]^2$. At this point we have the Cartesian coordinates, $(x,y) \in \mathsf{D}$, and the general curvilinear coordinates, $(\xi,\eta) \in \mathsf{I}$, related through the map, $(x,y) = \Psi(\xi,\eta)$. The map, $\Psi : \mathsf{D} \to \mathsf{I}$, plays an important role in the application of polynomial methods to problems in general geometries. To establish a one to one correspondence between the unit square and the general quadrilateral we construct the global map using transfinite blending functions. We refer to [28] or chapter 2 for a thorough account of this procedure.

Once the global map, Ψ, has been constructed, we may compute the metric of the mapping, the corresponding transformation Jacobian and outward pointing normal vectors at all points of the enclosing edges of the quadrilateral.

Approximation in I is done by a standard pseudospectral method using tensor products of interpolating Lagrange polynomials based on the Chebyshev Gauss-Lobatto quadrature points. Hence, we seek solutions to Eq.(6.3) of the form

$$\mathcal{I}_N \boldsymbol{q}(x,y) = \sum_{i=0}^{N} \sum_{j=0}^{N} \boldsymbol{q}(x(\xi_i,\eta_j), y(\xi_i,\eta_j)) L_i^T(\xi(x,y)) L_j^T(\eta(x,y)) \ ,$$

where $L_i^T(\xi)$ and $L_j^T(\eta)$ correspond to the interpolating Lagrange polynomials based on the Chebyshev Gauss-Lobatto quadrature points in ξ and η, respectively. We refer to [28] for a thorough discussion of multi-domain solution of wave dominated problems using spectral methods.

Within this setting we need to solve K independent problems, Eq.(6.3), in the individual subdomains. However, to obtain the global solution we have to pass information between the subdomains in a way consistent with the dynamics of Maxwell equations. Since these equations constitute a hyperbolic system it is natural to transfer information between the various subdomains using the characteristic variables as introduced in chapter 2, the detail of which will be given shortly.

On the surface of the scatterer, we apply the same kind of treatment as that for the Fourier-Chebyshev method. We impose the exact boundary condition for E_z and use the characteristic variables to recover the remaining field values.

6.3.3 Multidomain Patching

For both the Fourier-Chebyshev and the Chebyshev-Chebyshev scheme we developed, we need to patch solutions at subdomain interfaces. Let us consider two neighboring subdomains and also introduce the corresponding characteristic variables, $\boldsymbol{Q}_{\eta,1} = (Q^0_{\eta,1}, Q^-_{\eta,1}, Q^+_{\eta,1})^T$ and $\boldsymbol{Q}_{\eta,2} = (Q^0_{\eta,2}, Q^-_{\eta,2}, Q^+_{\eta,2})^T$, referring to the three characteristic variables in domain 1 and 2. Here Q^0_η represents the non-propagating characteristic, while Q^-_η and Q^+_η refers to the incoming and outgoing characteristic variable along $\nabla\eta$, respectively, as decided using the convective speeds of propagation of the characteristic variables, i.e. the diagonal entries of Λ.

Following the patching procedure introduced in chapter 2, the proper boundary conditions at the interface of the two subdomains are obtained as

$$Q^-_{\eta,1} = Q^+_{\eta,2} \quad , \quad Q^-_{\eta,2} = Q^+_{\eta,1} \quad ,$$

where the right-hand-side of the equations signifies computed values and the left-hand-side refers to the sought after boundary conditions. The non-propagating characteristic variables, $Q^0_{\eta,1}$ and $Q^0_{\eta,2}$ are enforced to be continuous across the interface, while the outgoing characteristic variables, $Q^+_{\eta,1}$ and $Q^+_{\eta,2}$, are preserved in each subdomain. The actual field values at the interfaces are then obtained by multiplying the updated characteristic variables with S. A similar procedure is applied along the other edge in the η-direction and for Chebyshev-Chebyshev method, also the edges in the ξ-direction, if necessary.

6.4 Absorbing Boundary Conditions for Maxwell's Equations

We have applied various absorbing boundary conditions with the Fourier-Chebyshev method and the Chebyshev-Chebyshev method.

6.4.1 The Characteristic and the ML Methods

The characteristic type boundary condition is used with spectral methods in many applications. It can also be used as an absorbing boundary condition by just imposing the incoming characteristic variable to be zero. The following example illustrate the shortcoming of this approach.

Consider the plane wave solutions of the non-dimensional Maxwell's equations, Eq. (6.1):

$$\begin{cases} H_x = \quad \sin\phi e^{i\omega(t - x\cos\phi - y\sin\phi)} \\ H_y = -\cos\phi e^{i\omega(t - x\cos\phi - y\sin\phi)} \\ E_z = e^{i\omega(t - x\cos\phi - y\sin\phi)} \end{cases} , \tag{6.7}$$

with ϕ being the angle of propagation of the plane wave.

For a circular exterior boundary, one applies the characteristic boundary conditions by enforcing the incoming characteristic variable to be zero:

$$\sin\theta H_x - \cos\theta H_y + E_z = 0 \ . \tag{6.8}$$

For the plane wave solutions, Eq. (6.7), we have

$$\sin\theta H_x - \cos\theta H_y + E_z = (1 - \cos(\theta - \phi))e^{i\omega(t - x\cos\phi - y\sin\phi)} \ . \tag{6.9}$$

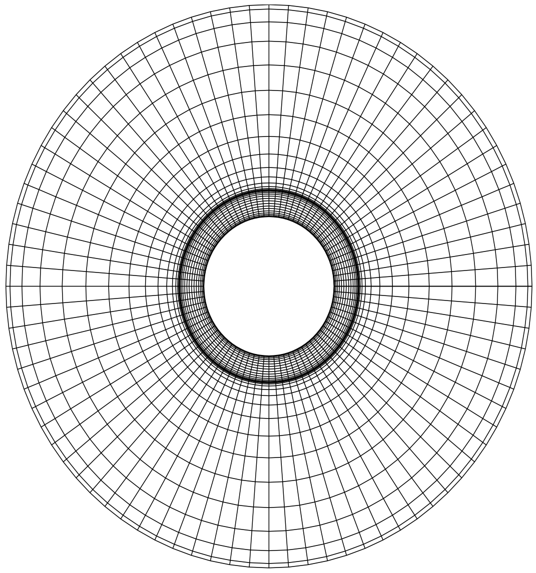

Figure 6.1: An explanatory circular mesh that uses a cubic grid mapping in the radial direction.

This boundary condition is exact only if $\theta = \phi$, i.e. when the plane wave propagates perpendicular to the exterior boundary. The error in applying the characteristic type boundary condition is $O((\theta - \phi)^2)$.

One solution to this problem is to apply the multi-domain approach and push the outer boundary of the out-most subdomain away from the scatter. If r is large enough, the solution of electromagnetic wave scattering problems will be composed of plane waves with local direction $\phi \approx \theta$. In the multi-domain formulation we use a cubic grid mapping for the Chebyshev grid in the radial direction. Thus the grid in the radial direction transits gradually from fine to coarse away from the scatter as illustrated in Fig. 6.1. The grid becomes so coarse near the outer boundary that the π points per wavelength rule [22] is violated. We find that it is necessary to apply a high order filter (Eq. (2.30), with the order of the filter m being close to N) following each time integration step.

A better method is to combine the matched layer (ML) method with the grid mapping and the high order filtering technique. The ML method solves the non-dimensional Maxwell's equations in the absorbing medium:

$$\frac{\partial W}{\partial t} = A\frac{\partial W}{\partial x} + B\frac{\partial W}{\partial y} - f(x,y)W \ , \tag{6.10}$$

where $f(x, y) \geq 0$ in the layer and $f(x, y) = 0$ at the vacuum-layer interface. The ML layer is put in the out-most subdomain at some distance from the subdomain interface and the cubic grid mapping is used to generate a mesh that is coarse in the part of the outer subdomain covered by the ML layer. Since a coarse mesh is used there, the number of grid points per wavelength decreases, and hence the frequency of waves propagating into that area will increase. With the help of a low pass filter, the reflections in the ML region, being of high frequency relative to the local grid, will be filtered out. The position of the ML layer, the conductivity profile of the layer (usually $2nd$ to $4th$ order) and the cubic grid mapping can be tuned to reduce the reflections from the layer.

6.4.2 Comparison of PML Methods

In chapter 3 we introduced both the split-field and the well-posed PML methods in various coordinates in 3-D. These methods can be reduced to 2-D Cartesian and polar coordinate system, which is applied in our 2-D simulations. In the following we shall briefly discuss different formulations and implementations of the PML methods that shall provide the basis for the comparative studies in the subsequent section.

The Rectangular PML Method

In [3], Berenger proposed a PML method in rectangular coordinates. We present it here with some simple modifications. Consider the non-dimensional PML type equations with spatially varying absorbing terms:

$$\left\{\begin{aligned} \frac{\partial H_x}{\partial t} &= -\frac{\partial(E_{zx}+E_{zy})}{\partial y} - \sigma_y(y)H_x \\ \frac{\partial H_y}{\partial t} &= \frac{\partial(E_{zx}+E_{zy})}{\partial x} - \sigma_x(x)H_y \\ \frac{\partial E_{zx}}{\partial t} &= \frac{\partial H_y}{\partial x} - \sigma_x(x)E_{zx} \\ \frac{\partial E_{zy}}{\partial t} &= -\frac{\partial H_x}{\partial y} - \sigma_y(y)E_{zy} \end{aligned}\right. , \tag{6.11}$$

where $\sigma_x(x)$ and $\sigma_y(y)$ are functions of x and y, respectively. Formally, we have the following plane wave solutions to the above PML type equations:

$$\begin{cases} H_x = & \sin\phi e^{i\omega(t-x\cos\phi-y\sin\phi)} e^{-\sigma_x(x)\cos\phi-\sigma_y(y)\sin\phi} \\ H_y = & -\cos\phi e^{i\omega(t-x\cos\phi-y\sin\phi)} e^{-\sigma_x(x)\cos\phi-\sigma_y(y)\sin\phi} \\ E_{zx} = & \cos^2\phi e^{i\omega(t-x\cos\phi-y\sin\phi)} e^{-\sigma_x(x)\cos\phi-\sigma_y(y)\sin\phi} \\ E_{zy} = & \sin^2\phi e^{i\omega(t-x\cos\phi-y\sin\phi)} e^{-\sigma_x(x)\cos\phi-\sigma_y(y)\sin\phi} \end{cases} . \tag{6.12}$$

It is important that the solution is continuous across the interface between the free space region and the PML region. This dictates that $\sigma_x(x)$ and $\sigma_y(y)$ must vanish on the interface boundary. If we also impose the condition that $\sigma_x(x)$ and $\sigma_y(y)$ vanish at the interface then the equations are well defined globally in free space as well as inside the PML layer and we have a set of plane wave solutions (6.12), decaying in the layer region for all frequencies, ω, and directions of propagation, ϕ, while remaining continuous across the vacuum-layer interface. Such solutions (6.12) will be referred to as the matched plane wave solutions.

We assume that the PML region is outside a square bounded by $|x| = a$ and $|y| = a$ and choose $\sigma_x(x)$ as

$$\sigma_x(x) = \begin{cases} 0 & |x| < a \\ C|x-a|^n & |x| \geq a \end{cases} \tag{6.13}$$

where $n > 2$ and $C > 0$ are constants used to control the strength of the absorbing layer. The definition of $\sigma_y(y)$ is similar.

The original PML method, proposed in [3], is given in Cartesian coordinates, i.e. a rectangular vacuum-layer interface is implicitly assumed although not necessarily required as discussed in [56].

As shown in [3] and further discussed in [56], Eq.(6.11) allows for plane wave solutions that decay inside the layer irrespective of the frequency and angle of propagation of the wave while remaining continuous across the vacuum-layer interface provided $\sigma_x(x)$ and $\sigma_y(y)$ are sufficiently smooth.

The Polar PML Methods

A natural vacuum-layer interface for scattering problems appears to be a cylindrical interface as the outward propagating waves, at least far away from the scatter, approach a cylindrical wave.

Consider the non-dimensional Maxwell's equations in polar coordinates:

$$\left\{\begin{array}{l} \dfrac{\partial H_r}{\partial t} = -\dfrac{1}{r}\dfrac{\partial E_z}{\partial \theta} \\ \dfrac{\partial H_\theta}{\partial t} = \dfrac{\partial E_z}{\partial r} \\ \dfrac{\partial E_z}{\partial t} = \dfrac{\partial H_\theta}{\partial r} + \dfrac{H_\theta}{r} - \dfrac{1}{r}\dfrac{\partial H_r}{\partial \theta} \end{array}\right. , \tag{6.14}$$

with the plane wave solutions given as

$$\left\{\begin{array}{l} H_r = H_x \cos\theta + H_y \sin\theta = -\sin(\theta-\phi) e^{i\omega(t - r\cos(\theta-\phi))} \\ H_\theta = -H_x \sin\theta + H_y \cos\theta = -\cos(\theta-\phi) e^{i\omega(t - r\cos(\theta-\phi))} \\ E_z = e^{i\omega(t - r\cos(\theta-\phi))} \end{array}\right. . \tag{6.15}$$

The extension of the PML method, proposed by Navarro et al. [41], results in the following split-field equations:

$$\left\{\begin{array}{l} \dfrac{\partial H_r}{\partial t} = -\dfrac{1}{r}\dfrac{\partial (E_{zr}+E_{z\theta})}{\partial \theta} \\ \dfrac{\partial H_\theta}{\partial t} = \dfrac{\partial (E_{zr}+E_{z\theta})}{\partial r} - g(r) H_\theta \\ \dfrac{\partial E_{zr}}{\partial t} = -\dfrac{1}{r}\dfrac{\partial H_r}{\partial \theta} \\ \dfrac{\partial E_{z\theta}}{\partial t} = \dfrac{\partial H_\theta}{\partial r} + \dfrac{H_\theta}{r} - g(r) E_{z\theta} \end{array}\right. . \tag{6.16}$$

We refer to this method as the Navarro polar PML method. This approach is also suggested by Rappaport in [44]. However, as we shall show through experiments, this method does not perform well in practice. We therefore suggest the following split-field equations for the polar PML method instead:

$$\left\{\begin{array}{lcl}\dfrac{\partial H_r}{\partial t} &=& -\dfrac{1}{r}\dfrac{\partial(E_{zr}+E_{z\theta})}{\partial\theta} - \dfrac{\sigma_r(r)}{r}H_r \\ \dfrac{\partial H_\theta}{\partial t} &=& \dfrac{\partial(E_{zr}+E_{z\theta})}{\partial r} - \sigma_r'(r)H_\theta \\ \dfrac{\partial E_{zr}}{\partial t} &=& \dfrac{H_\theta}{r} - \dfrac{1}{r}\dfrac{\partial H_r}{\partial\theta} - \dfrac{\sigma_r(r)}{r}E_{zr} \\ \dfrac{\partial E_{z\theta}}{\partial t} &=& \dfrac{\partial H_\theta}{\partial r} - \sigma_r'(r)E_{z\theta}\end{array}\right. . \tag{6.17}$$

where $\sigma_r(r)$ is a function to be specified later.

It can be verified that these equations admit the following plane wave solutions:

$$\left\{\begin{array}{l} H_r = -\sin(\theta-\phi)e^{i\omega(t-r\cos(\theta-\phi))}e^{-\sigma_r(r)\cos(\theta-\phi)} \\ H_\theta = -\cos(\theta-\phi)e^{i\omega(t-r\cos(\theta-\phi))}e^{-\sigma_r(r)\cos(\theta-\phi)} \\ E_{zr} = \sin^2(\theta-\phi)e^{i\omega(t-r\cos(\theta-\phi))}e^{-\sigma_r(r)\cos(\theta-\phi)} \\ E_{z\theta} = \cos^2(\theta-\phi)e^{i\omega(t-r\cos(\theta-\phi))}e^{-\sigma_r(r)\cos(\theta-\phi)}\end{array}\right. . \tag{6.18}$$

Let the vacuum-layer interface be at $r = r_0$. Hence, we should have $\sigma_r(r) = 0$ for $r < r_0$. Following the considerations of the absorbing and reflectionless properties of the polar PML method, $\sigma_r(r)$ must satisfy the requirements:

$$\sigma_r(r_0) = 0 \ , \tag{6.19}$$

$$\sigma_r(r) > 0 \quad \text{for } r > r_0 \ , \tag{6.20}$$

so that the plane wave solutions decays for $r > r_0$. We also require that

$$\sigma_r'(r) > 0 \quad \text{for } r > r_0 \ . \tag{6.21}$$

In the present work we use

$$\sigma_r(r) = \left\{\begin{array}{ll} 0 & r < r_0 \\ C(r-r_0)^n & r \geq r_0 \end{array}\right. \tag{6.22}$$

where $n > 2$ and $C > 0$ are constants used to control the strength of the absorbing layer. Here r_0

signifies the radius of the circular vacuum-layer interface.

One difference between the new polar PML method and the rectangular PML method is that the interface of the new polar PML is a circle and can be represented by one grid line in polar coordinates, while the interfaces of the rectangular PML method is a rectangle and is represented by four grid lines. The complexity of the interface of the rectangular PML method results in several regions of different properties in the layer, which are not optimal for reflectionless wave absorption.

The difference between the polar PML method proposed here and previously proposed polar PML methods in [41, 44], Eq. (6.16), lies in the way the equations are split, i.e. in the present version the low-order term is applied in the third equation while previous methods include this term in the fourth equation of Eq.(6.17). Although this latter choice may appear more natural it has been shown to lead to significantly larger errors.

A Well-Posed Rectangular PML Method (WPML)

As shown in [2], the original PML method discussed in the previous section suffers from being only weakly well-posed as a consequence of the splitting of Maxwell's equations. Although, in a multi-domain setting, these equations are solved in a small part of the computational domain only, this property is certainly undesirable.

Recently, an unsplit well-posed PML (WPML) method was proposed to circumvent this problem [1], which, for TM-scattering, is given as

$$\begin{aligned}
\frac{\partial H_x}{\partial t} &= -\frac{\partial E_z}{\partial y} - 2\sigma_y(y)H_x - \sigma_y(y)P_y \quad , \\
\frac{\partial H_y}{\partial t} &= \frac{\partial E_z}{\partial x} - 2\sigma_x(x)H_y - \sigma_x(x)P_x \quad , \\
\frac{\partial E_z}{\partial t} &= \frac{\partial H_y}{\partial x} - \frac{\partial H_x}{\partial y} - \sigma'_x(x)Q_x + \sigma'_y(y)Q_y \quad ,
\end{aligned} \tag{6.23}$$

$$\begin{aligned}
\frac{\partial P_x}{\partial t} &= \sigma_x(x)H_y \quad , \quad \frac{\partial Q_x}{\partial t} = -\sigma_x(x)Q_x - H_y \quad , \\
\frac{\partial P_y}{\partial t} &= \sigma_y(y)H_x \quad , \quad \frac{\partial Q_y}{\partial t} = -\sigma_y(y)Q_y - H_x \quad ,
\end{aligned}$$

where $\sigma_x(x)$ and $\sigma_y(y)$ signifies the non-dimensional lossy material parameters. We immediately note that since Maxwell's equations are altered by low-order terms only, the system of partial differential equations are well-posed by construction with the introduction of 4 additional Debye-like equations describing the development of the artificial polarization currents, P_x and Q_x, along x and, likewise, P_y and Q_y, along y.

Indeed, for $\sigma_x(x) = \sigma_y(y) = 0$ we recover the free space Maxwell's equations ensuring that the fields are continuous at the vacuum-layer interface, at least up to the approximation error. In [1] it is shown that the well-posed PML method supports plane wave solutions that decay uniformly inside a layer in the x-direction irrespective of the frequency and the angle of propagation of the plane wave. Eq.(6.23) applies the idea in x-direction and y-direction and admits matched plane wave solutions in all the PML regions.

We assume that the PML region is outside a square bounded by $|x| = a$ and $|y| = a$, with $\sigma_x(x)$ and $\sigma_y(y)$ being specified in Eq.(6.13).

A Well-Posed Polar PML Method (WPPML)

Following the same line of reasoning leading to the well-posed PML in Cartesian coordinates, Eq.(6.23), we have derived a well-posed polar PML method, with a circular vacuum-layer interface, that has matched plane wave solutions that decay uniformly inside the layer independent of angle of propagation and frequency. The analysis leading to the actual scheme is similar to that in 3-D.

The well-posed polar PML (WPPML) method is given as

$$
\begin{aligned}
\frac{\partial H_r}{\partial t} &= -\frac{1}{r}\frac{\partial E_z}{\partial \theta} \ , \\
\frac{\partial H_\theta}{\partial t} &= \frac{\partial E_z}{\partial r} - \left(2r\sigma_r'(r) - \sigma_r(r)\right)\frac{H_\theta}{r} + \left(2r\sigma_r'(r) - \sigma_r(r)\right)^2 \frac{P}{r^2} \ , \\
\frac{\partial E_z}{\partial t} &= -\frac{1}{r}\frac{\partial H_r}{\partial \theta} + \frac{1}{r}\frac{\partial r H_\theta}{\partial r} + \sigma_r''(r) Q \ ,
\end{aligned}
\tag{6.24}
$$

$$\frac{\partial P}{\partial t} = H_\theta - \sigma_r(r)\frac{P}{r} \ , \ \ \frac{\partial Q}{\partial t} = H_\theta - \sigma_r'(r)Q \ ,$$

where $\sigma_r(r)$ is given in Eq.(6.22).

6.4.3 PML Implementation Issues

The calculations reported in this chapter had been carried out using the multi-domain approach. This is a very natural setting for the PML method as the free space equations are solved in the inner subdomains while the PML equations are solved in the outer subdomains only. Note, however, that the free space domain has only three unknowns (H_x, H_y and E_z in the rectangular case and H_r, H_θ and E_z in the polar case) whereas the PML layer involves four unknowns (the electric field E_z is split into two, see Eqs. (6.11) and (6.17)), and therefore the interface boundary conditions are nontrivial. To overcome this difficulty we first observe that the PML system has the same number of positive and negative eigenvalues as the free space system, the extra eigenvalue being zero (this is exactly the reason why the PML system is only weakly well-posed [2]). We also observe that by adding and subtracting the third and fourth equations in Eq. (6.11) we recover Maxwell's equations for H_x, H_y and $E_{zx} + E_{zy}$ and the unknown $E_{zx} - E_{zy}$ comes in the first three equations as a lower order term, thus not effecting the eigenvalues and the eigenvectors of the system. We therefore use the characteristic boundary treatment to patch H_x, H_y and $E_{zx} + E_{zy}$ in the PML subdomain with H_x, H_y and E_z in its neighboring subdomain, and patch H_r, H_θ and $E_{zr} + E_{z\theta}$ in the PML subdomain with H_r, H_θ and E_z in its neighboring subdomain in the polar case.

The above discussion indicates the importance of imposing $\sigma_x(x) = \sigma_y(y) = 0$ along the interface in the rectangular case and $\sigma_r'(r)|_{r=r_0} = 0$ in the polar case. For the polar PML method, one can choose the functions in Eq. (6.22) with $n \geq 2$ and the constant C can be tuned for specific computations, and needs to compute $\frac{\sigma_r(r)}{r}$ and $\sigma_r'(r)$ in the differential equations. In numerical computation, the maximum norms of the functions $\sigma_x(x)$, $\sigma_y(y)$, and $\sigma_r(r)$ are bounded by some constants of stability consideration of the numerical scheme used.

The rectangular PML method can be implemented in a circular mesh where the rectangular

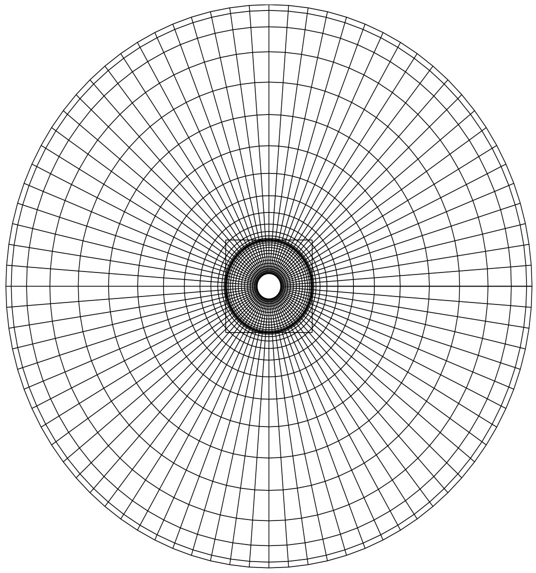

Figure 6.2: An explanatory mesh for the direct implementation of the rectangular PML method.

interface is fitted inside the exterior subdomain of the multi-domain mesh (see Figure 6.2 for a typical 2-domain grid and the rectangular interface). In order to maintain accuracy one needs a sufficiently large absorbing area, i.e. , the area outside the rectangular interface. We have applied the cubic grid mapping (2.31) for stretching in the radial direction for this purpose.

To test the reflecting and absorbing properties of the PML method, the layer is backed up by a perfectly electrical conductor by imposing $E_z = 0$ at the outer boundary. However, any ABC that is appropriate for the PML type equation can be applied at the outer boundary, e.g., characteristic type boundary conditions can be straightforwardly applied at the outer boundary.

6.5 Numerical Experiments (Fourier-Chebyshev)

We consider the TM case of 2-D wave scattering by circular and elliptic PEC cylinders. Due to the linearity of Maxwell's equation and the physical boundary condition at the scatterer surface, we compute the purely scattered field by using the boundary condition $(E_z)_{\mathrm{sc}} = -(E_z)_{\mathrm{inc}}$ at the cylinder surface.

Denote the radius of the circular cylinder by a and the wave number of the incident wave by k. The complexity of the problem increases with the frequency of the incident wave, e.g. the dynamic range for scattering by a circular PEC cylinder of electrical size $ka = 21\pi$ is about $30dB$, while the dynamic range for scattering by an elliptic PEC cylinder (major axis = $0.5m$, minor axis = $0.1225m$ and $k = 42\pi$) is about $35dB$.

To show the efficacy of the multi-domain pseudospectral methods in the simulation of electromagnetic wave scattering as well as the efficacy of the proposed absorbing boundary conditions, we have implemented the methods discussed in the previous sections. For comparison, the FD-TD method is also used to simulate the same problems but with meshes of substantially larger size. For the FD-TD method, the perfectly conducting cylinder is modeled as a cylinder with permittivity equal to that of free space but with a very high conductivity. We use the rectangular PML method [3] as an absorbing boundary condition.

The radar cross section (RCS) is adopted as a main criterion for assessing the accuracy of the calculation of different schemes. A near-to-far-field transformation is used to get the far-field RCS from the near-field values, see [51]. The RCS is validated in two ways. The near-to-far-field transformation and the corresponding RCS computed along different closed contours should be the same up to numerical error. We also evaluate the RCS in case of scattering by a circular cylinder using the infinite series analytical solution, see [6], and refer to this evaluated RCS as "exact". For some problems, we perform the computation on a mesh of a very large size and use that solution as reference. For these reference computations, we use the standard Fourier-Chebyshev mesh (without mapping) and the characteristic boundary condition at the outer boundary which is about 25 wavelengths away from the scatter.

In our presentation of the RCS results, the bistatic RCS's are plotted in cylindrical form or angle-dB form, whichever yields more information. In order to see the difference in the backscatter region, being the most difficult to resolve, we cut the forward scatter region in many plots.

As an convention for our spectral method mesh we use $l \times m \times n$, which stands for l points in the azimuthal direction, m points in the radial direction and n number of subdomains of size $l \times m$ (1 for each subdomain).

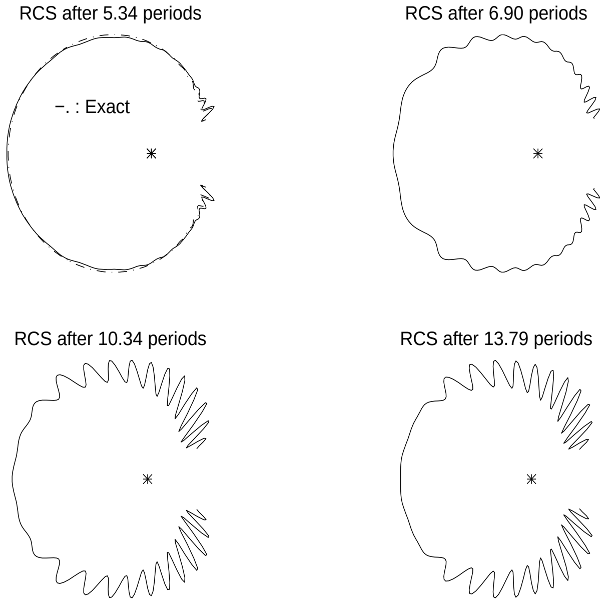

Figure 6.3: Comparison of RCS's at different time for the Fourier-Chebyshev method with characteristic boundary condition. Electrical size of the cylinder is $ka = 7\pi$.

6.5.1 Scattering By Circular Cylinders

Example 6.5.1 *The Characteristic Method for the Fourier-Chebyshev.*

In this example, the single domain Fourier-Chebyshev method with characteristic boundary condition is used. The electrical size of the cylinder is $ka = 7\pi$ (k: wave number and a: radius of the cylinder). The mesh we use is $84 \times 17 \times 1$ and the exterior boundary was placed 3 wavelengths away from the cylinder surface, a scenario similar to that in [30]. To show the accuracy of this approach, the RCS results at different times are compared in Fig. 6.3. One clearly observes that the results are accurate before the reflections from the exterior boundary returns, after which the accuracy deteriorates in time. This illustrates the insufficiency of the characteristic type boundary condition.

Example 6.5.2 *Comparison between the FD-TD Method with Rectangular PML and Fourier-Chebyshev Methods.*

Here and in all subsequent numerical experiments, the multi-domain Fourier-Chebyshev method is used. All the simulations are carried out over many wave periods to ensure that the RCS is stationary. The subdomain meshes (other than the exterior one) span only $\frac{4}{3}$ of a wavelength in

Table 6.1: Comparison of the FD-TD method with a 16-cell rectangular PML layer (FD-TD-PML) and the 2-subdomain Fourier-Chebyshev method with a rectangular PML layer (FC-PML), a new implementation of the ML layer (FC-ML) as well as a New Polar PML layer (FC-PPML)

Method	ka	Mesh	Discrete L_2 RCS Error (dB)	CPU Time (seconds)
FD-TD-PML	π	321×321	4.50E-2	1402
FC-PML	π	$18 \times 17 \times 2$	9.88E-3	37
FC-ML	π	$18 \times 17 \times 2$	6.26E-3	32
FC-PPML	π	$18 \times 17 \times 2$	6.40E-4	27

the radial direction. In the exterior subdomain we use the direct implementation of the rectangular PML method (6.11), the new implementation of the ML method (6.10), or the new polar PML method (6.17).

In Table 6.1, we compare the discrete L_2 error of the RCS and the computation time of the FD-TD method and the Fourier-Chebyshev methods. The computations are terminated after 30 wave periods for both the FD-TD method and the Fourier-Chebyshev methods. In the FD-TD method we used a grid of 321×321, corresponding to 160 grid points per wave-length. We used two subdomains for the Fourier-Chebyshev method, so the interface of the absorbing layers is less than 1.4 wavelength away from the cylinder surface. The electrical size of the cylinder being simulated is $ka = \pi$. Indeed, we find that comparing accuracy as well as computational efficiency supports the use of pseudospectral method for scattering problems with the new polar PML leading to the most accurate results.

In Fig. 6.4, we plot the RCS resulting from using the FD-TD method and the Fourier-Chebyshev method for simulating scattering from a cylinder of larger electrical size: $ka = 7\pi$. Both methods use the rectangular PML as the ABC. For the spectral time domain PML method, we use an $84 \times 17 \times 2$ mesh. For the FD-TD method, we have to use a very fine grid, 1101×1101, to ensure a reasonable accuracy. The RCS of the FD-TD method has obvious oscillation in the back scatter region while that of the spectral PML method agrees very well with the exact RCS. We recall from the results given in Table 6.1 that the results obtained using the rectangular PML method are inferior to those obtained using the polar PML as well as the matched layer emphasizing that the results illustrated Fig. 6.4 can be improved considerably for the pseudospectral method.

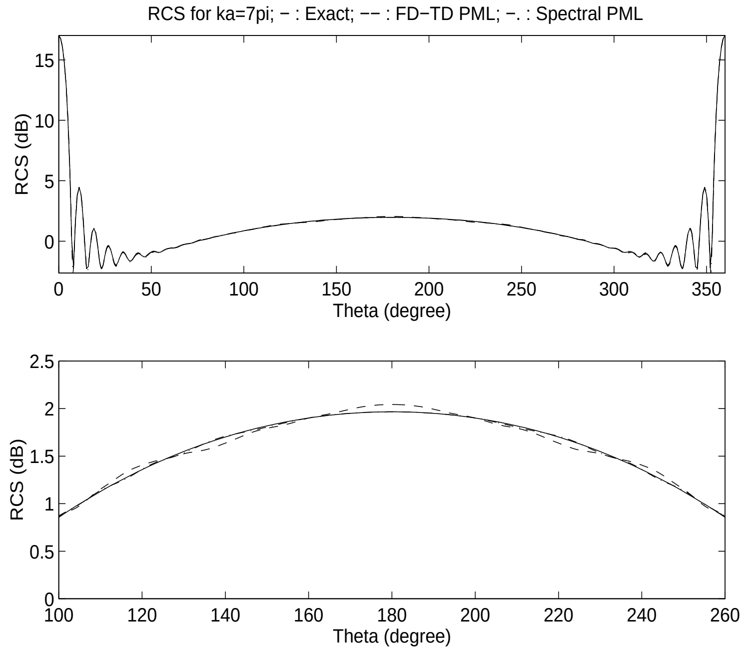

Figure 6.4: RCS comparison for the FD-TD method and the spectral method with the rectangular PML method. Electrical size of the cylinder is $ka = 7\pi$.

Example 6.5.3 *Comparison between the Navarro Polar PML Method (6.16) and the New Polar PML Method (6.17).*

Here, we compare the effectiveness of the Navarro polar PML method and the new polar PML method as an ABC for the multi-domain Fourier-Chebyshev method. The electrical size of the cylinder is still $ka = 7\pi$. The mesh we use is the standard Fourier-Chebyshev mesh of size $84 \times 17 \times 2$ for both methods. In Fig. 6.5 we compare the results of the two approaches. We find that the new polar PML method increases the accuracy substantially over the Navarro polar PML method. The discrete L_2 error of the RCS obtained using the new polar PML method is only 3.4 percent of that of the Navarro polar PML method. We also observe in our numerical experiments that the best results of the Navarro polar PML method are obtained by using $g(r) = f_0'(r)$, with $f_0(r)$ being the best choice for the function $\sigma_r(r)$ in the new polar PML method.

Example 6.5.4 *Numerical Simulations of an Electrically Large Size Problem by the Rectangular PML (6.11), the New Implementation of the ML (6.10) and the new Polar PML Method (6.17).*

In this example, the cylinder we consider is of electrical size, $ka = 21\pi$. This problem is out of the computational capacity of the FD-TD method on most computers, since a mesh larger than

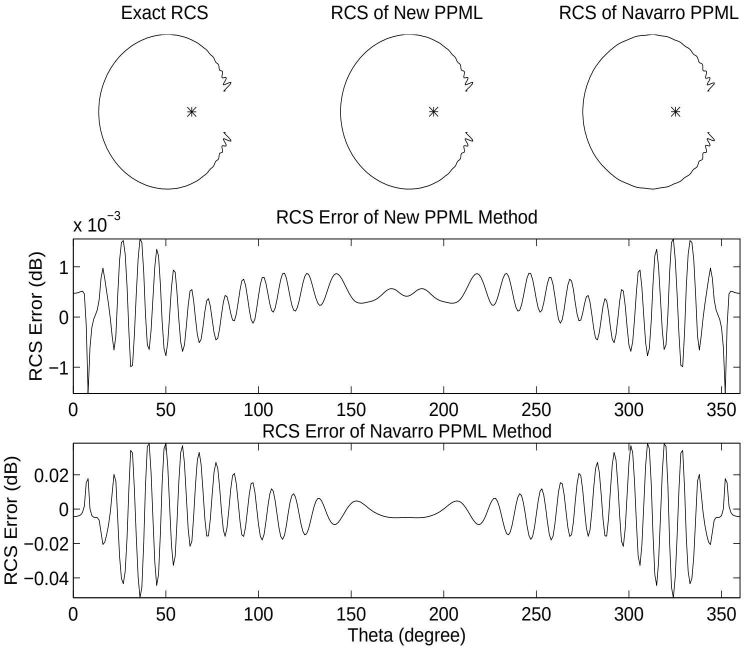

Figure 6.5: RCS comparison for the new polar PML (PPML) method and the Navarro polar PML (PPML) method. Electrical size of the cylinder is $ka = 7\pi$.

2000×2000 should be used, this estimate being based on the accuracy obtained for the case of $ka = 7\pi$.

For the simulations of this electrically large size scattering problem, we use the multi-domain Fourier-Chebyshev method with the following absorbing boundary layers as the ABC: the direct implementation of the rectangular PML, the new implementation of the ML method, or the new polar PML method. For all three methods, the computational domain is backed up by PEC ($E_z = 0$) at the outer domain boundary.

The computational grid we use for all methods is $256 \times 17 \times 2$, i.e. just about 2 points per wavelength in the azimuthal direction. See Fig. 6.6 for a comparison of the RCS error for the three methods. We also compute the same problem using a mesh of very large size ($256 \times 17 \times 20$), and take this solution as the reference to obtain the normalized error of the scattered field, E_z. See Table 6.2 for the comparison of the discrete L_2 error for both the RCS and the normalized error for the scattered field E_z.

One observes that all three methods give satisfying results for this problem, and the polar PML method is the best even though only the standard Fourier-Chebyshev mesh is used in its computation. One also observes that the error of the new implementation of the ML method is only $20-30$ percent

Table 6.2: Comparison of the discrete L_2 error of the rectangular PML method (FC-PML), the new implementation of the ML method (FC-ML) and the new polar PML method (FC-PPML)

Error	Method FC-PML	Method FC-ML	Method FC-PPML
Error for RCS (dB)	4.90E-2	1.54E-2	2.60E-3
Normalized Error for E_z	3.50E-3	7.13E-4	1.41E-4

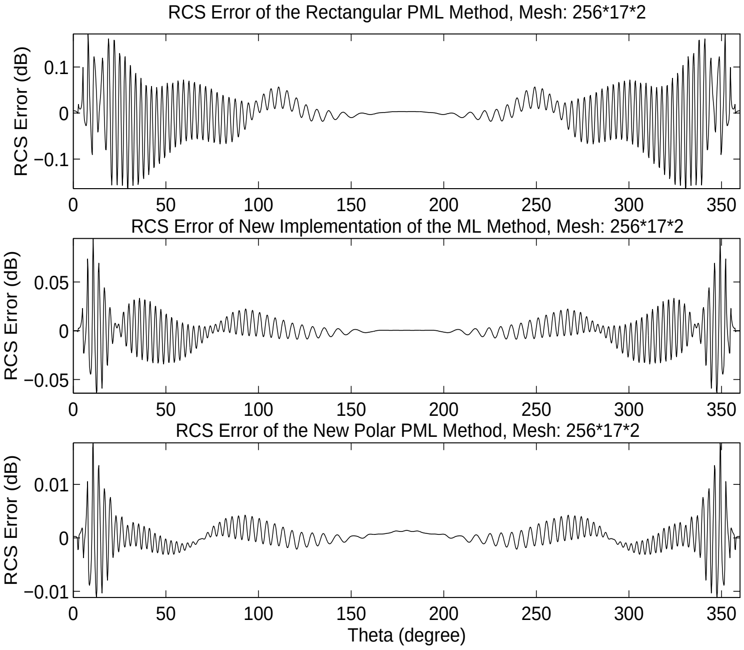

Figure 6.6: RCS error plots of the rectangular PML method, the new implementation of the ML method and the polar PML method. Electrical size of the cylinder is $ka = 21\pi$.

of that of the direct implementation of the PML method. Note that we have to use the cubic mapping technique with the rectangular PML method and the new implementation of the ML method in order for the results to be comparable to that of the new polar PML method.

For the new polar PML method, an even more accurate result can be obtained by refining the mesh in the azimuthal direction. In this experiment, we use a $384 \times 17 \times 2$ mesh and get a better result for the RCS, as observed in Fig. 6.7. The highly oscillatory RCS is resolved to within $3.0E-3dB$ of the exact one.

The above results clearly show the efficacy of the new polar PML as a reflectionless absorbing boundary layer in polar coordinates. They also fully demonstrate the capability of the proposed three methods in solving problems involving electrically very large objects.

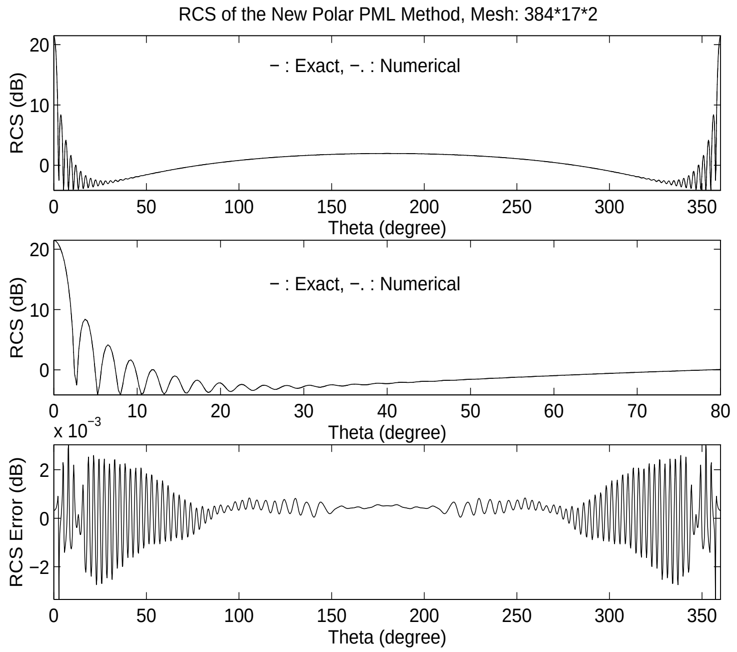

Figure 6.7: RCS result of the polar PML method for a finer mesh. Electrical size of the cylinder is $ka = 21\pi$.

6.5.2 Scattering By Elliptic Cylinders

Here we present two simulations of electromagnetic wave scattering by elliptic cylinders, where the direct implementation of the rectangular PML method or the new implementation of the ML method are used as an ABC. The elliptic cylindrical coordinates, (u,v), are related to the rectangular Cartesian coordinates, (x,y), by the transformation

$$\begin{aligned} x &= \tfrac{1}{2}d \cdot \cosh u \cdot \cos v \ , \\ y &= \tfrac{1}{2}d \cdot \sinh u \cdot \sin v \ , \end{aligned} \tag{6.25}$$

where $0 \leq u < \infty$, $0 \leq v < 2\pi$ and d is the interfocal distance. The scattering body is the elliptic cylinder with the surface $u = constant$.

When the elliptic cylinder is fat, i.e. an aspect ratio about 1, one can use this transformation to generate the mesh outside the elliptic cylinder. However, when the elliptic cylinder is thin, the grid points generated by this transformation tend to cluster towards the cylinder surface, especially in the x-direction. This induces an unwanted time step restriction in the computation, as well as loss of accuracy in regions where the mesh is coarse. The Chebyshev grid point distribution in the y-direction tends to get too coarse away from the thin ellipse.

We consider, therefore, the following kind of modified transformation in our mesh generation:

$$\begin{aligned} x &= \tfrac{f(u)}{2} d \cdot \cosh u \cdot \cos v \ , \\ y &= \tfrac{1}{2} d \cdot \sinh u \cdot \sin v \ , \end{aligned} \tag{6.26}$$

where $f(u)$ is chosen to balance the grid point distribution in the x-direction and the y-direction. We may also apply the cubic grid mapping in the inner domains to balance the grid distribution in the radial direction.

In the numerical experiments, waves of any angle of incidence and elliptic cylinders of different ratios between the major and minor axes are considered. Having made the validations for the circular cylinder case, we will use the result of a very large mesh ($l \times 17 \times 20$) as reference, referred to as "exact". It is verified that the RCS obtained in different subdomains of the large mesh is almost invariant.

In the first simulation, the major axis of the ellipse is $0.5m$ and the minor axis of the ellipse is $0.3808m$ and we use only $l = 20$ Fourier modes in the azimuthal direction. The wave number of the incident wave is $k = 2\pi$. The angle of the incident wave is 45 degrees. We use the multi-domain Fourier-Chebyshev method with the direct implementation of the PML method as an ABC. See Fig. 6.8 for the mesh generated for this problem. We use the cubic grid mapping in both subdomains. In Fig. 6.9, we give the RCS comparison. Note that the two-domain result is resolved to within $0.018dB$ of the reference.

In the second simulation, the major axis of the ellipse is $0.5m$ and the minor axis of the ellipse is $0.1225m$. The wave number of the incident wave is $k = 42\pi$ and we use $l = 256$ Fourier modes in the azimuthal direction. The angle of the incident wave is 45 degrees. The dynamic range of this problem is about $35dB$, and the bistatic RCS is highly oscillatory. We use the ML method with the cubic grid mapping and solution filtering techniques for this simulation. The type of transformation given in Eq. (6.26) is also applied to generate the mesh for this problem, see Fig. 6.10. In Fig. 6.11 we show the RCS results. Note that the highly oscillatory RCS is resolved to within $0.2dB$ of the reference.

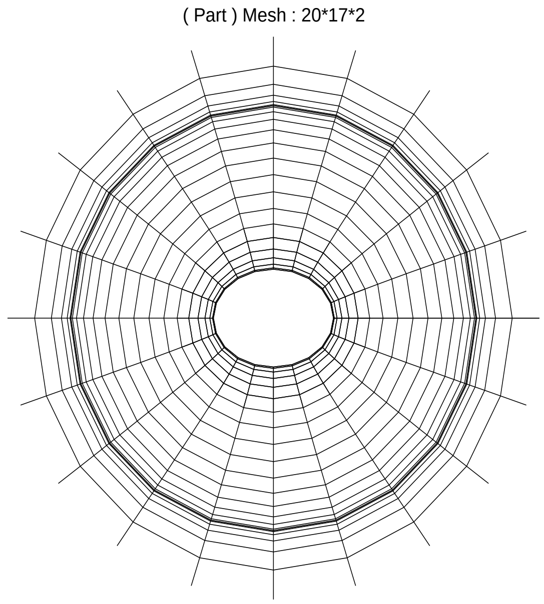

Figure 6.8: The mesh used for simulating scattering from a mildly elliptic cylinder.

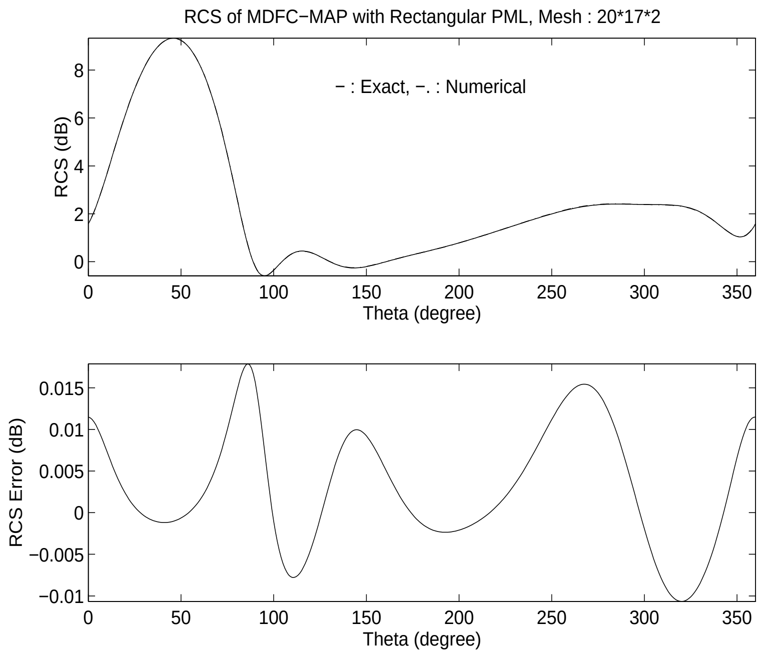

Figure 6.9: RCS result of the rectangular PML method for simulating scattering by an elliptic cylinder.

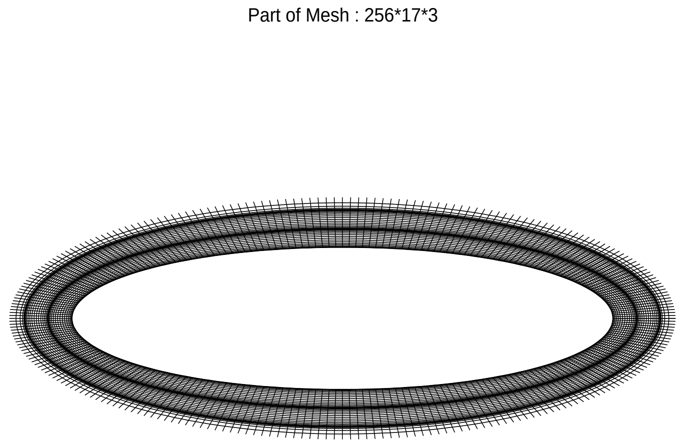

Figure 6.10: The mesh used for simulating scattering from a strongly elliptic cylinder.

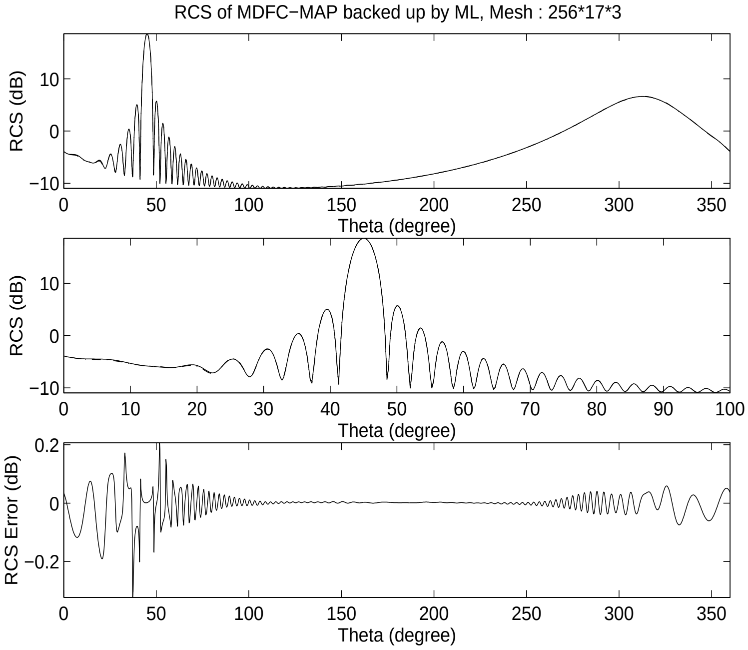

Figure 6.11: RCS result of the new implementation of the ML method for scattering by an elliptic cylinder.

6.6 Numerical Experiments (Chebyshev-Chebyshev)

6.6.1 2-D Multidomain Meshes

We consider the case of 2D-TM scattering from perfectly conducting cylinders of circular and square cross-section, respectively. As in the Fourier-Chebyshev case, we only compute the purely scattered field while the excitation is introduced through imposing the boundary conditions $(E_z)_{\mathrm{sc}} = -(E_z)_{\mathrm{inc}}$ at the cylinder surface.

In Fig. 6.12 we show examples of the multi-domain meshes used in the following computations. We observe that the multi-domain approach allows for dealing with rectangular and circular vacuum-layer interfaces with equal ease and that scattering by more general objects can be computed by the exact same approach as discussed here for generic shapes. We also find it advantageous to apply a cubic mapping [56] in the outer domains when considering a rectangular vacuum-layer interface while this is not the case for the circular interface.

We use the RCS results to compare different PML methods as in the Fourier-Chebyshev case. For comparison we also computed the RCS using a second order FD-TD method [51] with Eq.(6.11) as the absorbing boundary conditions.

6.6.2 Scattering by a Circular Cylinder

We first consider the problem of scattering by a $ka = \pi$ circular cylinder where a represents the radius of the cylinder and we use the exact series solution as the reference.

On the left of Fig. 6.13 we show the computed RCS using different methods and absorbing boundary conditions with a rectangular vacuum-layer interface, i.e. Eq.(6.11) and Eq.(6.23). It is clear that the spectral solutions are superior to the FD-TD solution, in particular in the backscatter region.

A more quantitative comparison is shown in Table 6.3 where we give the L_2 error of the computed RCS and the CPU-time required to obtain the result for the various versions of PML methods introduced previously. Indeed, at first we observe that the spectral scheme is significantly faster as

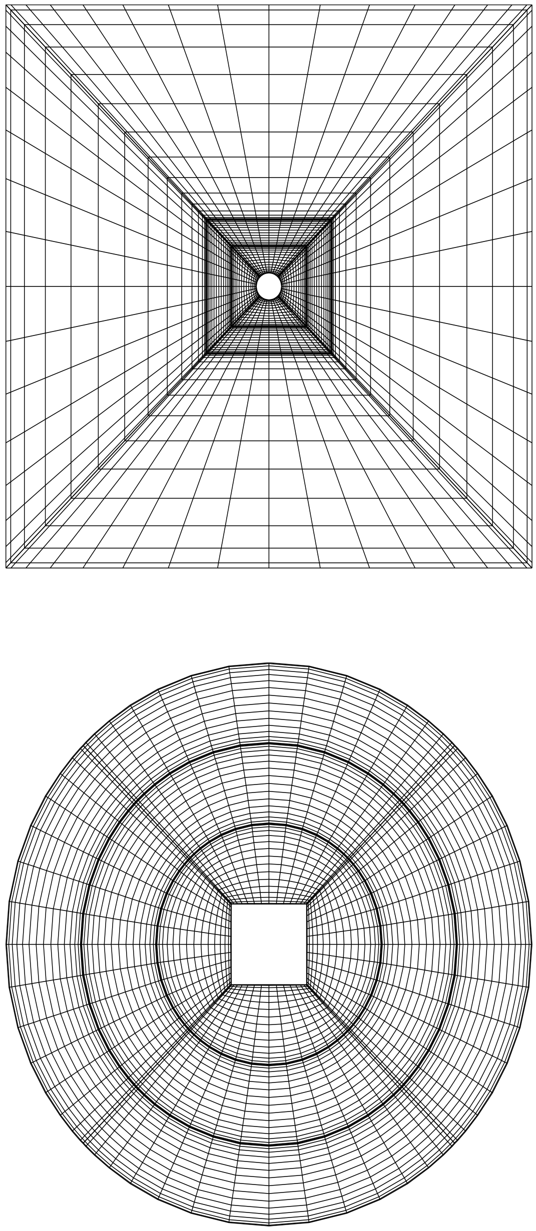

Figure 6.12: Examples of multi-domain meshes used for the computation of 2D-TM scattering by cylinders with cylindrical and square cross-sections.

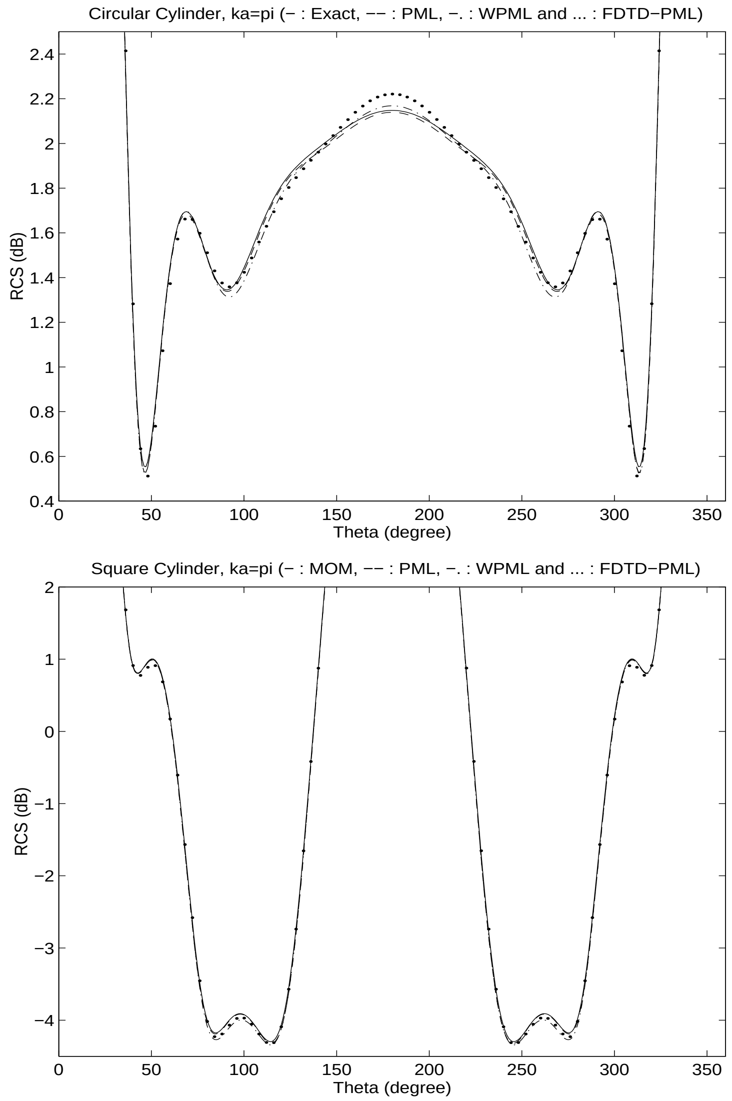

Figure 6.13: Radar-Cross-Sections (RCS) computed using the spectral multi-domain method with various choices of absorbing boundary conditions. On the left we show the RCS for scattering for a $ka = \pi$ circular cylinder computed using also the FD-TD method and compared with the exact solution. The right displays the RCS for scattering from a $ka = \pi$ square cylinder compared with the result obtained using a FD-TD scheme with the MoM result taken to be the reference solution.

well as more accurate than the FD-TD method. We also observe that the polar PML methods are consistently more accurate than the PML methods with a rectangular vacuum-layer interface while the well-posed formulations of the PML methods appears to be less accurate that the PML methods based on the split set of equations.

We attribute these observations to several effects. The matched plane wave solutions for the well-posed PML methods are more complicated than the solutions associated with the split field PML methods, which may explain the observed difference. The rectangular PML methods, on the other hand, suffers from the requirement that plane waves at grazing incidence must propagate all the way to the corner before experiencing the effect of the layer while no such thing is required in the polar formulation of the PML method.

6.6.3 Scattering by a Square Cylinder

Let us also consider the case of TM scattering from a square $ka = \pi$ cylinder with a being half a side length. No exact solution is known for this problem and we use a 10 point/wavelength MoM solution as the reference solution. We note that the MoM solution suffers from ill-conditioning for large number of points/wavelength making it impossible to obtain very accurate solutions of the RCS, i.e. it is not possible to arrive at quantitative measures of the same quality as in the previous section.

On the right of Fig. 6.13 we show the computed RCS using different methods and absorbing boundary conditions with a rectangular vacuum-layer interface, i.e. Eq.(6.11) and Eq.(6.23). In this case we find little difference between the FD-TD solution and those obtained with the spectral scheme, although, as shown in Table 6.4, the spectral solutions are obtained significantly faster. Again we observe that the polar PML methods outperforms the rectangular PML methods for the reasons discussed in the previous section.

6.7 Concluding Remarks

In this chapter we have presented a multi-domain Fourier-Chebyshev method and a multi-domain Chebyshev-Chebyshev method for simulating electromagnetic wave scattering by simple two-dimensional objects. A crucial component of the method is the far field boundary conditions. We have shown that the characteristic method is not suitable, and we have applied various types of PML methods.

In the first part of the simulations, we use the Fourier-Chebyshev method. For the circular cylinder case we have considered four far field boundary treatments: 1) A new implementation of the matched layer method. 2) The Berenger PML method in rectangular coordinates. 3) The PML method in polar coordinates as suggested by Navarro. 4) A new polar PML method suggested in this chapter.

The last method is about 20 times more accurate than the rectangular PML method and about 30 times more accurate than the Navarro polar PML method. It is also more accurate than the suggested implementation of the ML method. For the elliptic cylinder case we had only methods 1 and 2 and the first performed much better than the PML method. All of the above methods were orders of magnitude better than the usual FD-TD second order schemes and significantly faster.

The second part of the simulations uses the Chebyshev-Chebyshev method. The purpose of the work has been two-fold. The development and implementation of the Chebyshev-Chebyshev multi-domain scheme for the solution of Maxwell's equations establishes a high-order algorithm, flexible enough to handle arbitrary geometric complexity, while being computational highly efficient and suitable for parallel as well as three-dimensional extensions.

We have also addressed the issue of properly formulating and implementing perfectly absorbing boundary conditions in the context of the multi-domain approach. The results clearly illustrate the superior accuracy, obtained at lower computational cost than when using FD-TD methods, attainable when combining PML methods with the accurate spectral methods. In particular we have shown that the polar PML methods seems to offer higher accuracy than the rectangular PML methods. And we believe that using the well-posed PML methods is the proper choice, in particular when considering problems with transient excitation.

Table 6.3: Comparison of accuracy and CPU-time from scattering by a circular cylinder, $ka = \pi$. The computational grid is constructed using K domains, each with a resolution of N, and the L_2-error and the required CPU-time are shown for the test cases considered here. The series solution is used as the exact solution against which to compare.

Method - ABC	N	K	L_2-error (dB)	CPU-time (sec)
Spectral - PML	16	12	1.43E-02	387
Spectral - WPML	16	12	2.42E-02	376
Spectral - PPML	16	12	8.60E-04	320
Spectral - WPPML	16	12	9.47E-03	330
FD-TD - PML	320	1	4.50E-02	1402

Table 6.4: Comparison of accuracy and CPU-time from scattering by a rectangular cylinder, $ka = \pi$. The computational grid is constructed using K domains, each with a resolution of N, and the L_2-error and the required CPU-time are shown for the test cases considered here. The MoM-solution with 10 points/wavelength is assumed to represent the exact solution against which to compare.

Method - ABC	N	K	L_2-error (dB)	CPU-time (sec)
Spectral - PML	16	12	2.78E-02	387
Spectral - WPML	16	12	4.16E-02	376
Spectral - PPML	16	12	1.64E-02	326
Spectral - WPPML	16	12	1.61E-02	335
FD-TD - PML	320	1	3.71E-02	1383

Chapter 7

Multidomain Absorbing Layer Methods in 2-D

7.1 Introduction

One way of terminating the computational domain, which is an important issue in computational electromagnetics, is by adding an absorbing layer to absorb the waves, while the layer causes no or little reflection back to the computational domain of interest, such as the PML methods discussed in chapter 3. The absorbing layer may be based on a mathematical construction and may not be physically reliable. The essential requirement for the absorbing layer methods is that it should have little effect on the inner computational domain, which is shown to be satisfied by the PML methods.

However, the vacuum-layer interfaces for the PML methods we have discussed so far are rectangular, spherical, or cylindrical. Though they can be applied in many simulation problems, a PML method having vacuum-layer interface of a more general type is still necessary and meaningful in some applications. We shall address this issue in this chapter. The absorbing layer methods we consider in this chapter have vacuum-layer interfaces that are general polygons, such as parallelogram and rectangle. Vacuum-layer interfaces of this type are flexible enough to contain any scatterer basically, while it is not natural and efficient to use a rectangle to contain a triangle, which shows the shortcoming of the rectangular PML method.

Though to extend the rectangular interface to a polygonal interface seems to be not difficult and there should exist more than one ways, caution must be taken in doing the work. We will present a simple example to show this, where we want to design a PML method with a parallelogram vacuum-layer interface. It will be demonstrated that a seemingly natural and perfect approach has a major problem and leads to unsatisfying numerical results in numerical experiments. It is labeled as an ill-formed PML method. On the contrary, we propose a multidomain PML method approach that is not perfectly matched at the layer-layer interface but gives much better numerical results. The multidomain approach is further justified in obtaining a working PML method with a triangular vacuum-layer interface. The multidomain PML method should be regarded as an absorbing layer method that is not directly related with any multidomain numerical scheme, though the method should be more amenable to multidomain numerical schemes.

Through the examples, we want to highlight the importance of the decaying property of the PML methods in the direction of propagation. In [56], we gave a polar PML method that has the property that its plane wave solutions decay in all directions of propagation, while the rectangular PML method has plane wave solutions that decay in all directions of propagation except the grazing direction. In this chapter, we want to show that this property of different PML methods is even more essential than the perfectly matching property, through the comparison of the ill-formed PML method and the multidomain PML method.

Besides from justifying the multidomain PML method that is not perfectly matched at the layer-layer interface, we also present an approximately matched absorbing layer method, like the multidomain PML method, leading to numerical results that are clearly more accurate than that of the ill-formed PML method in the simulation of scattering by a parallelogram cylinder.

The approximately matched absorbing layer (AML) method uses the real and imaginary parts of an analytical function to design the low-order absorbing terms one needs to add to the original Maxwell's equations. The layer has decay-in-all-direction-of-propagation property of its plane wave solutions. The method requires less computational resource than PML methods. Though the layer is only approximately matched, the difference between the plane wave solutions in free-space and a corresponding set of decaying plane wave solutions in the layer can be made exponentially small. The approximately matched absorbing layer method can be easily applied in simulations where a polygonal vacuum-layer interface is desired. To enhance its efficiency, we propose a multidomain implementation of the AML method, where we apply the same idea as that in the multidomain PML method.

Extensive numerical experiments, simulating electromagnetic wave scattering by perfectly electrically conducting cylinders whose cross sections are circles, rectangles, parallelograms, or triangles, are done to validate our conclusions and methods. The numerical results of the multidomain PML method and the multidomain AML method are as accurate as that of the original PML method. The AML method has another advantage that it requires less computation time and memory.

7.2 Extension of PML Method to Non-Rectangular Coordinate System

In this chapter we consider the two-dimensional transverse magnetic (TM) mode. The non-dimensionalized Maxwell's equations in 2-D for the TM case are:

$$\frac{\partial W}{\partial t} = A\frac{\partial W}{\partial x} + B\frac{\partial W}{\partial y} \ , \tag{7.1}$$

where $W = (H_x, H_y, E_z)^T$ and

$$A = \begin{pmatrix} 0 & 0 & 0 \\ 0 & 0 & 1 \\ 0 & 1 & 0 \end{pmatrix}, \quad B = \begin{pmatrix} 0 & 0 & -1 \\ 0 & 0 & 0 \\ -1 & 0 & 0 \end{pmatrix} . \tag{7.2}$$

7.2.1 An Ill-formed PML Method

We illustrate this approach in the setting of designing a PML method for a parallelogram computational domain with a parallelogram vacuum-layer interface. The interface consists of segments of lines $y = \pm C$ and $x - y = \pm C'$ with C and C' being constants. By considering the following transformation:

$$\begin{aligned} \xi &= x - y \ , \\ \eta &= y \ , \end{aligned} \tag{7.3}$$

we can transform the parallelogram interface to a rectangular interface in the $\xi - \eta$ plane. Note that we have the following

$$\begin{aligned} \xi_x &= 1, \quad \xi_y = -1 \ , \\ \eta_x &= 0, \quad \eta_y = 1 \ , \\ x_\xi &= 1, \quad x_\eta = 1 \ , \\ y_\xi &= 0, \quad y_\eta = 1 \ , \end{aligned} \tag{7.4}$$

for the transformation. Formally, one can easily derive a PML method in $\xi - \eta$ coordinates:

$$\begin{aligned} \frac{\partial H_x}{\partial t} &= \frac{\partial (E_{z\xi} + E_{z\eta})}{\partial \xi} - \frac{\partial (E_{z\xi} + E_{z\eta})}{\partial \eta} - F_\xi H_y - G_\eta (H_x - H_y) \ , \\ \frac{\partial H_y}{\partial t} &= \frac{\partial (E_{z\xi} + E_{z\eta})}{\partial \xi} - F_\xi H_y \ , \\ \frac{\partial E_{z\xi}}{\partial t} &= \frac{\partial (H_y + H_x)}{\partial \xi} - F_\xi E_{z\xi} \ , \\ \frac{\partial E_{z\eta}}{\partial t} &= -\frac{\partial H_x}{\partial \eta} - G_\eta E_{z\eta} \ . \end{aligned} \tag{7.5}$$

Moreover, let

$$\alpha = \cos\theta, \ \beta = \sin\theta \ , \tag{7.6}$$

with θ being the incident angle of the plane wave, one can verify that the following plane wave solutions:

$$
\begin{aligned}
H_x &= \beta(E_{z\eta} + E_{z\xi}) \ , \\
H_y &= -\alpha(E_{z\eta} + E_{z\xi}) \ , \\
E_{z\eta} &= \beta(\alpha+\beta)e^{i\omega(t-\alpha x-\beta y)}e^{-f(x,y)\alpha - g(x,y)\beta} \ , \\
E_{z\xi} &= (\alpha-\beta)\alpha e^{i\omega(t-\alpha x-\beta y)}e^{-f(x,y)\alpha - g(x,y)\beta} \ .
\end{aligned}
\tag{7.7}
$$

where

$$
\begin{aligned}
f(x,y) &= F(\xi) + G(\eta) \ , \\
g(x,y) &= G(\eta) \ ,
\end{aligned}
\tag{7.8}
$$

are indeed solutions of the PML equations by noticing

$$
\begin{aligned}
\frac{\partial f(x,y)}{\partial \xi} &= F_\xi(\xi)\frac{\partial x}{\partial \xi} \ , \\
\frac{\partial g(x,y)}{\partial \xi} &= F_\xi(\xi)\frac{\partial y}{\partial \xi} \ , \\
\frac{\partial f(x,y)}{\partial \eta} &= G_\eta(\eta)\frac{\partial x}{\partial \eta} \ , \\
\frac{\partial g(x,y)}{\partial \eta} &= G_\eta(\eta)\frac{\partial y}{\partial \eta} \ .
\end{aligned}
\tag{7.9}
$$

By choosing $F(\xi)$ and $G(\eta)$ appropriately, one can easily make the plane wave solutions of the PML equations satisfy the property that H_x, H_y, and $E_{z\xi} + E_{z\eta}$ match perfectly with the non-decaying plane wave solutions H_x, H_y, and E_z respectively at the parallelogram vacuum-layer interface. The plane wave solutions also seem to decay exponentially if

$$
F(\xi) > 0, \ G(\eta) > 0 \ , \tag{7.10}
$$

in the layer region away from the interface.

Hence we have obtained a PML that matches perfectly with free space at the vacuum-layer interface, and the decaying plane wave solutions have a decaying factor that decays exponentially. But this absorbing layer has an unsatisfying drawback, that is, the plane wave solutions do not

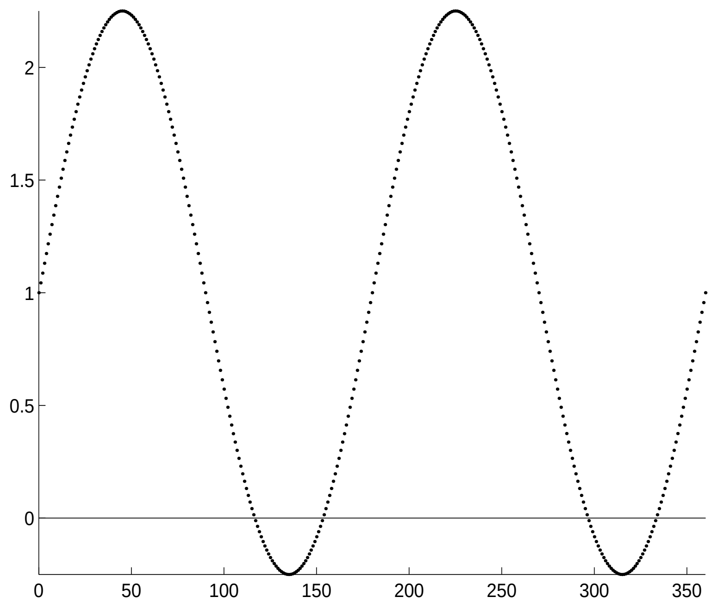

Figure 7.1: The variation of $\alpha^2 - \alpha\beta$ (in the directional derivative of the decaying factor) with the wave propagation angle θ.

decay in all directions of propagation. To see this, let us examine the directional derivative of the decaying factor in the layer region where $G_\eta(\eta) = 0$:

$$
\begin{aligned}
&\frac{\partial e^{-f(x,y)\alpha - g(x,y)\beta}}{\partial \mathbf{l}} \\
&= -F_\xi(\xi)(x_\xi \xi_x \alpha^2 + (x_\xi \xi_y + y_\xi \xi_x)\alpha\beta + y_\xi \xi_y \beta^2) \\
&= -F_\xi(\xi)(\alpha^2 - \alpha\beta) \ .
\end{aligned}
$$

Since $\alpha^2 - \alpha\beta$ changes sign for $\theta \in [0, 2\pi]$, the decaying factor can both decrease and increase in directions of wave propagation. In Fig. (7.1) we plot the values of $\alpha^2 - \alpha\beta$ for $\theta \in [0, 2\pi]$. The plane waves will increase in the layer when the values are negative.

7.2.2 A Multidomain Approach

Knowing that the straightforward approach in designing a PML with a parallelogram vacuum-layer interface is not satisfying, we want to study an alternative approach for the same problem that may seem to be imperfect at first, but is actually a better approach for this type of problems where a vacuum-layer interface other than a rectangle is desired, which is verified in our numerical experiments.

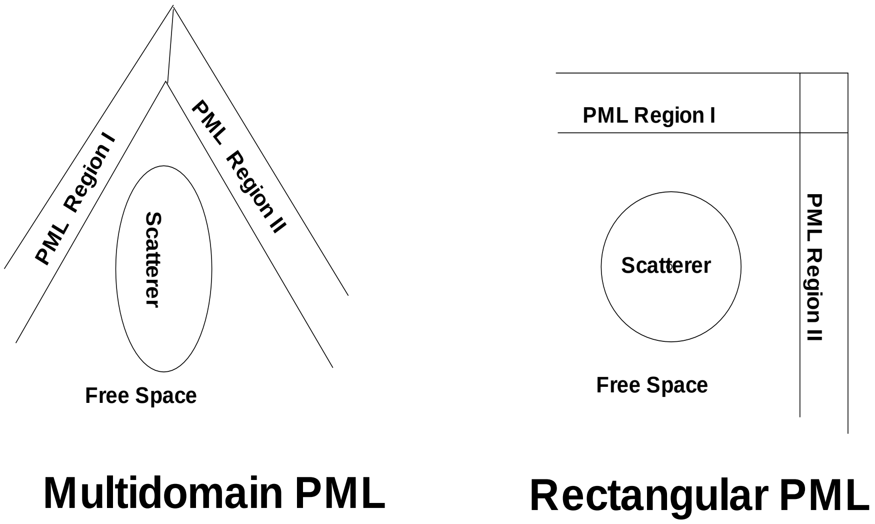

Figure 7.2: A multidomain implementation of the PML method: two neighboring PML regions.

What we propose is a multi-domain approach for the application of PML method in polygonal computational domain with a polygonal vacuum-layer interface. One can easily apply it with multidomain schemes. However, it is an absorbing layer method, defined by differential equations in layer regions, that should be applicable with other numerical methods. In Fig. 7.2, we give an illustrative figure to show the design of two neighboring PML regions. Note that the layer-layer interface is chosen such that it lies on the line dividing the angle at the vertex by half. Each PML region is bounded by 4 straight lines with one of them being the vacuum-layer interface, one of them being the outer boundary, and two others being the layer-layer interfaces.

In the PML region, the following orthogonal transformation is applied:

$$\begin{aligned} \xi &= x\cos\theta + y\sin\theta \ , \\ \eta &= -x\sin\theta + y\cos\theta \ , \end{aligned} \tag{7.11}$$

with θ being the angle between the vacuum-layer interface and the x axis. Correspondingly, the following split-field equations are solved in the PML region:

$$\begin{aligned}
\frac{\partial H_\xi}{\partial t} &= -\frac{\partial (E_{z\xi}+E_{z\eta})}{\partial \eta} - G_\eta H_\xi \quad , \\
\frac{\partial H_\eta}{\partial t} &= \frac{\partial (E_{z\xi}+E_{z\eta})}{\partial \xi} - F_\xi H_\eta \quad , \\
\frac{\partial E_{z\xi}}{\partial t} &= \frac{\partial H_\xi}{\partial \xi} - F_\xi E_{z\xi} \quad , \\
\frac{\partial E_{z\eta}}{\partial t} &= -\frac{\partial H_\eta}{\partial \eta} - G_\eta E_{z\eta} \quad ,
\end{aligned} \tag{7.12}$$

where

$$\begin{aligned}
H_\xi &= \cos\theta H_x + \sin\theta H_y \quad , \\
H_\eta &= -\sin\theta H_x + \cos\theta H_y \quad .
\end{aligned} \tag{7.13}$$

In the layer region, we are assured that the plane wave solutions decay in all directions of propagation that is not the grazing direction, which is proved in the following.

Theorem 7.2.1 *If $f(x,y)$ and $g(x,y)$ satisfy the following conditions,*

$$\begin{aligned}
\frac{\partial f(x,y)}{\partial \xi} &= C(\xi,\eta)\frac{\partial x}{\partial \xi} \quad , \\
\frac{\partial g(x,y)}{\partial \xi} &= C(\xi,\eta)\frac{\partial y}{\partial \xi} \quad , \\
\frac{\partial f(x,y)}{\partial \eta} &= D(\xi,\eta)\frac{\partial x}{\partial \eta} \quad , \\
\frac{\partial g(x,y)}{\partial \eta} &= D(\xi,\eta)\frac{\partial y}{\partial \eta} \quad ,
\end{aligned} \tag{7.14}$$

with

$$C(\xi,\eta) \geq 0, \;\; D(\xi,\eta) \geq 0 \quad , \tag{7.15}$$

and if the curvilinear coordinates are orthogonal, i.e.

$$\nabla\xi \cdot \nabla\eta = 0 \quad , \tag{7.16}$$

we have

$$\frac{\partial e^{-f(x,y)\alpha - g(x,y)\beta}}{\partial \mathbf{l}} \leq 0 \quad , \tag{7.17}$$

where $\mathbf{l} = (\alpha,\ \beta)$.

Proof: *A sketch of the proof is giving in the following:*

$$\frac{\partial e^{-f(x,y)\alpha - g(x,y)\beta}}{\partial \mathbf{l}}$$

$$= -[\alpha(f_x\alpha + g_x\beta) + \beta(f_y\alpha + g_y\beta)]e^{-f(x,y)\alpha - g(x,y)\beta}$$

$$= -[f_x\alpha^2 + (f_y + g_x)\alpha\beta + g_y\beta^2]e^{-f(x,y)\alpha - g(x,y)\beta}$$

$$= -[(f_\xi\xi_x + f_\eta\eta_x)\alpha^2 + (f_\xi\xi_y + f_\eta\eta_y + g_\xi\xi_x + g_\eta\eta_x)\alpha\beta + (g_\xi\xi_y + g_\eta\eta_y)\alpha^2]e^{-f(x,y)\alpha - g(x,y)\beta}$$

$$= -[(C(\xi,\eta)x_\xi\xi_x + D(\xi,\eta)x_\eta\eta_x)\alpha^2 + (C(\xi,\eta)(x_\xi\xi_y + y_\xi\xi_x) + D(\xi,\eta)(x_\eta\eta_y + y_\eta\eta_x))\alpha\beta$$

$$+(C(\xi,\eta)y_\xi\xi_y + D(\xi,\eta)y_\eta\eta_y)\beta^2]e^{-f(x,y)\alpha - g(x,y)\beta}$$

$$= -[C(\xi,\eta)(x_\xi\xi_x\alpha^2 + (x_\xi\xi_y + y_\xi\xi_x)\alpha\beta + y_\xi\xi_y\beta^2)$$

$$+D(\xi,\eta)(x_\eta\eta_x\alpha^2 + (x_\eta\eta_y + y_\eta\eta_x)\alpha\beta + y_\eta\eta_y\beta^2)]e^{-f(x,y)\alpha - g(x,y)\beta}$$

$$= -[C(\xi,\eta)(\sqrt{x_\xi\xi_x}\alpha + \sqrt{y_\xi\xi_y}\beta)^2$$

$$+D(\xi,\eta)(\sqrt{x_\eta\eta_x}\alpha + \sqrt{y_\eta\eta_y}\beta)^2]e^{-f(x,y)\alpha - g(x,y)\beta} \quad .$$

Because the PML-PML interface shown in Fig. 7.2 is set to lie on the line that divides the angle at the vertex by half, we have the following observations. First, if the the propagation direction of the plane wave solution is along the PML-PML interface, then the corresponding decaying plane wave solutions in PML region I and in PML region II can be matched with each other, with the proper choice of the decaying parameters. Second, any plane wave that has incident angle not parallel to the interface gets reflected at the layer interface and will get decayed eventually in the same PML region. The only direction that the plane wave solution does not decay is the η direction, but plane waves propagating in the η direction will be reflected at the layer-layer interface and the new propagation direction is in the direction other than the η direction.

With this multi-domain approach, one can have the flexibility of using essentially body conforming polygonal vacuum-layer interface instead of rectangular vacuum-layer interface, while preserving the property that the plane wave solutions in the PML regions decay in any propagation direction that is not the grazing direction. In practical computation, this approach is found to have a better performance that the approach using the non-orthogonal PML method in designing the non-rectangular PML, i.e. the ill-formed PML method.

7.3 Solutions of Maxwell's Equations with Absorbing Terms

In this section, we discuss the solutions of Maxwell's equations with low-order absorbing terms. The normalized Maxwell's equations, Eq. (7.1), have the following plane wave solutions:

$$\begin{cases} H_x = \sin\phi e^{i\omega(t-x\cos\phi-y\sin\phi)} \\ H_y = -\cos\phi e^{i\omega(t-x\cos\phi-y\sin\phi)} \\ E_z = e^{i\omega(t-x\cos\phi-y\sin\phi)} \end{cases}, \tag{7.18}$$

with ϕ being the angle of propagation of the plane wave.

Now we consider the plane wave solutions with a decaying factor of the following general form

$$e^{-f(x,y)\cos\phi-g(x,y)\sin\phi},$$

and we want the decaying waves to be the solutions of the Maxwell's equations plus some low-order absorbing terms. The result is concluded in the following lemma.

Lemma 7.3.1 *The following plane wave solutions*

$$\begin{cases} H_x = \sin\phi e^{i\omega(t-x\cos\phi-y\sin\phi)} e^{-f(x,y)\cos\phi-g(x,y)\sin\phi} \\ H_y = -\cos\phi e^{i\omega(t-x\cos\phi-y\sin\phi)} e^{-f(x,y)\cos\phi-g(x,y)\sin\phi} \\ E_z = e^{i\omega(t-x\cos\phi-y\sin\phi)} e^{-f(x,y)\cos\phi-g(x,y)\sin\phi} \end{cases}, \tag{7.19}$$

are the solutions of the following equations

$$\begin{cases} \frac{\partial H_x}{\partial t} = -\frac{\partial E_z}{\partial y} - g_y(x,y)H_x + f_y(x,y)H_y \\ \frac{\partial H_y}{\partial t} = \frac{\partial E_z}{\partial x} + g_x(x,y)H_x - f_x(x,y)H_y \\ \frac{\partial E_z}{\partial t} = \frac{\partial H_y}{\partial x} - \frac{\partial H_x}{\partial y} - f_x(x,y)E_z \end{cases}, \tag{7.20}$$

if and only if

$$w(z) = f(x,y) + g(x,y)\mathbf{i} \ ,$$

where $z = x + y\mathbf{i}$*, is an analytic function.*

Proof: *We prove the lemma for the third equation. Since* E_z *satisfies*

$$\frac{\partial E_z}{\partial t} = i\omega E_z \tag{7.21}$$

and

$$\begin{aligned}
\tfrac{\partial H_y}{\partial x} & -\tfrac{\partial H_x}{\partial y} - f_x(x,y)E_z = \\
& i\omega \cos^2\phi E_z + f_x(x,y)E_z\cos^2\phi + g_x(x,y)E_z\cos\phi\sin\phi \\
& +i\omega\sin^2\phi E_z + f_y(x,y)E_z\cos\phi\sin\phi + g_y(x,y)E_z\sin^2\phi - f_x(x,y)E_z \\
& = i\omega E_z + f_x(x,y)E_z\cos^2\phi + g_y(x,y)E_z\sin^2\phi \\
& +E_z\cos\phi\sin\phi(g_x(x,y) + f_y(x,y)) - f_x(x,y)E_z
\end{aligned} \tag{7.22}$$

We have

$$\frac{\partial H_y}{\partial x} - \frac{\partial H_x}{\partial y} - f_x(x,y)E_z = i\omega E_z \tag{7.23}$$

if and only if $w(z)$ *is analytic function,*

$$\frac{\partial f(x,y)}{\partial x} = \frac{\partial g(x,y)}{\partial y}, \quad \frac{\partial f(x,y)}{\partial y} = -\frac{\partial g(x,y)}{\partial x} \ . \tag{7.24}$$

Comparing (7.21) and (7.23), we have the conclusion that the third equation is satisfied if and only if $w(z)$ *is an analytic function. For the first and second equations, it is more straightforward to check that the same result holds.*

An energy estimate of the wave equations in (7.20) can be obtained. In fact, we have

$$
\begin{aligned}
&\tfrac{1}{2}\tfrac{\partial}{\partial t}(H_x^2 + H_y^2 + E_z^2) \\
&= H_x \tfrac{\partial H_x}{\partial t} + H_y \tfrac{\partial H_y}{\partial t} + E_z \tfrac{\partial E_z}{\partial t} \\
&= -H_x \tfrac{\partial E_z}{\partial y} - g_y H_x H_x + f_y H_x H_y + H_y \tfrac{\partial E_z}{\partial x} + g_x H_y H_x - f_x H_y H_y \\
&\quad + E_z \tfrac{\partial H_y}{\partial x} - E_z \tfrac{\partial H_x}{\partial y} - f_x E_z E_z \\
&= -\tfrac{\partial (H_x E_z)}{\partial y} + \tfrac{\partial (H_y E_z)}{\partial y} - f_x (H_x^2 + H_y^2 + E_z^2)
\end{aligned}
\tag{7.25}
$$

For problems with periodic boundary conditions, we have

$$
\frac{1}{2}\frac{\partial}{\partial t}(H_x^2 + H_y^2 + E_z^2) < 0 \tag{7.26}
$$

as long as

$$
\frac{\partial f(x,y)}{\partial x} > 0 \ . \tag{7.27}
$$

7.4 An Approximately Matched Absorbing Layer

In this section we give an absorbing layer that is approximately matched at the vacuum-layer interface. However, the difference between the decaying and non-decaying plane wave solutions at the interface can be reduced exponentially, with the choice of a parameter. The advantage of the absorbing layer is that one only needs to solve Maxwell's equations with absorbing terms in the layer. We shall show that if the layer has the desired absorbing property in the layer region, namely plane wave solutions decay in all direction of propagation, the absorbing layer is effective, since both incident waves and the waves reflected at the outer boundary can be absorbed in it. The reflection at the vacuum-layer interface can be controlled by reducing the difference between the non-decaying plane wave solutions and the decaying plane wave solutions.

Lemma 7.4.1 *If $f(x,y)$ and $g(x,y)$ satisfy Cauchy-Riemann condition and also satisfy the following condition*

$$\frac{\partial f(x,y)}{\partial x} = \frac{\partial g(x,y)}{\partial y} > 0, \tag{7.28}$$

then the wave solutions (7.19) decay exponentially in every propagation direction as

$$\frac{\partial}{\partial \mathbf{l}} e^{-f(x,y)\cos\phi - g(x,y)\sin\phi} > 0 \ , \tag{7.29}$$

where $\mathbf{l} = (\cos\phi, \sin\phi)$ is the normalized wave vector.

Proof:

$$\begin{aligned} & \tfrac{\partial}{\partial \mathbf{l}} e^{-f(x,y)\cos\phi - g(x,y)\sin\phi} \\ = & \left(-\tfrac{\partial f(x,y)}{\partial x}\cos^2\phi - \tfrac{\partial g(x,y)}{\partial y}\sin^2\phi - \left(\tfrac{\partial f(x,y)}{\partial y} + \tfrac{\partial g(x,y)}{\partial x}\right)\sin\phi\cos\phi\right) \\ & e^{-f(x,y)\cos\phi - g(x,y)\sin\phi} \\ = & -\tfrac{\partial f(x,y)}{\partial x} e^{-f(x,y)\cos\phi - g(x,y)\sin\phi} \ . \end{aligned} \tag{7.30}$$

Hence we have

$$\frac{\partial}{\partial \mathbf{l}} e^{-f(x,y)\cos\phi - g(x,y)\sin\phi} < 0 \ . \tag{7.31}$$

Aside from having good absorbing properties in the layer region, it is also important for the layer to have satisfying, if imperfect, matching condition at the vacuum-layer interface. For the approximately matched layer, the plane wave solution with an exponential factor (7.19) can not match exactly with the plane wave solutions in the free space (7.18) on any continuous line or curve, which can be seen in the following lemma.

Lemma 7.4.2

$$e^{-f(x,y)\cos\phi - g(x,y)\sin\phi} \equiv 1, \ \textit{for all } \phi \tag{7.32}$$

can **not** *be true on any continuous line or curve.*

This is obvious due to the fact that an analytic function can not equal to 0 on any continuous line or curve.

Though the plane wave solutions can not be matched exactly at the continuous interface, we are pursuing an alternative approach here to find some kind of approximate matching for the solutions, i.e.

$$e^{-f(x,y)\cos\phi - g(x,y)\sin\phi} \approx 1, \text{ for all } \phi \tag{7.33}$$

at the vacuum-layer interface. The reflections at the interface may be made smaller by using a better approximation then. It is optimal that the difference can be made exponentially small at the interface. Thus the influence of the absorbing layer on the electromagnetic fields can be made exponentially small at the interface.

In the following lemma, we give a relation between the order of the analytical function and the matching condition at the vacuum-layer interface which is assumed to be a unit circle.

Lemma 7.4.3 *Suppose*

$$w(z) \to Cz^n \text{ as } z \to \infty \tag{7.34}$$

for a constant C and

$$|w(z)| < \epsilon \ , \ |z| = 1 \ , \tag{7.35}$$

for a small constant ϵ, then we have

$$|w(z)| < \epsilon |z^n| \text{ as } z \to \infty \tag{7.36}$$

Proof: *Let*

$$v(z) = \frac{w(z)}{z^n} \ , \tag{7.37}$$

we have

$$v(z) \to C \ as \ z \to \infty \ . \tag{7.38}$$

Hence $v(z)$ is analytical in $|z| \geq 1$. Now we introduce the transformation

$$s = \frac{1}{z} \ . \tag{7.39}$$

Clearly, $v(s)$ is analytical in $|s| \leq 1$. Hence we have

$$|v(s)| < \epsilon \ , \ |s| \leq 1 \ , \tag{7.40}$$

i.e.

$$|w(z)| < \epsilon |z^n| \ as \ z \to \infty \tag{7.41}$$

This lemma essentially implies that for $w(z)$ to be exponentially small at the vacuum-layer interface, $|z| = 1$, and have a magnitude above a desired level in the outside region of the layer, $w(z)$ must grow exponentially. For the vacuum-layer interface that is a line, the same result holds since a line can be mapped into the unit circle analytically.

For our analytically matched layer, the function $w(z)$ is then chosen as

$$w(z) = e^{c(z-z_0)} = e^{c(x-x_0)} \cos(c(y-y_0)) + e^{c(x-x_0)} \sin(c(y-y_0))\mathbf{i} \ , \tag{7.42}$$

where $z_0 = x_0 + y_0\mathbf{i}$ and c are constants. Suppose that the vacuum-layer interface is the line $x = 0$, we can choose

$$x_0 > 0 \ , \ c > 0 \ , \tag{7.43}$$

and $w(z)$ decreases exponentially as x_0 and c increase.

For the purpose of the absorption of plane waves in every propagation direction, $w(z)$ needs to satisfy condition (7.28). This is only true for

$$-\frac{\pi}{2} < c(y - y_0) < \frac{\pi}{2} \ . \tag{7.44}$$

Note that in practical computations, the computational domain is of fixed size and we can always choose the constant c and y_0 to make inequality (7.44) hold. Moreover, one can use a multi-domain implementation which will be given in the following section.

7.5 Numerical Implementations and Results

The AML method can be easily extended to the cases where the vacuum-layer interface is an arbitrary straight line. Basically, one only needs to consider the analytical function

$$w(z) = e^{c(z-z_0)e^{\theta\mathbf{i}}} \ , \tag{7.45}$$

with the rotation angle θ being arbitrary. The equations and the solutions are similar. In our numerical examples, we test AML methods having vacuum-layer interfaces that are a square, a parallelogram, and a triangle.

To enhance the efficiency of the AML method, a multidomain implementation of the AML method is given in this section. In Fig. 7.3, we decompose the layer region into a number of strips along the x direction that have the same width d, i.e.

$$y_1 \le y \le y_2 \text{ with } y_2 - y_1 = d , \cdots , \tag{7.46}$$

and implementing the AML method in each strip by choosing the imaginary part of z_0 the central y coordinate, e.g.

$$y_0 = \frac{y_1 + y_2}{2} . \tag{7.47}$$

Note that the vacuum-layer interface in the figure is in the y direction.

With this implementation, we can have a wider choice for the constant c to maintain the absorbing strength we want, i.e. the magnitude of $e^{cx}\cos(cy)$, since the range of y becomes smaller.

For this implementation, we need to consider the matching condition at the strip interfaces. We have several observations. First, if the plane wave propagates along the strip interface, $\sin\phi = 0$, we have

$$E_z = e^{i\omega(t - x\cos\phi)} e^{-f(x,y)\cos\phi} , \tag{7.48}$$

then the corresponding decaying wave matches at the interface because $e^{c(x-x_0)}\cos(c\frac{d}{2}) = e^{c(x-x_0)}\cos(c\frac{-d}{2})$. Second, the magnitude of $e^{c(x-x_0)}\sin(c\frac{d}{2})$ approaches 0 if d approaches 0. Generally speaking, we may let $e^{cx}\sin(c\frac{d}{2})$ have a much smaller magnitude than $e^{cx}\cos(c\frac{d}{2})$. Last, even if the wave approaches the strip interface with an angle and gets reflected there, it will get decayed within the strip eventually due to the absorbing property of the AML.

The main numerical scheme we use in this work is the pseudo-spectral multi-domain Chebyshev-Chebyshev scheme. The scheme has been sucessfully used with various PML methods in electromagnetic wave scattering simulations [57] and is introduced in chapter 6.

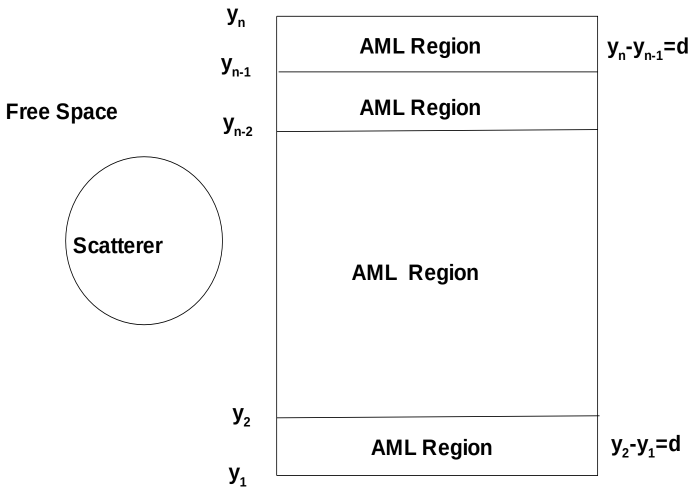

Figure 7.3: A multidomain implementation of the AML method.

7.6 Numerical Experiments

For numerical experiments, we consider the TM case of 2-D wave scattering by perfect electrically conducting cylinders. Due to the linearity of Maxwell's equations, we only compute the purely scattered field by using the boundary condition, $(E_z)_{\text{sc}} = -(E_z)_{\text{inc}}$, at the cylinder surface. Denote the wave number of the incident wave as k. In all the following numerical examples, we take $k = 2\pi$.

The radar cross section (RCS) is adopted as a main criterion for assessing the accuracy of the computation. A near-to-far field transformation is used to get the far-field RCS from the near-field values, see [51]. The RCS is validated in two ways. The near-to-far-field transformation results and the corresponding RCS computed along different closed contours should be the same up to numerical error. The accuracy of the RCS can also be evaluated by comparing with reference values.

7.6.1 Scattering by Rectangular and Circular PEC Cylinders

We first test various absorbing layer methods with rectangular vacuum-layer interfaces, where the original rectangular PML method is also applicable and can serve as a comparison.

The first example we consider is scattering by a square PEC cylinder, whose sides have length

Table 7.1: Comparison of the discrete L_2 RCS error and the computation time of the rectangular PML method and the AML method.

Error	PML Method	AML Method	Mesh
RCS Error (dB)	0.0161	0.0165	N=16, K=12
Computation Time (second)	417	373	N=16, K=12

Table 7.2: Comparison of the discrete L_2 RCS error and the computation time of the rectangular PML method and the AML method.

Error	PML Method	AML Method	Mesh
RCS Error (dB)	0.0153	0.0159	N=16, K=12
Computation Time (second)	417	365	N=16, K=12

equal to 1. The vacuum-layer interface for the AML method is a square. For this example, we use the RCS obtained by the MOM method as reference. We compare the accuracy and the computation time of the AML method and the rectangular PML method in Table 7.1. Both computations terminate after 30 wave periods. The result clearly shows that the AML method is as accurate as the PML method and needs less computation time. The AML method also needs less memory since the unsplit-field equations were solved.

The second example we consider is scattering by a circular PEC cylinder, whose radius is 0.5. The vacuum-layer interface for the AML method is a square. For this example, we use the RCS obtained by evaluating the exact analytical solution as reference. For a computational mesh of this simulation, one can refer to Fig. 6.12 in chapter 6. The comparison of the accuracy of AML method and rectangular PML method is given in Table 7.2.

7.6.2 Scattering by a Parallelogram PEC Cylinder

Now we simulate the electromagnetic wave scattering by a parallelogram PEC cylinder. The parallelogram is bounded by $x - y = -0.5$, $x - y = 0.5$, $y = -0.5$ and $y = 0.5$. For this simulation, it is natural and efficient to design an absorbing layer with a parallelogram vacuum-layer interface. A computational mesh is shown in Fig. 7.4, where an absorbing layer is put in the outer subdomains. For the absorbing layer, we compare the AML method and the ill-formed PML method where the non-Cartesian coordinate transformation given in Eq. (7.3). is applied.

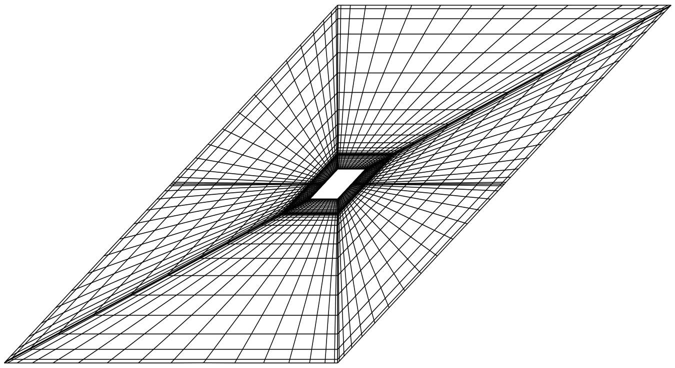

Figure 7.4: The mesh used for simulating scattering by a parallelogram cylinder.

For reference, we also compute the same problem using the FD-TD method with a very fine rectangular mesh, 860×640. The perfectly conducting parallelogram cylinder is modeled as a cylinder with permittivity equal to that of free space but with a very high conductivity. A 32-cell rectangular PML is used to terminate the computational mesh, which is necessarily non-conforming to the cylinder surface. The radar cross sections are shown in Fig. 7.5.

The result clearly shows the effectiveness of the AML method with parallelogram interface, which is much more accurate than the ill-formed PML method. It takes 8000 seconds to compute the reference RCS using FD-TD method with PML, while it takes only 288 seconds for the computation using the spectral method with AML. Both computations terminate after 15 wave periods or so.

7.6.3 Scattering by a Triangular PEC Cylinder

The last example we consider is scattering by a triangular PEC cylinder, whose sides are all one wavelength long. The vacuum-layer interface for the AML method is a triangle. For this example, we use the numerical RCS obtained by using a very large computational domain as reference. For the reference computation, the computational is so large that no reflection can propagate back to the area of computational interest. The computational grid is shown in Fig. (7.6). For simplicity, we use one layer of subdomains to surround the triangle. In each subdomain, we use a 32×32 mesh.

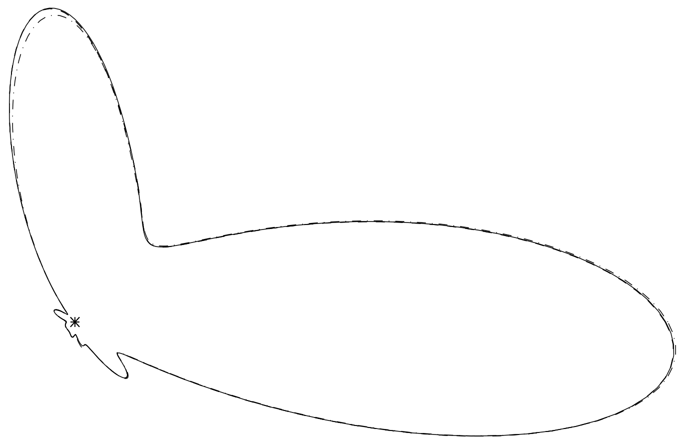

Figure 7.5: Radar cross section of scattering by a parallelogram cylinder simulated by the AML method, dashed line, and the ill-formed PML method, dash-dotted line, compared with the reference, solid line.

The AML is applied in the region outside the triangle DEF. In Fig. (7.7) we plot the RCS result for this computation and the reference RCS result. They agree with each other very well.

Further computation suggests that one can obtain even more accurate result with the AML method when one refines the mesh. In Fig. (7.8) we show the RCS result for computations using a finer mesh ($56 \times 56 \times 56$). From the figure, we can see no difference between the RCS results.

One can also apply the Multidomain PML method and obtain very accurate results in this simulation. This is shown in Fig. 7.9.

7.7 Conclusions

The purposes of this chapter are to find the appropriate approach to extend the rectangular PML method to computational domains with a polygonal vacuum-layer interface, and to propose an approximately matched layer method that is comparable to the rectangular PML method that can be applied easily with a non-rectangular vacuum-layer interface. The method has the advantage of solving the original Maxwell's equations with low-order absorbing terms only.

This chapter also points out the importance of decaying in all directions of wave propagation

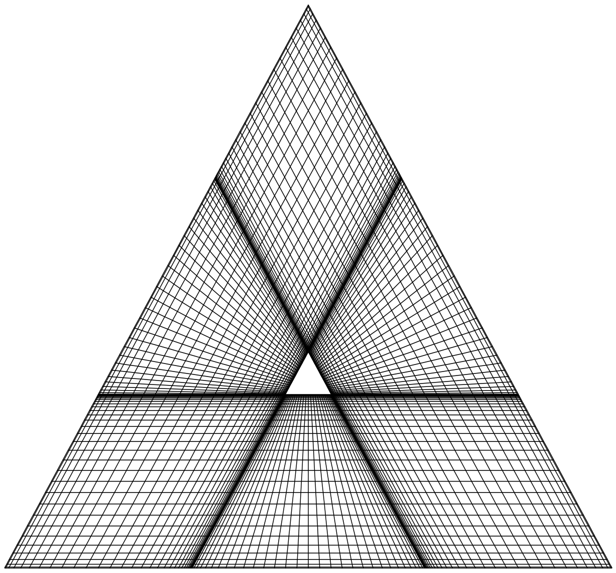

Figure 7.6: The computational mesh used for simulating scattering by a triangular cylinder.

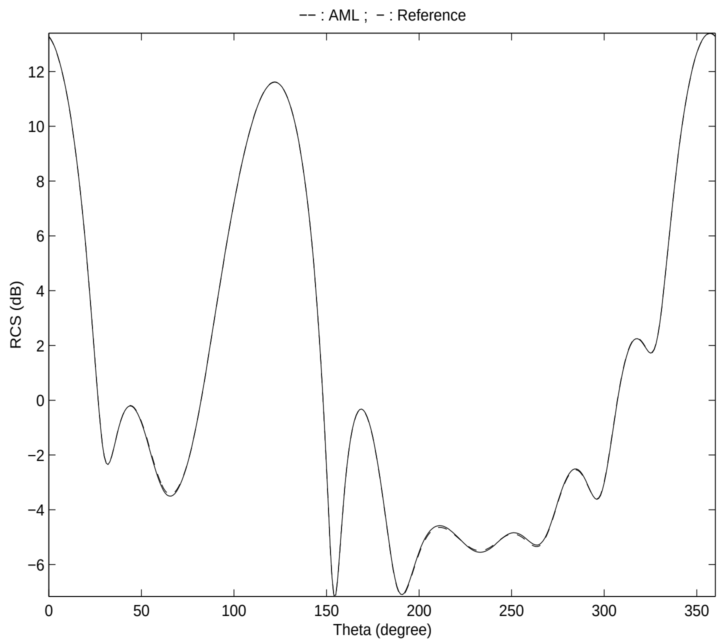

Figure 7.7: Radar cross section of scattering by a triangular cylinder simulated by the AML method, dashed line, and the reference, solid line.

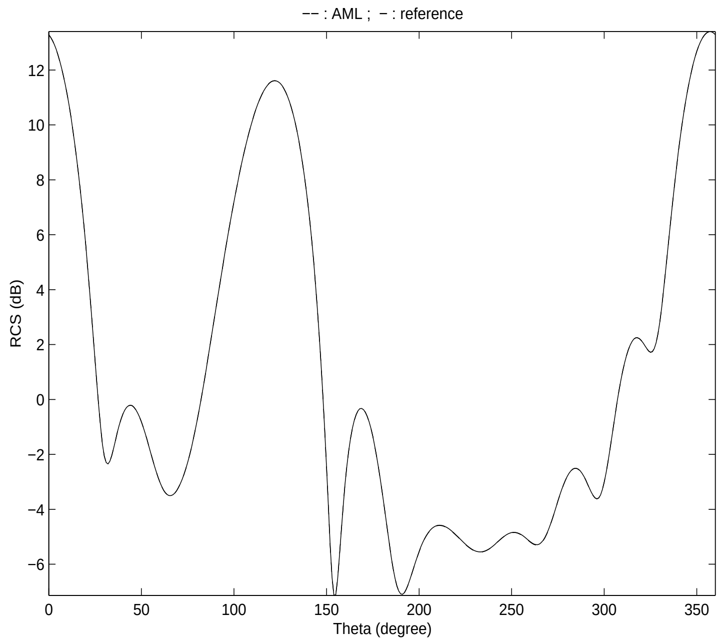

Figure 7.8: Radar cross section of scattering by a triangular cylinder simulated by the AML method with a fine mesh, dashed line, and the reference, solid line.

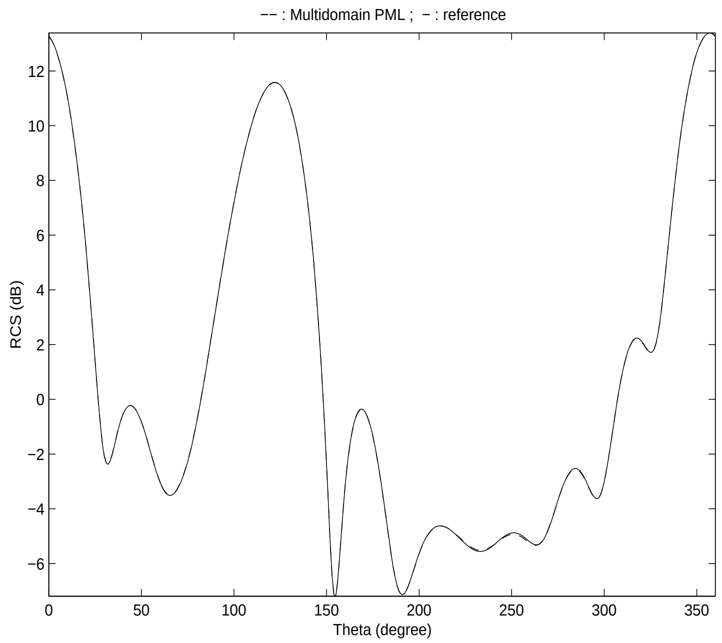

Figure 7.9: Radar cross section of scattering by a triangular cylinder simulated by the multidomain PML method, dashed line, and the reference, solid line.

property for PML methods. An ill-formed PML that does not have this property is found to give unsatisfying result in numerical computation. On the other hand, the multidomain PML method, which is not perfectly matched at the layer-layer interface, ant the AML method that have the property in the layer is found to give much better numerical results.

In numerical examples, we simulate scattering by PEC cylinders of a circle, a square, a parallelogram, and a triangle cross sections. The numerical result clearly shows the efficacy of the multidomain PML and the multidomain AML methods, comparable to the rectangular PML method. The new methods have a more flexible vacuum-layer interface and the AML method also needs less computation time and less machine memory.

Chapter 8

Simulations of 3-D Electromagnetic Scattering

8.1 Introduction

The aim of this chapter is to devise a general approach for obtaining approximate solutions to electromagnetic wave problems in the general three dimensional domain, $\Omega \subset \mathsf{R}^3$, enclosed by the boundary $\delta\Omega$. To obtain such solutions we employ polynomial approximations, Chebyshev polynomial at present, of the electromagnetic fields and their spatial derivatives, with the most natural and computationally efficient extension to several dimensions through the use of tensor products. A multidomain approach is used in our scheme to reduce the complexity of the geometry.

In our simulation of electromagnetic scattering by simple 3-D objects in this chapter, the computational domain is the outer domain surrounding the object and terminated by artificial boundary. Since a body-oriented, curvilinear coordinate system can greatly facilitate the computations of electromagnetic fields around a complex scatterer, we cast Maxwell's equations in a general curvilinear coordinate system. The eigenvalue and eigenvector structure of the equations is analyzed, which is much needed in the patching of the solutions of our multidomain pseudospectral scheme.

As the use of proper absorbing boundary condition is crucial for accurate electromagnetic scattering simulations, we consider the absorbing layer methods, mainly the PML methods, which have been introduced in chapter 3 and been shown to be successful in chapter 6 for 2-D simulations. To better accommodate the absorbing layer in the mesh, the multidomain mesh we generate has multi-layers that surround the scatterer, with the absorbing layer being put in the out-most layer. We shall continue to show the superior accuracy of spectral methods in this chapter. We shall also validate all the 3-D PML methods we proposed in chapter 3.

8.2 The Equations

In chapter 2, we gave the free-space non-dimensionalized Maxwell's equations in 3-D. In general curvilinear coordinates the system of equations becomes

$$\frac{\partial \hat{W}}{\partial t} = \hat{A}\frac{\partial \hat{W}}{\partial \xi} + \hat{B}\frac{\partial \hat{W}}{\partial \eta} + \hat{C}\frac{\partial \hat{W}}{\partial \zeta} \ , \tag{8.1}$$

where $\hat{W} = J[H_x,\ H_y,\ H_z,\ E_x,\ E_y,\ E_z]^T$ with J being the transformation Jacobian, while

$$\hat{A} = \begin{pmatrix} 0 & 0 & 0 & 0 & -\xi_z & \xi_y \\ 0 & 0 & 0 & \xi_z & 0 & -\xi_x \\ 0 & 0 & 0 & -\xi_y & \xi_x & 0 \\ 0 & \xi_z & -\xi_y & 0 & 0 & 0 \\ -\xi_z & 0 & \xi_x & 0 & 0 & 0 \\ \xi_y & -\xi_x & 0 & 0 & 0 & 0 \end{pmatrix} , \tag{8.2}$$

$$\hat{B} = \begin{pmatrix} 0 & 0 & 0 & 0 & -\eta_z & \eta_y \\ 0 & 0 & 0 & \eta_z & 0 & -\eta_x \\ 0 & 0 & 0 & -\eta_y & \eta_x & 0 \\ 0 & \eta_z & -\eta_y & 0 & 0 & 0 \\ -\eta_z & 0 & \eta_x & 0 & 0 & 0 \\ \eta_y & -\eta_x & 0 & 0 & 0 & 0 \end{pmatrix} , \tag{8.3}$$

$$\hat{C} = \begin{pmatrix} 0 & 0 & 0 & 0 & -\zeta_z & \zeta_y \\ 0 & 0 & 0 & \zeta_z & 0 & -\zeta_x \\ 0 & 0 & 0 & -\zeta_y & \zeta_x & 0 \\ 0 & \zeta_z & -\zeta_y & 0 & 0 & 0 \\ -\zeta_z & 0 & \zeta_x & 0 & 0 & 0 \\ \zeta_y & -\zeta_x & 0 & 0 & 0 & 0 \end{pmatrix} . \tag{8.4}$$

We assume that $\xi_x^2 + \xi_y^2 + \xi_z^2 = 1$ such that the eigenvalues of matrix $\hat{A}$ are:

$$\lambda_1 = \lambda_2 = -1,\ \lambda_3 = \lambda_4 = 1,\ \text{and}\ \lambda_5 = \lambda_6 = 0\ . \tag{8.5}$$

Now we want to show how to diagonalize $\hat{A}$ in ξ. The diagonalization of $\hat{A}$ in other directions are similar. The two orthogonal unit eigenvectors corresponding to eigenvalue 0 are $[\xi_x,\ \xi_y,\ \xi_z,\ 0,\ 0,\ 0]^T$ and $[0,\ 0,\ 0, \xi_x,\ \xi_y,\ \xi_z]^T$. We also have two orthogonal eigenvectors corresponding to eigenvalue 1: $[-\xi_x\xi_y,\ \xi_x^2+\xi_z^2,\ -\xi_y\xi_z,\ \xi_z,\ 0,\ -\xi_x]^T$ and $[-\xi_z,\ 0,\ \xi_x, -\xi_x\xi_y,\ \xi_x^2+\xi_z^2,\ -\xi_y\xi_z]^T$. However, the eigenvectors degenerate to zero vectors when $\xi_x = \xi_z = 0$. In that case, we need to find other formulations for representing eigenvectors. The formulations we have are: $[\xi_y^2+\xi_z^2,\ -\xi_x\xi_y,\ -\xi_x\xi_z,\ 0,\ -\xi_z,\ \xi_y]$ and $[0,\ \xi_z,\ -\xi_y,\ \xi_y^2+\xi_z^2,\ -\xi_x\xi_y,\ -\xi_x\xi_z]$. The above eigenvectors are also orthogonal to each other and degenerate to zero vectors when $\xi_y = \xi_z = 0$. Hence we can choose one of the two sets of vectors as eigenvectors in all cases. If the eigenvalue is -1, the situation is similar.

To conclude, when $\xi_x \neq 0$ or $\xi_z \neq 0$, $\hat{A}$ can be diagonalized as $S^T \hat{A} S = \Lambda$ with Λ being a diagonal matrix, where

$$S^T = \begin{pmatrix} \frac{\xi_x\xi_y}{\sqrt{\xi_x^2+\xi_y^2}} & \frac{-\xi_x^2-\xi_z^2}{\sqrt{\xi_x^2+\xi_y^2}} & \frac{\xi_y\xi_z}{\sqrt{\xi_x^2+\xi_y^2}} & \frac{\xi_z}{\sqrt{\xi_x^2+\xi_y^2}} & 0 & -\frac{\xi_x}{\sqrt{\xi_x^2+\xi_y^2}} \\ -\frac{\xi_z}{\sqrt{\xi_x^2+\xi_y^2}} & 0 & \frac{\xi_x}{\sqrt{\xi_x^2+\xi_y^2}} & \frac{\xi_x\xi_y}{\sqrt{\xi_x^2+\xi_y^2}} & \frac{-\xi_x^2-\xi_z^2}{\sqrt{\xi_x^2+\xi_y^2}} & \frac{\xi_y\xi_z}{\sqrt{\xi_x^2+\xi_y^2}} \\ -\frac{\xi_x\xi_y}{\sqrt{\xi_x^2+\xi_y^2}} & \frac{\xi_x^2+\xi_z^2}{\sqrt{\xi_x^2+\xi_y^2}} & -\frac{\xi_y\xi_z}{\sqrt{\xi_x^2+\xi_y^2}} & \frac{\xi_z}{\sqrt{\xi_x^2+\xi_y^2}} & 0 & -\frac{\xi_x}{\sqrt{\xi_x^2+\xi_y^2}} \\ -\frac{\xi_z}{\sqrt{\xi_x^2+\xi_y^2}} & 0 & \frac{\xi_x}{\sqrt{\xi_x^2+\xi_y^2}} & -\frac{\xi_x\xi_y}{\sqrt{\xi_x^2+\xi_y^2}} & \frac{\xi_x^2+\xi_z^2}{\sqrt{\xi_x^2+\xi_y^2}} & -\frac{\xi_y\xi_z}{\sqrt{\xi_x^2+\xi_y^2}} \\ \xi_x & \xi_y & \xi_z & 0 & 0 & 0 \\ 0 & 0 & 0 & \xi_x & \xi_y & \xi_z \end{pmatrix}.$$

The diagonal entries of Λ are eigenvalues -1, -1, 1, 1, 0, and 0. When $\xi_y \neq 0$ or $\xi_z \neq 0$, $\hat{A}$ can be diagonalized with

$$S^T = \begin{pmatrix} -\frac{\xi_y^2+\xi_z^2}{\sqrt{\xi_y^2+\xi_z^2}} & \frac{\xi_x\xi_y}{\sqrt{\xi_y^2+\xi_z^2}} & \frac{\xi_x\xi_z}{\sqrt{\xi_y^2+\xi_z^2}} & 0 & -\frac{\xi_z}{\sqrt{\xi_y^2+\xi_z^2}} & \frac{\xi_y}{\sqrt{\xi_y^2+\xi_z^2}} \\ 0 & \frac{\xi_z}{\sqrt{\xi_y^2+\xi_z^2}} & -\frac{\xi_y}{\sqrt{\xi_y^2+\xi_z^2}} & -\frac{\xi_y^2+\xi_z^2}{\sqrt{\xi_y^2+\xi_z^2}} & \frac{\xi_x\xi_y}{\sqrt{\xi_y^2+\xi_z^2}} & \frac{\xi_x\xi_z}{\sqrt{\xi_y^2+\xi_z^2}} \\ \frac{\xi_y^2+\xi_z^2}{\sqrt{\xi_y^2+\xi_z^2}} & -\frac{\xi_x\xi_y}{\sqrt{\xi_y^2+\xi_z^2}} & -\frac{\xi_x\xi_z}{\sqrt{\xi_y^2+\xi_z^2}} & 0 & -\frac{\xi_z}{\sqrt{\xi_y^2+\xi_z^2}} & \frac{\xi_y}{\sqrt{\xi_y^2+\xi_z^2}} \\ 0 & \frac{\xi_z}{\sqrt{\xi_y^2+\xi_z^2}} & -\frac{\xi_y}{\sqrt{\xi_y^2+\xi_z^2}} & \frac{\xi_y^2+\xi_z^2}{\sqrt{\xi_y^2+\xi_z^2}} & -\frac{\xi_x\xi_y}{\sqrt{\xi_y^2+\xi_z^2}} & -\frac{\xi_x\xi_z}{\sqrt{\xi_y^2+\xi_z^2}} \\ \xi_x & \xi_y & \xi_z & 0 & 0 & 0 \\ 0 & 0 & 0 & \xi_x & \xi_y & \xi_z \end{pmatrix}.$$

The characteristic variables, $S^T W$, are needed for applying characteristic boundary condition.

8.3 Multi-domain Grid Generation

In the multidomain pseudospectral computations, the first step is to generate a multidomain Chebyshev mesh of the computational domain. Though grid generation for a general 3-D computational domain is not easy, it is not difficult to generate a 3-D computational mesh for either the inner domain or the outer domain of some simple objects such as cubes, spheres, and finite cylinders. However, the algorithms we develop in this chapter are desired to be suitable for multidomain pseudospectral computation with absorbing layers such as the PML methods or the mapped ML method. It is meaningful in many ways to isolate the absorbing layer in the mesh. Hence, we develop algorithms to generate multi-layer multidomain body-conforming meshes. One can also adjust the size of the computational domain and the grid point distribution of the mesh with a few parameters. Currently, the algorithm has been used to generate meshes to surround cubes, spheres, and finite cylinders.

Our mesh-generation algorithm consists of two main steps. The first step is the block generator, where the computational domain is decomposed into blocks that are diffeomorphic to the unit cube. In this step, we also specify the connection information among the blocks. The next step is to generate a mesh suitable for pseudospectral method computation in each block. The global map, that maps the block to the unit cube is established with the metric of transformation being computed. In the following, we introduce our algorithm according to the two main steps.

8.3.1 Block Generation

The first step of our block generator is to introduce some straight lines radiating from the scatterer that divide the outer domain surrounding the object into subdomains. Take the unit cube for an example, and introduce line segments starting from the corners of the cube and extending to some distance away depending one how large we want the computational domain to be. The lines divide the space evenly as illustrated in Fig. 8.1. The length of the dividing lines should be the same and we can terminate our computational domain with a cube whose vertices are the ending points of the dividing lines.

The next step is to decompose the computational domain to a number of layers. We truncate the line segments at equal distances so that the truncating points are vertices of a cube too. This cube naturally divides the computational domain surrounding the unit cube to an inner layer and an outer layer. Generating multi-layer blocks is particularly useful when we use the absorbing layer methods, since we can then apply the absorbing layer only in the blocks that lie in the out-most layer. Then in the inner-layer blocks we can solve the original Maxwell's equations. We also avoid

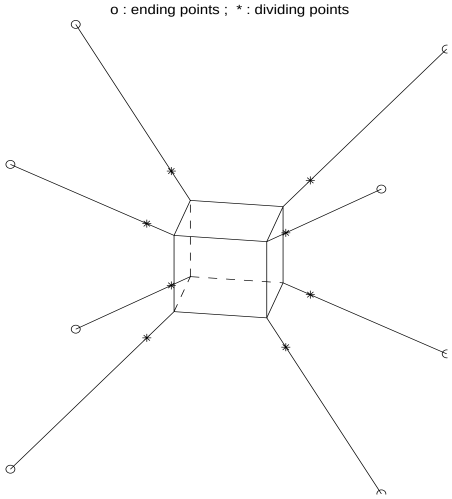

Figure 8.1: Block generation for a cube.

taking derivative across the vacuum-layer interface. Instead we apply some matching conditions. This is more natural since solutions in the vacuum and the layer have different properties. We also know from chapter 3 that the plane wave solutions across the interface are not very smooth, though being matched with each other.

Still consider the cube example, the 8 lines leave from the 8 corners and form equal angles with neighboring faces. We terminate the lines according to how far away we want the mesh to extend. Usually we want to have 2 layers of blocks. Hence we need to determine the dividing point of the two layers. In our work we choose the point such that the dividing subdomain interfaces of the two layers of blocks are one wavelength away from the cube faces. By applying absorbing layers in the outer blocks and a grid mapping technique, the ending point of the lines can be put several wavelengthes away from the cube in our computations. See Fig. (8.1) for an illustration of the dividing and ending points.

Having obtained the positions of dividing and ending points, we are able to describe the information about the blocks and the information regarding their connection. The x, y, and z coordinates of 8 corners of all the blocks are stored in arrays of dimensions $(1:8, 1:6, 1:N_{Layers})$ where N_{Layers} is the number of layers we desire. One notes that there are 6 blocks in each layer. The corners are arranged in such order as $(-\frac{1}{2},-\frac{1}{2},-\frac{1}{2})$- $(\frac{1}{2},-\frac{1}{2},-\frac{1}{2})$-$(\frac{1}{2},\frac{1}{2},-\frac{1}{2})$-$(-\frac{1}{2},\frac{1}{2},-\frac{1}{2})$- $(-\frac{1}{2},-\frac{1}{2},\frac{1}{2})$-$(\frac{1}{2},-\frac{1}{2},\frac{1}{2})$-

$(\frac{1}{2}, \frac{1}{2}, \frac{1}{2})$- $(-\frac{1}{2}, \frac{1}{2}, \frac{1}{2})$ for a unit cube centered at the origin. The 8 points are numbered from 1 to 8. For the first layer, we set the points from 1 to 4 to be those points on the cube surface, and let the two increasing directions of the block to coincide with the increasing directions of the cube on that face. Now the orientation of the blocks has also been determined. With this orientation, we can avoid the complexity in matching the grid points at two sides of the interface, for which rearranging the data structure according to the actual locations of the points on the face can be involved.

Then we write the information of the blocks to an output data file to be read by the mesh generator. By doing this, one can check the output data files for the blocks generated. The mesh generator generates the appropriate mesh for pseudospectral computation. If one wants to stretch the mesh, one only needs to extend the coordinates in $(1:8, 1:6, N_{Layers})$, i.e. the coordinates of the ending points. This is particularly useful when we use the mapped ML method in our simulation.

8.3.2 Mesh Generation in a Block

Since each block we generated is diffeomorphic to the unit cube, it can be easily decomposed into a number of subdomains that are diffeomorphic to the unit cube too. With this level of decomposition, one can refine the mesh as he desires by increasing the number of subdomains in each block. This is much easier compared with refining through the decomposition of the computational domain into more number of blocks which necessarily involve the complexity of the geometries in consideration.

After we decompose each block into a number of subdomains that are diffeomorphic to the unit cube I, we generate a 3-D computational mesh for Chebyshev method in each subdomain denoted by D. The construction of the map, $\Psi : \mathsf{D} \rightarrow \mathsf{I}$, using transfinite blending functions has been introduced in chapter 2. Using the method, we can obtain a 3-D mesh in the subdomain that is mapped to the standard 3-D Chebyshev mesh in the unit cube through the map Ψ.

In our 3-D computation, we decompose the block in two directions other than the direction going away from the scatterer, since in that direction one can easily shrink the blocks or generate more layers of blocks in the block generator. In practice, each block is decomposed into n^2 subdomain, where $n = 1, 2, \cdots$.

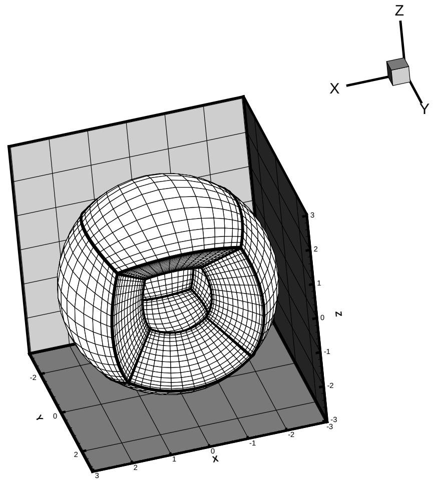

Figure 8.2: Multidomain mesh around a sphere.

8.4 The 3-D Numerical Scheme

8.4.1 The Multi-domain Pseudospectral Method

See Fig. 8.2 for some subdomains of the multidomain mesh we generated around a sphere using the procedure in last section. For simplicity, we assume that the number of nodes in ξ, η, and ζ is the same. Once we have mapped D onto I, we may proceed by constructing a multi-dimensional polynomial approximation of a function, $f[\mathsf{I}] : \mathsf{R}^3 \to \mathsf{R}$, using a tensor product formulation as

$$f(\boldsymbol{\xi}) \simeq \sum_{\Xi_N} f_{ijk} L_i^\alpha(\xi) L_j^\alpha(\eta) L_k^\alpha(\zeta) \ , \tag{8.6}$$

where $f_{ijk} = f|_{ijk} = f(\xi_i, \eta_j, \zeta_k)$ and we have introduced the interpolating Lagrange polynomials $L_i^\alpha(\xi)$, $L_j^\alpha(\eta)$ and $L_k^\alpha(\zeta)$ based on the nodal sets Λ_N^ξ, Λ_N^η and Λ_N^ζ, respectively, which are taken to be the Gauss-Lobatto quadrature points, e.g. Λ_N^ξ consists of the roots of the polynomial $(1 - \xi^2)(P_{N_\xi}^\alpha)'(\xi)$, where $P_{N_\xi}^\alpha$ represents the ultraspherical polynomial of order N_ξ, and likewise for Λ_N^η and Λ_N^ζ.

To seek approximate solutions to partial differential equations, we need to evaluate spatial derivatives at the nodal set, Λ_N. This is accomplished by approximating the continuous operators by differentiation matrices defined at the grid points. The explicit entries of the differentiation matrices can be found in chapter 2. To compute the multi-dimensional derivatives one may exploit the tensor-product nature of the approximation, Eq.(8.6), such that derivatives are computed through matrix products.

At the scatterer surfaces, the physical conditions are enforced along with applying the characteristic relations like what we do in 2-D. Absorbing boundary conditions are applied at the outer boundary. For the perfectly matched layer methods, one can refer to chapter 3.

Now we take the cube as an example to illustrate the multi-step procedure, introduced in chapter 2, for patching solutions at the subdomain interfaces. We first patch the solutions at the interfaces that separate different layers of subdomains applying the characteristic relations. Then the solutions are equal at the two sides of those interfaces. Hence we can view the subdomains as if there is only one layer. Then we are going to patch the interfaces that are parallel to the x-axis, the y-axis, and the z-axis at different steps. This procedure satisfies the above requirement to avoid contradiction in choosing outward normal vector. The procedure is verified to be stable and accurate in numerical experiments.

To explain what we do exactly to patch the solutions, let us consider two neighboring subdomains and also introduce the corresponding characteristic variables, $\boldsymbol{Q}_{\xi,1} = (Q^1_{\xi,1}, Q^2_{\xi,1}, Q^3_{\xi,1}, Q^4_{\xi,1}, Q^5_{\xi,1}, Q^6_{\xi,1})^T$ and $\boldsymbol{Q}_{\xi,2} = (Q^1_{\xi,2}, Q^2_{\xi,2}, Q^3_{\xi,2}, Q^4_{\xi,2}, Q^5_{\xi,2}, Q^6_{\xi,2})^T$, referring to the six characteristic variables in subdomains 1 and 2. Here Q^1_ξ and Q^2_ξ refer to the two incoming characteristic variables along $\nabla\xi$. Q^3_ξ and Q^4_ξ refer to the two outgoing characteristic variables along $\nabla\xi$. And Q^1_ξ and Q^2_ξ represent the two non-propagating characteristic variables. These are determined using the convective speeds of propagation of the characteristic variables, i.e. the diagonal entries of Λ.

The proper boundary conditions at the interface of the two subdomains are obtained as

$$Q^3_{\xi,1} = Q^5_{\xi,2} \ , \ \ Q^4_{\xi,1} = Q^6_{\xi,2} \ ,$$

$$Q^3_{\xi,2} = Q^5_{\xi,1} \ , \ \ Q^4_{\xi,2} = Q^6_{\xi,1} \ ,$$

where the right-hand-side of the equations signifies computed values and the left-hand-side refers to the sought after boundary conditions. Note that the characteristic variables on both sides of the equations need to correspond to eigenvectors spanning in the same direction. The non-propagating characteristic variables, $Q^1_{\xi,1}$ and $Q^1_{\xi,2}$ as well as $Q^2_{\xi,1}$ and $Q^2_{\xi,2}$ are enforced to be continuous across the interface, while the outgoing characteristic variables, $Q^5_{\xi,1}$ and $Q^6_{\xi,1}$ as well as $Q^5_{\xi,2}$ and $Q^6_{\xi,2}$, are preserved in each subdomain. The actual field values at the interfaces are then obtained by multiplying the updated characteristic variables with S. A similar procedure is applied on the other face in the ξ-direction the faces in the η and ζ-direction, if necessary.

8.4.2 Numerical Issues in 3-D Spherical Coordinates

When we use the formulation of Maxwell's equations in 3-D spherical coordinates, we have a singularity in the equations of $\frac{1}{\sin\theta}$. This occurs in the subdomains around the pole, see Fig. 8.2. With the multidomain pseudospectral method we use, there is a technique one can apply to avoid the singularity. The technique is to use a locally rotated coordinate system in the subdomains around the pole. We introduce the following rotation

$$x' = y,\ y' = z,\ z' = x\ . \tag{8.7}$$

Thus the corresponding spherical mesh in those subdomains are rotated away from the pole. In the locally rotated coordinate system, we also have a relation between the fields:

$$E'_x = E_y,\ E'_y = E_z,\ E'_z = E_x\ . \tag{8.8}$$

Hence when we patch the field values in different subdomains involving two local coordinate systems, we need to patch the pairs in the above equation. It is the same for the magnetic fields.

In spherical coordinates, what we compute is E_r, E_θ, and E_ϕ for the electric field. Before we can patch solutions in the above way, we need to compute E_x, E_y, and E_z from E_r, E_θ, and E_ϕ. After the multidomain patching procedures, we need to update E_r, E_θ, and E_ϕ values with the patched

E_x, E_y, and E_z values. In the following we give the relations to compute the values from each other.

$$
\begin{aligned}
E_x &= \cos\phi \sin\theta E_r + \cos\phi\cos\theta E_\theta - \sin\phi E_\phi \quad , \\
E_y &= \sin\phi\sin\theta E_r + \sin\phi\cos\theta E_\theta + \cos\phi E_\phi \quad , \\
E_z &= \cos\theta E_r - \sin\theta E_\theta \quad ,
\end{aligned}
\tag{8.9}
$$

in one way and

$$
\begin{aligned}
E_r &= \cos\phi\sin\theta E_x + \sin\phi\sin\theta E_y + \cos\theta E_z \quad , \\
E_\theta &= \cos\phi\cos\theta E_x + \sin\phi\cos\theta E_y - \sin\theta E_z \quad , \\
E_\phi &= -\sin\phi E_x + \cos\phi E_y \quad .
\end{aligned}
\tag{8.10}
$$

in the other way. The relations between the magnetic fields are the same. One notes that these transformations only need to be done at the interfaces of the subdomains that involve the pole. The computation time is negligible in this 3-D simulation.

8.5 Numerical Experiments

8.5.1 Scattering by a PEC Cube

Scattering by a PEC cube that has an edge length of 0.755λ is simulated and both the horizontal and vertical RCS results are plotted in Fig. 8.3. The results are found to be in agreement with those published in the literatures. For this simulation, we use the multidomain Chebyshev pseudospectral scheme with the mapped ML method as an ABC.

8.5.2 Scattering by Spheres

Scattering by PEC spheres is simulated using the multidomain Chebyshev pseudospectral scheme with the spherical PML methods, both the split-field one and the well-posed one. We use the Mie-series result as RCS reference. To determine the size of the reflection of the perfectly matched layers, we also compare the computed fields with the computed fields where we use a larger computational

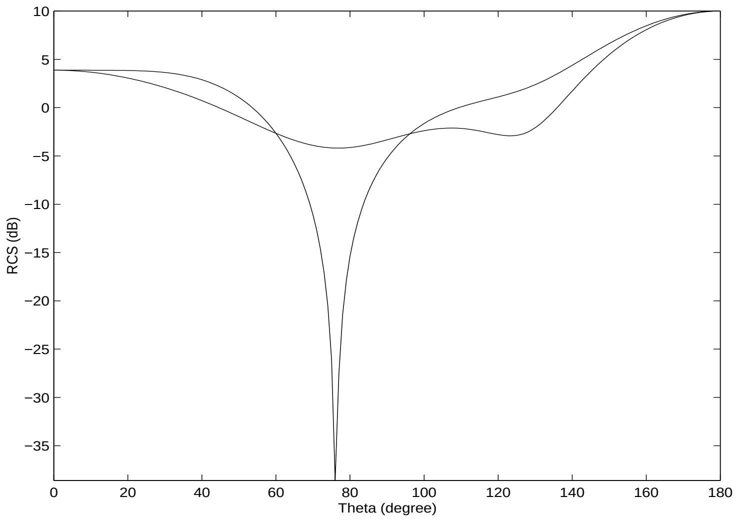

Figure 8.3: Numerical RCS result of scattering by a PEC cube having an edge length of 0.755λ using the the mapped ML method.

domain.

In Fig. 8.4 we present the RCS result of a PEC sphere of electrical size $ka = 5.3$. Here we use the multidomain spectral method with the split-field formulation of our spherical perfectly matched layer. The Mie-series RCS result is also plotted for reference. Note that one can barely tell any difference from the two RCS results.

In Fig. 8.5 we plot the E_x field $\frac{\lambda}{2}$ from the scatterer surface in the back scatter region, and the difference between the field and the one obtained in the reference computation using a larger computational domain. It is shown in the figure that the difference between the two fields is within 1×10^{-3} after the initial noise, which is the result of the initial non-smoothness of the type of excitation used.

In Fig. 8.6 we present the RCS result of a PEC sphere of electrical size $ka = 5.3$. Here we use the multidomain spectral method with the well-posed spherical perfectly matched layer method. The Mie-series RCS result is also plotted for reference. Note that one can barely tell any difference from the two RCS results.

In Fig. 8.7 we present the RCS result of a PEC sphere of electrical size $ka = 5.3$. Here we use the same multidomain spectral method with a direct application of Sacks' lossy uniaxial medium idea as

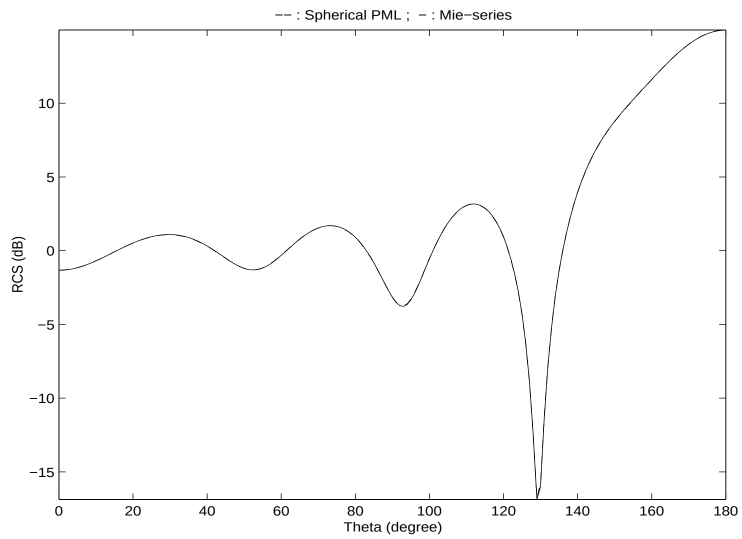

Figure 8.4: Comparison of RCS's obtained from spectral method with split-field spherical PML, dashed line, and Mie-series, solid line, for a PEC sphere with electrical size $ka = 5.3$.

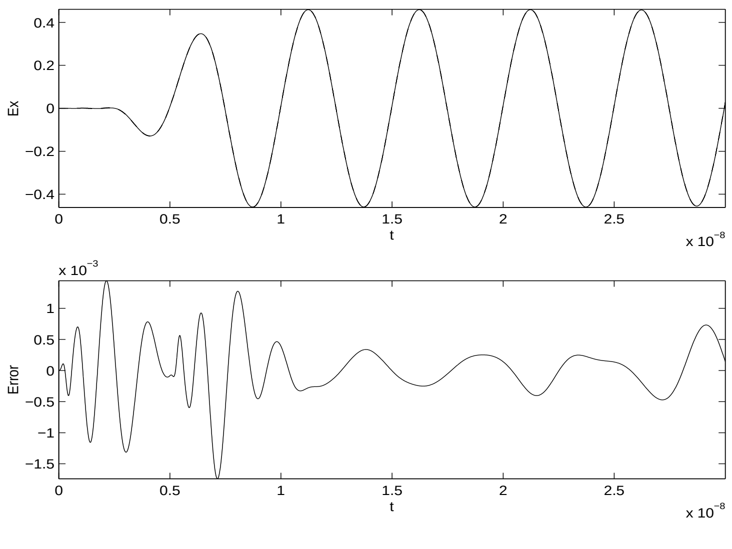

Figure 8.5: Comparison of field obtained from spectral method with split-field spherical PML, dashed line, and reference, solid line, for a PEC sphere with electrical size $ka = 5.3$.

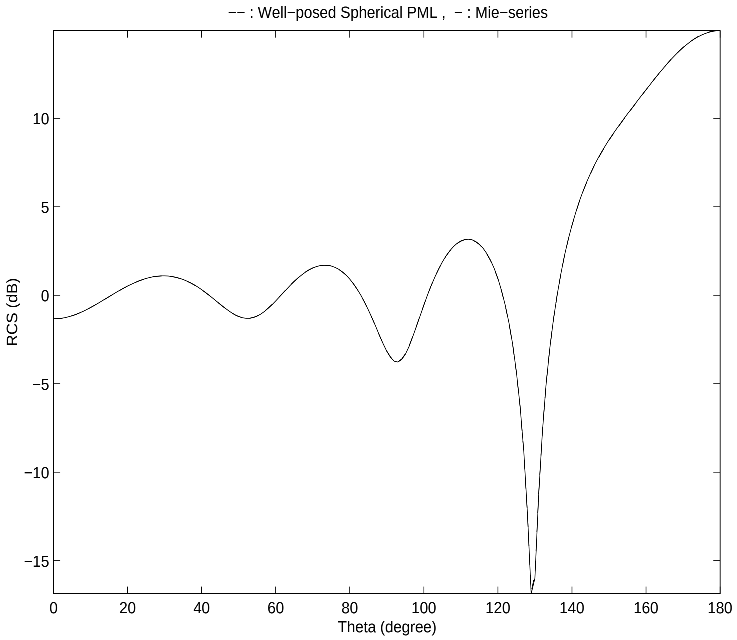

Figure 8.6: Comparison of RCS's obtained from spectral method with well-posed spherical PML, dashed line, and Mie-series, solid line, for a PEC sphere with electrical size $ka = 5.3$.

a PML in spherical coordinates. (Preliminary, still under investigation.) The same Mie-series RCS result is also plotted for reference. Note that now there is obvious difference between the two RCS results.

8.5.3 Scattering by Cylinders

In Fig. 8.8 we present the RCS result of a finite PEC cylinder of radius 2λ and height 2λ. Here we use the multidomain spectral method with the split-field formulation of our cylindrical perfectly matched layer. For reference, we scanned and measured the MOM results in [18] by Gedney and Mittra. Note that the numerical result is in good agreement with the reference.

In Fig. 8.9 we present the RCS result of scattering by the same cylinder where we use the multidomain spectral method with the well-posed cylindrical perfectly matched layer as absorbing boundary condition. The numerical result is in general agreement with the reference, not as good as that of the split-field cylindrical PML method.

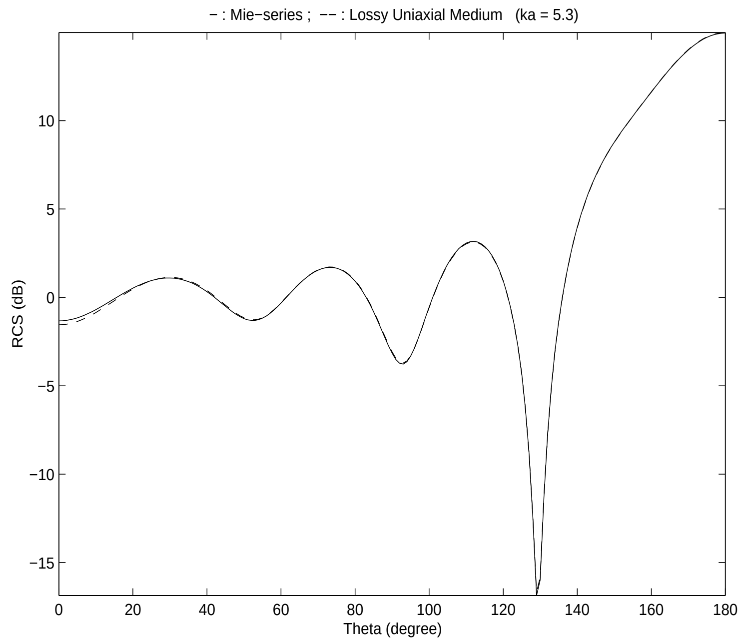

Figure 8.7: Comparison of RCS's obtained from spectral method with lossy uniaxial medium as PML, dashed line, and Mie-series, solid line, for a PEC sphere with electrical size $ka = 5.3$.

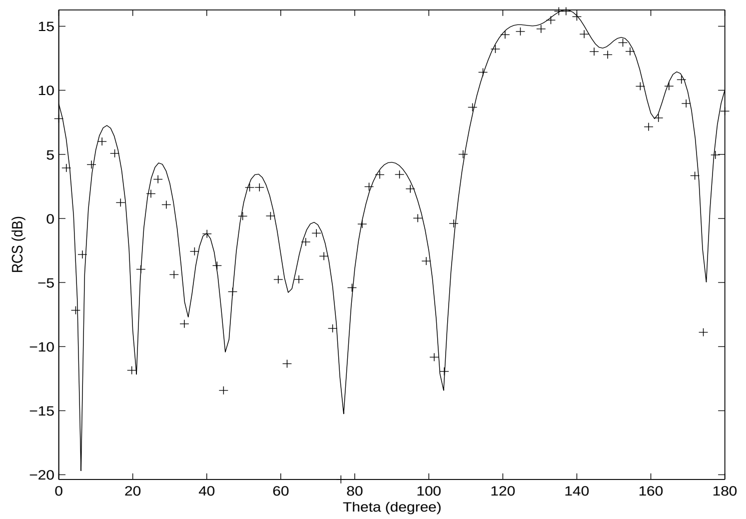

Figure 8.8: Comparison of RCS's obtained from spectral method with cylindrical PML, solid line, and reference, marked by "+", for a PEC cylinder of radius 2λ and height 2λ, horizontal polarization. ($\mathbf{E}^{inc} = \hat{\theta} \cdot E_\theta,\ \theta^{inc} = \frac{\pi}{4},\ \phi^{inc} = \frac{\pi}{2},\ \phi^{obs} = \frac{\pi}{3}$)

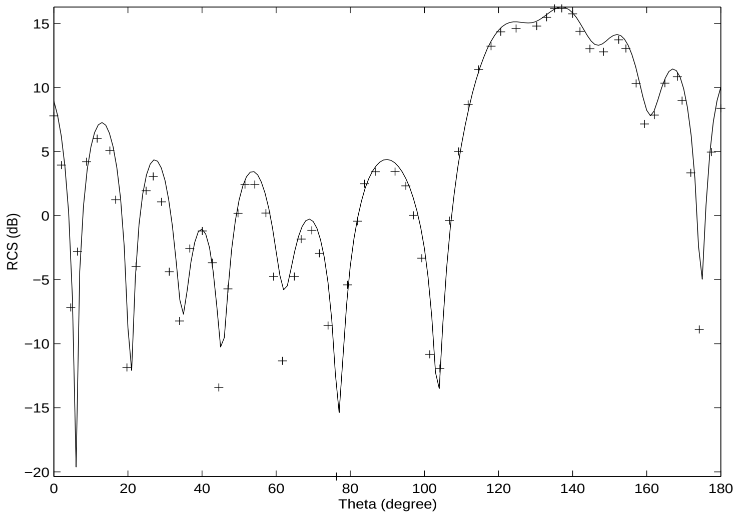

Figure 8.9: Comparison of RCS's obtained from spectral method with well-posed cylindrical PML, solid line, and reference, marked by "+", for a PEC cylinder of radius 2λ and height 2λ, horizontal polarization. ($\mathbf{E}^{inc} = \hat{\theta} \cdot E_\theta,\ \theta^{inc} = \frac{\pi}{4},\ \phi^{inc} = \frac{\pi}{2},\ \phi^{obs} = \frac{\pi}{3}$)

8.6 Concluding Remarks

In this chapter we give an introduction to the 3-D pseudospectral method we use in the simulation of electromagnetic scattering by simple 3-D objects including cubes, spheres, and finite cylinders. The blending-function interpolation method is used in the generation of mesh in curved element domains, i.e. , the subdomains in our multidomain mesh.

The spherical and cylindrical PML methods, both the split-field and the well-posed types, are used with the pseudospectral method as the absorbing boundary conditions (ABC). Numerical experiments show the high-order accuracy of the pseudospectral method and efficacy of the proposed PML methods as ABC.

Chapter 9

Scattering by Bodies of Revolution

In this chapter, a paper submitted to IEEE Transactions on Antennas and Propagation is presented without much change.

9.1 Introduction

With the development of new technologies such as ultra short pulse radars comes an increased need for the accurate and efficient modeling of the scattering problem under circumstances involving very broad band signals and often electrically large scatters.

In the past, the Method-of-Moments (MoM) has been extremely successful in addressing the problem of monochromatic plane wave scattering by very general objects. However, this choice of method is less attractive for these new types of problems for several reasons, e.g., the inherent monochromatic nature of the MoM makes the computation of broad band scattering a very expensive process. Moreover, regions of multiple scattering or electrically very large objects are known to cause severe ill-conditioning and extremely large linear systems, stretching the limits of modern computers.

The need for broad band excitation suggests the use of time-domain methods in which plane wave and short pulse excitation in handled with equal ease. Indeed, the advent of finite-difference time-domain (FD-TD) methods [51] was partly driven by the need for solving large scattering problems being illuminated by a time-dependent source. Moreover, the FD-TD approach has proven very fruitful in enabling the modeling of problems of very significant geometric complexity, possibly involving complex materials.

Although alleviating the problems associated with broad band excitation, the mainstream FT-TD method is troubled by the need of 10-20 points per wavelength to accurately resolve the wave dynamics of the scattering problem - and any other wave problem. The same phenomenon exists in the MoM approach and is an inherent consequence of these methods being of low order, e.g. most FD-TD schemes are only 2nd order accurate. The accurate modeling of electrically large objects thus becomes prohibitive and either the required accuracy or the maximum electric size is severely limited, a situation that is becoming increasingly unacceptable.

The quest for high accuracy time-domain solution and the ability to handle electrically large problems points towards the need for using high-order finite-difference methods for the solution of the scattering problem. In recent years intensive effort have been put into devising such schemes for Maxwell's equations, e.g. [42, 25], yielding superior accuracy at the expense of a somewhat more complicated computational framework.

In the present work we follow this line of thinking and develop pseudospectral time-domain methods suitable for the numerical solution of the scattering problem. To maintain geometric flexibility, essential for the solution of problems of a practical character, we continue the work initiated in [56, 57] and formulate a multi-domain scheme for the accurate and efficient computation of scattering by bodies-of-revolution (BOR). The pseudospectral schemes can be thought of as an infinite order finite-difference schemes and as such takes the role of the royals among numerical schemes for the solution of partial differential equations. As we shall see through discussions and numerous computations, properly formulated pseudospectral schemes yield not only superior accuracy but does so in a very efficient manner as compared to traditional low order FD-TD schemes.

9.2 The BOR Formulation of Maxwell's Equations

Consider the vacuum Maxwell's equations in cylindrical coordinates (r, ϕ, z),

$$\varepsilon \frac{\partial \boldsymbol{E}}{\partial t} = \nabla \times \boldsymbol{H} \ , \tag{9.1}$$

$$\mu \frac{\partial \boldsymbol{H}}{\partial t} = -\nabla \times \boldsymbol{E} \ , \tag{9.2}$$

where $\boldsymbol{E} = (E_r, E_\phi, E_z)^T$ and $\boldsymbol{H} = (H_r, H_\phi, H_z)^T$ signify the electric and magnetic field components while ε and μ refer to the vacuum permitivity and permeability, respectively, related to the vacuum speed of light, $c = (\varepsilon\mu)^{-1/2}$.

To arrive at the body-of-revolution (BOR) formulation of Maxwell's equations, the azimuthal field variation is accounted for analytically by the introduction of a Fourier expansion as

$$\boldsymbol{E}(r, \phi, z) = \sum_{m=0}^{\infty} (\tilde{\boldsymbol{e}}_u(r, z) \cos m\phi + \tilde{\boldsymbol{e}}_v(r, z) \sin m\phi) \ , \tag{9.3}$$

$$\boldsymbol{H}(r, \phi, z) = \sum_{m=0}^{\infty} (\tilde{\boldsymbol{h}}_u(r, z) \cos m\phi + \tilde{\boldsymbol{h}}_v(r, z) \sin m\phi) \ , \tag{9.4}$$

where m is the mode number and $\tilde{\boldsymbol{e}}_u = (\tilde{e}_{r,u}, \tilde{e}_{\phi,u}, \tilde{e}_{z,u})^T$, $\tilde{\boldsymbol{e}}_v = (\tilde{e}_{r,v}, \tilde{e}_{\phi,v}, \tilde{e}_{z,v})^T$ and likewise for $\tilde{\boldsymbol{h}}_u$ and $\tilde{\boldsymbol{h}}_v$. Hence, the first subscript refers to the field component while the second subscript refers to its azimuthal variation.

We recall that while the scatterer is assumed to possess an axis-symmetry, this is certainly not the case for the incident and scattered fields and introducing Eqs.(9.3)-(9.4) only supplied an efficient way to account for the azimuthal variation for each individual mode.

Substituting Eqs.(9.3)-(9.4) into Eqs.(9.1)-(9.2) and utilizing the orthogonality of the trigonometric polynomials, results in a pair of equations for the twelve unknowns, $\tilde{\boldsymbol{e}}_{u,v}$ and $\tilde{\boldsymbol{h}}_{u,v}$, for each azimuthal mode m as

$$\varepsilon \frac{\partial \tilde{\boldsymbol{e}}_{u,v}}{\partial t} = \nabla \times \tilde{\boldsymbol{h}}_{u,v} \pm \frac{m}{r} \hat{\boldsymbol{\phi}} \times \tilde{\boldsymbol{h}}_{v,u} \ , \tag{9.5}$$

$$\mu \frac{\partial \tilde{\boldsymbol{h}}_{u,v}}{\partial t} = -\nabla \times \tilde{\boldsymbol{e}}_{u,v} \mp \frac{m}{r} \hat{\boldsymbol{\phi}} \times \tilde{\boldsymbol{e}}_{v,u} \ . \tag{9.6}$$

These twelve equations separate into two independent sets of equations in six unknowns, representing fields that are azimuthally orthogonal.

In various special cases, depending on angle of incidence and polarization of the incident wave, only one of the two sets of equations are needed to solve the problem. However, in the general case, we need to advance all twelve equations subject to an incident field on the form

$$\left\{\begin{array}{c} \boldsymbol{E}^{inc} \\ \\ \boldsymbol{H}^{inc} \end{array}\right\} = \left\{\begin{array}{c} \boldsymbol{E}^{i} \\ \\ \boldsymbol{H}^{i} \end{array}\right\} \exp\left[ik^i\left(\hat{\boldsymbol{k}}^i \cdot \boldsymbol{r} - ct\right)\right] \quad , \tag{9.7}$$

where $k^i = 2\pi/\lambda$ relates to the wavelength, λ, of the incident wave approaching the scatter along the propagation vector

$$\hat{\boldsymbol{k}}^i = -\left(\sin\theta^i\cos\phi^i\hat{\boldsymbol{x}} + \sin\theta^i\sin\phi^i\hat{\boldsymbol{y}} - \cos\theta^i\hat{\boldsymbol{z}}\right) \quad ,$$

where (θ^i, ϕ^i) specifies the direction of the incoming field in the usual spherical basis, $(\hat{\boldsymbol{\rho}}, \hat{\boldsymbol{\theta}}, \hat{\boldsymbol{\phi}})$ and corresponding coordinates, (ρ, θ, ϕ), with the exception that we have chosen to measure θ^i as the angle to $-\hat{\boldsymbol{z}}$ such that $\hat{\boldsymbol{k}} = \hat{\boldsymbol{z}}$ for axial incidence, i.e. $\theta^i = 0$. Unless otherwise stated, we shall only consider the case of $\phi^i = 0$ for simplicity.

The polarization of the incoming field is specified through the components along $\hat{\boldsymbol{\theta}}$ and $\hat{\boldsymbol{\phi}}$ as

$$\boldsymbol{E}^{inc} = E_\theta^{inc}\hat{\boldsymbol{\theta}} + E_\phi^{inc}\hat{\boldsymbol{\phi}} \quad , \quad \boldsymbol{H}^{inc} = Z^{-1}\hat{\boldsymbol{k}}^i \times \boldsymbol{E}^{inc} \quad ,$$

where $Z = \sqrt{\mu/\varepsilon} = 120\pi$ ohm represents the intrinsic impedance. In accordance with standard notation we refer to the case of $E_\phi^{inc} = 0$ as horizontally polarized while $E_\theta^{inc} = 0$ is termed vertically polarized excitation.

9.2.1 Treatment of the Axial Singularity

The BOR equations, Eqs.(9.5)-(9.6), contains a coordinate singularity at $r = 0$ that requires proper treatment. For the case of the total field formulation, a popular approach [51] is to use l'Hospitals rule at the axis to turn the singular terms into derivatives. However, when using the scattered field formulation it remains unknown whether this limit exists, i.e. an alternative approach must be sought.

We apply a change of variables as

$$\boldsymbol{e}_{u,v} = r\tilde{\boldsymbol{e}}_{u,v} \quad , \quad \boldsymbol{h}_{u,v} = r\tilde{\boldsymbol{h}}_{u,v} \quad ,$$

which, after being introduced in Eqs.(9.5)-(9.6), yields

$$\varepsilon\frac{\partial \boldsymbol{e}_{u,v}}{\partial t} = \nabla_{\perp} \times \boldsymbol{h}_{u,v} + \frac{1}{r}\left[(\boldsymbol{h}_{u,v} \cdot \hat{\boldsymbol{z}})\,\hat{\boldsymbol{\phi}} \pm m\hat{\boldsymbol{\phi}} \times \boldsymbol{h}_{v,u}\right], \tag{9.8}$$

$$\mu\frac{\partial \boldsymbol{h}_{u,v}}{\partial t} = -\nabla_{\perp} \times \boldsymbol{e}_{u,v} - \frac{1}{r}\left[(\boldsymbol{e}_{u,v} \cdot \hat{\boldsymbol{z}})\,\hat{\boldsymbol{\phi}} \pm m\hat{\boldsymbol{\phi}} \times \boldsymbol{e}_{v,u}\right], \tag{9.9}$$

where we have introduced $\nabla_{\perp}$ as the usual perpendicular vector operator in the (r, z)-plane, i.e.

$$\nabla_{\perp} = \hat{\boldsymbol{r}}\frac{\partial}{\partial r} + \hat{\boldsymbol{z}}\frac{\partial}{\partial z} \quad .$$

Equations (9.8)-(9.9) still contains a number of singular terms at the axis. We shall consider the two cases of $m = 0$ and $m > 0$ separately.

$\underline{m = 0}$: In this case we only have singularities in equations of e_{ϕ} and h_{ϕ}. However, for $m \neq 1$, $\tilde{e}_{\phi}$ and $\tilde{h}_{\phi}$ are identically zero due to the nature of the fields at the axis [51]. Hence, we need not discretize the equations for the azimuthal field components at the axis but may simply impose the boundary conditions. Recall, that these arguments are valid only for the total fields, i.e. the boundary conditions for the scattered field are arrived at through the use of the prescribed incident field.

$\underline{m > 0}$: This case is slightly more complicated in that we have singularities in all equations. However, for $m > 0$, the $\tilde{e}_z$ and $\tilde{h}_z$ components of the total fields are identically zero along the axis due to that fact that any constant-r Faraday's Law path integral containing $r = 0$ integrates to zero, i.e., e_z and h_z are both identically zero along the axis [51]. Thus, rather than solving the equations for the axial components, we may simply impose the appropriate boundary condition which then couple into the equations of the radial variation.

As for the case of $m = 0$, we need to recover the scattered field boundary conditions for the remaining terms in Eqs. (9.8)-(9.9) since the above arguments is valid only for the total fields. However, since the incident field is prescribed at all times, this does not pose a problem.

We note that the above boundary conditions are arrived at without the use of approximations but rather derived solely on the basis of the properties of the fields and the knowledge of the prescribed incident fields along the axis, $r = 0$.

The two sets of equations, Eqs.(9.8)-(9.9), well suited for numerical treatment as we shall discuss shortly, are thus given as

$$\varepsilon \frac{\partial e_{r,u}}{\partial t} = -\frac{\partial h_{\phi,u}}{\partial z} + \frac{m}{r} h_{z,v} \quad , \tag{9.10}$$

$$\varepsilon \frac{\partial e_{\phi,v}}{\partial t} = \frac{\partial h_{r,v}}{\partial z} - \frac{\partial h_{z,v}}{\partial r} + \frac{1}{r} h_{z,v} \quad ,$$

$$\varepsilon \frac{\partial e_{z,u}}{\partial t} = \frac{\partial h_{\phi,u}}{\partial r} - \frac{m}{r} h_{r,v} \quad ,$$

$$\mu \frac{\partial h_{r,v}}{\partial t} = \frac{\partial e_{\phi,v}}{\partial z} + \frac{m}{r} e_{z,u} \quad ,$$

$$\mu \frac{\partial h_{\phi,u}}{\partial t} = -\frac{\partial e_{r,u}}{\partial z} + \frac{\partial e_{z,u}}{\partial r} - \frac{1}{r} e_{z,u} \quad ,$$

$$\mu \frac{\partial h_{z,v}}{\partial t} = -\frac{\partial e_{\phi,v}}{\partial r} - \frac{m}{r} e_{r,u} \quad ,$$

with the orthogonal counterpart being

$$\varepsilon \frac{\partial e_{r,v}}{\partial t} = -\frac{\partial h_{\phi,v}}{\partial z} - \frac{m}{r} h_{z,u} \quad , \tag{9.11}$$

$$\varepsilon \frac{\partial e_{\phi,u}}{\partial t} = \frac{\partial h_{r,u}}{\partial z} - \frac{\partial h_{z,u}}{\partial r} + \frac{1}{r} h_{z,u} \quad ,$$

$$\varepsilon \frac{\partial e_{z,v}}{\partial t} = \frac{\partial h_{\phi,v}}{\partial r} + \frac{m}{r} h_{r,u} \quad ,$$

$$\mu \frac{\partial h_{r,u}}{\partial t} = \frac{\partial e_{\phi,u}}{\partial z} - \frac{m}{r} e_{z,v} \quad ,$$

$$\mu \frac{\partial h_{\phi,v}}{\partial t} = -\frac{\partial e_{r,v}}{\partial z} + \frac{\partial e_{z,v}}{\partial r} - \frac{1}{r} e_{z,v} \quad ,$$

$$\mu \frac{\partial h_{z,u}}{\partial t} = -\frac{\partial e_{\phi,u}}{\partial r} + \frac{m}{r} e_{r,v} \quad .$$

9.2.2 Boundary Conditions at the Scatterer

To complete the specification of the problems to be solved, we need to briefly address the question of boundary conditions at the scatterer.

Since we confine our attention to the case of perfectly electrically conducting (PEC) objects, the boundary conditions takes the general form

$$\hat{\boldsymbol{n}} \times \boldsymbol{E} = 0 \quad , \quad \hat{\boldsymbol{n}} \cdot \boldsymbol{H} = 0 \quad ,$$

i.e. the total tangential electric and normal magnetic fields must vanish. Here $\hat{\boldsymbol{n}} = (\hat{n}_r, 0, \hat{n}_z)$ represents an outward pointing unit-vector at the object.

For the sake of simplicity we shall deal with the azimuthal components seperately and introduce the (r,z)-plane outward pointing normal vector, $\hat{\boldsymbol{n}} = (\hat{n}_r, 0, \hat{n}_z)$.

Let us introduce the scattered field formulation as

$$\boldsymbol{E} = \boldsymbol{E}^{inc} + \boldsymbol{E}^{s} \quad , \quad \boldsymbol{H} = \boldsymbol{H}^{inc} + \boldsymbol{H}^{s} \quad ,$$

where the incident fields, $\boldsymbol{E}^{inc}$ and $\boldsymbol{H}^{inc}$, are prescribed at all times through Eq.(9.7). Considering the electric field we obtain, due to the symmetry, the condition

$$E^s_\phi = -E^{inc}_\phi \quad , \tag{9.12}$$

while a second condition is obtained by requesting

$$\hat{\boldsymbol{\phi}} \cdot \left(\hat{\boldsymbol{n}} \times \boldsymbol{E}^{inc}\right) = -\hat{\boldsymbol{\phi}} \cdot \left(\hat{\boldsymbol{n}} \times \boldsymbol{E}^{s}\right) = \hat{n}_r E_z^s - \hat{n}_z E_r^s \quad . \tag{9.13}$$

This only yields one equation for the two unknown scattered field components. However, a third condition is arrived at by recalling the behavior of hyperbolic problems at solid walls, at which the outgoing characteristics are simply reflected [23]. Hence, for consistency we must also require that

$$\hat{\boldsymbol{n}} \cdot \boldsymbol{E}^{s} = \hat{n}_r E_r^s + \hat{n}_z E_z^s = \hat{\boldsymbol{n}} \cdot \boldsymbol{E}^{s,c} \quad , \tag{9.14}$$

where $\boldsymbol{E}^{s,c}$ signifies the computed scattered field. This yields additional the equation required to enforce the boundary condition on the electric field.

The situation for the magnetic field is very similar. Indeed, the physical condition yields

$$\hat{\boldsymbol{n}} \cdot \boldsymbol{H}^{inc} = -\hat{\boldsymbol{n}} \cdot \boldsymbol{H}^{s} = -\hat{n}_r H_r^s - \hat{n}_z H_z^s \quad , \tag{9.15}$$

with an additional condition appearing by requiring that

$$\hat{\boldsymbol{\phi}} \cdot \left(\hat{\boldsymbol{n}} \times \boldsymbol{H}^{s}\right) = \hat{n}_z H_r^s - \hat{n}_r H_z^s = \hat{\boldsymbol{\phi}} \cdot \left(\hat{\boldsymbol{n}} \times \boldsymbol{H}^{s,c}\right) \quad , \tag{9.16}$$

where $\boldsymbol{H}^{s,c}$ refers to the computed scattered field.

While Eqs.(9.12)-(9.16) uniquely determines the boundary conditions for the scattered field along smooth parts of the scatter, the formulation of boundary conditions along edges remains open.

The possibility of singular behavior of the field components along edges is detailed in [39] from which we infer that only E_ϕ and H_ϕ can be expected be finite in the general case. If we term the angle, $\alpha \in [0, 2\pi]$, of the wedge terminating in the edge, the remaining field components can be expected to scale as

$$E_r,\, E_z,\, H_r,\, H_z \sim t^{\alpha/\pi - \frac{1}{2}} \quad ,$$

where t signifies the distance to the edge. Hence, for convex wedges, $\alpha \in [0, \pi]$ the field components exhibit a weak singularity, while all field components remain regular for concave wedges.

We can certainly not hope to resolve such singular behavior. However, boundary conditions are still required along the edges of such convex wedges and we impose that E_ϕ vanishes at the edge while the remaining individual field components are continuous across the edge. While this is physically correct only for H_ϕ it is a reasonable assumption also for the remaining field components, which are still allowed to grow unboundedly in accordance with [39]. Moreover, the procedure ensures smooth fields for edges of concave wedges in accordance with the expected behavior.

9.3 The Numerical Scheme

In the following we shall describe in some detail the individual elements of and the reasoning behind the complete multi-domain scheme for the solution of Eqs.(9.10)-(9.11) subject to the prescribed initial and boundary conditions.

9.3.1 Chebyshev Spectral Methods

The schemes presented in this chapter are all based on Chebyshev collocation methods, which, due to their superior approximation properties, are widely used for the solution of partial differential equations.

The Chebyshev polynomial of order k is defined as

$$T_k(x) = \cos(\, k \, \cos^{-1} x \,) \ ,$$

where $|x| \leq 1$. In the following sections we will consider collocation methods, where the $N+1$ collocation points are chosen to be the Chebyshev-Gauss-Lobatto points found as the roots of the polynomial $(1-x^2)T'_N(x)$, i.e.

$$x_i = -\cos\left(\frac{i\pi}{N}\right) \quad , \quad 0 \leq i \leq N \ .$$

When applying a Chebyshev collocation method, the function, $f(x)$, is approximated by a grid function, $f_i = f(x_i)$, where the grid-points are the Gauss-Lobatto points. We construct a global Nth order Chebyshev interpolant, I_N, to obtain the approximation of the function

$$(I_N f)(x) = \sum_{i=0}^{N} f_i \, g_i(x) \quad .$$

The interpolating Chebyshev-Lagrange polynomials are given as

$$g_i(x) = \frac{(1-x^2)T_N'(x)\,(-1)^{i+1}}{c_i N^2 (x - x_i)} \quad ,$$

where $c_0 = c_N = 2$ and $c_i = 1$ for $1 \leq i \leq N-1$. It is easily verified that by construction

$$(I_N f)(x_i) = f_i \quad .$$

To seek approximate solutions, $(I_N f)(x)$, to a partial differential equation we ask that the equation is satisfied in a collocation sense, i.e., at the collocation points. Hence, we need to obtain values of the spatial derivatives at the collocation points. This is accomplished by approximating the continuous differential operator by a matrix operator with the entries given as

$$\mathrm{D}_{ij} = g_j'(x_i) \quad ,$$

such that the derivative of f at a collocation point, x_i, may be approximated as

$$\frac{df}{dx}(x_i) \approx \frac{d(I_N f)}{dx}(x_i) = \sum_{j=0}^{N} \mathrm{D}_{ij}\, f(x_j) \quad ,$$

and likewise for higher derivatives. For the explicit expressions of the entries of the matrix operator and further details on collocation methods, we refer to [9].

The extension of this one-dimensional framework to a multi-dimensional setting is most easily accomplished through the use of tensor products, e.g., given the function, $f(x,y)$, we construct the two-dimensional approximation

$$(I_{M,N}f)(x,y) = \sum_{i=0}^{M}\sum_{j=0}^{N} f(x_i,y_j)\, g_i(x) g_j(y) \quad ,$$

where we have introduced the Chebyshev Gauss-Lobatto grid, y_j, along y. The advantage of this approach is that derivatives are still computed through the use of one-dimensional differentiation matrices and matrix-matrix products. However, the use of tensor products also requires that $f(x,y)$ is defined on a rectangular grid, a restriction that we shall overcome shortly by introducing a multi-domain formulation.

Filtering of the solution may be used when unresolved gradients are presents, as we may expect to be the case at edges. In the implementation of the present scheme, we employ an exponential filter of the type

$$\sigma_i = \begin{cases} 1 & 0 \le i \le N_c \\ \exp\left[-\alpha\left(\frac{i-N_c}{N-N_c}\right)^{\gamma}\right] & N_c < i \le N \end{cases} \quad , \tag{9.17}$$

where N_c is a cut-off mode number, γ is the order of the filter and $\alpha = -\ln \varepsilon_M$ with ε_M being the machine accuracy. This choice of filter function is by no means unique and alternatives may be found in [10]. The filtering may conveniently be expressed as a matrix operator, $\mathcal{F}$, with the entries given as

$$\mathcal{F}_{ij} = \frac{2}{c_j N}\sum_{k=0}^{N}\frac{\sigma_k}{c_k} T_k(x_i) T_k(x_j) \quad .$$

9.3.2 The (r,z) Equations in Curvilinear Form

The first step towards a geometrically flexible spectral scheme is to extend the use of polynomial expansions to the general curvilinear quadrilateral domain. We assume the existence of a smooth non-singular mapping function, Ψ, relating the (r,z) coordinate system to the general curvilinear

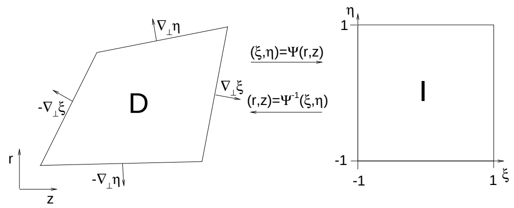

Figure 9.1: Illustration of the mapping between physical coordinates, (r, z), and general curvilinear coordinates, (ξ, η), required for the construction of the general multi-domain scheme.

coordinate system (ξ, η) as

$$\xi = \xi(r, z) \quad , \quad \eta = \eta(r, z) \quad ,$$

as illustrated in Fig. 9.1. We shall return to the actual specification and construction of the smooth map, $\boldsymbol{\Psi}$, shortly.

Utilizing this notation transforms Eqs.(9.10)-(9.11) into two hyperbolic system

$$\frac{\partial \boldsymbol{q}_1}{\partial t} = \mathrm{A}(\nabla_\perp \xi)\frac{\partial \boldsymbol{q}_1}{\partial \xi} + \mathrm{A}(\nabla_\perp \eta)\frac{\partial \boldsymbol{q}_1}{\partial \eta} + \frac{1}{r}\left(\mathrm{C} + \mathrm{D}\right)\boldsymbol{q}_1 \quad , \tag{9.18}$$

and

$$\frac{\partial \boldsymbol{q}_2}{\partial t} = \mathrm{A}(\nabla_\perp \xi)\frac{\partial \boldsymbol{q}_2}{\partial \xi} + \mathrm{A}(\nabla_\perp \eta)\frac{\partial \boldsymbol{q}_2}{\partial \eta} + \frac{1}{r}\left(\mathrm{C} - \mathrm{D}\right)\boldsymbol{q}_2 \quad , \tag{9.19}$$

where we have the two state vectors

$$\boldsymbol{q}_1 = \left[e_{r,u}, e_{\phi,v}, e_{z,u}, h_{r,v}, h_{\phi,u}, h_{z,v}\right]^T \quad ,$$

$$\boldsymbol{q}_2 = \left[e_{r,v}, e_{\phi,u}, e_{z,v}, h_{r,u}, h_{\phi,v}, h_{z,u}\right]^T \quad ,$$

containing the twelve unknown field components. The form of Eqs.(9.18)-(9.19) emphasizes that the two sets of equations differ only through the forcing term, constructed from the two matrices

$$
\mathrm{C} = \begin{bmatrix} 0 & 0 & 0 & 0 & 0 & 0 \\ 0 & 0 & 0 & 0 & 0 & 1/\varepsilon \\ 0 & 0 & 0 & 0 & 0 & 0 \\ 0 & 0 & 0 & 0 & 0 & 0 \\ 0 & 0 & -1/\mu & 0 & 0 & 0 \\ 0 & 0 & 0 & 0 & 0 & 0 \end{bmatrix} ,
$$

and

$$
\mathrm{D} = \begin{bmatrix} 0 & 0 & 0 & 0 & 0 & m/\varepsilon \\ 0 & 0 & 0 & 0 & 0 & 0 \\ 0 & 0 & 0 & -m/\varepsilon & 0 & 0 \\ 0 & 0 & m/\mu & 0 & 0 & 0 \\ 0 & 0 & 0 & 0 & 0 & 0 \\ -m/\mu & 0 & 0 & 0 & 0 & 0 \end{bmatrix} .
$$

The general operator, $\mathrm{A}(\boldsymbol{n})$, with $\boldsymbol{n} = (n_r, n_z)$ representing the local metric, is given as

$$
\begin{bmatrix} 0 & 0 & 0 & 0 & -n_z/\varepsilon & 0 \\ 0 & 0 & 0 & n_z/\varepsilon & 0 & -n_r/\varepsilon \\ 0 & 0 & 0 & 0 & n_r/\varepsilon & 0 \\ 0 & n_z/\mu & 0 & 0 & 0 & 0 \\ -n_z/\mu & 0 & n_r/\mu & 0 & 0 & 0 \\ 0 & -n_r/\mu & 0 & 0 & 0 & 0 \end{bmatrix} .
$$

This operator diagonalizes under the similarity transform, $\mathrm{A}(\boldsymbol{n}) = \mathrm{S}^{-1}(\boldsymbol{n})\,\Lambda(\boldsymbol{n})\,\mathrm{S}(\boldsymbol{n})$, where the diagonal eigenvalue matrix, $\Lambda(\boldsymbol{n})$, has the entries

$$
\Lambda(\boldsymbol{n}) = |\boldsymbol{n}| \mathrm{diag}\,[0, 0, c, c, -c, -c] \quad , \tag{9.20}
$$

corresponding to two non-propagating waves and two waves propagating along $\boldsymbol{n}$ with the speed of light, c, while two waves propagate along $-\boldsymbol{n}$ at the same speed. Here we have that $|\boldsymbol{n}|$ represents the length of the vector $\boldsymbol{n}$, such that $\boldsymbol{n} = |\boldsymbol{n}|(\hat{n}_r, \hat{n}_z)$. The diagonalizing matrix, $\mathrm{S}(\boldsymbol{n})$, is given as

$$\mathrm{S}(\boldsymbol{n}) = \begin{bmatrix} \hat{n}_r & 0 & Z\hat{n}_z & 0 & -Z\hat{n}_z & 0 \\ 0 & 0 & 0 & Z & 0 & Z \\ \hat{n}_z & 0 & -Z\hat{n}_r & 0 & Z\hat{n}_r & 0 \\ 0 & \hat{n}_r & 0 & -\hat{n}_z & 0 & \hat{n}_z \\ 0 & 0 & 1 & 0 & 1 & 0 \\ 0 & \hat{n}_z & 0 & \hat{n}_r & 0 & -\hat{n}_r \end{bmatrix},$$

from which we may obtain

$$\boldsymbol{R} = \mathrm{S}^{-1}(\boldsymbol{n})\boldsymbol{q} = \begin{bmatrix} R_1 \\ R_2 \\ R_3 \\ R_4 \\ R_5 \\ R_6 \end{bmatrix} = \frac{1}{2} \begin{bmatrix} 2\boldsymbol{e} \cdot \tilde{\boldsymbol{n}} \\ 2\boldsymbol{h} \cdot \tilde{\boldsymbol{n}} \\ (\boldsymbol{h} + Z^{-1}\tilde{\boldsymbol{n}} \times \boldsymbol{e}) \cdot \hat{\boldsymbol{\phi}} \\ (Z^{-1}\boldsymbol{e} - \tilde{\boldsymbol{n}} \times \boldsymbol{h}) \cdot \hat{\boldsymbol{\phi}} \\ (\boldsymbol{h} - Z^{-1}\tilde{\boldsymbol{n}} \times \boldsymbol{e}) \cdot \hat{\boldsymbol{\phi}} \\ (Z^{-1}\boldsymbol{e} + \tilde{\boldsymbol{n}} \times \boldsymbol{h}) \cdot \hat{\boldsymbol{\phi}} \end{bmatrix},$$

which we recognize as the characteristic variables, propagating along $\boldsymbol{n}$, with the speeds given by the entries of $\Lambda(\boldsymbol{n})$, Eq.(9.20). Here we have used the general form $\boldsymbol{q} = [\boldsymbol{e}, \boldsymbol{h}]^T$ and introduced $\tilde{\boldsymbol{n}} = (n_r, 0, n_z)$ for clarity.

Besides from revealing information about the dynamics of the fields, the identification and use of characteristic variables plays, as we shall see shortly, an integral role in the specification of the multi-domain scheme, which is the topic of the following section.

9.3.3 The Multi-Domain Formulation

We wish to solve Eqs.(9.18)-(9.19) within a general computational domain, $\Omega \in \mathsf{R}^2$, in the (r, z)-plane with $r \geq 0$. As we have briefly discussed, the most natural and computational efficient way of applying polynomial expansions in several dimensions is through the use of tensor products. This procedure, however, requires that the computational domain can be smoothly mapped to the unit square. To surround this quite severe limitation, we construct Ω using K non-overlapping general curvilinear quadrilaterals, $\mathsf{D}^k \subset \mathsf{R}^2$, such that $\Omega = \bigcup_{k=1}^{K} \mathsf{D}^k$.

The advantages of such an approach, besides from providing the geometric flexibility, are many. In particular in connection with spectral methods, the multi-domain framework results in a lower total operation count and high allowable time-step while providing a very natural data-decomposition, well suited for the implementation on contemporary parallel computers. We refer to [15, 27] for a thorough discussion of the advantages associated with a multi-domain formulation when solving wave-dominated problems.

Once we have split the global computational domain into K subdomains, we need to construct the map, $\Psi : \mathsf{D} \to \mathsf{I}$, (see Fig. 9.1) where $\mathsf{I} \subset \mathsf{R}^2$ is the unit square, i.e., $\mathsf{I} \in [-1, 1]^2$. At this point we have the Cartesian coordinates, $(r, z) \in \mathsf{D}$, and the general curvilinear coordinates, $(\xi, \eta) \in \mathsf{I}$, related through the map, $(x, y) = \Psi(\xi, \eta)$. To establish a one to one correspondence between the unit square and the general quadrilateral we construct the local map for each subdomain using transfinite blending functions [20]. We refer to [28] for a thorough account of this procedure within the present context.

Once the global map, Ψ, has been constructed, we may compute the metric of the mapping and outward pointing normal vectors at all points of the enclosing edges of the quadrilateral.

Within this multi-domain setting we need to solve K independent problems in the individual subdomains. However, to obtain the global solution we have to pass information between the subdomains in a way consistent with the dynamics of Maxwell's equations. Since these equations, Eqs.(9.18)-(9.19), constitute a hyperbolic system it is natural to transfer information between the various subdomains using the characteristic variables introduced in the previous section.

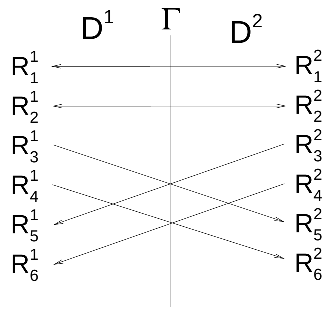

Figure 9.2: Illustration of the patching of subdomains through the use of characteristic variables.

The characteristic variables, $\boldsymbol{R}$, are convected along the normal, $\hat{\boldsymbol{n}}$, with a speed given by the diagonal elements of $\Lambda(\boldsymbol{n})$, Eq.(9.20). Hence, once the outward normal vector at the enclosing boundary of the subdomain is known, as it is once the map, Ψ, is constructed, we may uniquely determine which characteristics are leaving the subdomain and which are entering and thus needs specification. Indeed, we observe from Eq.(9.20) that while R_3 and R_4 are always leaving the domain and therefore need no boundary conditions, R_5 and R_6 are always entering the computational domain and requires specification to ensure wellposedness. Based on this observation, we sketch in Fig. 9.2 the scheme for patching of two subdomains, D^1 and D^2, sharing the common edge, Γ. The two characteristic variables, R_3^1 and R_4^1, leaving D^1, supplies the sought after boundary conditions for R_5^2 and R_6^2 and reversely for the specification of R_5^1 and R_6^1. For the non-propagating R_1 and R_2 we simply use the average across Γ. Once the characteristic variables have been adjusted, the physical fields are simply recovered through the relation $\mathrm{S}(\boldsymbol{n})\boldsymbol{R} = \boldsymbol{q}$. This procedure is applied along all interface points, including the vertices where it is done dimension-by-dimension, to arrive at the global solution at each times-step. As we shall see shortly, this procedure of patching hyperbolic systems is stable as well as accurate. Moreover, in a parallel setting the communication between subdomains grows only like the surface of the geometric building block rather than the volume.

9.3.4 Far Field Boundary Conditions

A long standing problem in computational electromagnetics has been the issue of finding infinite space solutions on a finite computational domain. The critical issue is how to construct appropriate boundary conditions that prevent outgoing waves from being reflected from the artificial numerical boundaries.

Characteristic boundary condition is used in different numerical schemes in many types of applications, see e.g. [48]. It can serve as an absorbing boundary condition by imposing the incoming characteristic variables to be zero. However, it was shown in [56] that the accuracy of the approach is limited, in particular when the artificial boundary is placed close to the scatterer, as is often a necessity when considering computational intensive problems involving e.g. electrically large or transient problems.

The introduction of the perfectly matched layer (PML) methods [3] has spawned significant research into such methods. However, serious problems with these types of boundary conditions has recently been exposed [2] for the two-dimensional PML methods while the mathematical properties of the recently developed three-dimensional PML methods [4] remains unknown. Moreover, the development of well behaved PML methods suitable for the BOR formulation of Maxwell's equations remains an open challenge.

In [56] we introduced a matched layer (ML) method, well suited for use in connection with multi-domain methods. An absorbing layer, introduced through terms like $-\sigma(\xi,\eta)\boldsymbol{q}_{1,2}$ in Eqs.(9.18)-(9.19), is put in the out-most subdomain at some distance from the subdomain interface and a cubic grid mapping is used to generate a mesh that is coarse in the part of the outer subdomain covered by the layer. With the help of a low pass filter, the reflections in the ML region, being of high frequency relative to the local grid, is then being filtered out. Despite its simplicity, the ML method was shown to perform very well in [56], with the additional advantages of being mathematically sound and simple to implement.

9.4 Numerical Experiments

To validate the accuracy and computational efficiency of the complete computational framework discussed in the previous sections, we have computed plane wave scattering by a number of perfectly conducting bodies of revolution, previously studied through the use of analytic or alternative numerical schemes, e.g., BOR methods-of-moments [37].

To assess the accuracy of the computational framework we use the bistatic Radar Cross Section (RCS), $\sigma(\theta,\phi)$, yielding a measure between the time-averaged incident and the scattered fields and formally defined as [31]

$$\sigma(\theta,\phi) = \lim_{r\to\infty} 4\pi r^2 \frac{|\boldsymbol{E}^s_\infty|^2}{|\boldsymbol{E}^{inc}|^2} \quad ,$$

where (θ,ϕ) measures the angles between the incident wave vector, $\boldsymbol{k}^i$, and the scattered wave vector, $\boldsymbol{k}^s$, given as

$$\boldsymbol{k}^s = Z\frac{\boldsymbol{E}^s_\infty \times \boldsymbol{H}^s_\infty}{|\boldsymbol{E}^s_\infty|^2} \quad ,$$

where $\boldsymbol{E}^s_\infty$ and $\boldsymbol{H}^s_\infty$ signifies the far field values of the scattered fields. Unless otherwise stated we normalize σ with the square of the wavelength, λ, of the incident wave and define

$$\mathrm{RCS}(\theta,\phi) = 10\log_{10}\frac{\sigma(\theta,\phi)}{\lambda^2} \quad ,$$

as our measure of accuracy. As we are only computing the near fields, we apply a near-field to far-field transformation, see e.g., [51], with the enclosing surface being chosen to coincide with grid lines and a Chebyshev-Clenshaw-Curtis integration [10] is used for approximating the integrals.

Only the scattered fields are computed and the objects are illuminated through the boundaries as discussed in Sec. 9.2.2. To advance the fields in time we use a 4th order Runge-Kutta scheme [10] and we enforce the boundary conditions as well as perform the patching of the local solutions at the intermediate time-steps of the integration. The time-step is chosen below the stability limit

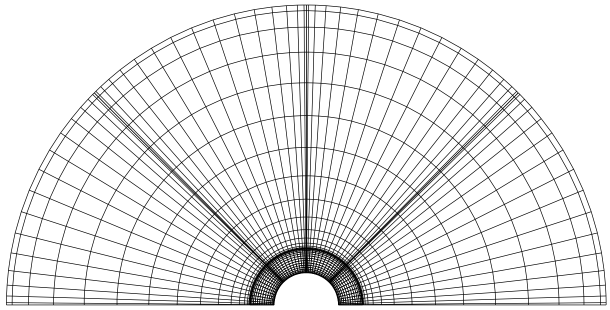

Figure 9.3: Typical multi-domain grid for the computation of scattering by a sphere. Note the stretching of the grid in the outer subdomains in order to successfully absorb outgoing waves in the ML layer without increasing the computational work.

to avoid severe dispersion errors and we apply a filter, as described in Sec. 9.3.1, with $N_c = 0$ and $\gamma \sim N$, following the completion of each time-step.

9.4.1 Scattering by a Sphere

Scattering by perfectly conducting spheres serves as an optimal test case since the analytical solution is known in terms of a Mie series [6]. We need only to consider axial illumination, i.e. only the $m = 1$ mode in Eqs.(9.3)-(9.4) is required due to the symmetry of the scatterer and the properties of the fields. In accordance with standard notation the RCS is normalized with πa^2 rather than with the wavelength of the incident wave.

In Fig. 9.3 we show a typical grid layout for the computation of scattering by the sphere. We use 8 subdomains in two layers surrounding the upper half ($r \geq 0$) of the sphere with the number of modes in each subdomain depending on the electrical size of the problem.

In Fig. 9.4 we compare the analytic solution for plane wave scattering by a $ka = 8.3$ sphere with the solution obtained using the multi-domain scheme with $K = 8$, as in Fig. 9.3, and $N = 16$ in all domains. For the numerical solution we use either characteristic boundary conditions or the ML layer technique discussed in Sec. 9.3.4. Indeed, we clearly observe the 2nd order accuracy of the characteristic boundary conditions [56] in the back scatter region while the ML solutions and the analytic solution overlap completely, illustrating the expected accuracy of the spectral multi-domain

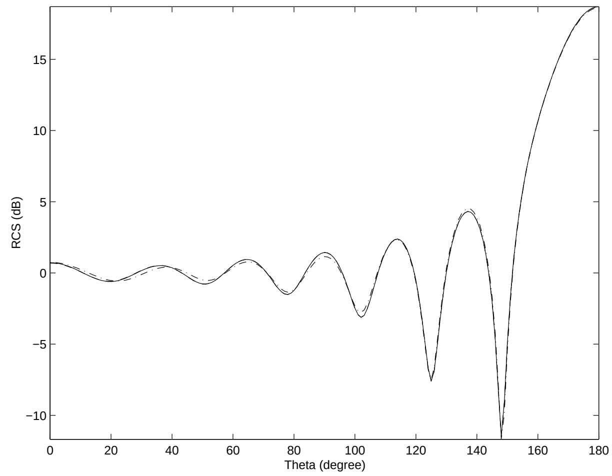

Figure 9.4: RCS(θ,0) for a perfectly conducting sphere, $ka = 8.3$. We compare the exact Mie series (dashed), the spectral multi-domain solution with characteristic boundary conditions (dashed-dotted) and using the ML far field boundary conditions (full).

framework.

To emphasize the strength of spectral methods when addressing electrically large problems, we show in Fig. 9.5 a comparison between the analytic solution and the computed solution obtained with a $K = 20$ and $N = 16$ spectral multi-domain solution for a $ka = 40.0$ sphere. Indeed, we find, even in the highly sensitive backscatter region, close to perfect agreement between the two solutions.

The solution of the $ka = 40.0$ scattering remains a significant challenge for conventional methods like MoM or FD-TD due to e.g. ill-conditioning or prohibitive errors and size of the computational problem associated with the solution of electrically large problems. Using the present scheme the solution shown in Fig. 9.5 is obtained in about 20 minutes using an average sized work station.

Although scattering from a sphere may serve as an excellent starting point for the evaluation of a new numerical scheme, it is certainly of only marginal practical importance. In the following we shall study the performance of the multi-domain scheme for scattering problems of a more general character. Due to lack of analytic solutions we shall compare the computed RCS with results from the open literature.

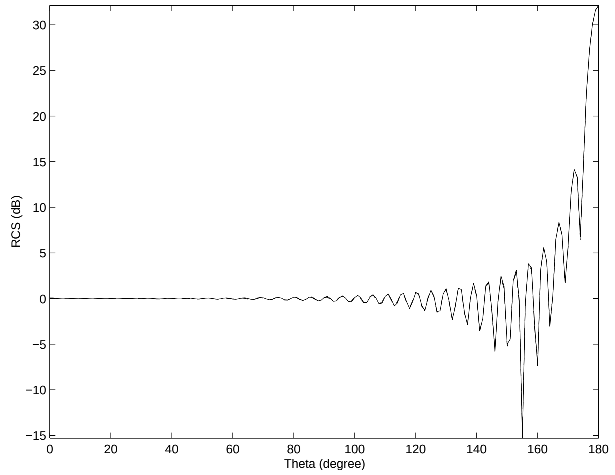

Figure 9.5: RCS(θ,0) for a perfectly conducting sphere, $ka = 40.0$. We compare the exact Mie series (dashed) and the spectral multi-domain solution using the ML far field boundary conditions (full).

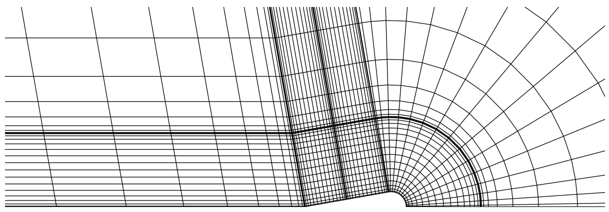

Figure 9.6: Fraction of a typical multi-domain grid for the computation of plane wave scattering by a smooth sphere-cone.

9.4.2 Scattering by Generic Objects - Axial Incidence

Due to the simplicity of the problem, i.e., we only need to consider the $m = 1$ mode in Eqs.(9.3)-(9.4), let us first look at scattering of plane waves impinging axially.

In Fig. 9.6 we show part of a typical grid for the computation of scattering by a 20 deg. cone smoothly joined with a spherical cap having a radius of 0.2λ. This case was first considered in [37] in which the problem is solved using a MoM scheme.

The RCS, as computed using $K = 8$ and $N = 16$ in all domains, is compared in Fig. 9.7 with the results reported in [37] for horizontal and vertical polarization of the incident fields. This being an electrically small object, we should expect excellent agreement between the MoM result [37] and

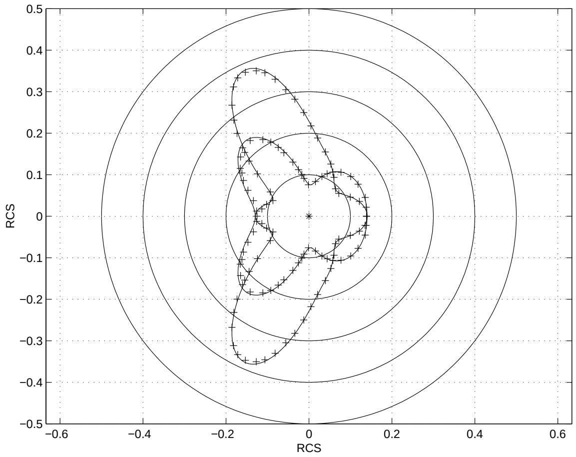

Figure 9.7: RCS(θ,0) for smooth cone-sphere with axial incidence. The reference solution, marked by "+", is taken from [37].

the multi-domain solution and this is indeed confirmed in Fig. 9.7.

A more challenging test is that of plane wave scattering by a 45 deg. cone joined non-smoothly with a spherical cap of radius $kr = 10$. The total length of the scatter is $ka = 20$, similar to the problem considered in [38]. We recall that the field components in the (r, z)-plane may exhibit weak singular behavior as discussed in Sec. 9.2.2.

In Fig. 9.8 we compare the computed RCS for axial incidence with the results reported in [38]. Indeed, compared with the scenario in Fig. 9.7, we observe a dramatic increase in the dynamic range of the RCS due to the larger electric size and increased geometric complexity but we maintain excellent agreement between the reference and the results obtained using the multi-domain spectral scheme. The grid, a fraction of which is given in Fig. 9.9, consists of $K = 8$ domains, each employing a resolution of $N = 16$ modes in each direction. We note in particular that no effort has been put into selective refinement of the grid around the edges, something that would have been crucial in case a low order scheme was used.

9.4.3 Scattering by Generic Objects - Oblique Incidence

As the next level of added complexity, we consider scattering by generic objects, much like in the previous sections, however subject to oblique illumination. This problem is more complicated in that

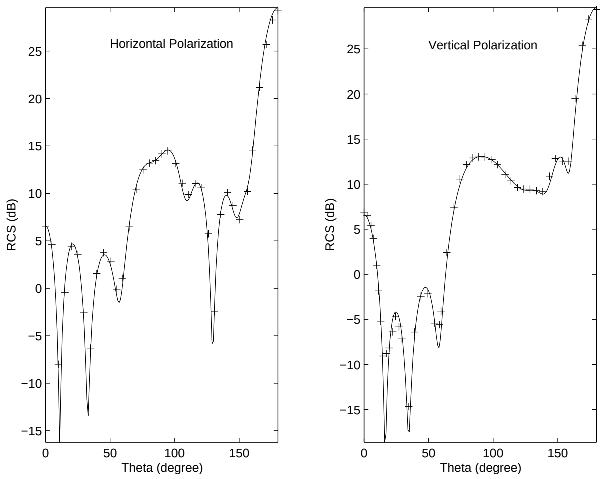

Figure 9.8: RCS(θ,0) for non-smooth cone-sphere with axial incidence. The reference solution, marked by "+", is taken from [38].

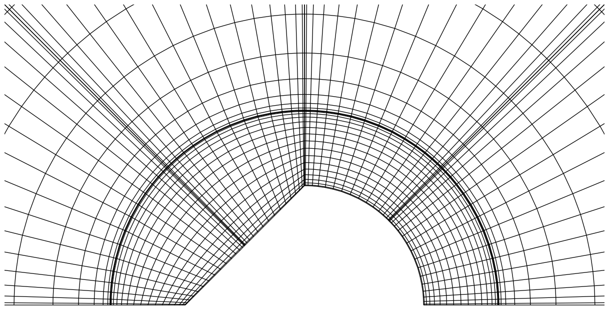

Figure 9.9: Typical multi-domain grid used for the computation of scattering by a non-smooth sphere-cone.

the number of modes required in the azimuthal expansions of the fields, Eqs.(9.3)-(9.4), is larger than for axial incidence where only one mode is required due to the properties of the fields.

The number of modes required in the azimuthal expansion is naturally problem dependent. However, since the fields can be assumed to process a high degree of regularity one can expect that using only a few modes yields accurate results.

The first case, the grid of which is given in Fig. 9.9, is the non-smooth cone-sphere considered in the last section, but illuminated with a wave impinging at a 20 deg. angle, and we use 12 Fourier modes to approximate the azimuthal field variation. The grid is similar to the case of axial

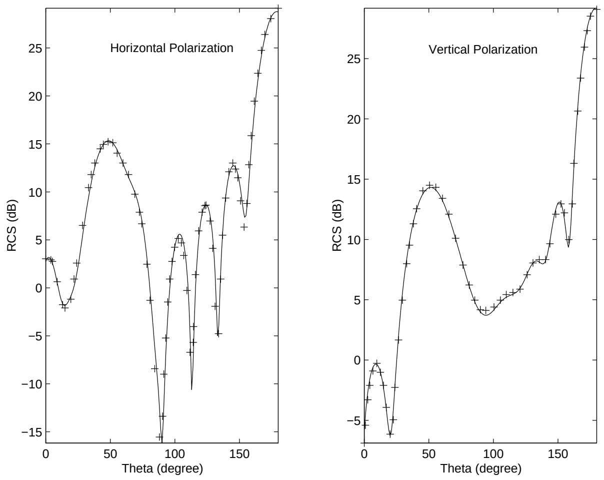

Figure 9.10: RCS(θ,0) for scattering of a 20 deg. obliquely incident wave by a non-smooth cone-sphere. The reference solution, marked by "+", is taken from [38].

illumination and in Fig. 9.10 we compare the computed RCS with the solution reported in [38], observing excellent agreement over a more than 40 dB dynamic range.

As a second example of oblique scattering we consider scattering by a finite cylinder, illuminated by a plane wave impinging at 45 deg. The length as well as the radius of the cylinder is 2λ and we use a $K = 12$ and $N = 16$ grid for solving the problem which was previously considered in [18].

In Fig. 9.11 we show the computed cross section, as obtained using 14 Fourier modes, enough to arrive at a converged result, and compared with the results of [18] for horizontal polarization. The result for vertical polarization is given in Fig. 9.12 and we observe close agreement between the different approaches to the scattering problem, confirming the accuracy and efficacy of the spectral multi-domain scheme developed here.

9.4.4 Scattering by General Objects

As a final illustration of the versatility of the multi-domain scheme for the accurate modeling of scattering by objects of arbitrary geometric complexity, we consider the problem of scattering by a perfectly conducting missile illuminated by a 4 GHz plane wave at axial/nose incidence. The missile is about 7.25 wavelengths long and the diameter of the main body is 1 wavelength in diameter.

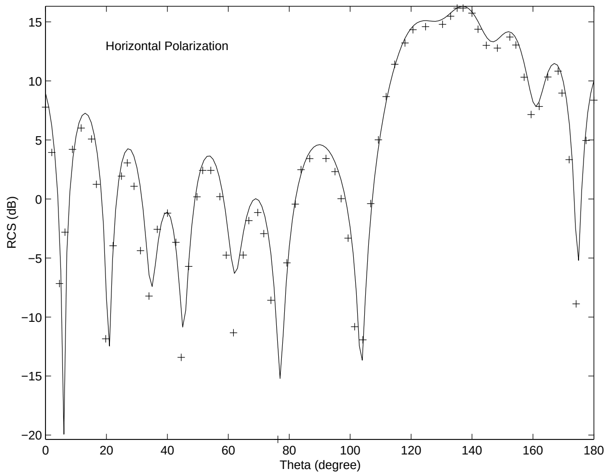

Figure 9.11: RCS(θ,60) for scattering by a finite cylinder, illuminated by a horizontally polarized plane wave impinging at 45 deg.. The reference solution, marked by "+", is taken from [18].

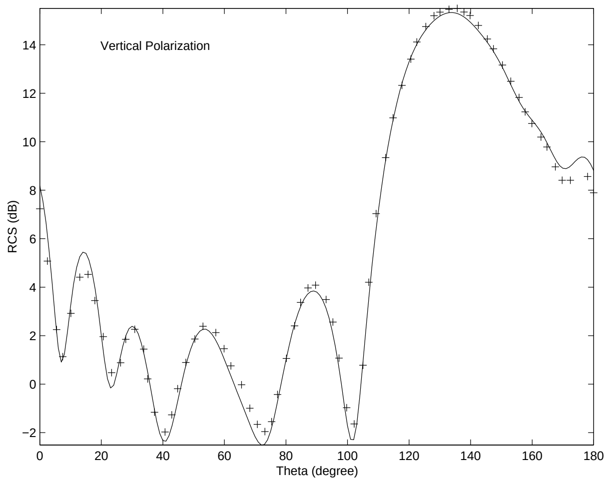

Figure 9.12: RCS(θ,60) for scattering by a finite cylinder, illuminated by a vertically polarized plane wave impinging at 45 d ... from [18].

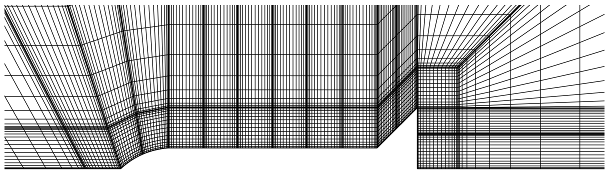

Figure 9.13: Typical multi-domain grid for the solution of the scattering by a missile.

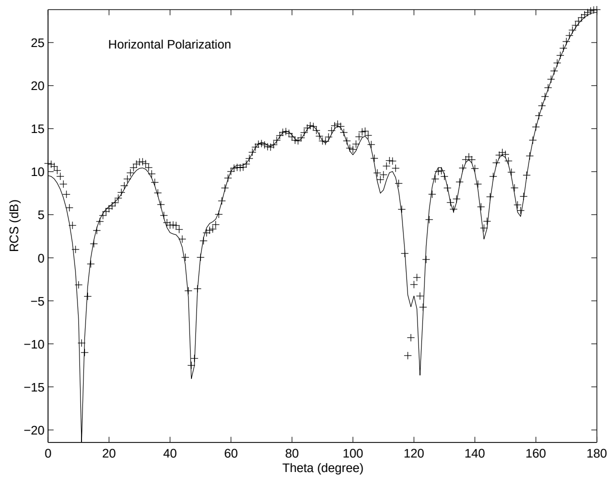

Figure 9.14: RCS(θ,0) for a missile subject to axial illumination by a horizontally polarized plane wave. The reference solution, marked by "+", was provided by [50].

In Fig. 9.13 we show a fraction of the computational grid, illustrating that while the object is of only moderate electric size, it is of considerable geometric complexity and contains features like a sharp wedge at the tail. The grid is constructed using $K = 31$ subdomains, each employing a resolution of $N = 16$.

For axial incidence of a horizontally polarized plane wave, we show in Fig. 9.14 the computed cross section compared with that obtained using a standard MoM approach [50]. We observe excellent agreement to within a few dB over a dynamic range of close to 60 dB. The difference between the present solution and the MoM solution is most pronounced in the backscatter region which is well known to be very sensitive to modeling errors. However, it remains unknown which result is most accurate. We recall, though, that the MoM is known to process certain accuracy problems for increasing size and geometric complexity, suggesting that the results of the present scheme might well be superior.

In Fig. 9.15 we compare the results for the case of vertical polarization, confirming the overall accuracy and versatility of the pseudospectral multi-domain scheme.

9.5 Concluding Remarks

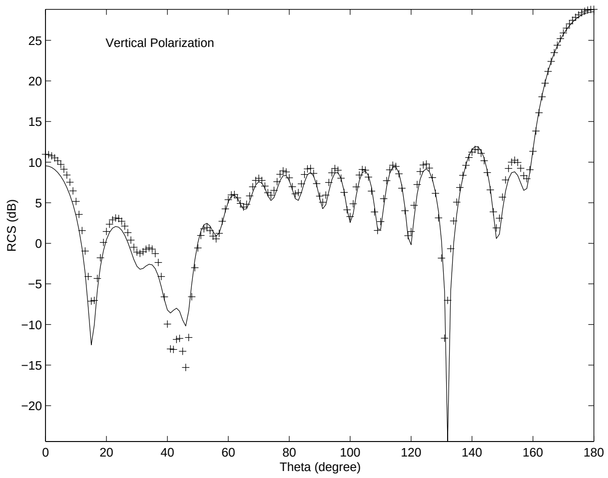

Figure 9.15: RCS(θ,0) for a missile subject to axial illumination by a horizontally polarized plane wave. The reference solution, marked by "+", was provided by [50].

The purpose of this chapter has been two-fold. We wanted, on one hand, to illustrate to the reader the benefits of using high-order/spectral multi-domain schemes for the solution of problems in electromagnetics, in this case the scattering problem. As we experienced through discussions as well as numerical studies, the use of pseudospectral multi-domain methods for the time-domain solution of scattering problems yields not only results of superior accuracy, but does so in a very efficient manner compared with more conventional low order FD-TD schemes. Indeed, computational electromagnetics of the future will require the ability to handle accurate long time integration often involving electrically large structures - a scenario for which the use of high-order/pseudospectral methods is likely to be the optimal choice of method.

The second objective of this chapter was to continue the detailed development and evaluation of the pseudospectral time-domain method initiated in our previous work [56, 57] in which we dealt with two dimensional problems. Here we have developed a multi-domain scheme for the computation of scattering by arbitrary bodies of revolution and illustrated the superior properties of such a scheme through numerous computations and successful comparisons with results from the literature.

Although the development of the BOR scheme opens up for the computation of large complex axis-symmetric bodies, hitherto intractable through direct numerical modeling, many issues remain open in the quest towards a general purpose multi-domain pseudospectral scheme. Apart from issues like grid generation, a severe problem independent of the method of choice, we need to address problems beyond the pure scattering problem discussed here. Indeed, the development and evaluation of high-order/pseudospectral schemes for problems involving various types of materials remains the most immediate open issue and we hope to report on development along these lines in a not too distant future.

Chapter 10

Scattering by Dielectric Spheres

10.1 Introduction

In the previous chapters, we only considered PEC scatterers. In this chapter, we try to extend the area of applicability of pseudospectral methods by focusing on problems involving complex materials. Such a development will allow us to extend our area of practical application to many problems in high-speed integrated electronic circuits, integrated optical systems, wireless communication, or microstrip antennas. For one example, it will help to maintain and improve international safety standards applicable to the use of cellular radio telephones where reliable calculations of the electromagnetic field intensities in the human head, brain, and neck are required. The human head/cellular telephone problem requires the calculation of the electromagnetic field components within a lossy dielectric structure, with the size of a wavelength of the incident radiation.

It is well known that one can not use the limiting analytical solutions for small or large objects when the characteristic scale is around a wavelength of the incident radiation. Instead, numerical methods find their great use in these applications. Among them there are time domain methods such as the FD-TD method and the spectral time domain methods we have developed. Since spectral methods require only a few grid points per wavelength to accurately capture the dynamics, it is optimal for the applications we mentioned.

There are a few difficulties associated with these applications. Since the fields can be discontinuous at the interface between different materials, proper boundary condition or matching condition has to be found there. Another difficulty lies in the difference between the characteristic lengths in different materials. Using a uniform mesh and a uniform time step, which is adopted in most computations, may waste a great deal of computational resource. Finding an optimal computational model for problems with different characteristic lengths is meaningful in problems involving different materials.

In this chapter, we will use our BOR multidomain pseudospectral method to simulate scattering by dielectric spheres. Patching conditions at the dielectric-vacuum interface will be investigated.

10.2 Computational Model

At the interface between two media, the properties of the overall medium change discontinuously, and this may result in discontinuities in some components of the field. The transition relating the fields on the two sides of the interface have been given in Eqs. (2.5)-(2.8). If neither medium is a PEC (perfect electric conductor) or PMC (perfect magnetic conductor), the interface cannot support a surface current, and $\mathbf{J}_{e(s)} = 0$. The resulting boundary conditions are

$$[\hat{n} \times \mathbf{E}]_{-}^{+} = 0 \ , \qquad [\hat{n} \times \mathbf{H}]_{-}^{+} = 0 \ , \tag{10.1}$$

showing the continuity of the tangential components of the electric and magnetic fields across the interface. Moreover, if either medium has non-zero (but finite) loss, $\rho_{e(s)} = \rho_{m(s)} = 0$ and hence

$$[\hat{n} \cdot \epsilon\mathbf{E}]_{-}^{+} = 0 \ , \qquad [\hat{n} \cdot \mu\mathbf{H}]_{-}^{+} = 0 \ , \tag{10.2}$$

showing that the normal components of the electric and magnetic fields across the interface can be discontinuous.

For the dielectric spheres we consider in this chapter, all the relations in Eqs. (10.1) and (10.2)

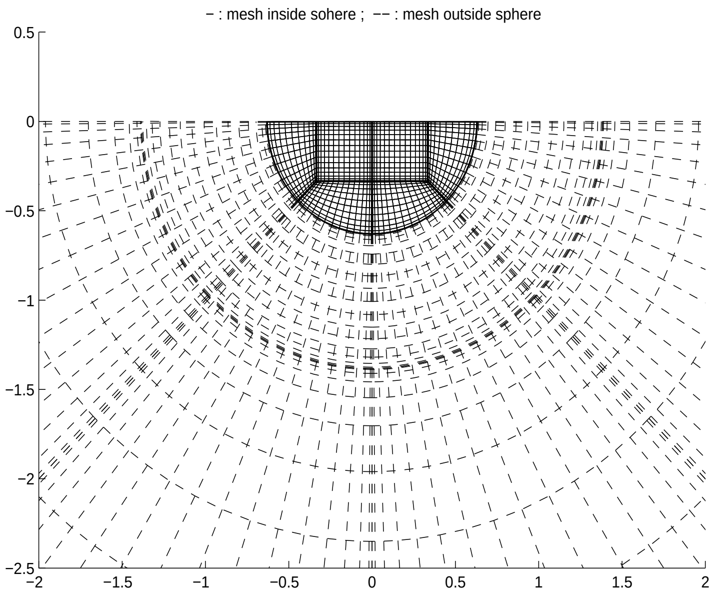

Figure 10.1: The mesh used for simulating scattering by a dielectric sphere.

are satisfied at the interface, i.e. the sphere surface. In the numerical simulation, we extend the BOR multidomain pseudospectral scheme that was introduced in the last section to include structures of different electric and magnetic properties. In Fig. (10.1) we show the multidomain mesh we use for simulation. Note that the sphere itself is also simulated now.

In this simulation, we apply the total-field/scattered-field idea to excite the computation. The total field and the scattered field are related by

$$\vec{E}_t = \vec{E}_{sc} + \vec{E}_{inc} \ ,$$

and the same for $\vec{H}$, where the subscript $_{sc}$ stands for the scattered field, the subscript $_{inc}$ for the incident field, and the subscript $_t$ for the total field. In the out-most subdomains, the scattered field formulation is used for computation, while in other subdomains, the total field formulation is used. At the interface between total field and scattered field, the patching condition can be found since the incident field is known and the total field equals scattered field added with incident field.

At the surface of the dielectric sphere, the values of ϵ and μ may be different from the values of the ϵ_0 and μ_0 in free space. Thus some components of the fields can be discontinuous, and the usual patching procedure does not apply here directly. Instead, we apply the transition conditions of the

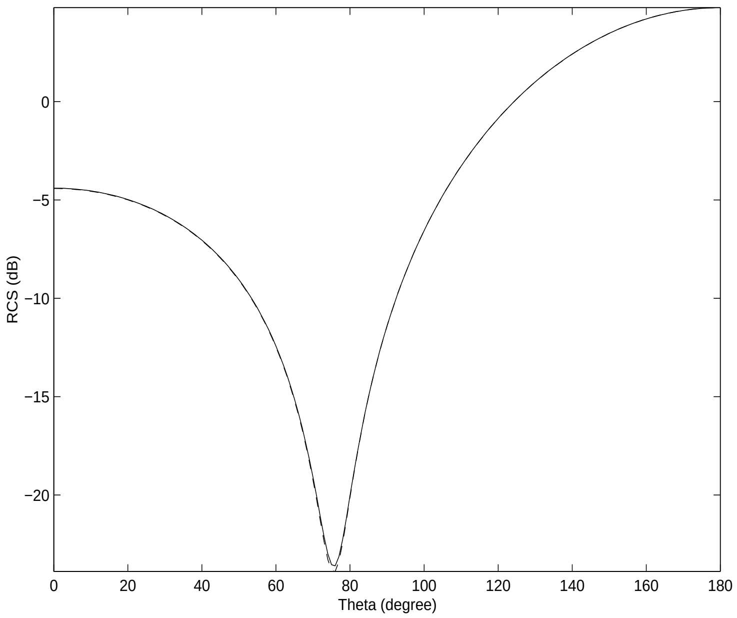

Figure 10.2: Numerical RCS result of scattering by a dielectric sphere: ka=0.2, $\epsilon_r = 3$, and $\mu_r = 1$, dashed line, compared with Mie-series result, solid line.

fields in Eqs. (10.1)-(10.2).

10.3 Numerical Results

In this section we give some RCS results of scattering by dielectric spheres. For reference, we use the Mie-series results. In these numerical experiments, the sphere is also simulated and we use the total-field/scattered-field to excite the computation.

In Fig. 10.2 we show the RCS result of the simulation of scattering by a sphere whose relative permittivity $\epsilon_r = 3$ and relative permeability $\mu_r = 1$. The size of the sphere is $ka = 0.2$ with k being the free-space wave number. This is a small-size problem, and the numerical result we obtain by advancing our scheme for about 10 wave periods agrees well with the analytical one.

In Fig. 10.3 we show the RCS result of the simulation of scattering by a sphere with relative permittivity $\epsilon_r = 3$ and relative permeability $\mu_r = 1$. The size of the sphere is $ka = 5.3$. For this problem, the numerical result agrees with the analytical one very well. One can barely see any difference in the RCS plots. We need to run for almost 40 wave periods to get the RCS result in Fig. 10.3, which agrees with the analytical one very well.

In Fig. 10.4 we show the RCS result of the simulation of scattering by a sphere whose relative

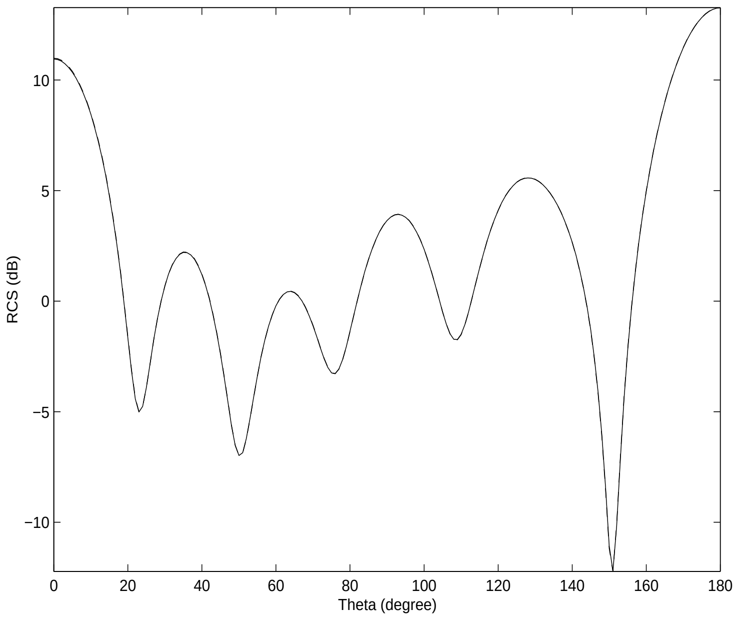

Figure 10.3: Numerical RCS result of scattering by a dielectric sphere: ka = 5.3, $\epsilon_r = 3$, and $\mu_r = 1$, dashed line, compared with Mie-series result, solid line.

permittivity $\epsilon_r = 4$ and relative permeability $\mu_r = 1$. The size of the sphere is the same as that in Fig. 10.3. One notices that the RCS changes a lot when ϵ_r changes from 3 to 4, which suggests that ϵ_r has large effects on the scattered fields. In this simulation, the numerical result converges to the analytical one about two times slower. By advancing our scheme for almost 70 wave periods, we are able to obtain the RCS result in Fig. 10.4, which is satisfying but not as accurate as the result in Fig. 10.3. Any technique that can increase the convergence rate will make a big difference in the simulation of scattering by dilectrics.

10.4 Concluding Remarks

In this chapter, we present some preliminary results on the simulation of scattering by dielectric sphere. Numerical results suggest that scattering by dielectrics, and also other complex materials, are more demanding than the simulation of scattering by PEC objects. We believe that spectral methods are of great use here and this is our future research area.

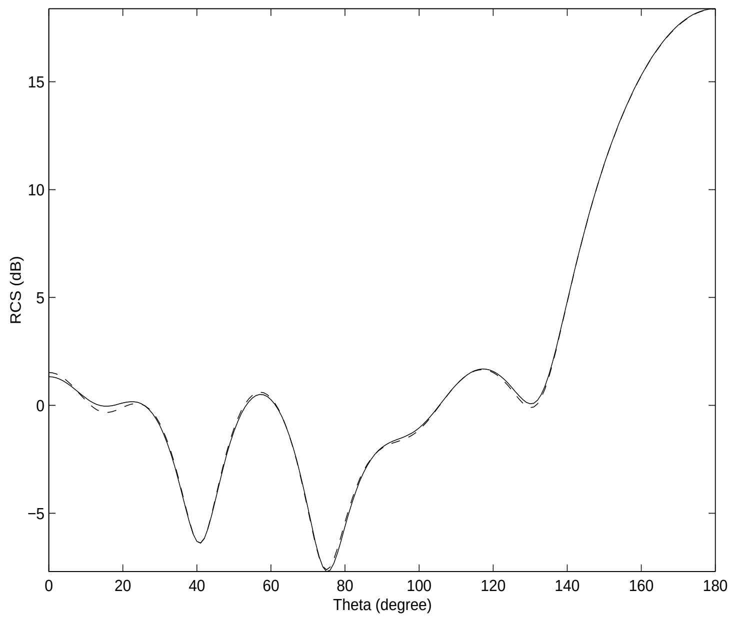

Figure 10.4: Numerical RCS result of scattering by a dielectric sphere: ka = 5.3, $\epsilon_r = 4$, and $\mu_r = 1$, dashed line, compared with Mie-series result, solid line.

Bibliography

[1] S. Abarbanel and D. Gottlieb, On the construction and analysis of absorbing layers in C.E.M, in *Proc. of the 13'th Annual Review of Progress in Applied Computational Electromagnetics*, 1997.

[2] S. Abarbanel and D. Gottlieb, A mathematical analysis of the PML method, *J. Comput. Phys.*, vol. 134, no. 2, pp. 357-363, 1997.

[3] J. P. Berenger, A perfectly matched layer for the absorption of electromagnetic waves, *J. Comput. Phys.*, vol. 114, pp. 185-200, 1994.

[4] J. P. Berenger, Three-dimensional perfectly matched layer for the absorption of electromagnetic waves, *J. Comput. Phys.*, vol. 127, pp. 363-379, 1996.

[5] D. P. Bouche, F. A. Molinet and R. Mittra, Asymptotic and hybrid techniques for electromagnetic scattering, *Proceedings of the IEEE*, vol. 81, no. 12, pp. 1658-1684, December 1993.

[6] J. J. Bowman T. B. A. Senior and P. L. E. Uslenghi, Electromagnetic and acoustic scattering by simple shapes, Hemisphere Publishing Corporation, New York, 1987.

[7] A. Erdely, Higher transcendental functions, Krieger Publishing Co., Melbourne, Fl, 1981

[8] D. Funaro, Domain decomposition methods for pseudospectral approximations. Part one: Second order equations in one dimension., *Numer. Math.*, vol. 52, pp. 329-344, 1988.

[9] D. Funaro, Polynomial approximation of differential equations, vol. m8 of *Lecture Notes in Physics*, Springer Verlag, Berlin, 1992.

[10] C. Canuto, M. Y. Hussaini, A. Quarteroni and T. A. Zang, Spectral methods in fluid dynamics, *Springer Series in Computational Physics*, Springer Verlag, New York, 1987.

[11] L. Dettori and B. Yang, On the Chebyshev penalty method for parabolic and hyperbolic equations, *Mathematical Modeling and Numerical Analysis*, Vol. 30-7, pp. 907-920, 1996.

[12] W. S. Don and A. Solomonoff, Accuracy and speed in computing the Chebyshev collocation derivative,

[13] W. S. Don and D. Gottlieb, The Chebyshev-Legendre method: implementing Legendre methods on Chebyshev points, *SIAM J. Numer. Anal.*, 6 (1994) pp. 1519-1534.

[14] B. Engquist and A. Majda, Absorbing boundary conditions for the numerical simulation of waves, *Math. Comput.*, vol. 31, pp. 629-651, 1977.

[15] P. Fischer and D. Gottlieb, On the optimal number of subdomains for hyperbolic problems on parallel computers, *Int. J. Supercomputer Appl. High Perform. Comput.*, vol. 11, no. 1, pp. 65-76, 1997.

[16] D. Funaro and D. Gottlieb, A new method of imposing boundary conditions for hyperbolic equations, *Math. Comput.*, vol. 51, pp. 599-613, 1988.

[17] D. Funaro and D. Gottlieb, Convergence results for pseudospectral approximations of hyperbolic systems by a penalty-type boundary treatment, *Math. Comput.*, vol. 57, pp. 585-596, 1991.

[18] S. D. Gedney and R. Mittra, The use of the FFT for the efficient solution of the problem of electromagnetic scattering by a body of revolution, *IEEE Trans. Antennas Propagat.*, vol. 38, no. 3, pp. 313-322, 1990.

[19] Stephen D. Gedney, An anisotropic perfectly matched layer-absorbing medium for the truncation of FD-TD lattices, *IEEE Trans. Antennas and Propagat.*, vol. 44, pp. 1630-1639, December 1996.

[20] W. J. Gorgon and C. A. Hall, Transfinite element methods: Blending-Function interpolation over arbitrary curved element domains, *Numer. Math.*, vol. 21, pp. 109-129, 1973.

[21] W. J. Gorgon and C. A. Hall, Construction of curvilinear co-ordinate systems and applications to mesh generation, *Int. J. Numer. Mech. Eng.*, vol. 7, pp. 461-477, 1973.

[22] D. Gottlieb and S. A. Orszag, Numerical analysis of spectral methods: Theory and applications, vol. 26 of *CBMS-NSF Regional Conference Series in Applied Mathematics*, SIAM Publications, Philadelphia, 1977.

[23] D. Gottlieb, M. Gunzburger and E. Turkel, On numerical boundary treatment for hyperbolic systems, *SIAM J. Numer. Anal.*, vol. 19, pp. 671-697, 1982.

[24] D. Gottlieb, M. Y. Hussaini and S. A. Orszag, Theory and application of spectral methods, in: R. Voigt, D. Gottlieb and M.Y. Hussaini, ds., Spectral Methods for Partial Differential Equations (SIAM-CBMS, Philadelphia, PA, 1984) pp. 1-94.

[25] D. Gottlieb and B. Yang, Comparisons of staggered and non-staggered schemes for Maxwell's equations, in *Proc. of the 12'th Annual Review of Progress in Applied Computational Electromagnetics*, Naval Postgraduate School, Monterey, CA, March 1996, vol. II, pp. 1122-1131.

[26] M. J. Grote and J. B. Keller, Nonreflecting boundary conditions for Maxwell's equations, *J. Comp. Phys.* - to appear, 1997.

[27] J. S. Hesthaven, A stable penalty method for the compressible Navier-Stokes equations. II. One dimensional domain decomposition schemes, *SIAM J. Sci. Comp.*, vol. 18, pp. 658-685, 1997.

[28] J. S. Hesthaven, A stable penalty method for the compressible Navier-Stokes equations. III. Multi dimensional domain decomposition schemes, *SIAM J. Sci. Comp.*, 1997, Accepted.

[29] R. L. Higdon, Numerical boundary conditions for the wave equation, *Math. Comput.*, vol. 49, pp. 65-90, 1987.

[30] Adour V. Kabakian, A spectral algorithm for electromagnetic wave scattering in the time domain application to RCS computation, *AIAA Paper* 96-2334.

[31] E. F. Knott J. F. Shaeffer and M. T. Tuley, Radar cross section, Aztech House, Boston, 1993.

[32] D.A. Kopriva and J.H. Kolias, A conservative staggered-grid Chebyshev multidomain method for compressible flows, ICASE Report No. 95-18, 1995.

[33] H. Kreiss and J. Oliger, Methods for the approximate solution of time dependent problem, Garp Publication Series No. 10, 1973.

[34] H. O. Kreiss and J. Oliger, Comparison of accurate methods for the integration of hyperbolic equations, *Tellus*, vol. 24, pp. 199-215, 1972.

[35] M. Kuzuoglu and R. Mittra, Investigation of nonplanar perfectly matched absorbers for finite-element mesh truncation, *IEEE Trans. Antennas and Propagat.*, vol. 45, pp. 474-486, March 1997.

[36] Jian-Ming Jin and Weng Cho Chew, Combining PML and ABC for the finite-element analysis of scattering problems, *Microwave and Optical Technology Letters*, vol. 12, no. 4, 1996.

[37] J. R. Mautz and R. F. Harrington, Radiation and scattering from bodies of revolution, *Appl. Sci. Res.*, vol. 20, pp. 405-435, 1969.

[38] L. N. Medgyesi-Mitschang and D. Wang, Hybrid solutions for scattering from perfectly conducting bodies of revolution, *IEEE Trans. Antennas Propagat.*, vol. 31, no. 6, pp. 570-583, 1983.

[39] J. Meixner, The behavior of electromagnetic fields at edges, *IEEE Trans. Antennas Propagat.*, vol. 20, no. 4, pp. 442-446, 1972.

[40] G. Mur, Absorbing boundary conditions for the finite-difference approximation of the time-domain electromagnetic field equations, *IEEE Trans. Electromagn. Compat.*, vol. EMC-23, pp. 377-382, 1981.

[41] E. A. Navarro, C. Wu, P. Y. Chung and J. Litva, Application of PML superabsorbing boundary condition to non-Orthogonal FD-TD method, *IEE Electron. Lett.* **30**(1994), pp. 1654-1655.

[42] P. G. Petropoulous, Phase error control for FD-TD methods of second and fourth order accuracy, *IEEE Trans. Antennas Propagat.*, vol. 42, no. 6, pp. 859-862, 1994.

[43] P. Petropoulos, L. Zhao and A. C. Cangellaris, A reflectionless sponge layer absorbing boundary condition for the solution of Maxwell's equations with high-Order staggered finite difference schemes, *J. Comp. Phys.* - submitted, 1996.

[44] C. M. Rappaport, Perfectly matched absorbing boundary conditions based on anisotropic lossy mapping of space, *IEEE Microwave Guid. Wave Lett.* **5**(1995), pp. 94-96.

[45] Z. S. Sacks, D. M. Kingsland, R. Lee, and J. F. Lee, A perfectly matched anisotropic absorber for use as an absorbing boundary condition, *IEEE Trans. Antennas and Propagat.*, vol. 43, pp. 1460-1463, December 1995.

[46] T. B. A. Senior and J. L. Volakis, Approximate boundary conditions in electromagnetics, *IEE Electromagnetic Waves Series* 41, 1995.

[47] J. S. Shang, A comparative study of characteristic-based algorithms for the Maxwell equations, *J. Comput. Phys.*, vol. 125, pp. 378-394, 1996.

[48] J. S. Shang, Time-domain electromagnetic scattering simulations on multicomputers, *J. Comput. Phys.*, vol. 128, no. 2, pp. 381-390, 1996.

[49] J. S. Shang, Scattering simulation of computational electromagnetics, *AIAA*, 96-2337, 1996.

[50] J. S. Shang, Private communication, 1997.

[51] A. Taflove, Computational electrodynamics: The Finite-Difference Time-Domain method, Artech House, Boston · London, 1995.

[52] F. L. Teixeira and W. C. Chew, PML-FDTD in cylindrical and spherical grids, *IEEE Microwave Guided Wave Lett.*, vol. 7, no. 9, pp. 285-287, September 1997.

[53] F. L. Teixeira and W. C. Chew, Systematic derivation of anisotropic PML absorbing media in cylindrical and spherical coordinates, *IEEE Microwave Guided Wave Lett.*, vol. 7, no. 11, pp. 371-373, November 1997.

[54] K. S. Yee, Numerical solution of initial boundary value problem involving Maxwell's equations in isotropic media, *IEEE Trans. Antennas and Propagat.*, vol. AP-14, pp. 302-307, 1966.

[55] E. Turkel and A. Yefet, Absorbing boundary layers for wave-like equations, *Applied Numerical Mathematics* - submitted, 1997.

[56] B. Yang, D. Gottlieb and J. S. Hesthaven, Spectral simulations of electromagnetic wave scattering, *J. Comput. Phys.*, vol. 134, pp. 216-230, 1997.

[57] B. Yang, D. Gottlieb and J. S. Hesthaven, On the use of PML ABC's in spectral time-Domain simulations of electromagnetic scattering, in *Proc. of the 13'th Annual Review of Progress in Applied Computational Electromagnetics*, 1997.

[58] L. Zhao and A. C. Cangellaris, A general approach for the development of unsplit-field time-Domain implementations of perfectly matched layers for FD-TD Grid truncation, *IEEE Microwave Guided Wave Lett.* **6**(1996), pp. 209-211.

[59] R. W. Ziolkowski, Time-derivative Lorentz-Material model based absorbing boundary conditions - preprint, 1996.

[60] R. W. Ziolkowski, The design of Maxwellian absorbers for numerical boundary conditions and for practical applications using engineered artificial materials, *IEEE Trans. Antennas and Propagat.*, vol. 45, pp. 656-671, April 1997.